STRUCTURAL AND FUNCTIONAL STUDIES OF RUBRERYTHRIN FROM

DESULFOVIBRIO VULGARIS

by

SHI JIN

(Under the direction of Dr. Donald M. Kurtz, Jr.)

ABSTRACT

Rubrerythrin (Rbr), found in anaerobic or microaerophilic bacteria and archaea, is a non-heme iron protein containing an oxo-bridged diiron site and a rubredoxin-like [Fe(SCys)$_4$] site. Rbr has NADH peroxidase activity and it has been proposed as one of the key enzyme pair (Superoxide Reductase/Peroxidase) in the oxidative stress protection system of anaerobic microorganisms. In order to probe the mechanism of the electron pathway in Rbr peroxidase reaction, X-ray crystallography and rapid reaction techniques were used. Recently, the high-resolution crystal structures of reduced Rbr and its azide adduct were determined. Detailed information of the oxidation state changes of the irons at the metal-binding sites during the oxidation of Rbr by hydrogen peroxide was obtained using stopped-flow spectrophotometry and freeze quench EPR. The structures and activities of Rbrs with Zn(II) ions substituted for iron(III) ions at different metal-binding sites, which implicate the influence of positive divalent metal ions to the Rbr, are also investigated. The molecular mechanism for Rbr peroxidase reaction during the turnover based on results from X-ray crystallography and kinetic studies is proposed.

INDEX WORDS: Rubrerythrin, *Desulfovibrio vulgaris*, NADH peroxidase, Alternative oxidative stress defense system, Crystal structures, Oxidized form, Reduced form, Azide adduct, Hydrogen peroxide, Internal electron transfer, Zinc ion derivatives

STRUCTURAL AND FUNCTIONAL STUDIES OF RUBRERYTHRIN FROM *DESULFOVIBRIO VULGARIS*

by

SHI JIN

B.S., Peking University, P. R. China, 1998

A Dissertation Submitted to the Graduate Faculty of The University Georgia in Partial Fulfillment of the Requirements for the Degree

DOCTOR OF PHILOSOPHY

ATHENS, GEORGIA

2002

STRUCTURAL AND FUNCTIONAL STUDIES OF RUBRERYTHRIN FROM

DESULFOVIBRIO VULGARIS

by

SHI JIN

Approved:

Major Professor: Donald M. Kurtz, Jr.

Committee: Jonathan I. Amster
Michael K. Johnson
Robert S. Phillips
Robert A. Scott

Electronic Version Approved:

Gordhan L. Patel
Dean of the Graduate School
The University of Georgia
August 2002

TABLE OF CONTENTS

Page

CHAPTER

CHAPTER I

INTRODUCTION

I.A. Oxidative stress

Three and a half billion years ago, iron superoxide dismutases (FeSODs) already existed in some anaerobes to help survive the severe environmental conditions, even though atmospheric dioxygen was only 0.1% of the current level (*1*) (**Figure I-1**). With the increasing level of atmospheric oxygen, a result of the evolution of cyanobacteria and geological transformation, dioxygen became a significant biological electron acceptor, which could be used to supply energy to organisms. Dioxygen also functions as a substrate for oxidases and oxygenases. However, oxygen can also be toxic to living organisms. Reactive oxygen species, including oxygen free radicals and hydrogen peroxide (a source of hydroxyl radicals), are generated from normal metabolism as well as from environmental sources, such as radiation, environmental chemicals, etc (*2, 3*). In humans, free radicals are produced by phagocytic cells of the immune system, and are important in the activation of transcription factors and in cell signal transduction and gene expression (*4*). However, adventitious production of free radicals can damage proteins, lipids and DNA, cells and tissues, which is associated with the aging process and more than a hundred chronic diseases (*4*). Oxidative stress is defined as an imbalance between oxidants and antioxidants in favor of the former, potentially leading to biological damage (*5*). An effective oxidative stress defense is essential for life.

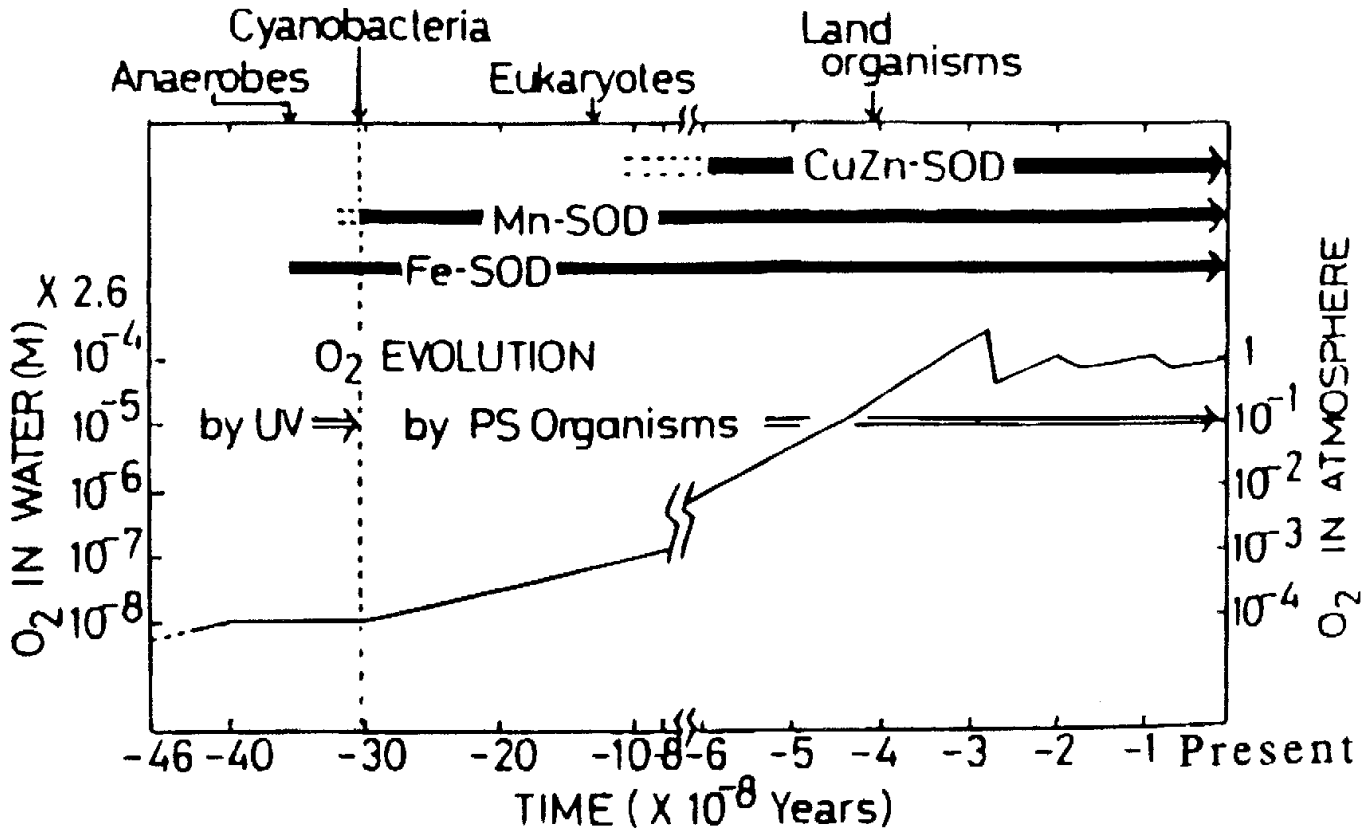

Figure I-1. Oxygen appearance, participation, and metabolism in evolutionary processes. Adapted from (*1*).

I.B. Oxidative stress defense

Nature has evolved defense mechanisms against the effects of reactive oxygen species at different levels: prevention, interception and repair, using both enzymes and non-enzymatic free radical scavengers (*5*). The enzymatic systems that remove reactive oxygen species will be discussed in detail here.

I.B.1 Properties of dioxygen species

Two oxygen atoms bonded together form a paramagnetic dioxygen molecule. Each atom has 5 atomic orbitals: one 1s, one 2s and three 2p, which together form 10 molecular orbitals: $(\sigma_{1s})^2(\sigma_{1s}^*)^2(\sigma_{2s})^2(\sigma_{2s}^*)^2(\sigma_{2p})^2(\pi_{2p})^2(\pi_{2p})^2(\pi_{2p}^*)^1(\pi_{2p}^*)^1(\sigma_{2p}^*)^0$. The ground triplet state of O_2 has two unpaired electrons with parallel spin located in two degenerate π^* orbitals, as required by Hund's rule. If these two electrons instead have anti-parallel spin and are located in either one π^* or separate π^* orbitals, the molecule is in a higher energy singlet state. Triplet O_2 is kinetically less reactive because it can accept a pair of electrons only if both have antiparallel spins, i.e. triplet O_2 is spin forbidden from reacting with singlet atoms or molecules. Due to its positive reduction potentials (**FigureI-2**), O_2 typically reacts by oxidizing other chemical species, although O_2^+ also exists in forms such as $[O_2^+,MF_6^-]$ (M = P, As, Sb, or Pt) (*6*). Adding one electron to one of the π^* orbitals of O_2 yields the superoxide radical anion O_2^-, and adding a second electron yields the peroxide ion, O_2^{2-}. **Table I-1** shows the bonding properties of these diatomic oxygen species. Because the electrons are added to antibonding orbitals, the O-O bond orders and energies are decreased and bond lengths are increased as electrons are added.

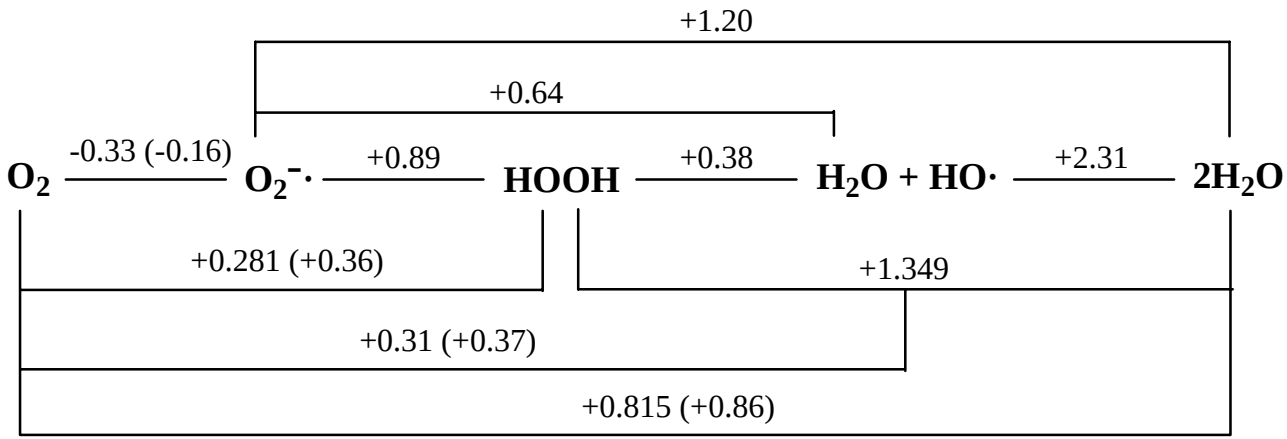

Figure I-2. Standard reduction potentials in volts for dioxygen species in water in equilibrium with O_2 at 1 atm or in parentheses for O_2 at unit activity, at pH 7.0. Adapted from (*6*).

Table I-1. The bonding properties of diatomic oxygen species. Adapted from (*8*).

Formula	e^- in π_{2p}^*	Bond order	Bond energy / $kJ \cdot mol^{-1}$	Bond length /pm	Magnetic properties
O_2^+	↑ _	2.5	626	112.3	Paramagnetic
O_2	↑ ↑	2.0	498	120.7	Paramagnetic
O_2^-	↑↓ ↑	1.5	398	128	Paramagnetic
O_2^{2-}	↑↓ ↑↓	1.0	126	149	Diamagnetic

Table I-2. The bond lengths and angles of H_2O_2. Adapted from (*8*).

H_2O_2	Solid state	Gaseous state
d (O-O) /pm	145.3	147.5
d (O-H) /pm	98.9	95.0
θ	102.7°	94.8°
φ	90.2°	111.5°

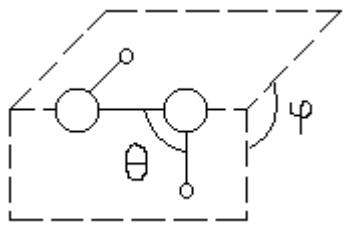

Figure I-3. The structure of H_2O_2.

The redox thermodynamics of O_2 are dependent on the proton activity (*6*). The reduction potentials for dioxygen species in water at pH 7.0, the conditions most relevant to biology, are summarized in **Figure I-2**. O_2 is a very weak one-electron oxidant but a strong two- and four-electron oxidant. However, once the electron source is adequate for the reduction of O_2, all other reduced O_2 species (O_2^-, HOOH, OH·) can be produced by reduction or disproportionation (*6*).

O_2^- has a high reduction potential and acts as a strong one-electron oxidant when protons are available (reaction 1), but not in the absence of protons because of the unstable product O_2^{2-}. O_2^- is a strong Brønsted base in aqueous solution due to its strong tendency towards disproportionation, which consumes protons (reaction 2) (*6, 7*). O_2^- is also a mild reducing agent and a strong nucleophile in reactions with oxidized organic compounds (*7*).

$$O_2^- + e^- + 2H^+ \longrightarrow H_2O_2 \quad (E^\varnothing = 0.89 \text{ V, pH 7}) \tag{1}$$

$$2O_2^- + 2H^+ \rightleftharpoons H_2O_2 + O_2 \quad (K = 4 \times 10^{20}, \text{ pH 7}) \tag{2}$$

The properties of H_2O_2 (H-O-O-H) are a combination of properties of O-H and O-O, as shown in **Table I-2** and **Figure I-3**. The O-H bond in H_2O_2 is chemically similar to the O-H in the water molecule; it can be ionized, and replaced to form H_2O_2 derivatives, such as NaOOH, and $HOSO_2OOH$ (*8*). The -O-O- unit in H_2O_2 is unstable with respect to oxidation to O_2^- (reaction 3), reduction to H_2O (reaction 4) and disproportionation (reaction 5).

$$O_2 + 2e^- + 2H^+ \longrightarrow H_2O_2 \quad (E^\varnothing = 0.28 \text{ V, pH 7}) \tag{3}$$

$$H_2O_2 + 2e^- + 2H^+ \longrightarrow 2H_2O \quad (E^\varnothing = 1.35 \text{ V, pH 7}) \tag{4}$$

$$2H_2O_2 \longrightarrow 2H_2O + O_2 \quad (E^\varnothing = 1.07 \text{ V, pH 7}) \tag{5}$$

Chemicals with reduction potential between 1.35 V and 0.28 V at pH 7, for instance, $E^{\varnothing}(Fe^{3+}/Fe^{2+}) = 0.77$ V, have the thermodynamic capability of catalyzing the decomposition of H_2O_2. H_2O_2 can be activated in the presence of ferrous ions to react with many organic compounds, first observed by Fenton in 1894 (*9*). This reactivity is most likely due to formation of hydroxyl radicals, the most reactive member of the family of oxygen radicals (HO·, RO·, ·O·, HOO·, ROO·, and RC(O)O·) (*6*). The Fenton reaction is most likely a series of reactions (6a-6d):

$$Fe^{2+} + H_2O_2 = Fe^{3+} + OH^- + OH\cdot \quad (6a)$$

$$OH\cdot + H_2O_2 = HO_2\cdot + H_2O \quad (6b)$$

$$HO_2\cdot + H_2O_2 = O_2 + H_2O + OH\cdot \quad (6c)$$

$$Fe^{2+} + OH\cdot = Fe^{3+} + OH^- \text{ (stopped)} \quad (6d)$$

I.B.2. Superoxide dismutase, catalase and peroxidase in aerobic organisms

In biological systems, O_2 molecules that passively diffuse into cells are converted to O_2^- and H_2O_2 by auto-oxidation of respiratory chain components (*2*). O_2^- ions can oxidize the iron-sulfur clusters in dehydratases. The resulting H_2O_2 and the released iron ions can undergo the Fenton reaction, generating OH· that damage proteins and nucleic acids (*2*). The superoxide dismutases (*10*), catalases and peroxidases (*11*) catalyze the decomposition of O_2^- and H_2O_2 and maintain the concentrations of O_2^- and H_2O_2 at tolerable levels in cells.

Superoxide dismutase

Superoxide dismutase (SOD) catalyzes the disproportionation of superoxide to hydrogen peroxide and oxygen (reaction 2). Typically, SOD is classified as three types: CuZnSOD, FeSOD, and MnSOD (*12-14*). CuZnSODs are mostly found in eukaryotes

although they also occur in some bacteria. FeSODs and MnSODs are found in prokaryotes (Fe, Mn), mitochondria (Mn), and plants (Fe) (*15*). A fourth type, Ni-containing SOD, has more recently been found in *Streptomyces griseus* and *S. coelicolor* (*16-18*). FeSOD and MnSOD share homologous amino acid sequences and have similar structures at the mononuclear metal binding site, but their SOD activities are usually metal-specific (*19*). The Fe or Mn ions undergo the reaction 7a and 7b in catalyzing SOD activity where x = 2. CuZnSODs show no sequence or structural homology to Fe/MnSODs, and have a unique imidazolate group bridging Cu(II) and Zn(II) . Copper ion participates in the catalytic reactions (7a and 7b, where x = 1), and zinc ion stabilizes the metal site structure.

$$M^{(x+1)+} + O_2^- \longrightarrow M^{x+} + O_2 \qquad (7a)$$

($M^{(x+1)+}$ = Cu^{2+} (CuZnSOD), Fe^{3+} (FeSOD), Mn^{3+} (MnSOD))

$$M^{x+} + O_2^- + 2H^+ \longrightarrow M^{(x+1)+} + H_2O_2 \qquad (7b)$$

Catalases and peroxidases

In all organisms, H_2O_2 comes mainly from the dismutation of O_2^- (reaction 2) (*20*). Many enzymes, such as glycollate oxidase, D-amino acid oxidase, and urate oxidase also produce H_2O_2 from O_2 without the detectable formation of O_2^- (*9*). There are two types of enzyme that decompose H_2O_2 in cells. One is catalase, which catalyzes the disproportionation of H_2O_2 to water and O_2 (reaction 8), and the other is peroxidase, which catalyzes the reduction of H_2O_2 to water using an external electron donor as substrate (reaction 9). Catalase-peroxidases, a subgroup of the catalase family, have both catalase and peroxidase activities optimized at different pH values (*21*).

$$H_2O_2 \xrightarrow{\text{catalase}} 2H_2O + O_2 \qquad (8)$$

$$H_2O_2 + SubH_2 \xrightarrow{\text{peroxidase}} 2H_2O + Sub \quad (9)$$

Most aerobic organisms and several anaerobic bacteria have catalases (*9*). Catalases are usually homo-tetrameric proteins, and each subunit contains a heme prosthetic group. Non-heme binuclear manganese-containing pseudocatalases have also been found in a few microorganisms, such as *Lactobacillus plantarum* and *Thermoleophilum album* (*22, 23*). The mechanism of heme-catalase reactions involves a high-valent oxoferryl intermediate, as shown in reaction 10a and 10b, where $P^{\bullet+}$ = porphyrin cation radical, and $P^{\bullet+}Fe(IV)=O$ is referred to as compound I (*24*):

$$\text{Catalase-PFe(III)} + H_2O_2 \longrightarrow \underset{\text{Compound I}}{P^{\bullet+}Fe(IV)=O} + H_2O \quad (10a)$$

$$\underset{\text{Compound I}}{P^{\bullet+}Fe(IV)=O} + H_2O_2 \longrightarrow \text{catalase-PFe(III)} + H_2O + O_2 \quad (10b)$$

There are several peroxidases (cf. **Table I-3**), including glutathione peroxidase, NADH peroxidase, cytochrome c peroxidase, non-specific peroxidase, chloroperoxidase, and ascorbate peroxidase, etc., distinguished by the exogenous electron donors. The O_2-carrying proteins, hemoglobin and myoglobin, have also been observed to have peroxidase activities *in vitro*.

Glutathione peroxidase (GPx) catalyzes the reduction of H_2O_2 by reduced glutathione (GSH). GPx is found in animals and some algae and fungi (*25*). GSH is a tripeptide (glutamic acid-cysteine-glycine). Two GSH molecules joined together by a disulfide bond between the two cysteines form the oxidized glutathione, GSSG. GPx contains four subunits. In each subunit, a selenium atom replaces the sulfur in the cysteine residue at the active center. The mechanism of GPx catalyzed H_2O_2 reduction is (*26*):

$$GSH + \text{GPx-SeOH} \longrightarrow \text{GPx-SeSG} + H_2O \quad (11a)$$

$$GSH + \text{GPx-SeSG} \longrightarrow \text{GPx-SeH} + GSSR \quad (11b)$$

Table I-3. Types and properties of peroxidases.

Protein		Source	Active center structures	Substrate
Glutathione peroxidase		Animals, algae and fungi	Selenocysteine	GSH
Cytochrome c peroxidase		Yeast, bacteria	Heme	Cyt-c(Fe^{2+})
NADH peroxidase	Heme containing NADH peroxidase	*E.coli*	Heme	NADH
	NADH peroxidase	Lactic acid bacteria	FAD, Cys-SOH	
	Rbr, Ngr	Anaerobic bacteria and archaea	Diiron site, $[Fe(SCys)_4]$	
Nonspecific peroxidase: Lactoperoxidase, myeloperoxidase, thyroid peroxidase, uterine peroxidase, horseradish peroxidase, etc.		Plant and bacteria	Heme	Nonspecific substrates: Guaiacol, benzidine, *o*-dianisidine, etc.
Chloroperoxidase, bromoperoxidase		Plants and bacteria	Heme	Cl^-, Br^-, I^- and nonspecific substrates
Ascorbate peroxidase		Higher plants and green alga	Heme	Ascorbate

$$H_2O_2 + GPx\text{-}SeH \longrightarrow GPx\text{-}SeOH + H_2O \quad (11c)$$

In lactic acid bacteria that cannot synthesize heme, such as *Streptococcus faecalis* (*27*), FAD-dependent NADH peroxidases (Npx) are found which catalyze reaction 12:

$$NADH + H^+ + H_2O_2 \longrightarrow NAD^+ + 2H_2O \quad (12)$$

Npx is a unique flavoprotein, because it catalyzes reaction 12 by an unusual cysteine-sulfenic acid (Cys-SOH) redox center in the absence of metal ion cofactors (*28*). The oxidized enzyme is reduced by NADH in an initial priming step; in the steady state the enzyme cycles between EH_2-NADH* and E-NADH forms (*29*) according to steps 12a-12e:

$$E(FAD, Cys\text{-}SOH) + NADH + H^+ \longrightarrow EH_2(FAD, Cys\text{-}SH) + NAD^+ + H_2O \quad (12a)$$

$$EH_2 + NADH \longrightarrow EH_2\text{-}NADH^* \quad (12b)$$

$$EH_2\text{-}NADH^* + H_2O_2 \longrightarrow E\text{-}NADH + H_2O \quad (12c)$$

$$E\text{-}NADH + H^+ \longrightarrow EH_2\text{-}NAD^+ + H_2O \quad (12d)$$

$$EH_2\text{-}NAD^+ \longrightarrow EH_2 + NAD^+ \quad (12e)$$

Heme-containing nonspecific peroxidases are found in plants and bacteria. These peroxidases are able to function on a wide range of substrates, such as guaiacol, benzidine, *o*-dianisidine, etc. Among these peroxidases, horseradish peroxidase is the best characterized (*30*). It undergoes a series of reactions with H_2O_2 and a reducing substrate, SH_2 (reaction 13a, 13b, 13c) (*9, 30*). Reaction 13a is a two-electron step in which the ferric heme active site is oxidized by H_2O_2 to give Compound I. SH· radicals, generated from one-electron reaction 13b and 13c, will disproportionate to S and SH_2 or can combine to S_2.

$$\underset{\text{Resting enzyme}}{PFe(III)} + H_2O_2 \longrightarrow \underset{\text{Compound I}}{P^{\cdot+}Fe(IV)=O} \quad (13a)$$

$$\underset{\text{Compound I}}{P^{\cdot+}Fe(IV)=O} + SH_2 \longrightarrow \underset{\text{Compound II}}{PFe(IV)=O} + SH^{\cdot} \quad (13b)$$

$$\underset{\text{Compound II}}{PFe(IV)=O} + SH_2 \longrightarrow \underset{\text{Resting enzyme}}{PFe(III)} + SH^{\cdot} \quad (13c)$$

Cytochrome c peroxidase (Ccp) is a membrane protein found in yeast mitochondria and some bacteria (*31, 32*). A stable intermediate of enzyme-substrate complex was observed in the catalytic reaction 14a and 14b, which is different from Compound I intermediate observed in other peroxidases. For most peroxidases, removing an electron from the porphyrin ring generates the radical in the intermediate, but, for Ccp, the electron is removed from a Trp residue that is in van der Waals contact with the heme (*30*).

$$\text{Enzyme} + H_2O_2 \longrightarrow \text{complex (complex: heme Fe(IV)=O + Trp radical)} \quad (14a)$$

$$\text{Complex} + 2\text{cyt-c}(Fe^{2+}) \longrightarrow \text{enzyme} + 2\text{cyt-c}(Fe^{3+}) + 2OH^- \quad (14b)$$

Chloroperoxidase catalyzes the addition of halogen atoms onto various substrates in the presence of H_2O_2 and halide ions (X^-), in the overall reaction (*9*):

$$SubH + X^- + H_2O_2 + H^+ \longrightarrow SubX + 2H_2O \quad (15)$$

Ascorbate peroxidases (Apx) are found in chloroplasts of higher plants and some green alga (*33*), where neither catalases nor other peroxidases are found. Apx catalyzes the reaction 16:

$$\text{Ascorbate} + H_2O_2 \longrightarrow 2H_2O + \text{dehydroascorbate} \quad (16)$$

Heme-containing NAD(P)H peroxidase has also been found in *Escherichia coli* (*34*).

I.B.3. Superoxide reductase, and peroxidase in anaerobic bacteria and archaea

Strictly anaerobic bacteria and archaea have a wide range of oxygen tolerance. Although some anaerobic bacteria and archaea have genes encoding SOD or catalase, many others do not have such genes (*35, 36*) or lack detectable SOD or catalase activities

(*37*). The O_2 generated from O_2^- and H_2O_2 decompositions by SOD/catalase (reaction 2 and 8) could be toxic to the anaerobic species. An alternative oxidative stress defense system is proposed to function in the cytoplasm of at least some anaerobic microorganisms (*38, 39*) (**Figure I-4**). Superoxide reductase (SOR) and rubrerythrin (Rbr), a NADH peroxidase, are proposed to be an enzyme pair that catalyzes reduction of O_2^- and H_2O_2 to water in sulfate-reducing bacteria.

One of the SORs, rubredoxin oxidoreductase (Rbo), found in some sulfate-reducing bacteria (*40*), is a nonheme homodimeric protein with two mononuclear iron centers (**Figure I-5**). Center I is a rubredoxin-like $[Fe(SCys)_4]$ site and Center II is a $[Fe(NHis)_4(SCys)]$ site that resembles the single iron site in neelaredoxin, an SOR from the sulfate-reducing bacterium *Desulfovibrio gigas* (*41, 42*). Rbo has been demonstrated to catalyze the reduction of superoxide to hydrogen peroxide (reaction 1) *in vitro*, but little or no SOD activity was detected for Rbo (*43, 44*). The Center I is assumed to transfer electrons to Center II, where superoxide is rapidly reduced (*43*). A Δ*rbo* strain of *D. vulgaris* was found to be more sensitive to both oxygen and superoxide than the wild type (*38, 45*). Also, *Desulfoarculus baarsii* Rbo was able to restore aerobic growth to a mutant *E. coli* strain which lacks cytoplasmic SODs (*46, 47*).

A nonheme diiron protein, rubrerythrin (Rbr), and a rubrerythrin-like protein nigerythrin (Ngr), found so far exclusively in air-sensitive bacteria and archaea, have been observed to have NADH peroxidase activity *in vitro* (*48, 49*), and were implicated to protect air-sensitive microbes from H_2O_2 stress (*38, 50, 51*). The structure of *D. vulgaris* Rbr and mechanism of reaction 12 catalyzed by Rbr are the subjects of investigations in this thesis.

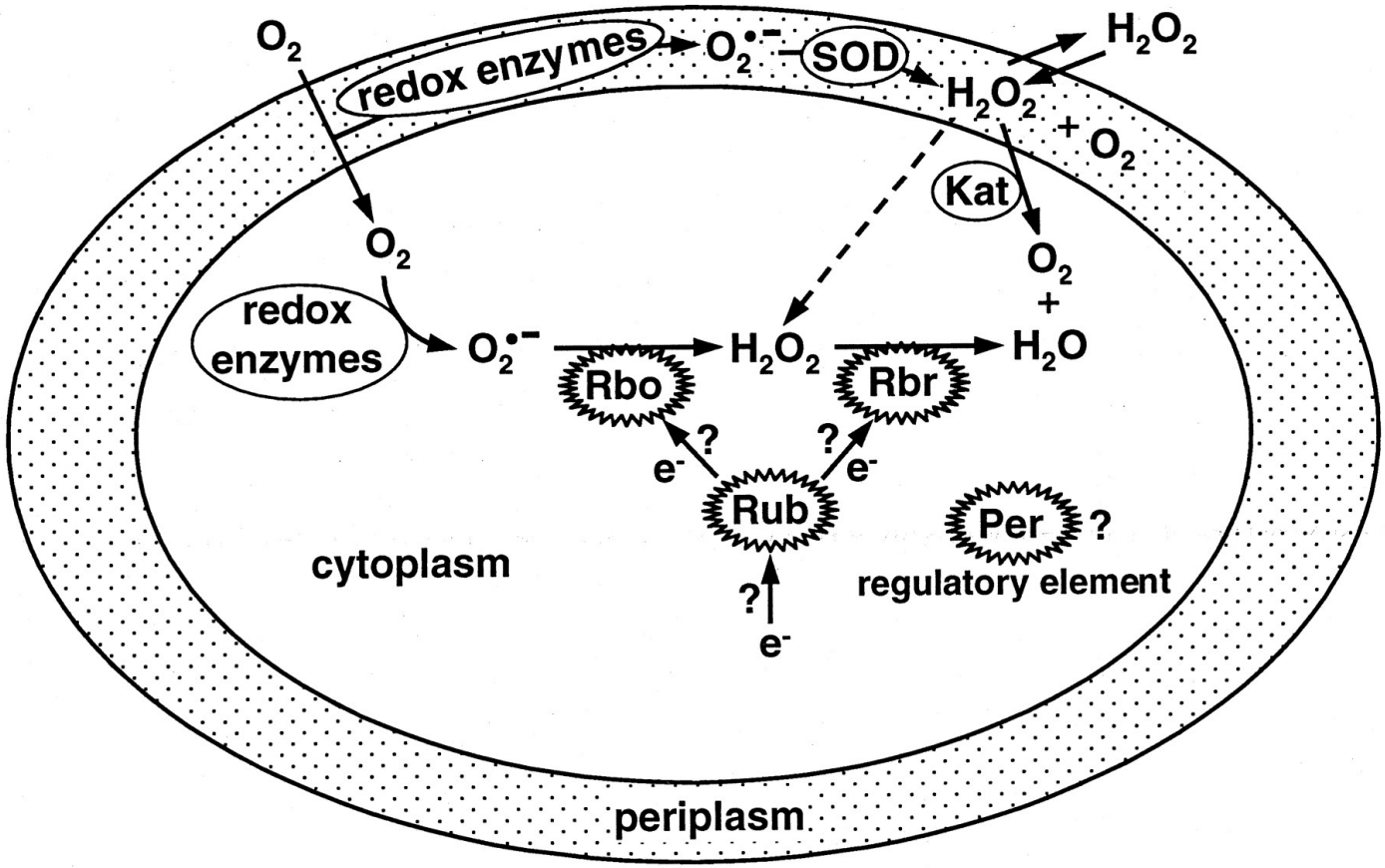

Figure I-4. Proposed model for oxidative stress protection by Rbo and Rbr in *D. vulgaris* (*38*).

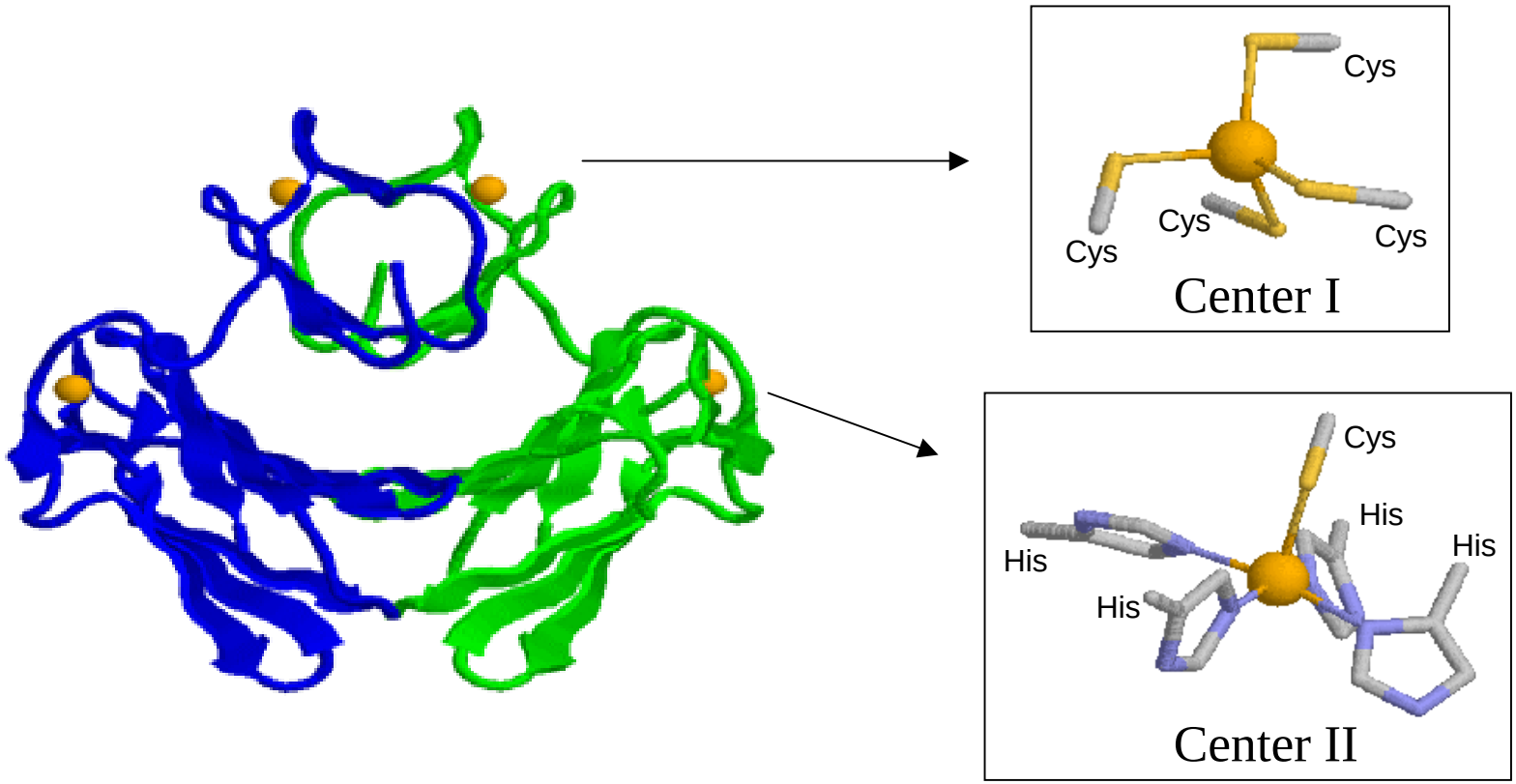

Figure I-5. The structure of the homodimer (left) and Centers I and II (boxed, right) in rubredoxin oxidoreductase (Rbo) from *D. desulfuricans* (*40*). Spheres represent iron atoms.

I.C. Structural and spectroscopic properties of Rbr

I.C.1. Sources and amino acid sequences

Rubrerythrin (Rbr) is an ~190-residue protein, which was first isolated from the anaerobic sulfate reducing bacteria *Desulfovibrio (D.) vulgaris* (*52-54*), and *D. desulfuricans* (*54*). A second Rbr-like protein called nigerythrin, isolated from *D. vulgaris*, has an amino acid sequence that is 34% identical to that of *D. vulgaris* Rbr, and contains the same two iron sites (*54*). Rbr was more recently isolated from another anaerobic bacterium, *Clostridium (C.) perfringens* (*37*). An Rbr-like protein was also isolated and partially sequenced from *Spirillum volutans*, a micro-aerophilic bacterium (*50*). The amino acid sequence of Rbr indicates a diiron-protein-like domain that contains two characteristic $EX_{30-34}EX_2H$ motifs, and a C-terminal rubredoxin-like domain that has two CX_2C motifs (**Figure I-6**). *Rbr*-like sequences, i.e., a single open reading frame containing these two motifs, have also been found in the genomes of the anaerobic bacteria *C. acetobutylicm* (2 found) (*55*), *C. perfringens* (2 found) (*55*), *C. dificile* (*55*), *Thermotoga maritima* (*55*), *Porphyromonas gingivalis* (*55*), and the archaea *Methanococcus jannaschii* (*55*), *M. thermoautotrophicum* (2 found) (*55*), *Archaeogolobus fulgidus* (4 found) (*55*), *Pyrococcus abysii* (*55*), and *P. furiosus* (*55*).

I.C.2. Three-dimensional structure

D. vulgaris Rbr is the best characterized among those that have been isolated. It is a 44-kDa homodimer in solution, as shown by gel filtration (*52, 56*). However, the electrospray ionization (ESI) with time-of-flight (TOF) mass spectrometry studies of Rbr revealed a tetramer (*57*), which agrees with the X-ray crystal structure of *D. vulgaris* Rbr (*58*).

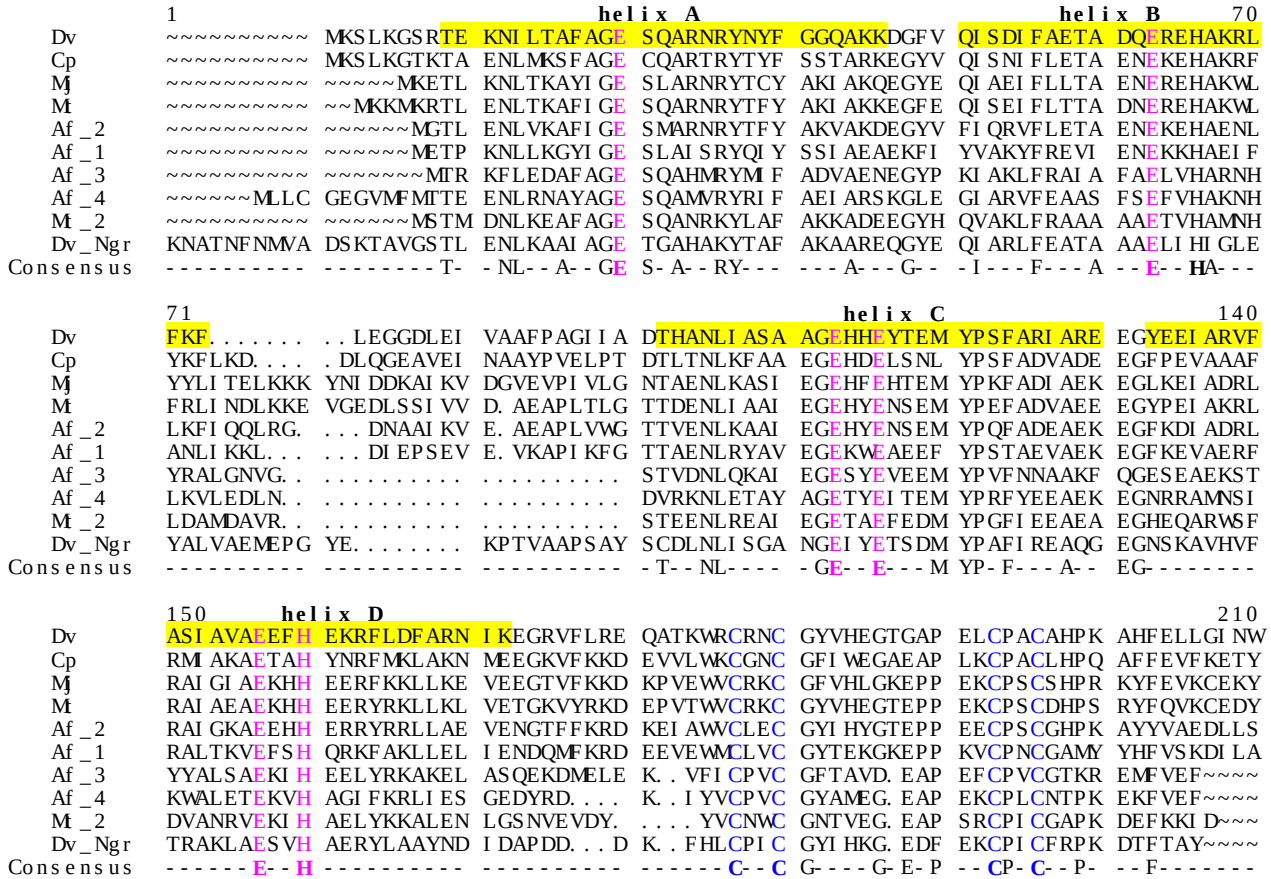

Figure I-6. Amino acid sequence alignment using computer programs PILUP and PRETTY (Wisconsin Package Version 9.1, Genetics Computer Group, Madison, MI) of Rbrs from *Desulfovibrio vulgaris* (Dv) (134119), *Clostridium perfringens* (Cp) (1710808), *Methanococcus jannaschii* (Mj) (2500684), *Methanobacterium thermoautotrophicum* (Mt) (Mt_1, 2621845; Mt_2, 2621913), *Archaeoglobus fulgidus* (Af) (Af_1, 2649783; Af_2, 2649773; Af_3, 2648916; Af_4, 2648207). Ngr = nigerythrin. Numbers in parentheses are NCBI Genbank accession numbers. Yellow shaded residues indicate helical regions in *D. vulgaris* Rbr, and magenta and blue highlighted residues indicate metal ligands in the diiron and rubredoxin-like sites, respectively. Adapted from (*49*).

In the crystal, Rbr is a homotetramer. Each subunit has two domains: one N-terminal diiron-binding domain with 146 residues in the form of a four-α-helix bundle, and one C-terminal rubredoxin-like [$Fe(SCys)_4$] domain with 45 residues. Two different types of dimer interactions occur within the tetramer, as shown in **Figure I-7**. One interaction is a "head-to-head" dimer involving a two-stranded β-sheet between the long non-helical loops of the four-helix bundle diiron domains. The other is a "head-to-tail" dimer contact involving one rubredoxin-like iron domain in one subunit and a diiron domain in the other. This latter contact makes the shortest inter-subunit Fe-Fe distance ~ 12 Å.

The structure of the Rbr dimer in solution has not been conclusively established. It could be an equilibrium between "head-to-tail" and "head-to-head" dimers. The tetramer shown in the ESI-TOF mass spectra of Rbr is apparently due to aggregation of the dimers because of the low ionic strength of the buffer used for the mass spectrometry experiments (*57*). The tetramer in the crystal could be due to the precipitant (PEG) used for crystallization of Rbr, which is well known to cause protein aggregation.

I.C.3. Iron centers

The UV-vis absorption spectrum (**Figure I-8**) of Rbr in the oxidized form shows two prominent features: one is at 494 nm (ε = 10,600 $M^{-1}cm^{-1}$ per dimer), due to the [$Fe(SCys)_4$] site, which resembles that of oxidized rubredoxins, and the other is at 370 nm, which is due to combined absorptions of the Fe(III)-μ-oxo-Fe(III) and [$Fe(III)(SCys)_4$] sites. Although Rbr isolated from *D. vulgaris* ("as-isolated" Rbr) showed lower absorbance ratios of A_{370}/A_{494} (~1.7) and lower iron content (~4 per dimer) than recombinant *D. vulgaris* Rbr (A_{370}/A_{494} ~2 and 6 iron per dimer), both "as-isolated" and recombinant Rbrs showed identical signals in the EPR spectra and Mössbauer spectra, i.e.

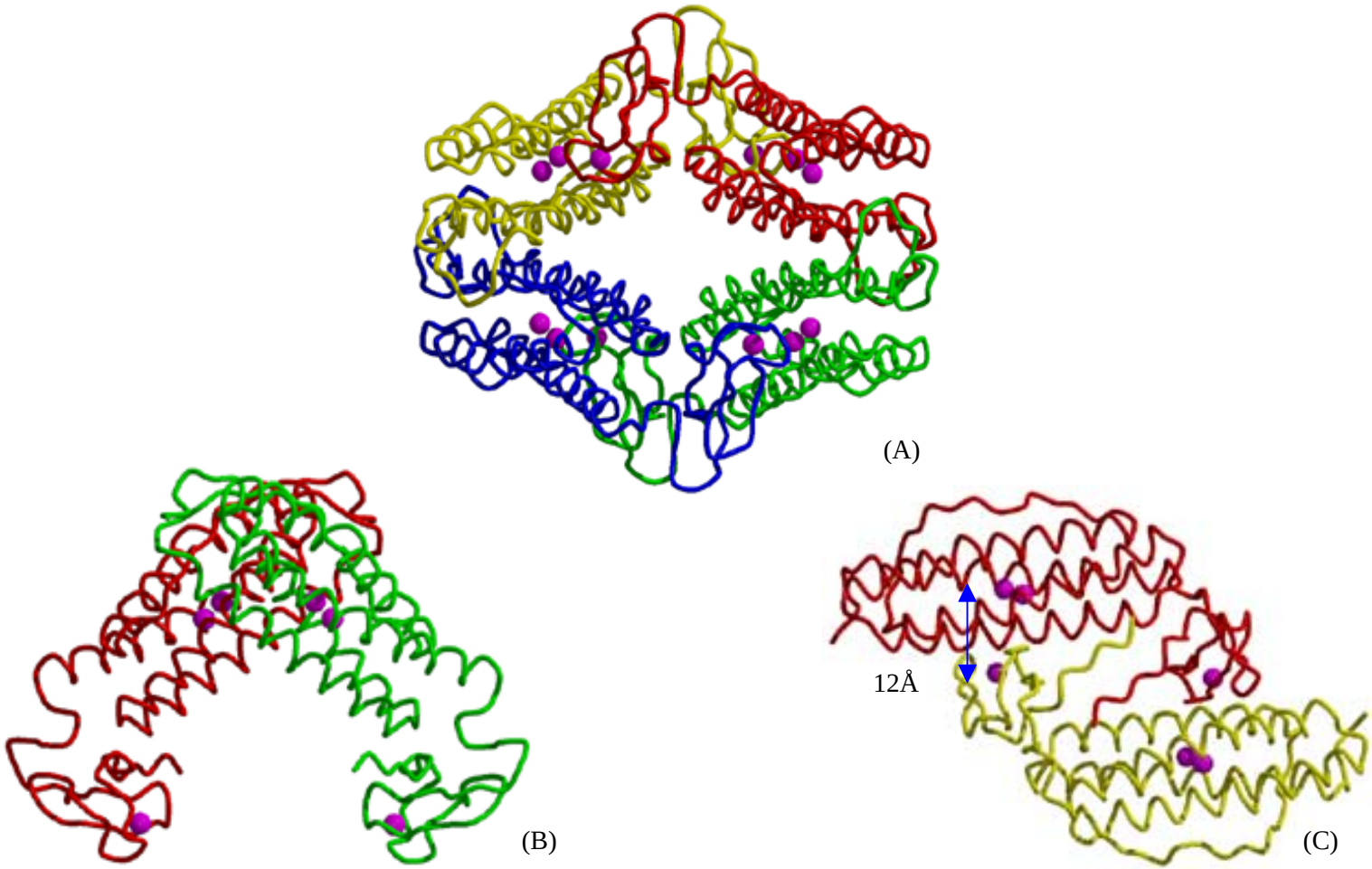

Figure I-7. Views of the crystal structure of recombinant *D. vulgaris* Rbr (PDB code: 1ryt). (A) Rbr tetramer. (B) Head-to-head dimer. (C) Head-to-tail dimer. Spheres represent iron atoms. Arrows indicates distance between $[Fe(SCys)_4]$ and diiron sites across the head-to-tail dimer interface.

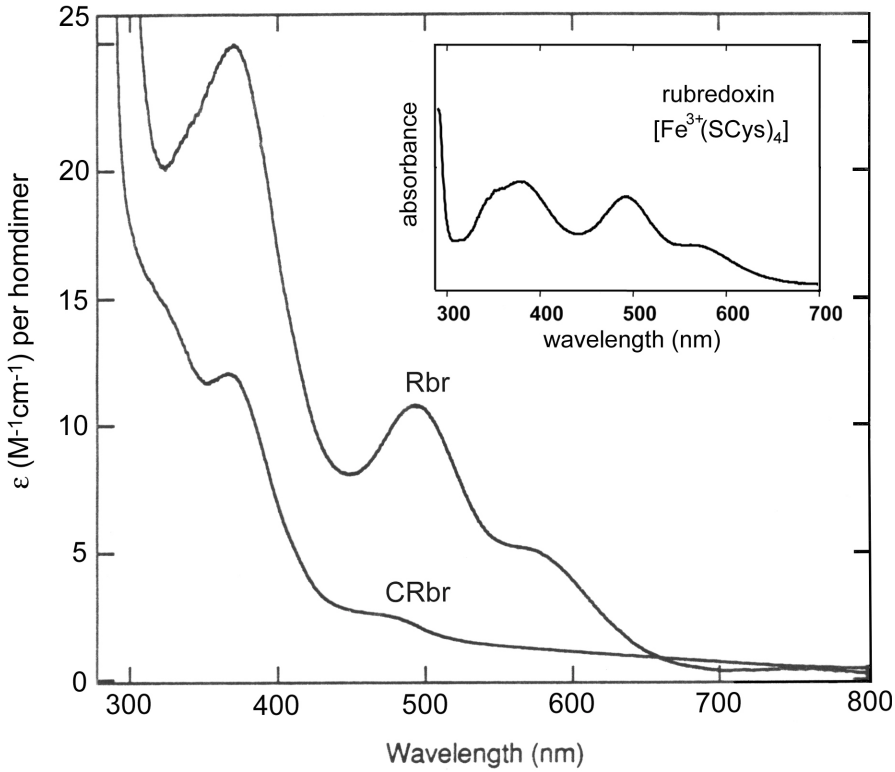

Figure I-8. Visible absorption spectra of oxidized recombinant *D. vulgaris* Rbr and an engineered form, CRbr, in which the C-terminal [Fe(SCys)$_4$] domain was removed. Inset: visible absorption spectrum of oxidized rubredoxin, which contains only an [Fe(SCys)$_4$] site. Adapted from (*105*).

[Fe(III)$(SCys)_4$] site signals and a minor portion of mixed-valent diiron site signals in the EPR spectra and the diferric site signals in Mössbauer spectra (*52, 59*). The reduced recombinant Rbr is colorless and EPR silent, but the reduced Rbr azide adduct is EPR active with an integer spin signal at g ~ 19.8, which indicates a diferrous site in Rbr (*59*). The resonance Raman spectra of as-isolated *D. vulgaris* Rbr also demonstrated the presence of both [Fe(III)$(SCys)_4$] and oxo-bridged diiron(III) sites (*56*). "Chopped" rubrerythrin (CRbr) in which the [Fe$(SCys)_4$] domain was deleted, but which has an identical N-terminal diiron domain as *D. vulgaris* Rbr (residues 1-152), is also a homodimer and contains one oxo-bridged diiron site per subunit (*59*) (**Figure I-8**).

In the crystal structure of recombinant *D. vulgaris* Rbr, (**Figure I-9**) the Fe1 and Fe2 at the diiron site share a bridging oxo ion and two bidentate carboxylates from Glu53 and Glu128. With a terminal bidentate carboxylate ligand from Glu20 and a terminal monodentate carboxylate ligand from Glu97 for Fe1, and a terminal bidentate carboxylate ligand from Glu94 and Nδ ligand from His131 for Fe2, the two iron atoms are approximately octahedrally coordinated. The [Fe$(SCys)_4$] center with four sulfur ligands from Cys158, Cys161, Cys174 and Cys177 forms a pseudo-tetrahedral coordination structure. His56, which is close to the diiron center, forms a hydrogen bond with the carbonyl of Cys161 that furnishes a ligand to the [Fe$(SCys)_4$] center across the "head-to-tail" dimer subunit interface. In that position, His56 conceivably plays a key role in electron transfer reactions between the two iron sites. The diiron site structure in Rbr resembles those in a class of O_2 activating enzymes, which are discussed in Section I.D.

More recently, X-ray crystallography studies of "as-isolated" *D. vulgaris* Rbr indicated a Zn, Fe binuclear site structure (*60, 61*), which is in conflict with the previous

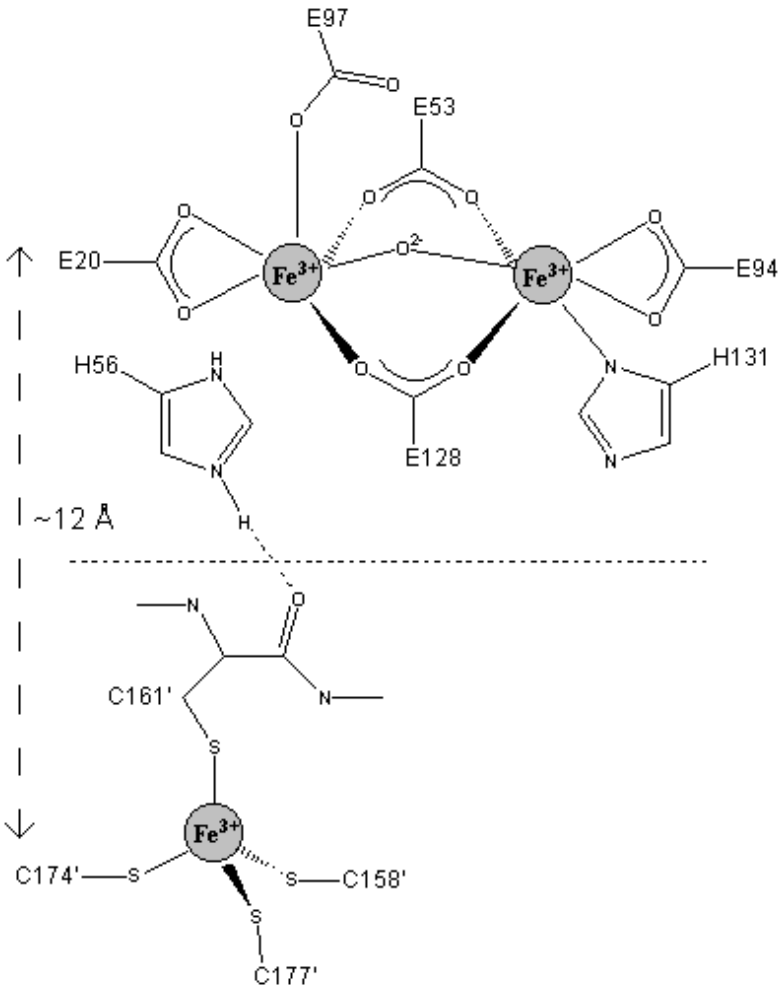

Figure I-9. Schematic drawing of *D. vulgaris* Rbr iron sites across the "head-to-tail" dimer interface (*58*).

spectroscopic evidence on the same as-isolated protein. The coordination properties of the binuclear sites are significantly different from that of the X-ray crystal structure of recombinant *D. vulgaris* Rbr (*58*). Whether the putative zinc atom was introduced during the isolation of Rbr or the crystallization step is not clear. The functional wild type Rbr in *D. vulgaris* is still considered to be an all-iron protein with a diiron site and a rubredoxin-like site in each subunit. A diiron site was also clearly identified by EPR spectroscopy in nigerythrin, as isolated from the same organism (*54*).

The major difference in the "as-isolated" Rbr structure is found at the binding site presumed to be occupied by Zn (**Figure I-10** (A)). The Zn is tetrahedrally coordinated with one terminal monodentate carboxylate ligand from Glu20, two bidentate carboxylates from Glu53 and Glu128, and one Nδ ligand from His56. The movement of Zn away from Glu97 and towards His56 is similar to the Fe1 in the crystal structure of the recombinant Rbr E97A variant (**Figure I-10** (B)). But in E97A Rbr, a solvent bridge was still observed between Fe1 and Fe2 (*62*).

I.D. Other non-heme diiron proteins

A class of non-heme iron proteins that activate dioxygen feature a diiron cluster buried in four α-helix bundles with a hydrophobic core (**Figure I-11**). The two irons are separated by distances ranging from 3 - 4 Å, and have ligand sets consisting of histidines as terminal ligands and carboxylate groups as bridging and or terminal ligands, and a bridging O(H) (*63*). This class of proteins is involved in either oxygen-carrying or activation, except purple acid phosphatase, which catalyzes hydrolysis of phosphate esters (*64*).

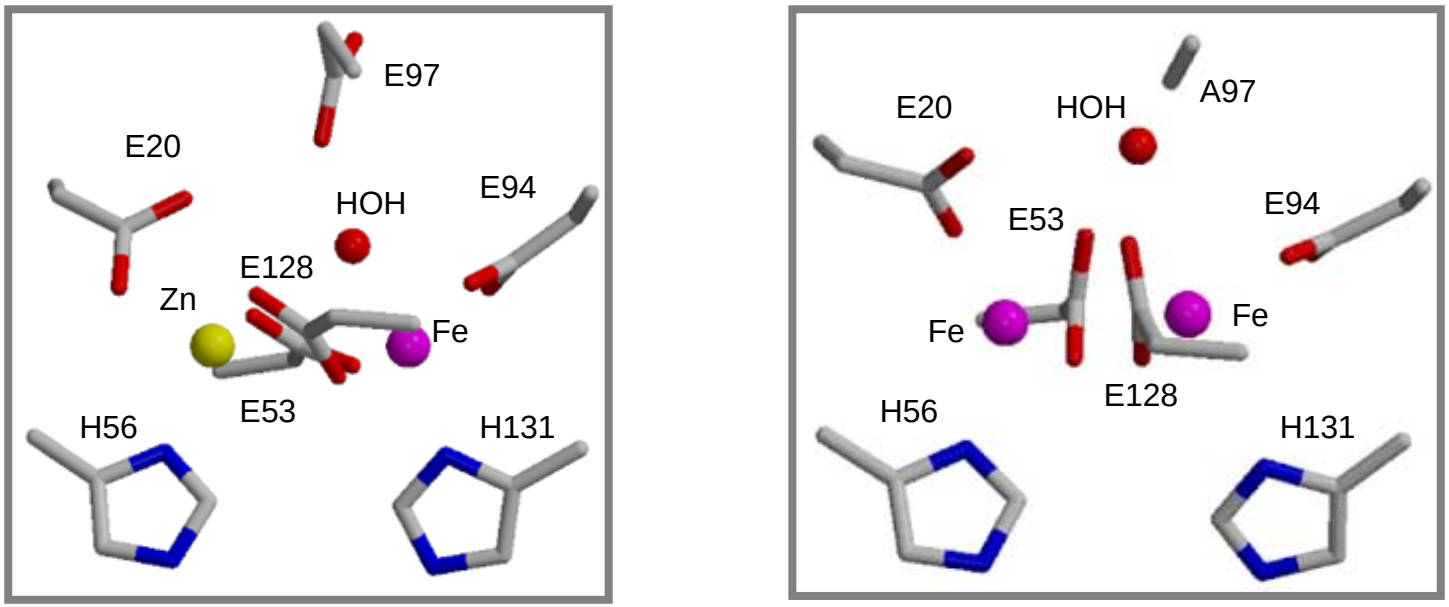

(A) (B)

Figure I-10. The diiron site structures of *D. vulgaris* Rbrs. (A) Rbr with Zn (yellow sphere) substituted at diiron site (*60*, *61*). (B) Rbr E97A (*62*) .

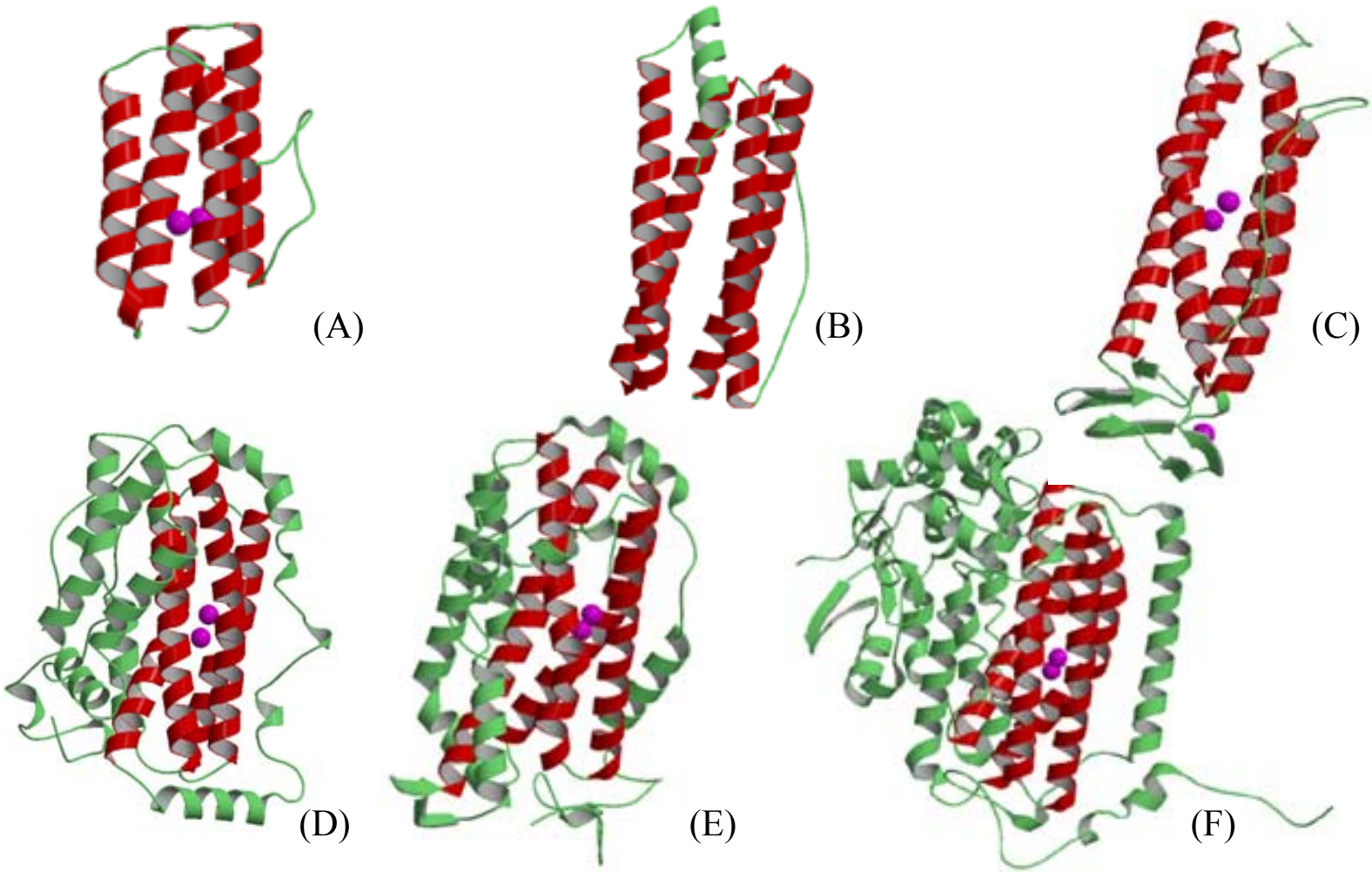

Figure I-11. Tertiary structures of some diiron proteins: (A) hemerythrin (PDB code: 1hmo), (B) ferritin (1eum), (C) Rbr (1ryt), (D) stearoyl acyl carrier protein Δ^9-desaturase (1afr), (E) ribonucleotide reductase R2 α subunit (1rib), (F) methane monoxygenase hydroxylase α subunit (1mty). The iron atoms (spheres) are colored in magenta, and the four-helix bundle is colored in red in each protein subunit.

I.D.1. Hemerythrin and myohemerythrin

Oxygen carriers, hemerythrins (Hrs) and myohemerythrins (MyoHrs), which reversibly bind O_2, were found in different body parts of marine invertebrates (*65*). Hr often occurs as an octamer, whereas MyoHr is invariably monomeric. Their tertiary structure is the smallest and simplest one among the diiron class of proteins, consisting only of a four-helix bundle and a loop at the beginning (*66*). The five terminal histidine ligands, two bridging carboxylate ligands, and a μ-oxo/hydroxo ligand are found in the diiron centers in all deoxy-, oxy-, met- and azidomet- forms of Hr as shown in their crystal structures (*67, 68*). (See **Figure I-12**.) Therefore, the distances between Fe1 and Fe2 are fixed at 3.2 Å to 3.3 Å in all forms. Unlike other diiron proteins, the orientation of the Fe1-Fe2 axis is approximately perpendicular to the long axis of the four-helix bundle. The Fe1 is six-coordinated while Fe2 is five-coordinated in deoxy- and met-forms, which leaves an open position for exogenous ligands (O_2 in the deoxy form and azide in the met form) to bind with Fe2 in an end-on manner, without significant change of amino acid ligands around the two irons.

I.D.2. Methane monoxygenase

Methane monoxygenase (MMO) catalyzes the oxidation of methane to methanol by O_2 with electrons transferred from NADH in methanotrophic bacteria (*69, 70*). MMO consists of three proteins: a reductase (MMOR), a coupling protein B (MMOB), and the hydroxylase (MMOH). The dioxygen activation and substrate hydroxylation occur at the diiron center buried in the four-helix bundle of α-subunit in an $\alpha_2\beta_2\gamma_2$ oligomer of MMOH. In all crystal structures of the oxidized form of MMOH, both Fe1 and Fe2 are octahedrally coordinated, each has a histidine ligand, and a terminal monodentate

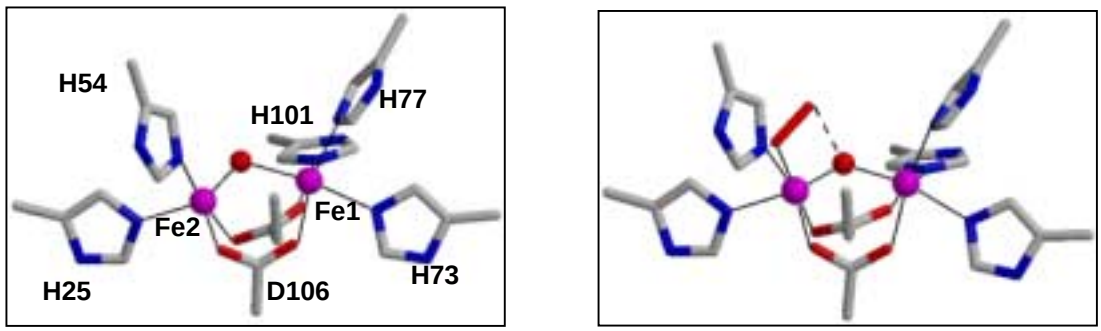

deoxyHr oxyHr

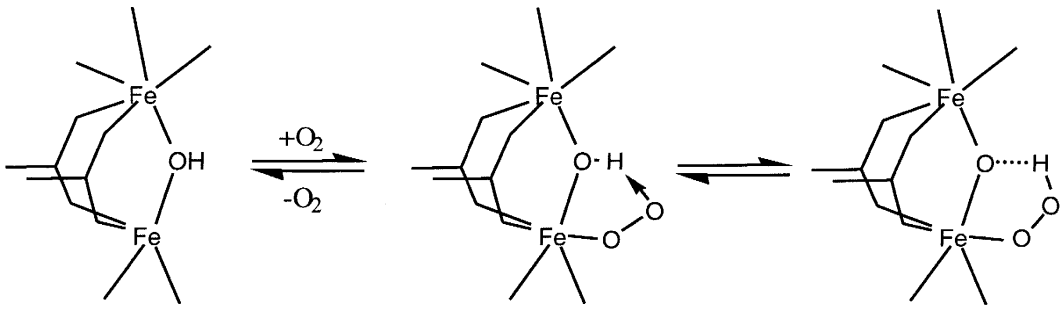

deoxy oxy

Figure I-12. The diiron site structures of Hr in deoxy form (1hmd) and oxy form (1hmo), and (bottom) the mechanism of O_2 binding at the diiron site of Hr and myoHr.

carboxylate ligand, however, Fe1 has an extra water ligand and Fe2 has an extra terminal monodentate carboxylate ligand. (See **Figure I-13**.) The two irons share a bridging hydroxide ion and a bridging bidentate carboxylate ligand, and a third bridging ligand either solvent or small organic compounds. In the reduced form crystal structures, the most significant change is the shift of one of the carboxylate ligands of Fe2 (E243 in **Figure I-13**). E243 replaces the hydroxide ligand to form a bidentate ligand to Fe2, and also a monodentate ligand to Fe1. The Fe2 site shows higher flexibility than Fe1 in the crystal structures. The single turnover reaction of MMOH with O_2 has allowed detection of several intermediates using UV-Vis, EXAFS and Mössbauer spectroscopies (*71*). The structures of MMOH-P, a μ-1,2 peroxo diferric complex, and MMOH-Q, a diamond core $(\mu\text{-}O)_2$ diferryl complex, have been proposed as shown in the bottom of **Figure I-13**.

I.D.3. Ribonucleotide reductase R2

Ribonucleotide reductase catalyzes the reduction of ribonucleotides to deoxyribonucleotides in DNA synthesis (*72*). The β subunit of the $\alpha_2\beta_2$ tetramer in RNR class I, namely, RNR-R2, contains the diiron center (*66*). An adjacent stable tyrosine radical is generated during the oxidation of the diiron site by O_2. This tyrosine radical is involved in subsequent catalytic reactions in RNR-R1, the α subunit of the $\alpha_2\beta_2$ tetramer in RNR class I. The crystal structure of the reduced diferrous form of RNR-R2 reveals a quite symmetric diiron site (**Figure I-14** (top)). Both Fe1 and Fe2 have a tetrahedral geometry. Each iron has a histidine ligand and a terminal monodentate carboxylate ligand, which belongs to the EX_2H motif, and two bridging bidentate carboxylate ligands. When oxidized to diferric, the distance between Fe1 and Fe2 is shortened from 3.9 Å to 3.4 Å with formation of a μ-oxo bridge (**Figure I-14** (middle)). Both of the irons become

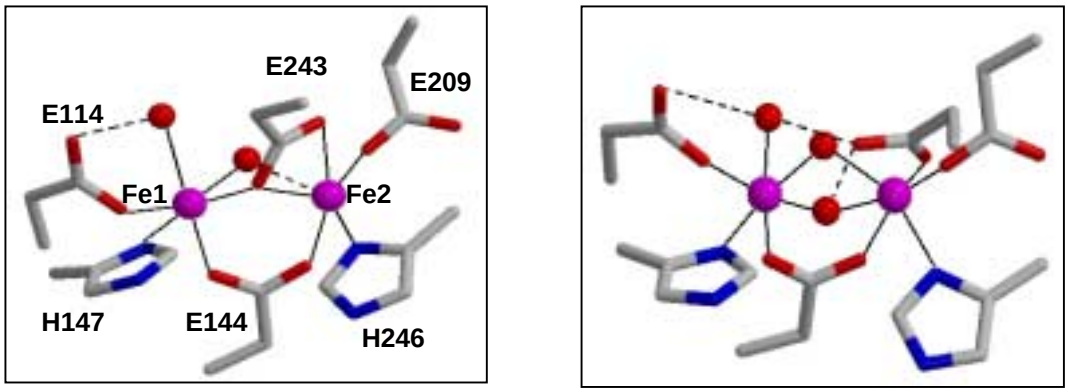

$MMOH_{red}$ $MMOH_{ox}$

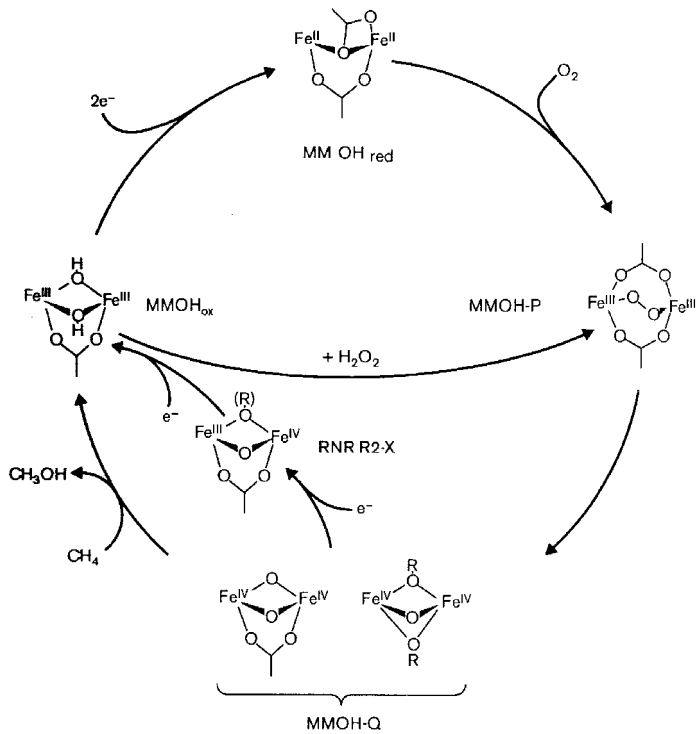

Figure I-13. The diiron site structures of MMOH in reduced ($MMOH_{red}$) (1fyz) and oxidized ($MMOH_{ox}$) (1mty) forms, and (bottom) the catalytic cycle of MMOH and RNR R2, adapted from (*70*).

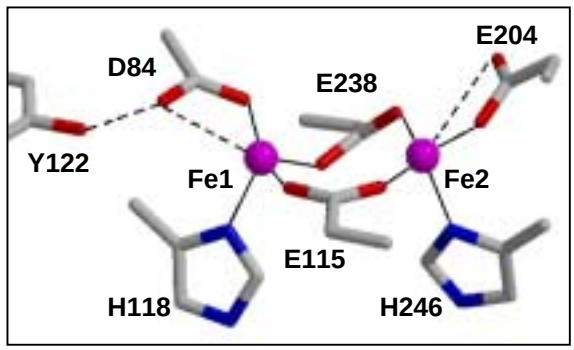

RNR $R2_{red}$

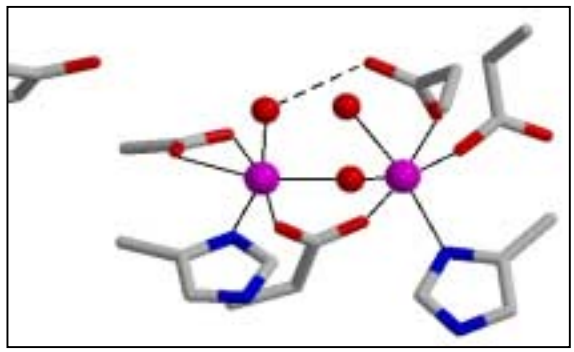

RNR $R2_{ox}$

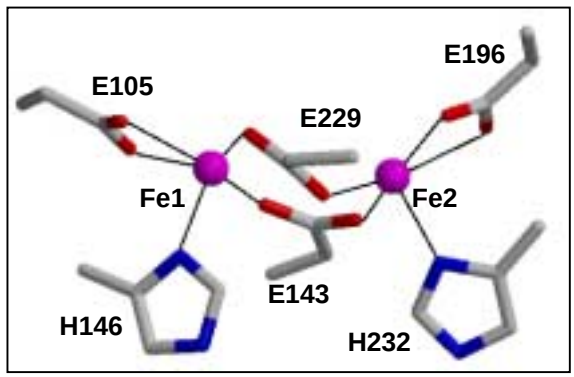

Δ9D

Figure I-14. The diiron site structures of RNR R2 in (top) reduced form (RNR $R2_{red}$) (1xik) and (middle) oxidized form (RNR $R2_{ox}$) (1rib), and (bottom) the reduced form of Δ9D (1afr).

octahedrally coordinated with a solvent ligand added to each iron and rearrangements of three of the four carboxylate ligands. Spectroscopic studies of the dioxygen activation reaction of RNR-R2 and mutants indicate a μ-1,2 peroxo diferric intermediate and a high valent species, X, with a diamond core $(\mu\text{-}O)_2$ Fe(III)Fe(IV) structure (*73*). (See **Figure I-13** (bottom).)

I.D.4. Stearoyl-acyl carrier protein (ACP) Δ^9-desaturase

Stearoyl-acyl carrier protein Δ^9-desaturase (Δ9D) is the prototype of a group of plant-soluble fatty acid desaturases that catalyze O_2 activation and the introduction of a double bond into a saturated fatty acid at a specific position (*74*). Δ9D is a homodimeric protein with 11 α-helices per subunit (cf. **Figure I-11**). The crystal structure of Δ9D shows a diiron center within a four-helix bundle and a pocket capable of binding an 18-carbon substrate adjacent to the diiron site. The structure of the diiron site (**Figure I-14** (bottom)) shows no detectable oxo-bridge between two iron ions, which are separated by 4.2Å, indicating a diferrous form. As in RNR $R2_{red}$ the coordination spheres of the two iron ions are tetrahedral and highly symmetric. Each iron has one histidine ligand and one terminal bidentate carboxylate ligand, and two bridging bidentate carboxylate ligands. Spectroscopic studies, including optical, Mössbauer (*75*), resonance Raman (*76*), and EXAFS (*77*), indicate the diferric form of Δ9D does have an oxo bridge. A long-lived cis μ-1,2 peroxo diferric intermediate was observed during the reaction of reduced Δ9D with 18:0-ACP and O_2 at room temperature (*78*). This intermediate reacts to yield a peroxo-cycled complex that could represent a substrate complex state (*79*).

I.D.5. Ferritin

The iron-storage proteins ferritin and bacterioferritin allows up to 4500 Fe^{3+} to accumulate within its hollow core of 24 subunits (*80*). Two types of subunits, H and L, are found in vertebrate ferritins, whereas only H chain was found in plants and bacterial ferritins (*81*). The H chain, but not L chain, contains a catalytic site for the ferroxidase reaction (reaction 17) during ferritin biomineralization. The four-helix bundle structure of each subunit in ferritin and bacterioferritin (**Figure I-11** (B)) resembles the N-terminal domain of the Rbr more closely than the other diiron proteins (**Figure I-15**) (*58*). The H-chain-specific diiron site structure contains only one EXXH sequence, whereas bacterioferritin diiron site contains two EXXH sequences. A μ-oxo or μ-hydroxo bridged Fe^{3+} dimer is the product of the ferroxidase reaction under low iron loading conditions as shown by the Mössbauer and transient absorption spectra (*82*). The initial reaction of the diferrous site with O_2 yields a μ-1,2 peroxo diferric intermediate, which was detected by rapid freeze-quench (RFQ) resonance Raman (*82*), RFQ Mössbauer, stopped-flow spectroscopy (*83*), and x-ray absorption spectroscopy (XAS) (*84*). The XAS of ferritin reveals an unusually short Fe-Fe distance (2.53Å) in this intermediate, which implicates a triply bridged peroxo-diiron structure.

$$Fe^{2+}_{(aq)} + O_2 \longrightarrow Fe^{3+}_{(aq)} + [O]_{red} \qquad (17)$$

I.E. Reactions of Rbr

The recombinant Rbr and CRbr have much higher midpoint diiron site reduction potentials (+290mV, +220mV *vs* NHE at pH 7 for [Fe(III)-O-Fe(III)] → [Fe(III),Fe(II)] and [Fe(III), Fe(II)]→[Fe(II), Fe(II)], respectively) (*59*) than that of the two-electron

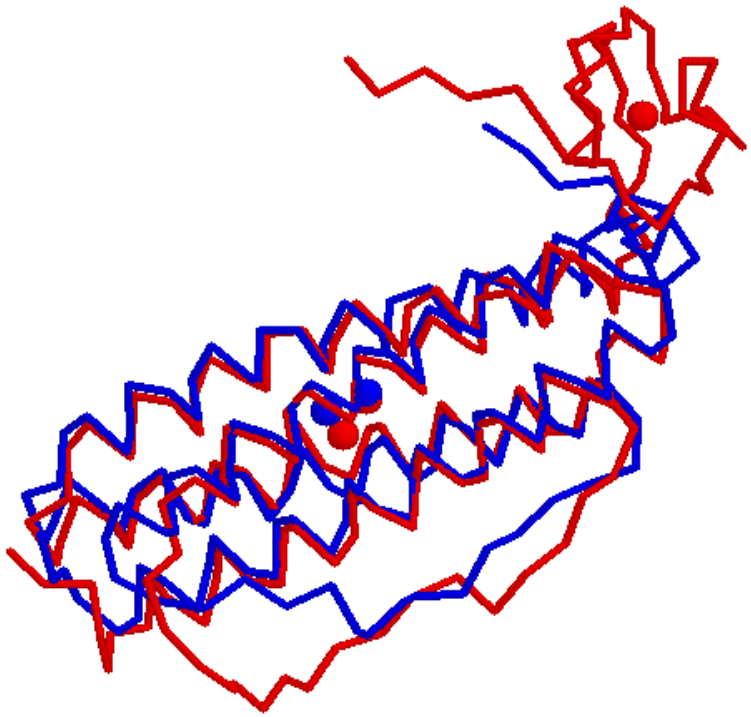

Figure I-15. Superposition of the four-helix bundles of *D. vulgaris* Rbr (red) and *E. coli* bacterioferritin (blue). Adapted from (*93*).

reduction of the diiron site in RNR R2 proteins (-115 mV *vs* NHE at pH 7.6) (*85*) and the two sequential one-electron reduction of the diiron site in MMOH (+76, +21 mV *vs* NHE at pH 7) (*86*). The Rbr diiron site is also much more solvent-accessible (*58*) (**Figure I-16**), compared to those in ferritin and bacterioferritin, and particularly those of MMOH or RNR-R2.

Rbr has tested negative for catalase, and phosphatase activities, and cannot function as a MMOH or RNR-R2 in vitro, (*54, 63*). Pyrophosphatase (*87*) and superoxide dismutase activities of Rbr (*87*) had been reported, but have not been reproduced (*48, 54, 63*).

Rbr had also been suggested to play a role in iron metabolism in *D. vulgaris*, since: (1) the tertiary structure of diiron domain is nearly superimposable on that of the ferritin and bacterioferritin subunits, both of which are iron–storage proteins (*58*) (**Figure I-11** (B)), (2) *D. vulgaris* Rbr shows ferroxidase activity in vitro (reaction 17) (*88*), and (3) in *D. vulgaris*, the Rbr gene is co-transcribed with a homologue of a *fur* (ferric-uptake-regulator) gene (*89*) (**Figure I-17**).

However, as discussed above (Section I.B.3), the most recent in vivo and in vitro studies indicate that Rbr and Rbo, as a peroxidase and a superoxide reductase, respectively, function in an alternative oxidative stress defense system to the catalase and SOD system in the cytoplasm of *D. vulgaris* and other anaerobic microorganisms (*38*).

In vivo, a H_2O_2-resistant mutant of the microaerophilic bacterium, *Spirillum volutans,* showed constitutive over-expression of a protein whose molecular weight and partial amino acid sequence resembled those of a subunit of Rbr, and cell extracts of this *S. volutans* mutant showed NADH peroxidase activity that was not present in the wild type strain (*50*). Expression of plasmid-borne Rbr failed to restore the aerobic growth of a

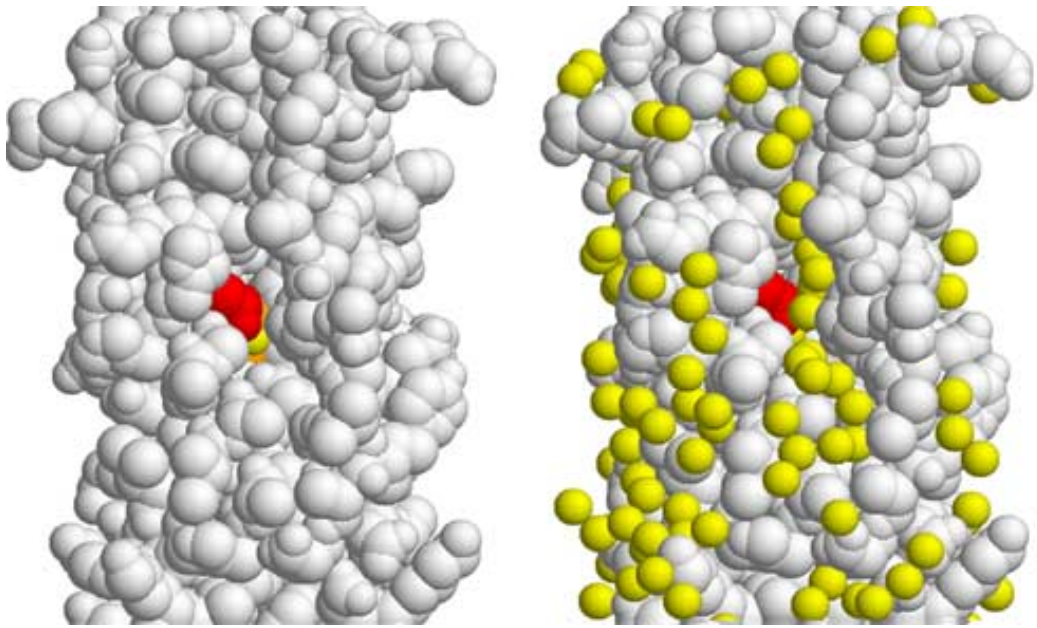

(A) (B)

Figure I-16. Stereo Space-filling views of the diiron domain of the *D. vulgaris* Rbr subunit oxidized form showing crevice exposing the diiron site, (A) with solvent ligands omitted, and (B) with solvent ligands included. Iron atoms (orange), Glu97 (red), and solvent ligands (yellow) are highlighted (1ryt) (*58*).

Figure I-17. Rubrerythrin operon in *D. vulgaris* (*89*).

SOD-deficient strain of *E. coli*, but increased the viability of a catalase-deficient strain of *E. coli* that had been exposed to H_2O_2 (*38*).

In vitro, Rbr from both *D. vulgaris* and *C. perfringens* and *D. vulgaris* Ngr all showed NADH peroxidase activities (reaction 12) (*48*). As shown in **Figure I-18**, NADH can reduce Rbr from all-ferric (Rbr_{ox}) to all-ferrous (Rbr_{red}) in seconds in the presence of a catalytic amount of BenC (a Fe-S, FAD containing NADH oxidoreductase from *Acinetobacter* sp. ADP1 (*90*)) (reaction 18a). The oxidation of the Rbr $[Fe(II)(SCys)_4]$ site with H_2O_2 was completed in about two hundred milliseconds, while with O_2 the same oxidation took minutes. Although not shown in **Figure I-18**, the diiron site is also rapidly reoxidized by H_2O_2; i.e. reaction 18b includes oxidation of both $[Fe(SCys)_4]$ and diiron sites. The sum of reactions 18a and 18b is the NADH peroxidase reaction 12.

$$NADH + Rbr_{ox} \xrightarrow{BenC} Rbr_{red} + NAD^+ + H^+ \quad (18a)$$

$$2H^+ + Rbr_{red} + H_2O_2 \longrightarrow Rbr_{ox} + 2H_2O \quad (18b)$$

(Rbr_{ox} and Rbr_{red} are the all-iron containing forms)

A study was conducted comparing the three known Rbr-catalyzed reactions: NADH peroxidase (reaction 12), ferroxidase (reaction 17), and *o*-dianisidine peroxidase (reaction 19):

$$o\text{-dianisidine} + H_2O_2 \longrightarrow o\text{-dianisidine quinonediimine} + 2H_2O \quad (19)$$

Recombinant wild type *D. vulgaris* Rbr showed 13-times and 130-times higher activities of the NADH peroxidase reaction 12 than ferroxidase reaction 17 and *o*-dianisidine peroxidase reaction 19, respectively (*49*). The NADH peroxidase activities of several Rbr mutants E97A, E97F, L60Y, Y27F, C161S, Rbr with Zn-substituted at the $[Fe(SCys)_4]$ site, and CRbr were also examined. The results showed that without the capability of

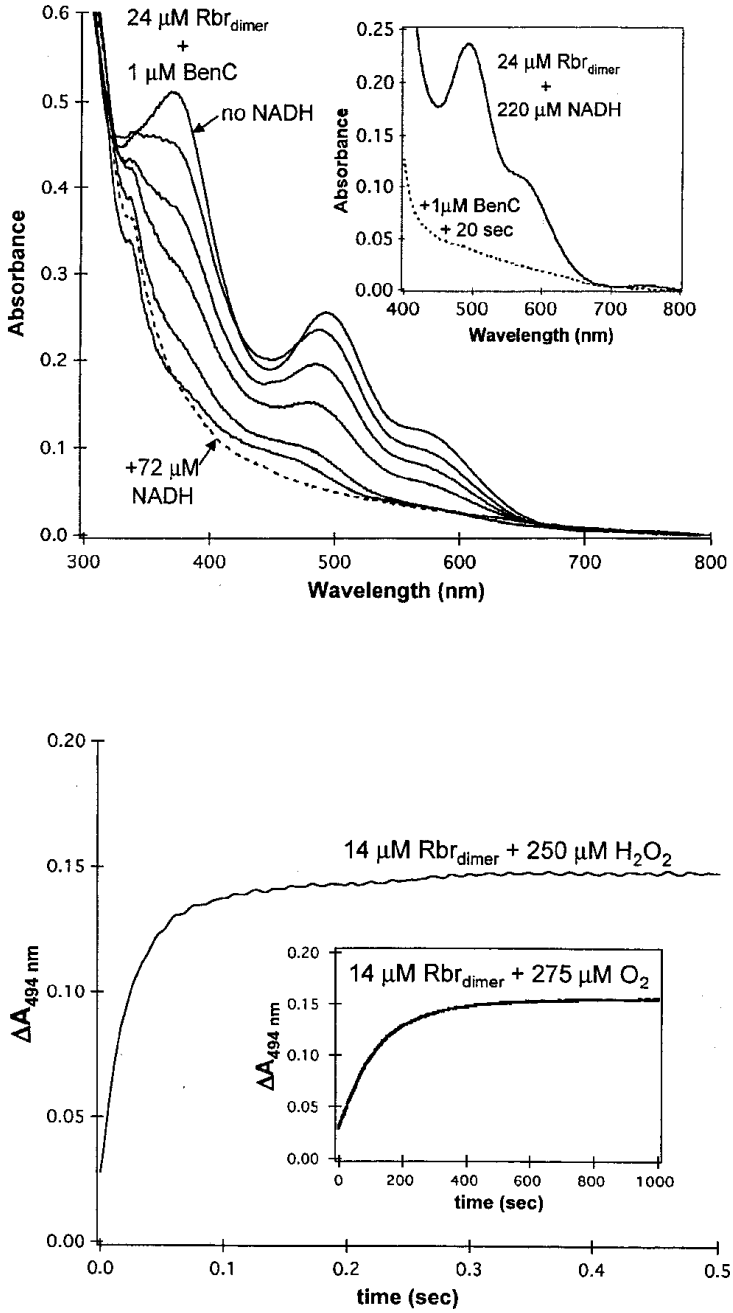

Figure I-18. (A) Anaerobic titration of oxidized Rbr with NADH in the presence of a catalytic amount of BenC, and NADH oxidoreductase. Inset shows that NADH cannot reduce Rbr until BenC is added. (B) Reduced Rbr oxidation kinetics: H_2O_2 *vs* O_2. Adapted from (*105*).

reduction of [Fe(SCys)$_4$] site, Rbr had no catalytic activities; the variants of diiron site ligands showed no activity; the activities of mutants of residues further away from diiron site showed less perturbation (*49*). A common electron transfer pathway in these three Rbr catalyzed reactions was suggested as a rapid intramolecular electron transfer from the [Fe(II)(SCys)$_4$] site to the diiron–oxo site across the dimer interface (**Figure I-19**). The results show that *D. vulgaris* Rbr is more likely to function as the terminal component of a NADH peroxidase than either a ferroxidase or non-specific peroxidase.

In searching for the native electron donor to Rbr in *D. vulgaris*, it was shown that *D. vulgaris* rubredoxin (Rub), a small (6-kD) protein containing a single [Fe(SCys)$_4$] site, effectively catalyzes the reduction of Rbr_{ox} by NADPH/FNR (reaction 20) (*91*).

$$3NADPH + Rbr_{ox}(dimer) \xrightarrow{FNR/Rub} 3NADP^+ + 3H^+ + Rbr_{red}(dimer) \qquad (20)$$

However, FNR, which is a ferredoxin-$NADP^+$ oxidoreductase, is still artificial. The FNR/Rub/Rbr system was also shown as a catalytically competent NADH peroxidase. A Rub-like protein Rdl, whose gene is co-transcribed with *rbr* and *fur* in *D. vulgaris* (**Figure I-17**) (*89*), was found to be a less efficient electron donor to Rbr than Rub, the reasons for which are still not clear. The co-transcribed *fur* gene is homologous to PerP, a peroxidase regulatory protein in *Bacillus subtilis* (*92*). Rdl may function as a peroxide sensor by transferring electrons to this PerP homolog (*93*).

I.F. Proposed mechanism of Rbr NADH/peroxidase reaction

A ligand exchange mechanism for Rbr NADH/peroxidase reaction was proposed (*49*) (**Figure I-19**). Based on Lewis acid/base considerations, iron should have higher affinity for His56 than Glu97 when Fe(III) is reduced to Fe(II) in the Rbr diiron site. X-ray crystallography shows that the Fe1 site structure is flexible to change, when the

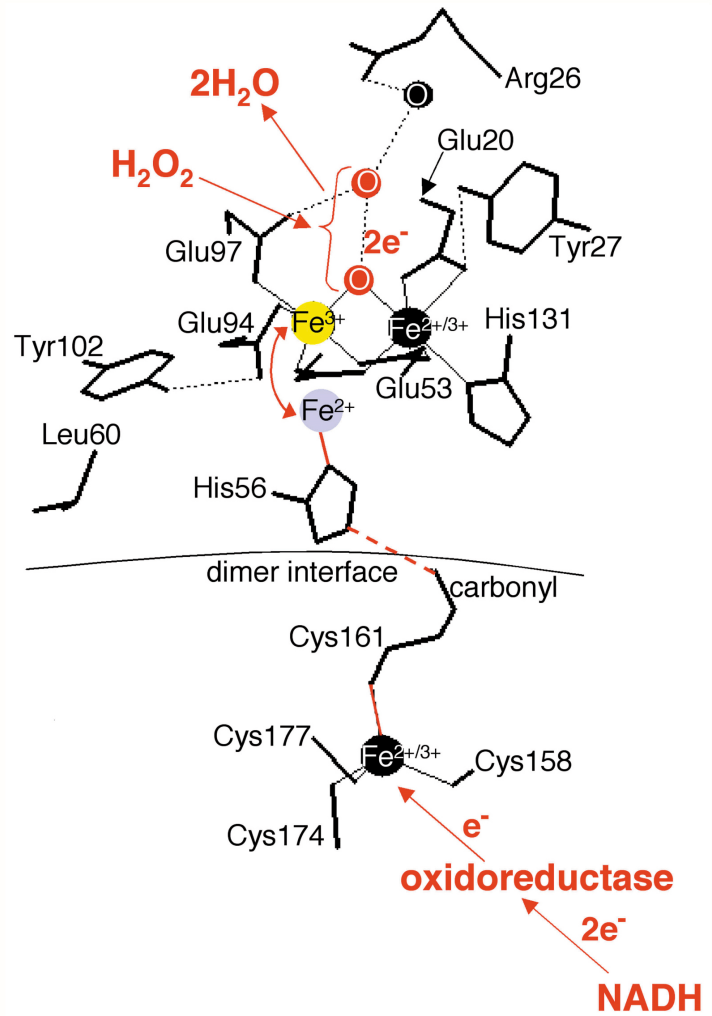

Figure I-19. A proposed ligand exchange mechanism for Rbr NADH/peroxidase reaction (*49*).

carboxylate ligand from Glu97 is not available (*62*) or the metal is less positively charged (*61*). Therefore, a diferric-Glu97 ↔ diferous-His56 ligand exchange in Rbr is a likely possibility during the turnover of Rbr NADH/peroxidase: the substrate H_2O_2 would enter the diiron site and form a μ-η^1:η^1-hydroperoxo bridge with the diferrous site, then the carboxylate of Glu97 would push electrons from the diferrous into the hydroperoxo bridge as it displaces His56, followed by electron flow from [Fe(II)$(SCys)_4$] site across the dimer interface to the diferric site. The studies described in this thesis address this mechanism by both structural and kinetics approaches.

I.G. Research Goals

The overall goal of this research is to probe the structural and functional relationships of a non-heme diiron-like protein rubrerythrin (Rbr). Rbr is proposed to function as a peroxidase in the oxidative stress response of anaerobic bacteria. We are interested in characterizing the reactive species of Rbr during the catalytic turnover reactions. The reduced (all-ferrous) form (Rbr_{red}) of Rbr rapidly reacts with hydrogen peroxide, which implicates the importance of Rbr_{red} in the mechanism. Stopped-flow spectrophotometry and freeze-quench EPR are used to investigate the kinetics and mechanism of this reaction. Structural evidence for the proposed ligand exchange mechanism of the NADH peroxidase reaction is investigated using X-ray crystallography of Rbr_{red} and an azide adduct of Rbr_{red}, which can serve as a substrate-binding model. The structures and activities of Rbrs with Zn(II) ions substituting iron(III) ions at different metal-binding sites, which investigates the influence of divalent metal ions to the Rbr structure and catalytic mechanism, are also investigated.

CHAPTER II

KINETIC STUDIES OF OXIDATION OF RBR BY HYDROGEN PEROXIDE

II.A. Background and significance

Rbr is a non-heme iron protein that features a diiron-oxo cluster buried within a four-helix bundle, and a rubredoxin-like [$Fe(SCys)_4$] center (*58*). The structure and function of Rbr and its relationship to the O_2-activating diiron enzyme was discussed in detail in Chapter I. The most relevant features are summarized here.

Most diiron proteins are functionally involved with dioxygen: hemerythrins are oxygen-carriers; ferritins are iron storage proteins, and there is a transient diiron site during their ferroxidase reaction. The diiron site structure in Rbr more closely resembles those of O_2-activating diiron enzymes such as methane monooxygenase hydroxylase (MMOH), and ribonucleotide reductase (RNR) R2, but the tertiary and quaternary structures of those O_2-activating enzymes are more complicated than for Rbr. The Rbr diiron site is unusually solvent-accessible (*58*), more so than in ferritins and bacterioferritins and much more so than in MMOH or RNR-R2, where O_2 arrives at the diiron site through a hydrophobic channel of their four-helix bundles. Rbr has much higher midpoint potentials for the two sequential one-electron reductions of the diiron site (+290, +220 mV *vs* NHE at pH 7.0) (*59*) than that of the two-electron reduction of the diiron site in RNR-R2 (-115 mV *vs* NHE at pH 7.6) (*85*) and the two sequential one-electron reduction of the diiron site in MMOH (+76, +21 mV *vs* NHE at pH 7) (*86*). It seems that the more polar H_2O_2 with its higher two-electron reduction potential is a better

substrate than O_2 for Rbr. Reduced, all-ferrous Rbr (Rbr_{red}) can be oxidized by H_2O_2 thousands of times more rapidly than by O_2 (*48*). NADH was found to be able to reduce oxidized, all-ferric Rbr (Rbr_{ox}) through an artificial oxidoreductase, BenC. Overall, Rbr can catalyze the reduction of H_2O_2 to water by NADH, i.e., the NADH peroxidase reaction (1). Rbr can also function as an efficient rubredoxin (Rub) peroxidase (reaction 2) (*91*).

$$NADH + H^+ + H_2O_2 \xrightarrow{Rbr} NAD^+ + 2H_2O \quad (1)$$

$$2H^+ + 2Rub_{red} + H_2O_2 \xrightarrow{Rbr} 2Rub_{ox} + 2H_2O \quad (2)$$

The NADH oxidase activity of Rbr was found to be only ~ 3% of its NADH peroxidase activity (*49*). The investigation of the rapid oxidation of Rbr by H_2O_2 is of particular importance for understanding the mechanism of its catalysis of the NADH peroxidase reaction. The electronic absorption of Rbr at 494 nm is mainly due to the oxidized rubredoxin like-center, whereas the oxo-bridged diferric site absorbs mostly in the 300~400 nm region. These differential absorption features could be used to differentiate the oxidation reactions of the rubredoxin-like center from that of the diiron sites. Rapid kinetic techniques including stopped-flow spectroscopy and freeze-quench EPR were used to characterize the transient species formed during the oxidation of Rbr_{red} by H_2O_2. ZnS_4Rbr, in which zinc was substituted at the rubredoxin like center (cf. Chapter IV), was also examined to help clarify the functions of the diiron site and the rubredoxin-like center during the oxidation of Rbr by H_2O_2.

II.B. Experimental section

II.B.1. Preparation of Rbr and ZnS_4Rbr in various oxidation states

As-isolated Rbr oxidized form: [Fe(III)Fe(III)]/[Fe(III)(SCys)$_4$](Rbr_{ox})

Recombinant Rbr was over expressed, reconstituted and purified as previously described (*49, 59*). The as-isolated recombinant Rbr is mostly Rbr_{ox} but usually contains small portion of mixed-valent diiron site (< 20%). Unless otherwise noted, all the following experiments were conducted in 0.1 M Tris-HCl, pH 7.3 (hereafter referred to as buffer) at room temperature, and Rbr concentrations are expressed as dimer.

Fully reduced Rbr: [Fe(II)Fe(II)]/[Fe(II)(SCys)$_4$](Rbr$_{red}$)

The procedure for reduction of as-isolated recombinant Rbr was analogous to that previously described (*48*). Two and a half milliliters of buffer in a 1-cm pathlength septum-sealed cuvette was made anaerobic by purging with nitrogen through a syringe needle for 30 min. The desired volumes of concentrated stock solutions of as-isolated Rbr (1 mM) and 5-deazaflavin (3,10-dimethyl-5-deazaisoalloxazine, MW: 269, 1 mM) in buffer (*94*) were then added via gas-tight syringe into the cuvette to achieve a mole ratio of ~ 10(Rbr):1(5-deazaflavin). The resulting Rbr:5-deazaflavin solution was irradiated using a 500-W GE projector lamp. For 20 μM, 75 μM, or 300 μM Rbr, about 1 hour, 3 hour, or overnight irradiation, respectively, at room temperature, was needed to obtain the fully reduced Rbr, as determined by UV-vis absorption spectroscopy.

Rbr with Mixed-valent diiron site and oxidized rubredoxin site:

[Fe(II)Fe(III)]/[Fe(III)(SCys)$_4$](Rbr$_{mv}$)

Rbr_{mv} in anaerobic buffer was obtained by adding an amount of H_2O_2 equivalent to the Rbr diiron sites directly to Rbr_{red} solutions. A small volume of concentrated H_2O_2 was transferred from a Hamilton gas-tight syringe to the sealed cuvette containing Rbr_{red} obtained by photochemical reduction anaerobically, and was thoroughly mixed by quickly flipping over the cuvette.

Oxidized Rbr with Zn substituted at rubredoxin site:

[Fe(III)Fe(III)]/[Zn(II)(SCys)$_4$](ZnS$_4$Rbr$_{ox}$)

The preparation and characterization of ZnS_4Rbr_{ox} used for the kinetics experiments are described in Chapter IV.

Reduced Rbr with Zn substituted at rubredoxin site:

[Fe(II)Fe(II)]/[Zn(II)(SCys)$_4$](ZnS$_4$Rbr$_{red}$)

ZnS_4Rbr_{ox} was reduced to ZnS_4Rbr_{red} as follows. Two and a half milliliters of buffer in a 1-cm pathlength septum-sealed cuvette was made anaerobic by purging with N_2 gas for 30 min, and then a small amount of concentrated ZnS_4Rbr_{ox} and 5-deazaflavin were added into the cuvette to give a concentration of 20 μM diiron sites (~ 65% of total protein, determined using ε_{370} = 7,800 $M^{-1}cm^{-1}$ per protein dimer, cf. Chapter IV) and 2 μM, respectively. The protein solution was irradiated for 1 hour using 500-W GE projector lamp. The photochemical reduction was monitored by UV-vis absorption spectroscopy.

II.B.2. UV-vis absorption spectra, metal contents and protein concentrations of Rbrs

UV-vis absorption spectra of Rbrs were recorded on a Shimadzu UV-210 PC spectrophotometer. Metal contents of Rbrs were determined by inductively coupled plasma-atomic emission analysis at the University of Georgia Chemical Analysis Facility. Protein concentrations were determined with the Bio-Rad protein assay using as-isolated Rbr_{ox} as standard, for which the concentration was determined by UV-vis absorption at 494 nm (ε = 10,600 $M^{-1}cm^{-1}$ per Rbr dimer (59)).

II.B.3 Kinetics of oxidation of Rbrs by Hydrogen Peroxide

Stopped-flow spectroscopy

Rapid-scan UV-vis spectra monitoring reactions of reduced Rbrs with hydrogen peroxide were measured on an OLIS RSM 1000 stopped-flow spectrophotometer (OLIS, Inc.) in the laboratory of Professor Robert Phillips at the University of Georgia. (See **Figure II-1**). The stopped-flow spectrophotometer is computer controlled. When the stopped-flow is fired, the flow actuator pushes a plunger block, which pushes drive syringe plungers, forcing approximately 100 μL of solution from each of the syringes into the mixing chamber. A stop syringe stops the solution in the observation cell, and the absorbance or fluorescence of the solution can then be monitored. Any previously mixed solution is forced from the observation cell into the stop syringe, and prior contents of the stop syringe are pushed into the waste syringe. The dead time of mixing is 1-2 ms for absorbance monitoring. The average reagent volume is ~120 μL/syringe/shot. (*95*)

For each experiment, approximately 100 mL of washing buffer (0.1 M Tris, pH 7.3) in a 250-mL Schlenk-type flask was alternately degassed and flushed with nitrogen using a vacuum manifold. The washing buffer, Rbr solution and H_2O_2 solution were loaded into separate syringes in a COY anaerobic chamber as follows. In the chamber, the degassed washing buffer was loaded into several 6-ml single-use plastic syringes. Ten millimolar sodium dithionite (SD) buffer for O_2-scavenging was made by diluting 100 μL 1 M SD buffer to 10 mL degassed buffer, and then the 10 mM SD buffer was separated into two 6-mL single-use plastic syringes. Approximately 2.5 mL ~20 μM Rbr_{red} was loaded into a 2.5-mL Hamilton gastight syringe. For pseudo first order reactions, at least 5-fold molar excess H_2O_2 to protein is required. In theory, three molecules of the two-electron oxidant, H_2O_2, can oxidize one Rbr_{red} dimer (i.e. six Fe(II)). Therefore, a 5-fold molar excess of H_2O_2 oxidizing equivalents for 20 μM Rbr should be 0.30 mM (5 x 3 x 20 μM = 0.30

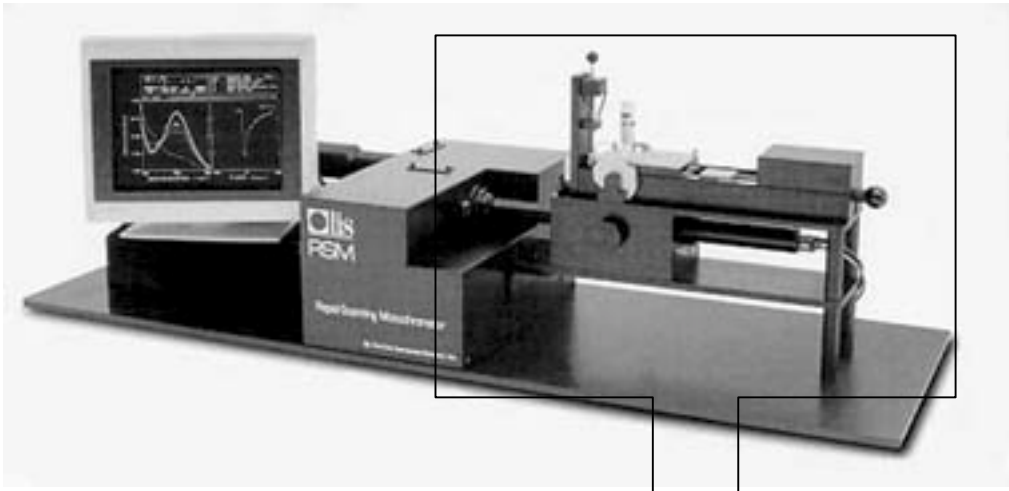

(A)

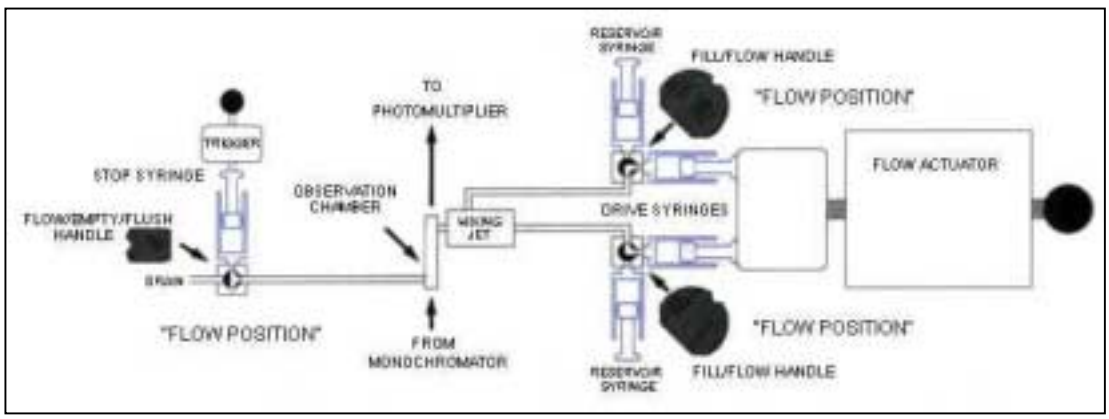

(B)

Figure II-1. (A) Photograph and (B) schematic diagram of the OLIS RSM 1000 stopped-flow spectrophotometer.

mM). A series of experiments using 5-, 50-, 300-, 500-fold molar excesses of H_2O_2 oxidizing equivalents over total iron in Rbr were carried out in order to obtain the rate constants of the reaction of Rbr_{red} with H_2O_2. Successive dilutions of H_2O_2 in degassed buffer (16.7 µL of 30% (v/v) (9 M) H_2O_2 to 5 mL buffer = 30 mM H_2O_2 (500-fold); 500 µL 30 mM H_2O_2 to 4.5 mL buffer = 3 mM (50-fold); 500 µL 3 mM H_2O_2 to 4.5 mL buffer = 0.3 mM) were used to prepare the 500-, 50-, and 5-fold H_2O_2. Dilution of 20 µL of 30% (v/v) (9 M) H_2O_2 to 10 mL buffer gave 18 mM H_2O_2 (300-fold). Each H_2O_2 solution was loaded into a 6-ml single-use plastic syringe. Capped needles were used to seal all the syringes.

The stopped-flow experiments were carried out at room temperature (~23 °C). The two drive syringes on the stopped-flow spectrophotometer were incubated with 10 mM SD buffer for 30 min. The sodium dithionite was removed by thoroughly washing the syringes with degassed washing buffer several times until the absorption peak at 340 nm due to SD was no longer detectable. The scan range of the stopped-flow spectrophotometer was set to 320 nm-570 nm, a range covering both 370- and 494-nm absorbance features of Rbr_{ox} (cf. **Figure I-8**, Chapter I). The protein solution and the control buffer (degassed buffer without H_2O_2) or H_2O_2 solutions of various concentrations were transferred into the drive syringes from the reservoir syringes with argon flowing around. During the stopped-flow experiments, the Rbr_{red} solution was mixed with H_2O_2 solution in a 1:1 (v/v) ratio. After mixing, the concentration of Rbr was ~9 µM. This concentration was chosen because it gave an easily measurable absorbance increase and also allowed the use of up to 500-fold molar excess of H_2O_2. The absorption spectrum of the mixed solution was scanned every 0.001, 0.016 or 0.1 second for 1-2, 15

or 150 seconds according to the individual experiments. Each experiment using a different excess concentration of H_2O_2 was repeated three times. The successive intermediates during the reactions and the oxidation rate constants (k_{obs}) of Rbrs were determined using OLIS Global fitting software for each experiment.

Rapid freeze-quench EPR spectroscopy

Rapid freeze-quench (RFQ) EPR experiments were carried out in Dr. Boi Hanh Huynh's lab at Emory University. **Figure II-2** shows a schematic diagram of the freeze-quench apparatus. As described in (*96, 97*), an Update Instrument unit is used to control the displacement of the syringe ram and the syringe plungers. The reactants are pushed into the mixer, flow through a plastic reaction tube into the nozzle, and are ejected as a fine stream into EPR tubes containing cold isopentane in a home-built quenching bath of which the temperature is maintained by liquid nitrogen at –140 °C. The quenched sample is packed firmly into the bottom of the EPR tube with a packer. Extra isopentane is removed from the EPR tubes through a long needle connected with a vacuum line, and samples are stored in liquid nitrogen for EPR experiments. The dead time of quenching is ~5 millisecond. The reaction times can be determined from the volume of the reaction tubes and the flow rate of reactants. The packed frozen samples usually have about 60% of the EPR signal intensity of normally frozen solutions.

The protein and H_2O_2 solutions were transferred into the RFQ drive syringes in an anaerobic chamber. The Rbr_{red} (300 μM) was mixed with H_2O_2 in a 2Rbr:1H_2O_2 (v/v) ratio. Assuming that H_2O_2 is a 2-electron oxidizing agent when reacting with Rbr_{ox}, then for oxidation of Rbr diiron sites by equimolar oxidizing equivalents of H_2O_2, 1.3 mM H_2O_2 (10% excess) (110% x 2 volume of Rbr x 2 diiron sites/dimer x 300 μM dimer =

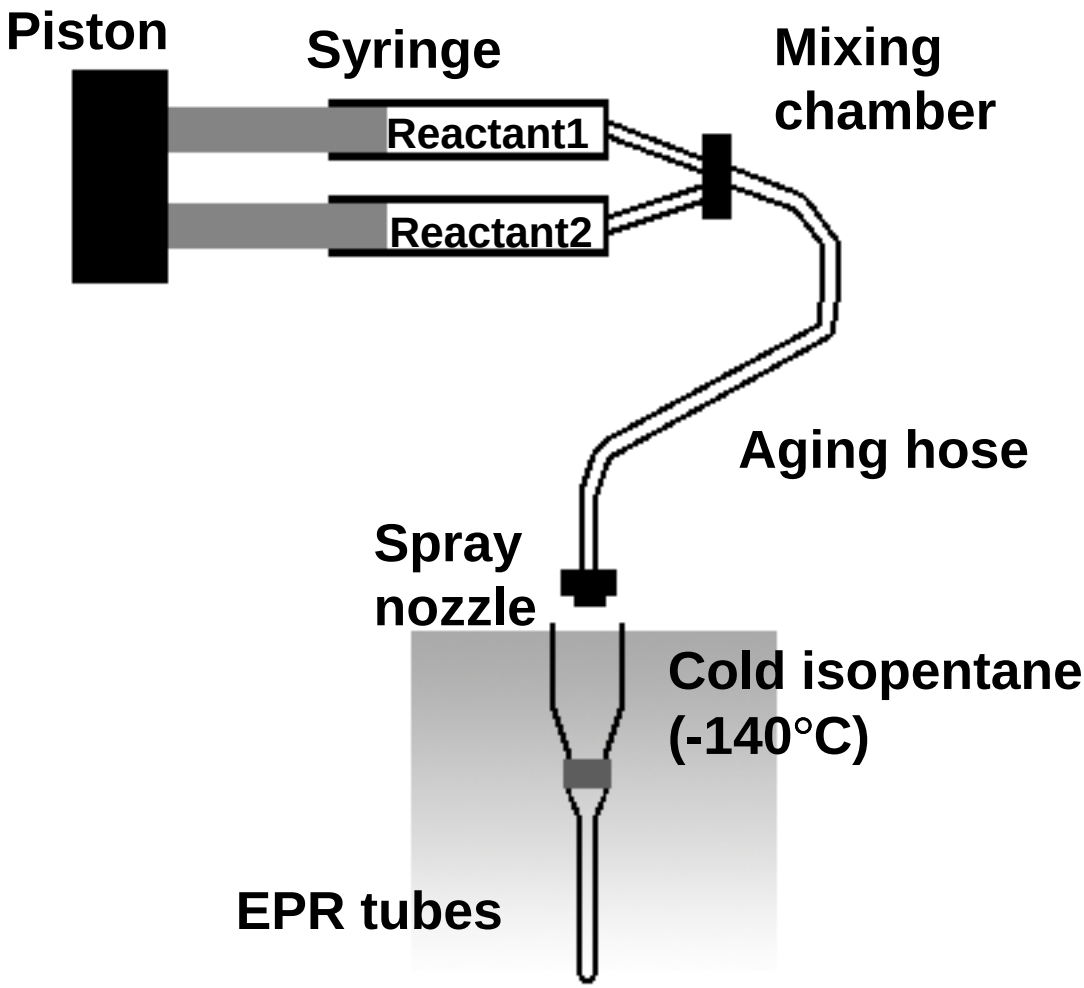

Figure II-2. Schematic diagram of Freeze-quench apparatus.

1.3 mM) in 0.1 M Tris, pH 7.3 was used, and for oxidation of the protein by 5-fold excess of H_2O_2 oxidizing equivalents over total iron in Rbr, 9 mM H_2O_2 (5 x 2 x 3 x 300 μM = 9 mM) in 0.1 M Tris, pH 7.3 with 1 mM DTPA was used. The reaction tubes were flushed with nitrogen gas just prior to use. Reactions were carried out at room temperature and were freeze-quenched at various times after mixing (26 ms to 10 s). The final concentration of Rbr after mixing was 200 μM.

For each RFQ experiment, the Rbr_{red} control was made by simply transferring 250 μL reduced Rbr_{red} (~300 μM) into an EPR tube at the same time the rest of the sample was transferred to the RFQ drive syringe. The EPR tube was capped to prevent O_2 entering, and was immediately frozen in liquid N_2 when it was taken out of the anaerobic chamber. The Rbr_{ox} control was made by manually adding a small volume of the concentrated H_2O_2 (~100-fold molar excess of H_2O_2) to the Rbr_{red} (300 μM). This solution was then transferred to an EPR tube and frozen in liquid nitrogen.

EPR spectra were measured using a Bruker ER200D spectrometer equipped with an Oxford Instruments ESR 910 continuous-flow cryostat. All spectra were obtained at 5 K with microwave power of 2 mW, frequency of 9.65 GHz, modulation amplitude of 1 mT, and modulation frequency of 100 kHz.

EPR monitoring disproportionation of Rbr_{mv}

Rbr_{mv} was made by injecting 4 μL of 88.5 mM H_2O_2 from a Hamilton syringe to a sealed cuvette containing 2 mL of photochemically prepared Rbr_{red}, 86.7 μM, in 0.1 M Tris, pH 7.3 in an anaerobic chamber and thoroughly mixing to achieve a molar ratio of H_2O_2 and Rbr diiron sites approximately 1:1. The protein solutions were then quickly transferred into several pre-capped EPR tubes using a gas tight syringe with a 6-inch long

needle. The samples were then removed from the anaerobic chamber and frozen in liquid nitrogen at various reaction times: 3 min, 30 min, 90 min and 180 min after mixing. Spin quantitations were performed by double integration using a 1.0039 mM Cu-EDTA standard under non-saturating conditions. EPR spectra were measured on a Bruker ESP 300E EPR spectrometer equipped with a liquid cryostat in the EPR facility at the University of Georgia. All spectra were obtained at 5.9 K with a microwave power of 0.2 mW for the reference and 2 mW for the protein samples, a frequency of 9.60 GHz, a modulation amplitude of 6.366 G, and a modulation frequency of 100 kHz.

II.C. Results and discussion

II.C.1. Characterization of Rbrs

II.C.1.1. All-iron Rbr

The UV-vis absorption spectra of as-isolated recombinant Rbr_{ox} and Rbr_{red} are shown in **Figure II-3** (top). The features of the Rbr_{ox} absorption spectrum are essentially identical to those previously reported for the "recombinant Rbr" (*59*). Rbr_{red} has very little absorption from 800 nm to 370 nm, and two shoulders at 310 nm and 335 nm, due to the reduced rubredoxin-like center. The absorbance ratios (see **Table II-1**) of A_{280}/A_{494} and A_{370}/A_{494} of Rbr_{ox} are slightly higher than reported for the "recombinant Rbr" (*59*). The zinc in the metal analysis (**Table II-1**) is probably due to adventitious metal binding at the protein surface. No zinc was observed in the crystal structure of recombinant Rbr_{ox} (cf. Chapter III).

II.C.1.2. ZnS_4Rbr

A detailed description of the crystal structure of ZnS_4Rbr_{ox} is given in Chapter IV. As shown in **Figure II-3** (bottom), the UV-vis absorption spectrum of ZnS_4Rbr_{ox} shows the

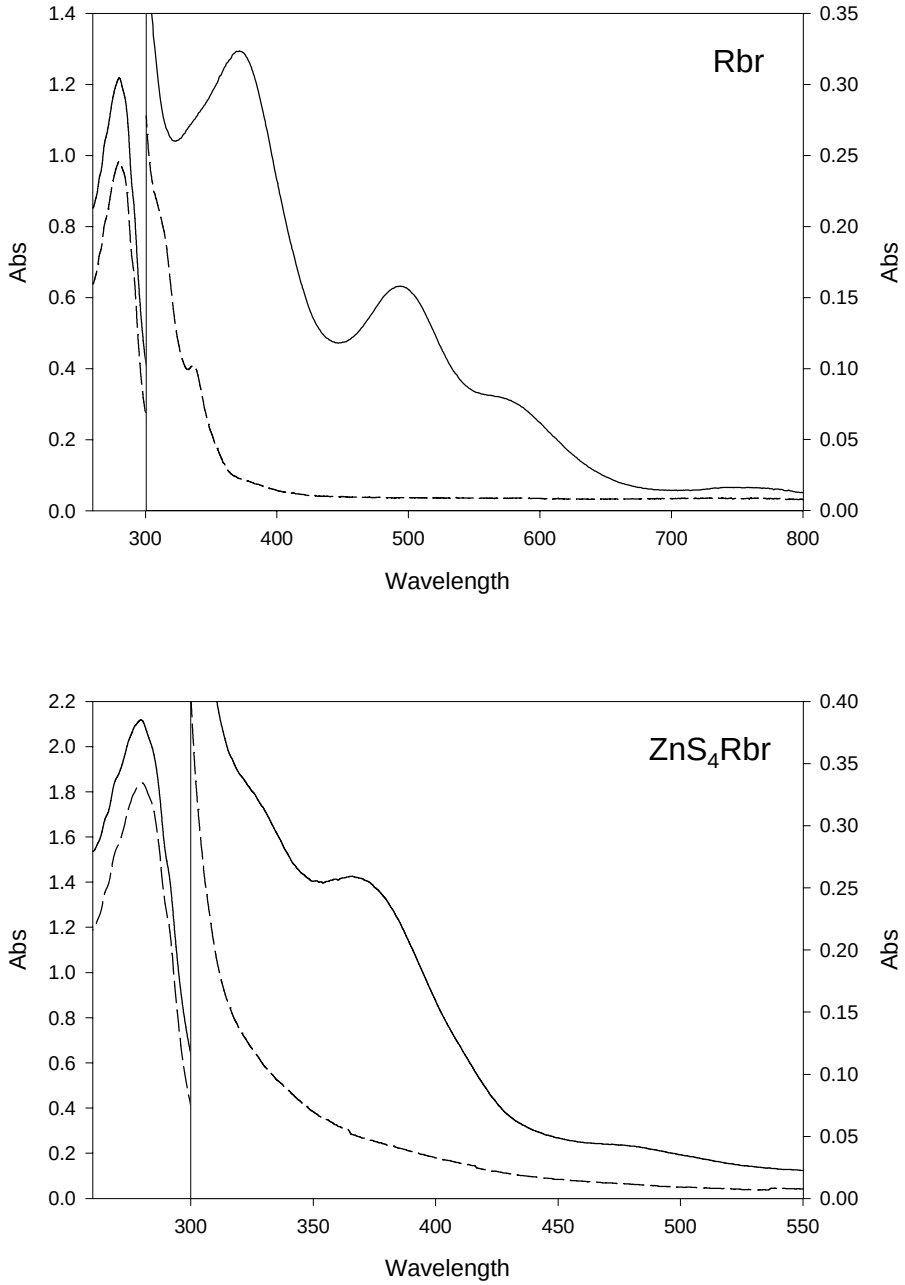

Figure II-3. UV-vis absorption spectra of (top) as-isolated recombinant *D. vulgaris* Rbr_{ox} (solid line), and Rbr_{red} (dash line), Rbr, ~ 15 µM, and (bottom) ZnS_4Rbr_{ox} (solid line), and ZnS_4Rbr_{red} (dash line), ZnS_4Rbr, ~ 10 µM at diiron site (dimer). All solutions were in 0.1 M Tris, pH 7.3.

Table II-1. UV-Vis absorbance ratios, extinction coefficient and metal contents of recombinant *D. vulgaris* Rbr examined in this work.

Protein		As-isolated Rbr_{ox}
Absorbance ratio	A_{280}/A_{494}	7.7
	A_{280}/A_{370}	3.8
	A_{370}/A_{494}	2.1
Extinction Coefficient $\varepsilon/mM^{-1}cm^{-1}$ (per dimer)	280 nm	82
	370 nm	22
	494 nm	10.6*
Metal content	Fe/dimer	6.45
	Zn/dimer	1.44

*Adapted from (*59*).

oxo-bridged diferric site features consisting of a shoulder at 330 nm and a peak 365 nm. The reduced form ZnS_4Rbr_{red} has no significant absorbance features between 800 nm and 300 nm consistent with substitution of Zn(II) for Fe(II) in the rubredoxin-like site (**Figure II-3** (bottom)). The diiron site in ZnS_4Rbr_{ox} is approximately 50%-60% occupied, as discussed in Chapter IV.

II.C.2. Stopped-flow kinetics of oxidation of Rbr_{red} by hydrogen peroxide

II.C.2.1 Rbr_{red}

When mixed with degassed buffer without H_2O_2 in the stopped-flow apparatus (cf. **Figure II-4** "reduced control"), the UV-vis absorption spectra of Rbr_{red} showed no features between 320-570 nm and no changes with time, which indicates that the anaerobic environment was well maintained during the experiments.

The reactions of Rbr_{red} with H_2O_2 were carried out by mixing equal volumes of each solution under pseudo-first order conditions with various excesses of H_2O_2. When oxidized by H_2O_2, the absorbance of Rbr_{red} increased throughout the scan range of 320-570 nm. The reactions showed four phases, as can be seen in **Figure II-4** and **Figure II-5**, from the experiments using 50-fold molar excess of H_2O_2 oxidizing equivalents over total iron in Rbr. In **Figure II-4**, each of the selected scans represents the typical spectrum at the end of each individual phase. The four successive phases (1-4) are described as follows:

(1): The very first spectrum obtained after the mixing dead time (1-2 ms) showed little absorbance at 494 nm, but a dramatic absorbance increase at 370 nm. The weak shoulder at 490 nm and more intense shoulder at 370 nm are the typical features of oxo, carboxylato-bridged diferric sites and resemble the spectrum of oxidized CRbr (cf.

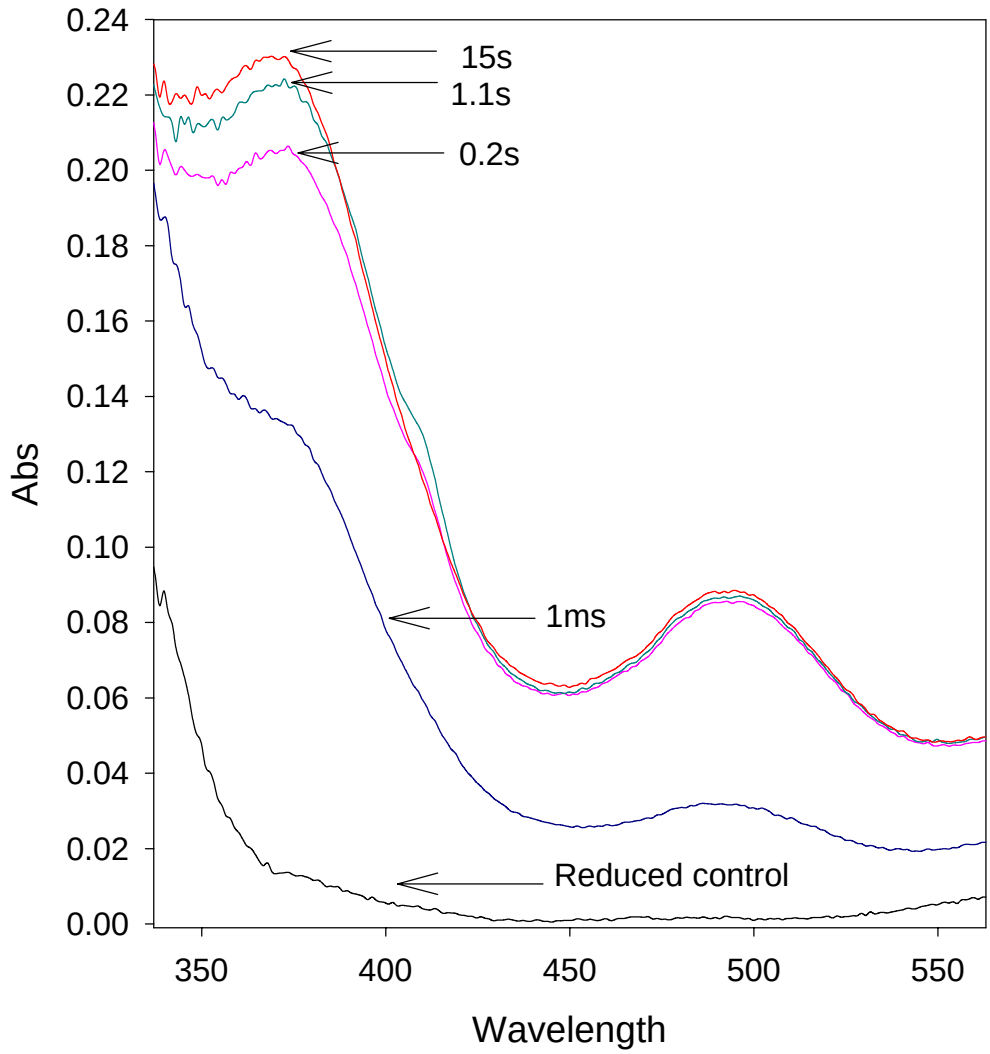

Figure II-4. Stopped-flow spectra at time points 1 ms, 0.2 s, 1.1 s and 15 s in a representative experiment of the reaction of Rbr_{red} with a 50-fold molar excess H_2O_2 oxidizing equivalents over total Rbr iron at room temperature. Final concentrations after mixing: Rbr, ~9 µM, H_2O_2, ~1.5 mM, 5-deazaflavin, ~ 1 µM, in anaerobic 0.1 M Tris buffer at pH 7.3. The stopped-flow scan mode is 62 scans/second. The reduced control is the spectrum of the Rbr_{red} mixed with the anaerobic buffer without H_2O_2 in the stopped-flow instrument at the time of 15 second after mixing.

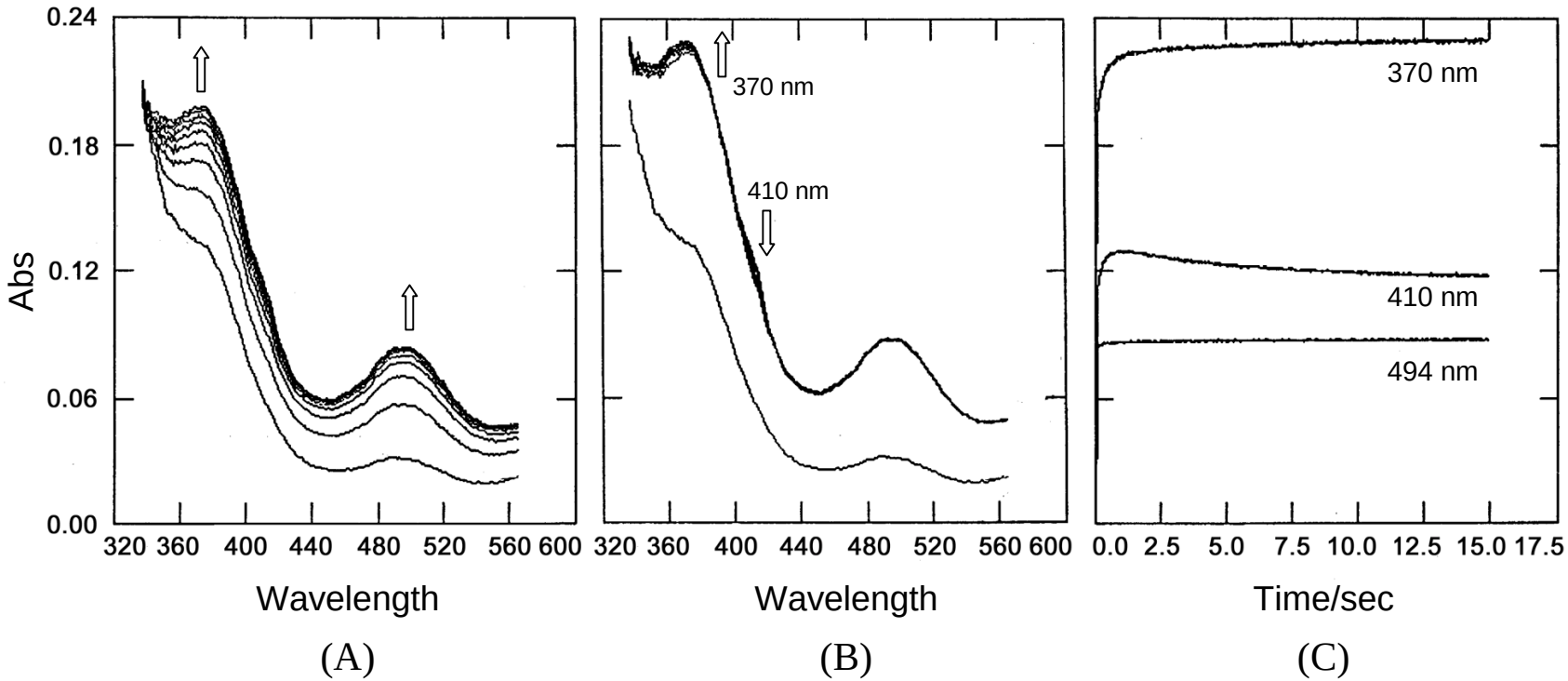

Figure II-5. A representative stopped-flow experiment of the reaction of Rbr_{red} with H_2O_2 (50-fold molar excess over total iron in Rbr) at room temperature. Final concentrations after mixing: Rbr, ~9 μM, H_2O_2, ~1.5 mM, 5-deazaflavin ~ 1 μM, in anaerobic 0.1 M Tris buffer at pH 7.3. Stopped-flow scan mode: 62 scans/second. (A) The spectra of 9 scans from 1 ms to 145 ms, interval: 16 ms. (B) The spectra of 9 scans from 1 ms to 13 s, interval: 1.6 s. Arrows indicate direction of absorbance change with time. (C) The kinetic traces of absorbance at 370 nm, 410 nm, and 494 nm.

Figure I-8, Chapter I) (*59*). The absorbance at 370 nm and 490 nm in **Figure II-4** ("1ms") for the spectrum is ~0.13 and ~0.03, respectively. Considering that the corresponding extinction coefficients for oxidized CRbr dimer are ε_{370} = 12,000 $M^{-1}cm^{-1}$ and ε_{490} = 2,000 $M^{-1}cm^{-1}$, and in the stopped-flow experiments, the concentration of Rbr wild type is ~9 μM, one can assume that the absorption features of this spectrum are due predominantly to the fully oxidized diiron sites and the reduced rubredoxin-like site in Rbr. Therefore, the first detectable phase of the reaction can be assigned to a rapid oxidation of the diferrous site of Rbr_{red} to the diferric form by H_2O_2, for which the k_{obs} is >700 s^{-1} (= 0.693 /2 msec dead time) and, therefore, cannot be monitored on the time scale of the stopped-flow instrument. This rapid oxidation occurred even when using concentrations of H_2O_2 as low as 20 μM after mixing (**Figure II-6**), which, for 9 μM Rbr_{red}, is just sufficient to oxidize all the diiron sites.

(2): Following the first phase the absorbance increased significantly at the both 370 nm and 494 nm (cf. **Figure II-4** and **Figure II-5**). However, the increase of A_{494} stopped at about 200 ms, whereas the increase of A_{370} continued until 10-25 sec for experiments using either 50-fold or 5-fold H_2O_2 oxidizing equivalents over Rbr iron, but for experiment using 500-fold H_2O_2, A_{370} stopped increasing after only 2 sec. The increase of A_{494} is due to the oxidation of the rubredoxin site. For 9 μM Rbr_{red}, when A_{494} stopped increasing, the absorption was ~0.9, which is close to that expected for ~9 μM in Rbr_{ox} with ε_{494} = 10,600 $M^{-1}cm^{-1}$ (*48*). All stopped-flow experiments using 5-fold, 50-fold and 500-fold molar excesses of H_2O_2, showed the same k_{obs} (~30 s^{-1}, calculated as described below) for oxidation of the rubredoxin site (**Figure II-7** (bottom)). The independence of k_{obs} on H_2O_2 concentration indicates that during the second phase the electron is

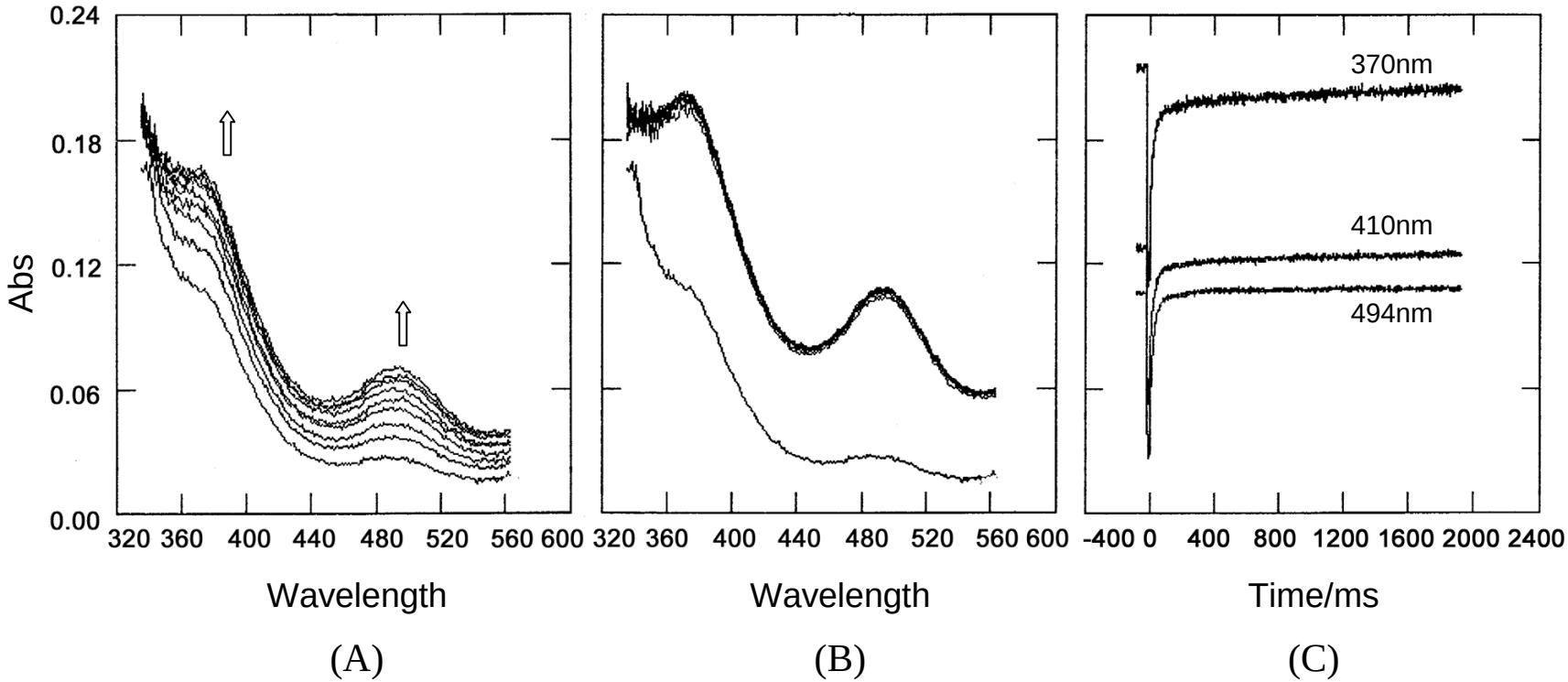

Figure II-6. A representative stopped-flow experiment monitoring the reaction of Rbr_{red} with H_2O_2 (~equimolar to the Rbr diiron site) at room temperature. Final concentrations after mixing: Rbr, ~9 µM, H_2O_2, ~ 20 µM, 5-deazaflavin, ~1 µM, in anaerobic 0.1 M Tris buffer at pH 7.3. Stopped-flow scan mode: 1000 scans/second. (A) The spectra of 9 scans from 1 ms to 19 ms, interval: 2 ms. (B) The spectra of 9 scans from 1 ms to 0.9 s, interval: 100 ms. (C) The kinetic traces of absorbance at 370 nm, 410 nm, and 494 nm. Arrows indicate direction of absorbance change with time.

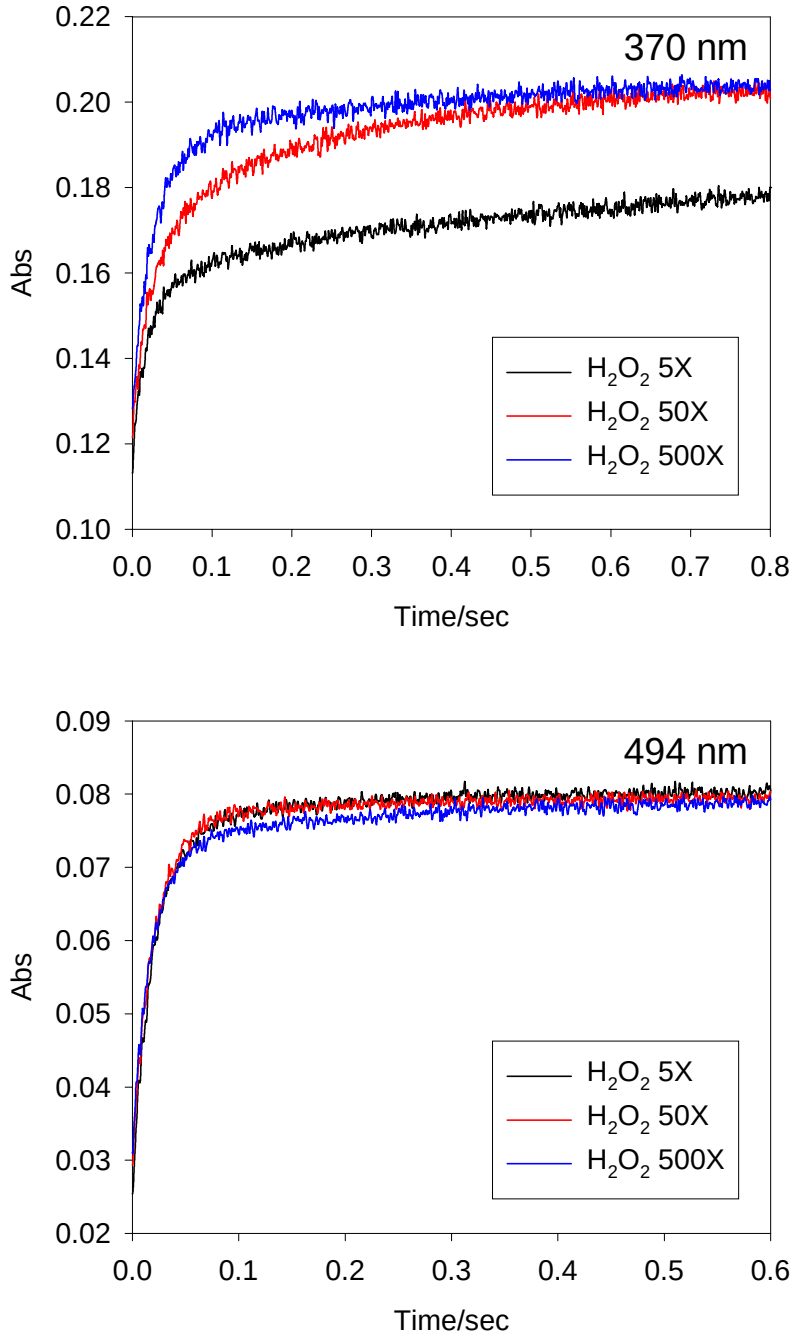

Figure II-7. Stopped flow UV-vis kinetic curves at (top) 370 nm, and (bottom) 494 nm monitoring the reaction of Rbr_{red} with excess H_2O_2 (5-, 50-, and 500-fold oxidizing equivalents over total iron in Rbr) at room temperature. Final concentrations after mixing: Rbr, ~8 μM, H_2O_2, ~0.15 mM (5-fold), ~1.5 mM (50-fold), ~15 mM (500-fold), 5-deazaflavin, ~1 μM, in anaerobic 0.1 M Tris, pH 7.3. Stopped flow scan mode: 1000 scans/second.

transferred from the reduced rubredoxin-like site to an internal site in the protein but not to the H_2O_2. The fully oxidized diiron site in Rbr after the first phase reaction is the obvious candidate. The diferric site in one subunit is ~12 Å away from the rubredoxin site in the other subunit in the Rbr "head-to-tail" dimer (cf. **Figure I-9** in Chapter I). Since only one electron is provided to the diferric site from the oxidation of each rubredoxin-like site, the diferric site will be reduced to a mixed-valent Fe(II)Fe(III) site. Based on published absorption spectra data for a synthetic complex, the mixed-valent Fe^{II}-(μ-OH)(μ-RCO_2)$_2$-Fe^{III} core should show approximately 40% of the absorbance at 350 nm as the corresponding oxo-bridged diferric core (*98*). (The corresponding oxo-bridged mixed-valent core would be expected to show an $Fe^{II} \rightarrow Fe^{III}$ inter-valence charge transfer band at ~690 nm, ε ~500 $M^{-1}cm^{-1}$ (*99*), which was not apparent in any of the kinetic studies reported here.) Therefore, the mixed-valent diiron site in Rbr would have ε_{370} ~ 4,800 $M^{-1}cm^{-1}$ (= 40% x ε_{370}(diferric site in $CRbr_{ox}$) = 40% x 12,000 $M^{-1}cm^{-1}$). The oxidized rubredoxin-like site also has a significant absorbance peak around 370 nm. Theoretically, the extinction coefficient of the oxidized rubredoxin-like site at 370 nm would be 13,000 $M^{-1}cm^{-1}$ (= ε_{370}(Rbr_{ox}) – ε_{370}(diferric site in $CRbr_{ox}$) = 25,000 $M^{-1}cm^{-1}$ – 12, 000 $M^{-1}cm^{-1}$ (*59*)). Thus, the total ε_{370} of Rbr_{mv} would be 17,800 $M^{-1}cm^{-1}$, i.e., the sum of ε_{370}(mixed-valent diiron site in Rbr) (4,800 $M^{-1}cm^{-1}$) and ε_{370}(oxidized rubredoxin-like center in Rbr) (13,000 $M^{-1}cm^{-1}$). EPR monitoring of the Rbr_{red} + H_2O_2 reaction (cf. Section II.C.2.4) are consistent with disproportionation of ~40% the mixed-valent diiron sites to the diferric and diferrous forms. If disproportionation of 40% mixed-valent diiron site to diferric and diferrous form occurred during this second phase, the ε_{370} would have increased to 18,300 $M^{-1}cm^{-1}$ (= 20% x 12,000 $M^{-1}cm^{-1}$ + 60% x 4,800

$M^{-1}cm^{-1}$ + 13,000 $M^{-1}cm^{-1}$). If all H_2O_2 were consumed during the first phase of the reaction, the A_{370} would stop increasing between ~0.12 (for diferric sites only) and ~0.24 (based on the final spectrum for fully oxidized Rbr_{ox}) for ~9 μM Rbr, as shown in the experiment using H_2O_2 at an equivalent concentration of Rbr_{red} diiron sites (**Figure II-6**). The ratio of A_{370}/A_{494} in the final spectrum (cf. **Figure II-6** (B)) is ~ 1.8, which is close to the theoretical ratio (18,300 $M^{-1}cm^{-1}$)/(10,600 $M^{-1}cm^{-1}$) as discussed above. However, with excess H_2O_2, the ratio of A_{370}/A_{494} in the final spectrum became much higher at the end of second phase, for example, ~ 2.4, in the reaction of Rbr_{red} with 50-fold molar excess of H_2O_2 oxidizing equivalents over total Rbr iron (cf. **Figure II-4**). Furthermore, the increase of A_{370} became [H_2O_2]-dependent (**Figure II-7** (top)), which indicates that oxidation of mixed-valent diiron sites by H_2O_2 starts during the second phase. The second phase thus consists of oxidation of the reduced rubredoxin site via transfer of electrons to the diferric site across the dimer interface of Rbr, and the diferric site is one-electron reduced to the mixed-valent form. The H_2O_2 then oxidizes the mixed-valent diiron form back to the diferric form, and this re-oxidation continues in the subsequent third phase.

(3) and (4): During the third phase an absorbance shoulder appears at 410 nm and reaches its maximum value at the end of the third phase. The 410-nm feature slowly decays during the fourth phase. Absorption difference spectra were obtained in the region of the 410-nm feature (**Figure II-8**) by subtracting the final spectrum of the experiment for which the shoulder at 410 nm was completely gone from the spectrum at the time of maximum A_{410}. These difference spectra, which are essentially identical using 5-, 50-, 500-fold molar excess H_2O_2 oxidizing equivalents over total iron in Rbr, show a sharp peak at 410 nm and less intense shoulder at 390 nm. These difference spectra are similar

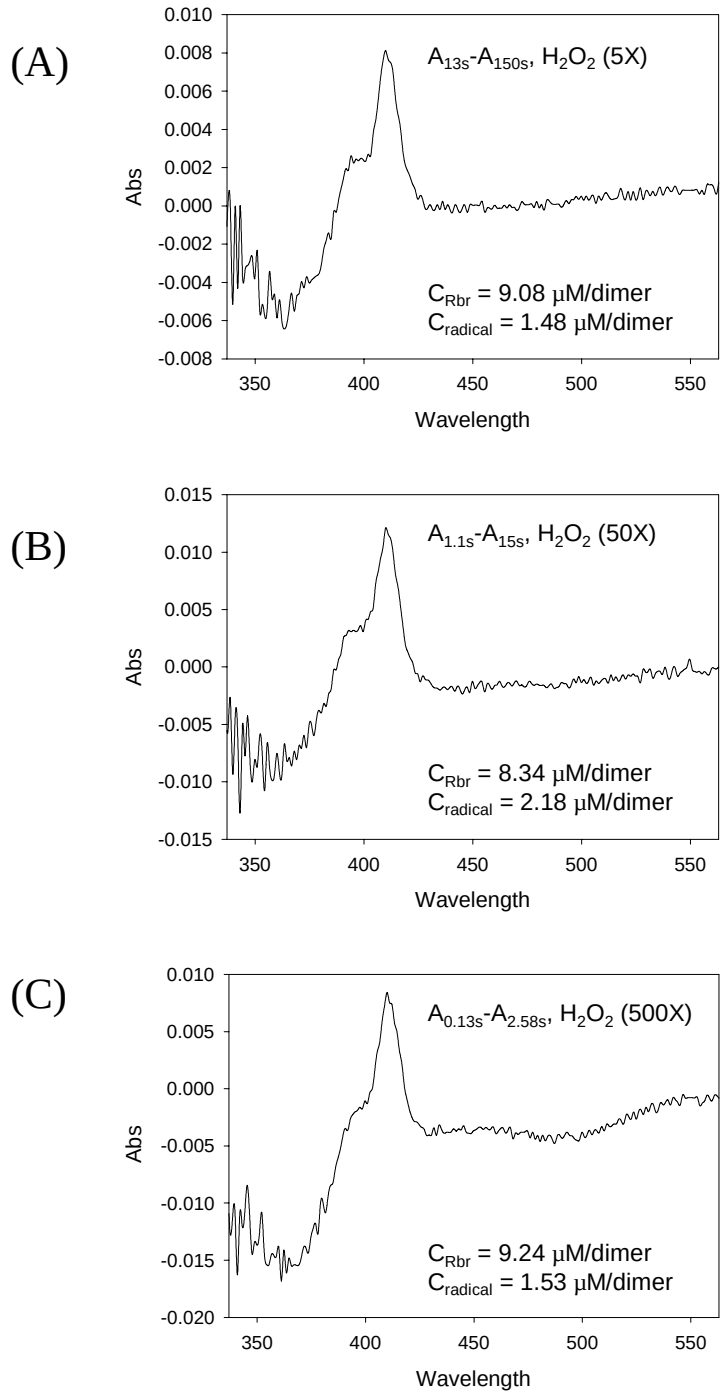

Figure II-8. The difference UV-vis absorption spectra of stopped-flow scans taken at the time points of (A) 13 s minus 150 s for the reaction of Rbr_{red} with 5-fold H_2O_2 oxidizing equivalents over total iron, (B) 1.1 s minus 15 s, with 50-fold H_2O_2, and (C) 0.13 s minus 2.58 s, with 500-fold H_2O_2. Final concentrations after mixing: Rbr, ~9 μM, H_2O_2, (A) ~0.15 mM (5-fold), (B) ~1.5 mM (50-fold), (C) ~15 mM (500-fold), 5-deazaflavin, ~1 μM, in anaerobic 0.1 M Tris buffer at pH 7.3, room temperature. The stopped-flow scan modes are (A) 10 scans/second, (B) 62 scans/second, and (C) 1000 scan/second .

to the spectrum of the tyrosyl radical (Figure **II-9**) (*100*). According to the extinction coefficient of the tyrosyl radical, 2,750 $M^{-1}cm^{-1}$, the amount of tyrosyl radicals generated in experiments using 5-, 50-, and 500-fold molar excess H_2O_2 oxidizing equivalents over total iron in Rbr were a maximum of 16%, 20%, and 16%, respectively, of the total Rbr dimer. All of the three reaction rates for generation and disappearance of 410-nm feature are [H_2O_2]-dependent. The third phase involves the oxidation of the majority of mixed-valent diiron sites to the diferric form by H_2O_2. The oxidation of the rubredoxin site has already been completed during the second phase, so no further change of absorbance is observed at 494 nm. In summary, the oxidation of the diiron site in Rbr_{red} by H_2O_2 is completed during the third phase, and a small amount of potential tyrosyl radicals is generated, which slowly decayed during the fourth phase in the presence of excess H_2O_2.

The OLIS Global fitting software (*95*) allows the data from a stopped-flow experiment consisting of hundreds to thousands of scans to be fitted with three dimensional data (absorbance, wavelength, and reaction time) for up to a six-species, five-rate equation. This software was used to analyze each set of stopped-flow data for the oxidation of Rbr_{red} by various excesses of H_2O_2. For experiments using a 50-fold molar excess of H_2O_2 oxidizing equivalents over total iron in Rbr, the global fit analysis automatically gave a four-species, three-rate fit with physically reasonable absorption spectra for each species, as shown in **Figure II-10**. These spectra are very similar to the actual spectra observed during the experiments (**Figure II-4**). The four species, A-D, represent four Rbr oxidation levels from three sequential pseudo first-order steps (A $\rightarrow$ B $\rightarrow$ C $\rightarrow$ D). Species A corresponds to the [Fe(III)Fe(III)]/[Fe(II)$(SCys)_4$] form, obtained near the end of the first phase described above, B corresponds to [Fe(III)Fe(II)]/Fe(III)$(SCys)_4$] +

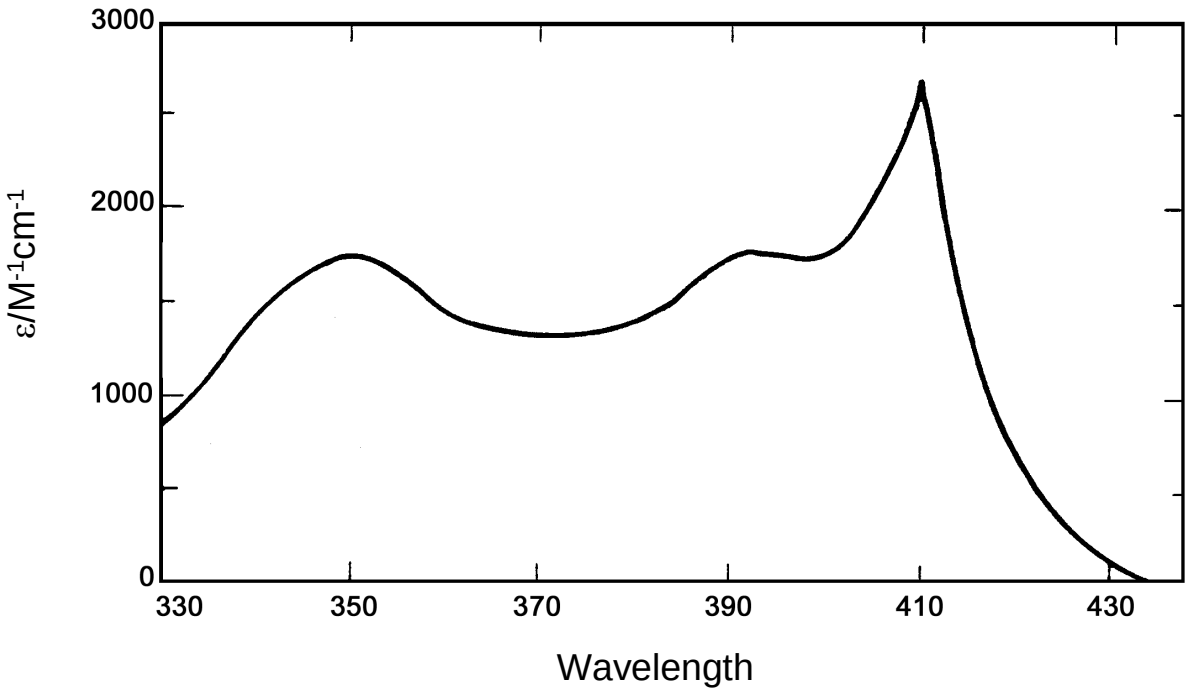

Figure II-9. Transient absorption spectrum of tyrosyl radical produced in the flash photolysis of oxygen-free aqueous solution of tyrosine (3.0×10^{-4} M) at pH 7.7. Reprinted from (*100*).

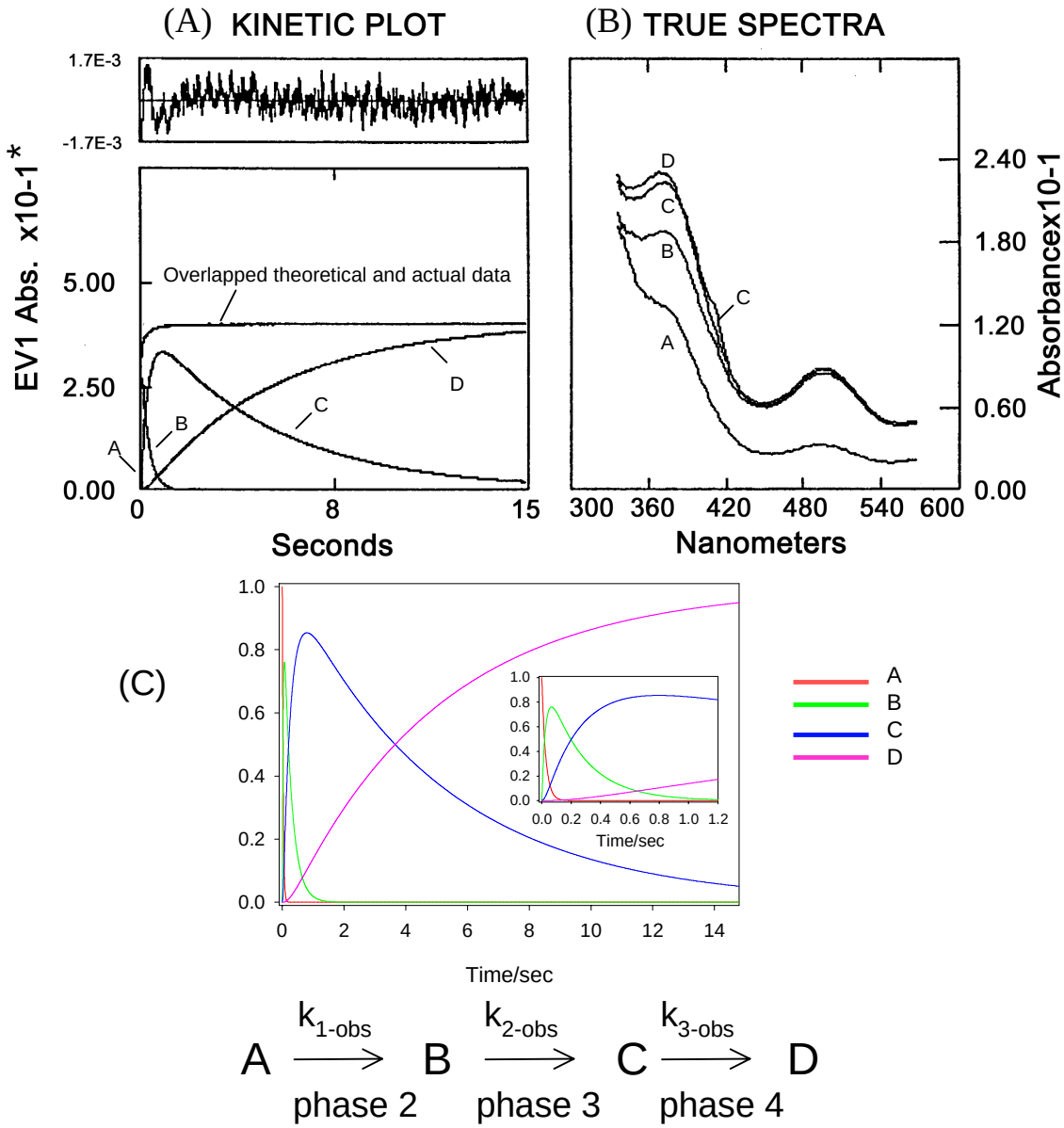

Figure II-10. A representative global fit analysis of the reaction of Rbr_{red} with H_2O_2 (50-fold molar excess oxidizing equivalents over total iron) at room temperature. Final concentrations after mixing: Rbr, ~9 µM, H_2O_2, ~1.5 mM, 5-deazaflavin, ~ 1 µM, in anaerobic 0.1 M Tris buffer at pH 7.3. Stopped-flow scan mode: 62 scans/second. (A) The fitted kinetic plots of the consecutive species A-D (the kinetic curve of species A is not quite visible due to the resolution of the figure. See species A in (C) inset). Top graph of (A) represent the fit residuals of theoretical and actual data. (B) The corresponding reconstructed spectra of the four species. (C) The fitted kinetic traces of the consecutive species A-D as in (A), replotted and shown in color. Inset: expanded traces of A-D at time range of 0-1.3 s. *The kinetic plot in (A) and true spectra in (B) are not on the same scale, whereas the kinetic data are normalized to one in (C).

[Fe(III)Fe(III)]/Fe(III)$(SCys)_4$], C corresponds to [Fe(III)Fe(III)]/Fe(III)$(SCys)_4$] + TyrO·, and D corresponds to [Fe(III)Fe(III)]/Fe(III)$(SCys)_4$] + TyrO(H). Using a 5-fold molar excess of H_2O_2 oxidizing equivalents over the total iron in Rbr, the last step, C → D, is much slower than the previous steps A → B → C in the experiments. It is, therefore, difficult to measure the entire reaction in one experiment using a 5-fold molar excess of H_2O_2. Instead, two sets of experiments were carried out using the same concentration of 5-fold molar excess of H_2O_2, but different scan modes. The first set of experiments was scanned at 62 scans/second for 15 seconds, and data were automatically fitted to three reactive species with two sequential pseudo first-order steps, A → B → C, as described above (**Figure II-11** (A) and (B)). The second set of experiments was scanned at 10 scans/second for 150 second, and data were automatically fitted to three reactive species with two sequential pseudo first-order steps, B → C → D (**Figure II-11** (C) and (D)). For experiments using 300- or 500-fold molar excess H_2O_2 oxidizing equivalents over total iron in Rbr, the reactions were manually fitted to a four-species, three-rate equation in order to obtain meaningful absorption spectra of each species. The resulting kinetic data from global fitting analysis for these experiments at all molar excesses of H_2O_2 used are shown in **Table II-2**.

The second phase, A → B ($k_{1\text{-obs}}$) (i.e., the phase following the rapid oxidation of the diferrous to diferric site by H_2O_2), is interpreted as a combination of steps 1a and 1b:

[Fe(III)Fe(III)]/[Fe(II)$(SCys)_4$]Rbr ⟶ [Fe(III)Fe(II)]/[Fe(III)$(SCys)_4$]Rbr (step 1a)

[Fe(III)Fe(II)]/Fe(III)$(SCys)_4$]Rbr + H_2O_2 ⟶

[Fe(III)Fe(III)]/Fe(III)$(SCys)_4$]Rbr + OH· + H_2O (step 1b)

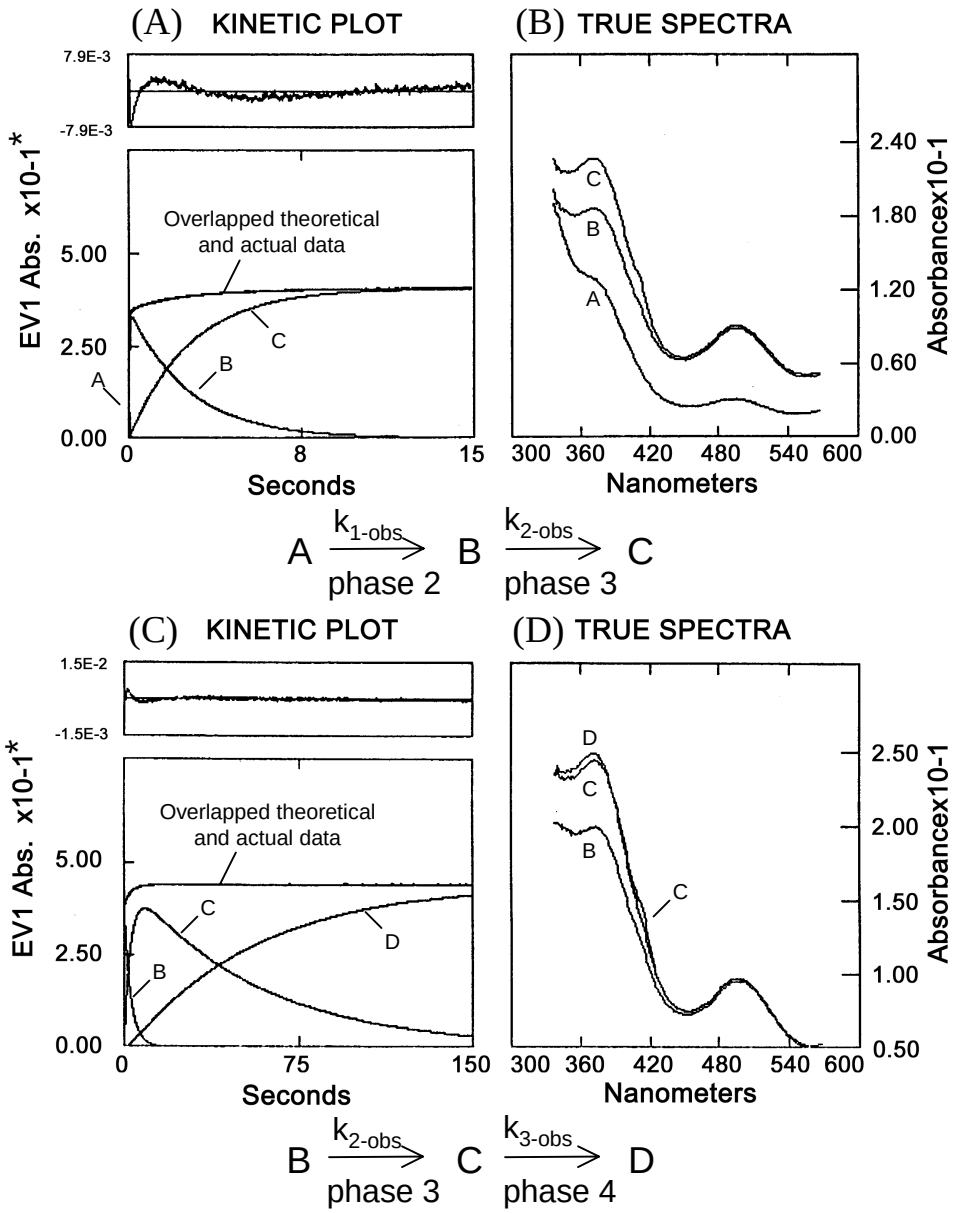

Figure II-11. A representative global fit analysis of the reactions of Rbr_{red} with H_2O_2 (5-fold molar excess oxidizing equivalents over total iron) at room temperature. Final concentrations after mixing: Rbr, ~9 µM, H_2O_2, ~0.15 mM, 5-deazaflavin, ~ 1 µM, in anaerobic 0.1 M Tris buffer at pH 7.3. Stopped-flow scan mode: (A) and (B) 62 scans/second; (C) and (D) 10 scans/second. (A) The fitted kinetic plots of consecutive species A-C (the kinetic curve of species A is not quite visible due to the resolution of the figure). (B) The corresponding reconstructed spectra of species A-C. (C) The fitted kinetic plots of consecutive species B-D. (D) The corresponding reconstructed spectra of species B-D. Top graphs of (A) and (C) represent the fit residuals of theoretical and actual data, respectively. *The kinetic plot in (A) and true spectra in (B) are not on the same scale, and the same to (C) and (D).

Table II-2. The observed rate constants determined using OLIS Global fitting software for oxidation Rbr_{red} by H_2O_2 (5-, 50-, 300-, and 500-fold molar excess oxidizing equivalents over total iron) at room temperature. Each reaction using different concentration of H_2O_2 was carried out for tree times. Final concentrations after mixing: Rbr, ~9 µM, 5-deazaflavin, ~1 µM, in anaerobic 0.1M Tris, pH 7.3.

$[H_2O_2]$/mM	$k_{1\text{-obs}}/s^{-1}$	$k_{2\text{-obs}}/s^{-1}$	$k_{3\text{-obs}}/s^{-1}$
0.15 (5-fold)	(3.0±0.6)E01	(3.8±0.3)E-01	-
	(2.9±0.5)E01	(3.99±0.21)E-01	-
	(3.0±0.6)E01	(3.7±0.3)E-01	-
	-	[(3.2±0.5)E-01]	(2.00±0.24)E-02
	-	[(2.71±0.16)E-01]	(3.9±1)E-02
	-	[(3.4±0.3)E-01]	(1.8±0.3)E-02
1.5 (50-fold)	(3.7±0.4)E01	(3.44±0.17)E00	(1.98±0.2)E-01
	(3.82±0.24)E01	(3.62±0.32)E00	(1.9±0.3)E-01
	(3.8±0.4)E01	(3.6±0.3)E00	(2.05±0.23)E-01
9.0 (300-fold)	(4.3±0.5)E01	(2.1±0.05)E01	(1.0±0.3)E00
	(5.6±0.3)E01	(1.5±0.4)E01	(9.5±1)E-01
	(4.14±0.22)E01	(2.17±0.13)E01	(8.8±0.9)E-01
15 (500-fold)	(7.0±0.9)E01	(3.1±0.4)E01	(2.09±0.24)E00
	(6.3±0.1)E01	(3.8±0.3)E01	(1.88±0.13)E00
	(7.5±1)E01	(2.8±0.4)E01	(1.9±0.5)E00

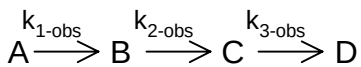

The rate constant for step1a should be $[H_2O_2]$-independent, whereas, step1b should be a $[H_2O_2]$-dependent second order reaction. The rate constant $k_{1b\text{-}obs}$ should, therefore, be equal to the product of the second order rate constant k_{1b}, times the concentration of H_2O_2, and the observed rate constant $k_{1\text{-}obs} = k_{1a} + k_{1b}[H_2O_2]$. As seen in **Figure II-12** (A), the plot of $k_{1\text{-}obs}$ vs $[H_2O_2]$ is linear with slope equal to k_{1a} and intercept equal to k_{1b}. The results show that the intramolecular electron transfer rate constant k_{1a} is equal to ~30 s^{-1}, and the second order rate constant k_{1b} for the oxidation of mixed-valent diiron form to the diferric form by H_2O_2 is equal to 2.4×10^3 $M^{-1}s^{-1}$ (cf. **Table II-3**). Therefore, the product of step1, i.e. species B, is: [Fe(III)Fe(II)]/[Fe(III)$(SCys)_4$]Rbr + [Fe(III)Fe(III)]/[Fe(III)$(SCys)_4$]Rbr. [Fe(III)Fe(III)]/[Fe(III)$(SCys)_4$]Rbr in B is the fully oxidized form, so it would not further react with H_2O_2.

As shown in **Figure II-12** (B) and **Figure II-13**, the steps B $\rightarrow$ C ($k_{2\text{-}obs}$) and C $\rightarrow$ D ($k_{3\text{-}obs}$) are $[H_2O_2]$-dependent second order reactions, so rate constants, $k_{2\text{-}obs}$ or $k_{3\text{-}obs}$, are equal to the product of a second order rate constant, k_2 or k_3, times the concentration of H_2O_2. The step B $\rightarrow$ C ($k_{2\text{-}obs}$) is interpreted as a combination of step 2a, which is the same as step1b, and step 2b, formation of tyrosyl radical:

[Fe(III)Fe(II)]/[Fe(III)$(SCys)_4$]Rbr + H_2O_2 $\longrightarrow$

[Fe(III)Fe(III)]/[Fe(III)$(SCys)_4$]Rbr + OH$\cdot$ + H_2O (step 2a)

[TyrOH]Rbr_{ox} + OH$\cdot$ $\longrightarrow$ [TyrO$\cdot$]Rbr_{ox} + H_2O (step 2b)

Step 2a is the rate-determining step, and the one-electron reduction of H_2O_2 would result in OH$\cdot$, which may then rapidly oxidize [TyrOH] to [TyrO$\cdot$], as in step 2b. Step 2a is the same reaction as step 1b; therefore, step 2a and 1b should have the same rate constants,

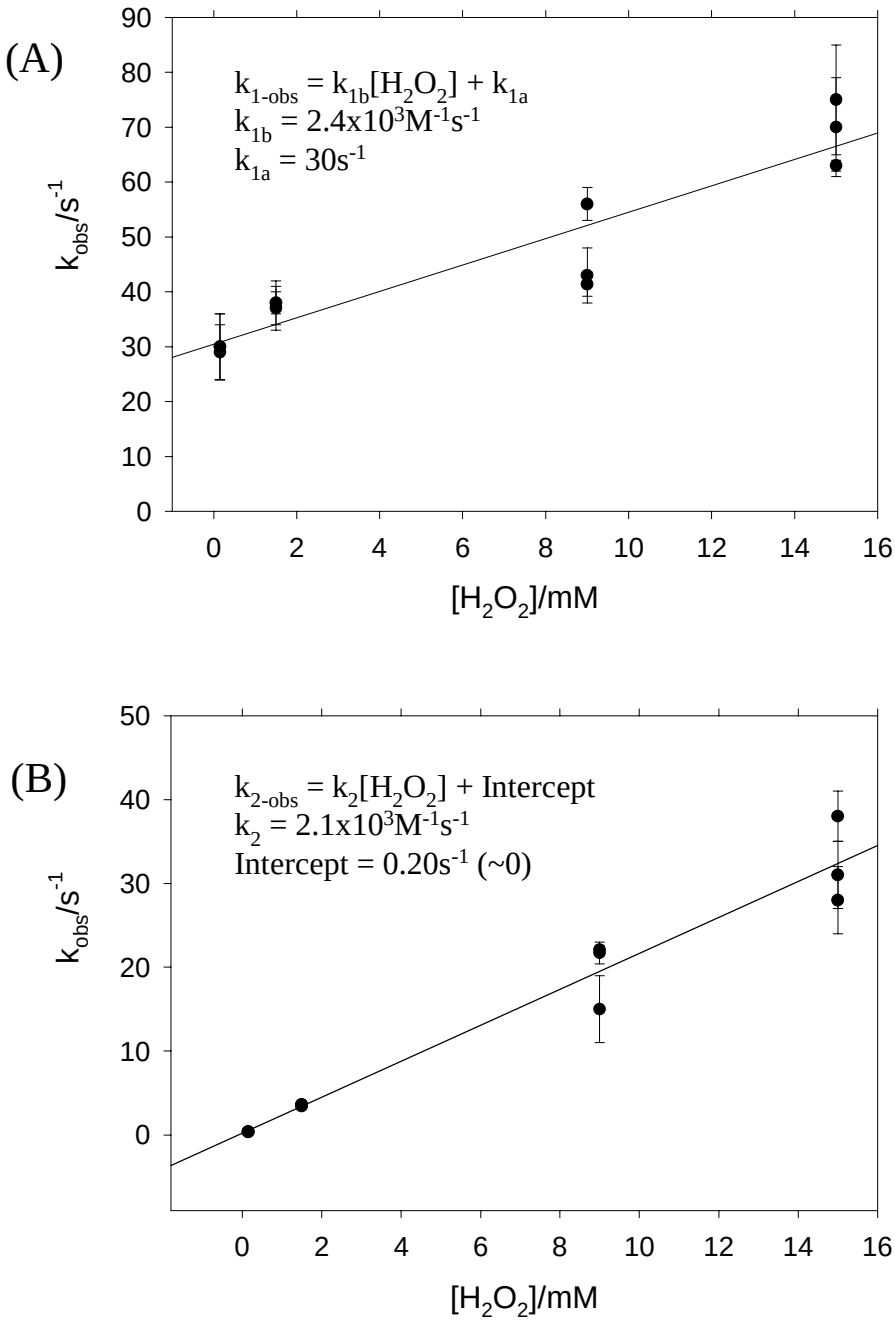

Figure II-12. (A) The plot of $k_{1\text{-obs}}$ vs $[H_2O_2]$, and (B) the plot of $k_{2\text{-obs}}$ vs $[H_2O_2]$, for the reaction of Rbr_{red} with H_2O_2 (5-, 50-, 300-, and 500-fold molar excess of oxidizing equivalents over total iron) at room temperature. Each reaction at a given concentration of H_2O_2 was carried out three times and all three data points are plotted. Error bars represent those in Table II-2 obtained from the global fit. Final concentrations after mixing: Rbr, ~9 µM, 5-deazaflavin, ~1 µM, in anaerobic 0.1 M Tris, pH 7.3.

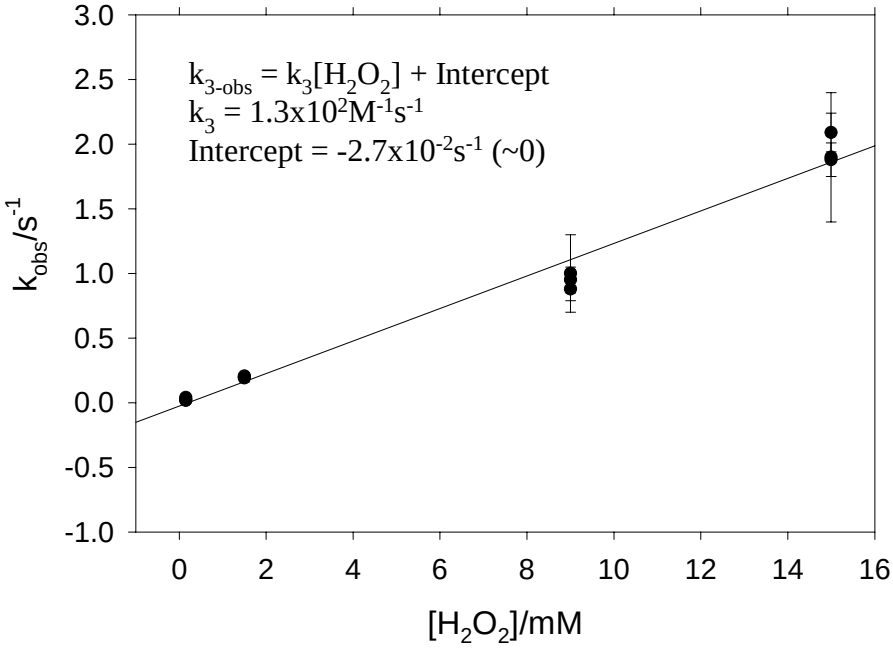

Figure II-13. The plot of $k_{3\text{-obs}}$ vs $[H_2O_2]$ for the reaction of Rbr_{red} with H_2O_2 (5-, 50-, 300-, and 500-fold molar excess of oxidizing equivalents over total iron) at room temperature. Each reaction at a given concentration of H_2O_2 was carried out three times and all three data points are plotted. Error bars represent those in Table II-2 obtained from the global fit. Final concentrations after mixing: Rbr, ~9 µM, 5-deazaflavin, ~1 µM, in anaerobic 0.1 M Tris, pH 7.3.

Table II-3. The summary of k_{1a}, k_{1b}, k_2, and k_3 for the reaction of Rbr_{red} with H_2O_2.

	Slope (k) / $M^{-1}s^{-1}$	Intercept / s^{-1}
$k_{1\text{-obs}} = k_{1b}[H_2O_2] + k_{1a}$	(2.4±0.3)E03	(3.0± 0.3)E01
$k_{2\text{-obs}} = k_2[H_2O_2]$	(2.1±0.1)E03	(0.2±1.2)E00 (~0)
$k_{3\text{-obs}} = k_3[H_2O_2]$	(1.3±0.1)E02	(-2.7 ±5.2) ± E-02 (~0)

i.e., $k_{2a} = k_2 \approx k_{1b}$. The second order rate constants are summarized in **Table II-3**. The results are consistent with this expectation: the experimentally derived k_2 of 2.1×10^3 $M^{-1}s^{-1}$ agrees well with that for k_{1b} of 2.4×10^3 $M^{-1}s^{-1}$. The plot of both $k_{2\text{-obs}}$ vs $[H_2O_2]$ should be linear with slope equal to the second order rate constant, k_2 and k_3, respectively, and intercepts equal to ~zero, as seen in **Figure II-12** (B) and **Figure II-13**.

The third step C $\rightarrow$ D ($k_{3\text{-obs}}$) is the decay of the tyrosyl radical, which, since it is $[H_2O_2]$-dependent, presumably involves oxidation of H_2O_2:

$$[\text{TyrO}\cdot]\text{Rbr}_{ox} + H_2O_2 \longrightarrow [\text{TyrO(H)}]\text{Rbr}_{ox} + O_2H\cdot \qquad \text{(step 3)}$$

The second order rate constant k_3 for step, C $\rightarrow$ D, is equal to 1.3×10^2 $M^{-1}s^{-1}$. As expected, the intercept of the plot of $k_{3\text{-obs}}$ vs $[H_2O_2]$ is quite small and can be considered ~zero within experimental error. It is not clear why the theoretical amount of tyrosyl radicals at maximum (83% of the Rbr diiron site concentration, independent of $[H_2O_2]$, as shown in the **Figure II-14** and **Scheme II-1**) during the reaction of Rbr with H_2O_2 are much higher than the observed amount (16-20% of the Rbr diiron site concentration, as described above). It is possible that not all of the OH· generated in step 2a reacted with tyrosine residues in Rbr, in which case the amount of TyrO· would be much less than expected.

When the reactions of Rbr_{red} with H_2O_2 at an oxidizing equivalent concentration equal to that of Rbr_{red} diiron sites were analyzed by the global fitting program, three species, two steps (A′ $\rightarrow$ B′ $\rightarrow$ C′) were automatically obtained, as shown in **Figure II-15**. The increases of both A_{370} and A_{494} are almost finished at the end of step A′ $\rightarrow$ B′ with first order rate constant $k_{1\text{-obs}} = 77 \pm 8$ s^{-1} (average of three runs). Step B′ $\rightarrow$ C′ shows continued increases of both A_{370} and A_{494} with a slower rate of $k_{2\text{-obs}} = 24 \pm 5$ s^{-1}.

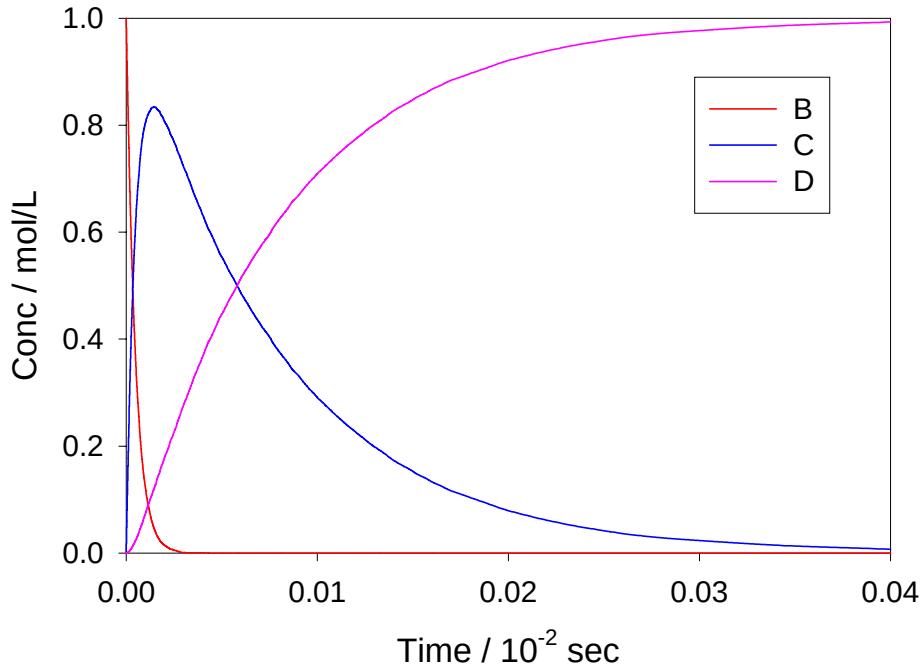

Figure II-14. Plots of simulated kinetic traces of the generation and decay of tyrosyl radicals generated during Rbr_{red} oxidation by H_2O_2, using Chemical Kinetics Simulator software. B = [TyrOH]Rbr, C = [TyrO•]Rbr, D = [TyrO(H)]Rbr.

Scheme II-1:

$$B \xrightarrow[H_2O_2]{k_2} C \xrightarrow[H_2O_2]{k_3} D$$

$$[C]_{max} = \frac{[B]_0 k_2}{k_3 - k_2} \left(e^{-k_2[H_2O_2]t} - e^{-k_3[H_2O_2]t}\right)$$

$$t_{max} = \frac{\ln(k_2/k_3)}{(k_2 - k_3)[H_2O_2]}$$

$[C]_{max} = 83\%[B]_0$,

for $k_2 = 2.1 \times 10^3\ M^{-1}s^{-1}$, and $k_3 = 1.3 \times 10^2\ M^{-1}s^{-1}$ (cf. Table II-3).

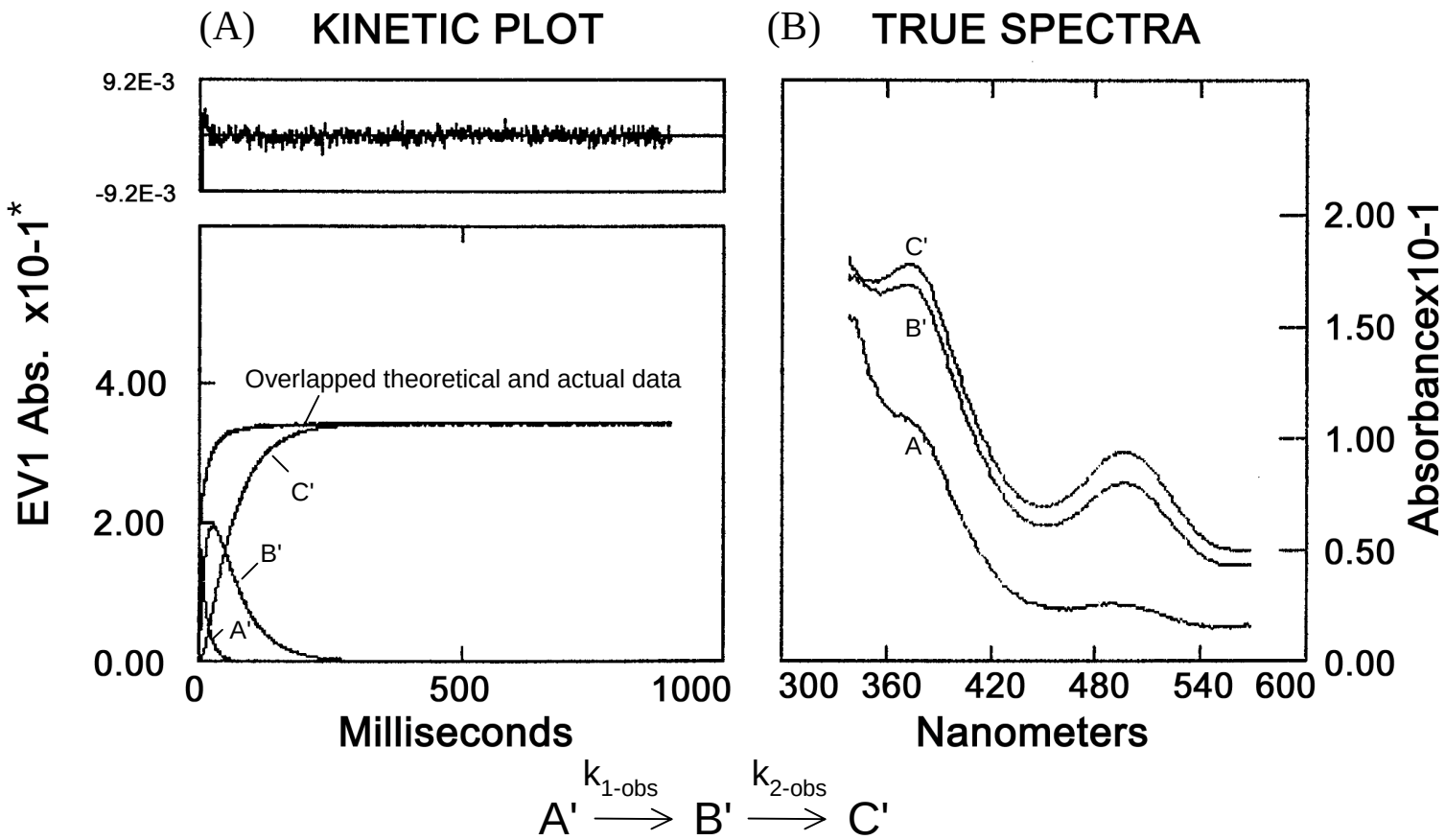

Figure II-15. A representative global fit analysis of the reaction of Rbr_{red} with H_2O_2 (equimolar over Rbr diiron site) at room temperature. Final concentrations after mixing: Rbr, ~9 µM, H_2O_2, ~20 µM, 5-deazaflavin, ~ 1 µM, in anaerobic 0.1 M Tris buffer at pH 7.3. Stopped-flow scan mode: 1000 scans/second. (A) The fitted kinetic plots of the consecutive species A'-C'. Top graph of (A) represent the fit residuals of theoretical and actual data. (B) The corresponding reconstructed spectra of the three species. *The kinetic plot in (A) and true spectra in (B) are not on the same scale.

Step A′ → B′ is apparently the same as step 1a with excess H_2O_2, i.e., the internal electron transfer reaction. However, the rate constant, $k_{1\text{-obs}}$ (77 ± 8 s^{-1}), for A′ → B′, obtained from the global fit, is higher than the corresponding k_{1a} (30 s^{-1}), obtained with excess H_2O_2. The reason for this difference is unclear, but might be due to the different proportion of the trace absorbance increase at A_{370} from the tail end of the very rapid first phase of the reaction, i.e., the oxidation of diferrous to diferric sites. If, instead of global fitting, the absorbance at 494 nm vs time is fit to a first order exponential rise (k_1 in **Table II-4**), the rate constant for increase of the A_{494} with equimolar H_2O_2 to the diiron site is approximately the same as for the reactions using excess H_2O_2. (The fitting analysis showed that a sum of two-first-order-exponentials gave better fits than one-first-order-exponential rise for all reactions using various concentrations of H_2O_2. An example from the reaction of Rbr_{red} with H_2O_2 equimolar to the diiron site is shown in **Figure II-16**.) Step B′ → C′ is likely an [H_2O_2]-independent disproportionation of mixed-valent diiron form of Rbr to diferric and diferrous forms (step 2′):

$$[Fe(III)Fe(II)]/[Fe(III)(SCys)_4]Rbr \longrightarrow [Fe(III)Fe(III)]/[Fe(III)(SCys)_4]Rbr + [Fe(II)Fe(II)]/[Fe(III)(SCys)_4]Rbr \quad \text{(step 2′)}$$

This disproportionation reaction was most likely out-competed by oxidation of the mixed-valent site by excess H_2O_2, since the third phase of the oxidation of Rbr_{red} in the presence of excess H_2O_2 is [H_2O_2]-dependent.

II.C.2.2. ZnS_4Rbr_{red}

For comparison, the stopped-flow experiments mixing ZnS_4Rbr_{red} with H_2O_2 were also performed. The control experiment was carried out by mixing 20 μM diiron sites of ZnS_4Rbr_{red} per dimer in 0.1 M Tris, pH 7.3 with anaerobic buffer without H_2O_2. The

Table II-4. The observed rate constants determined by fitting the absorbance at 494 nm vs time to first order exponential rise ($A = A_1 \times \exp(-k_1 \times t) + A_2 \times \exp(-k_2 \times t) + b$), for oxidation of Rbr_{red} by H_2O_2 (equimolar to the diiron sites, and 5-, 50-, and 500-fold molar excess oxidizing equivalents over total iron) at room temperature. Each reaction using different concentration of H_2O_2 was repeated for two or three times. Final concentrations after mixing: Rbr, ~9 µM, 5-deazaflavin, ~1 µM, in anaerobic 0.1 M Tris, pH 7.3. Stopped flow scan mode: 1000 scan/sec.

$[H_2O_2]$/mM	k_1	A_1	k_2	A_2
0.02 (~equimolar to the diiron sites)	(5.32±0.10)E01	(-5.68±0.08)E-02	(1.25±0.08)E01	(-9.0±0.09)E-03
	(5.53±0.11)E01	(-5.31±0.07)E-02	(1.20±0.11)E01	(-6.2±0.8)E-03
	(5.37±0.14)E01	(-4.57±0.01)E-02	(1.34±0.19)E01	(-4.8±1.0)E-03
0.15 (5-fold)	(5.45±0.09)E01	(-4.58±0.04)E-02	(8.3±0.04)E00	(-7.2±0.4)E-03
	(5.29±0.08)E01	(-4.67±0.04)E-02	(7.4±0.4)E00	(-6.5±0.3)E-03
	(5.42±0.08)E01	(-4.79±0.04)E-02	(8.2±0.5)E00	(-6.2±0.4)E-03
1.5 (50-fold)	(5.32±0.08)E01	(-4.42±0.04)E-02	(7.9±0.06)E00	(-4.4±0.3)E-03
	(5.10±0.07)E01	(-4.44±0.03)E-02	(6.2±0.5)E00	(-3.55±0.25)E-03
	(6.06±0.11)E01	(-4.12±0.04)E-02	(1.00±0.04)E01	(-9.2±0.4)E-03
15 (500-fold)	(5.52±0.11)E01	(-3.97±0.03)E-02	(4.05±0.18)E00	(-6.54±0.14)E-03
	(6.01±0.11)E01	(-3.81±0.03)E-02	(6.54±0.22)E00	(-9.45±0.25)E-03

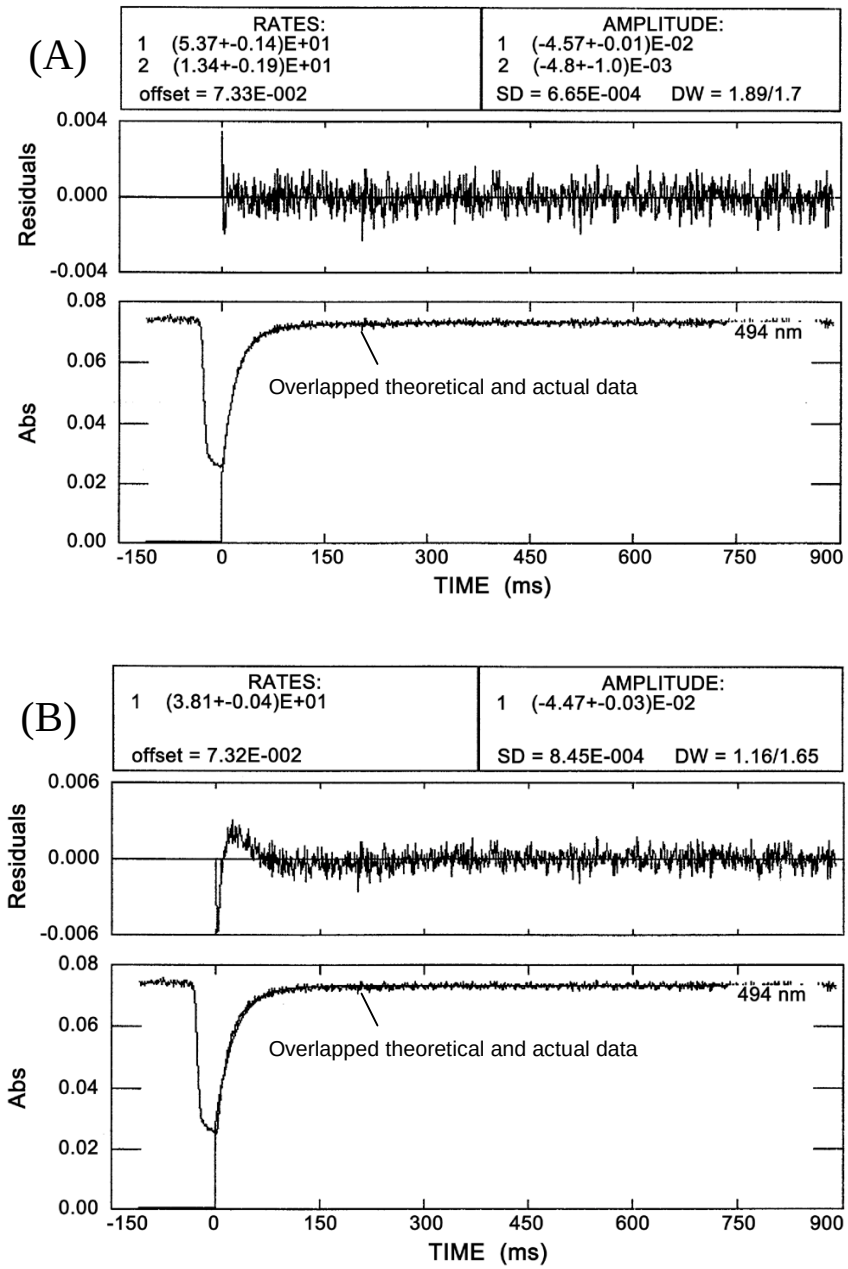

Figure II-16. Two representative single wavelength fit analysis of the reaction of Rbr_{red} with H_2O_2 (equimolar to the diiron sites) at room temperature. Final concentrations after mixing: Rbr, ~9 µM, H_2O_2, ~20 µM, 5-deazaflavin, ~ 1 µM, in anaerobic 0.1 M Tris buffer at pH 7.3. Stopped-flow scan mode: 1000 scans/second. The absorbance at 494 nm vs time was fitted to (A) first order two exponential rise ($A = A_1 \times \exp(-k_1 \times t) + A_2 \times \exp(-k_2 \times t) + b$) and (B) first order one exponential rise ($A = A_1 \times \exp(-k_1 \times t) + b$). Top graph of (A) and (B) represent the fit residuals of theoretical and actual data.

remaining ZnS_4Rbr_{red} was mixed with 200 μM H_2O_2 anaerobically. After mixing, the final concentration of ZnS_4Rbr diiron sites was 10 μM, and the H_2O_2 concentration was 100 μM, which is 5-fold molar excess of oxidizing equivalents over the ~50% occupied diiron sites (cf. Chapter IV). The absorption spectra for the reaction were scanned for 200 ms in scan mode of 1000 scans/second and scan range of 300-550 nm. In the control experiment, no increase in absorbance was observed, i.e., the protein remained reduced (**Figure II-17** (A) and (B)). When mixed with H_2O_2, however, the ZnS_4Rbr_{red} was rapidly oxidized by H_2O_2 (**Figure II-17** (C) and (D)), and the reaction was finished during the dead time of mixing. The Zn-substituted rubredoxin site in Rbr should have no absorption feature either at 370 nm or 494 nm as in the Zn-substituted *Clostridium pasteurianum* rubredoxin (*101*). Therefore, the shoulder at 330 nm and the peak at 370 nm in the first spectrum after mixing in this stopped-flow experiment can only be due to the oxidized diiron sites of ZnS_4Rbr. The absorption spectrum resembles that of oxidized CRbr and fully oxidized ZnS_4Rbr_{ox} (cf. **Figure II-3**), and is apparently due to the oxo-bridged diferric sites. Once the diiron site of ZnS_4Rbr is oxidized by H_2O_2, it cannot be reduced to the mixed-valent form as in the reaction of as-isolated Rbr with H_2O_2, since the reduced $[Fe(II)(SCys)_4]$ as the electron source does not exist. Therefore no further changes in absorbance would be expected and none are observed. Also no buildup of an A_{410} peak is observed. This result would suggest that TyrO· requires formation of a mixed-valent diiron site.

II.C.2.3. Rapid freeze-quench (RFQ) EPR spectroscopy of Rbr_{red} oxidation by H_2O_2

In an attempt to monitor the internal electron transfer reaction, Rbr_{red} was mixed with H_2O_2 at a concentration equimolar to the diiron sites in a rapid freeze quench apparatus

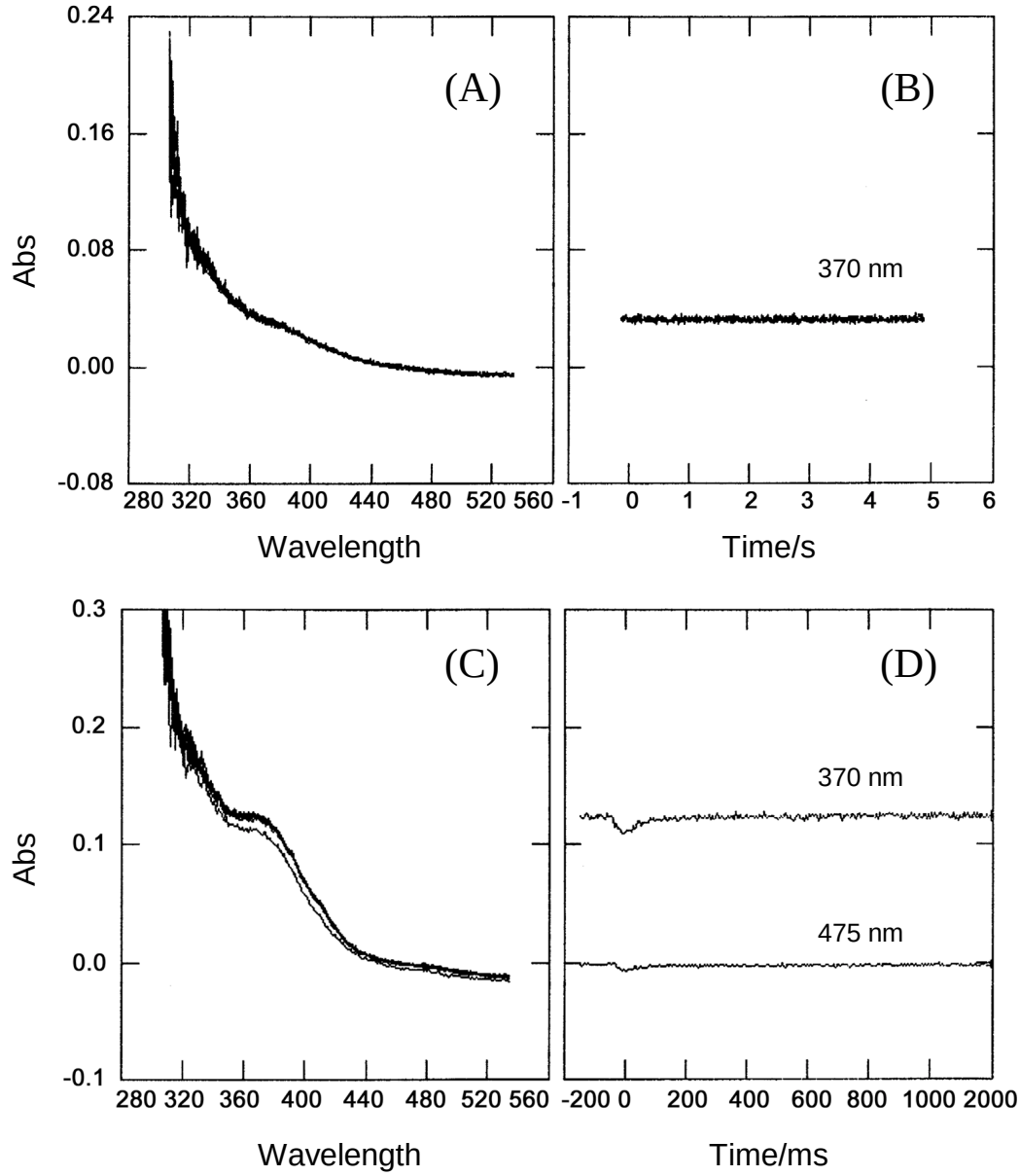

Figure II-17. A representative stopped-flow experiment of the reaction of ZnS_4Rbr_{red} form with H_2O_2 (5-fold molar excess of oxidizing equivalents over occupied diiron sites). (A) and (B) Control: Rbr, ~10 µM diiron sites (final concentration), in anaerobic 0.1 M Tris buffer, pH 7.3, mixed with the same buffer, at room temperature. Stopped-flow scan mode: 1000 scans/second. (A) The control spectra of 9 scans from 1 ms to 180 ms, interval: 20 ms. (B) The kinetic trace of absorbance at 370 nm for the reaction described in (A). (C) and (D) Reaction: Rbr, ~10 µM diiron sites (final concentration), in anaerobic 0.1 M Tris buffer, pH 7.3, mixed with the same buffer but containing H_2O_2, ~0.1 mM (final concentration), 5-deazaflavin, ~1 µM (final concentration), at room temperature. Stopped-flow scan mode: 1000 scans/second. (C) The reaction spectra of 9 scans from 1 ms to 180 ms, interval: 20 ms. (D) The kinetic traces of absorbance at 370 nm, and 475 nm for the reaction described in (C).

(cf. **Figure II-2**). In order to observe the EPR spectra, these experiments had to be performed at much higher concentrations of Rbr, H_2O_2, and 5-deazaflavin. **Figure II-18** shows the X-band RFQ EPR spectra, including the spectra of Rbr_{red} and as-isolated Rbr_{ox} (controls), and the spectra of the oxidation reaction at time point of 30 ms, 178ms and 5 s. As expected, no EPR signals were observed for the Rbr_{red} control. Also as expected, the EPR spectrum of the Rbr_{ox} control showed signals at g = 9.5 and 4.3, which are due to ground- and excited-Kramers doublets of the S = $^5/_2$ FeS_4 centers, and signal at g = 2.00, 1.77, and 1.66, which is due to a small portion of the mixed-valent diiron sites in the as-isolated Rbr_{ox} (*59*). The three spectra of the RFQ oxidation reaction 30 ms, 178 ms and 5 s after quenching show the signals at the similar g values to those of the Rbr_{ox} and no extra signals. The ratios of the mixed-valent EPR signal at g = 2.00 relative to the [Fe(III)$(SCys)_4$] signal at g = 4.3 did not vary at the various reaction quenching times, and the mixed-valent signal is relatively much more intense than that of the Rbr_{ox} control. (See **Figure II-19**.) This result was unexpected, in light of the results from the stopped-flow experiments. Because only H_2O_2 equimolar to the diiron sites was used in the RFQ experiments, all the H_2O_2 should have been consumed during the first phase of the oxidation reaction that finished in the dead time of stopped-flow experiments (~ 1 ms), which should, therefore, also be finished in the dead time of RFQ EPR experiments (~ 5 ms). If so, only the internal electron transfer reaction, step 1a, should be observed in the RFQ EPR. The expected initial product of this reaction, the [Fe(III)Fe(III)]/[Fe(II)$(SCys)_4$]Rbr form, is EPR silent, whereas, both the mixed-valent diiron site and oxidized rubredoxin site in the expected product of the internal electron transfer have EPR signals. Both of the intensities of g = 2.00 and g = 4.3 were, therefore,

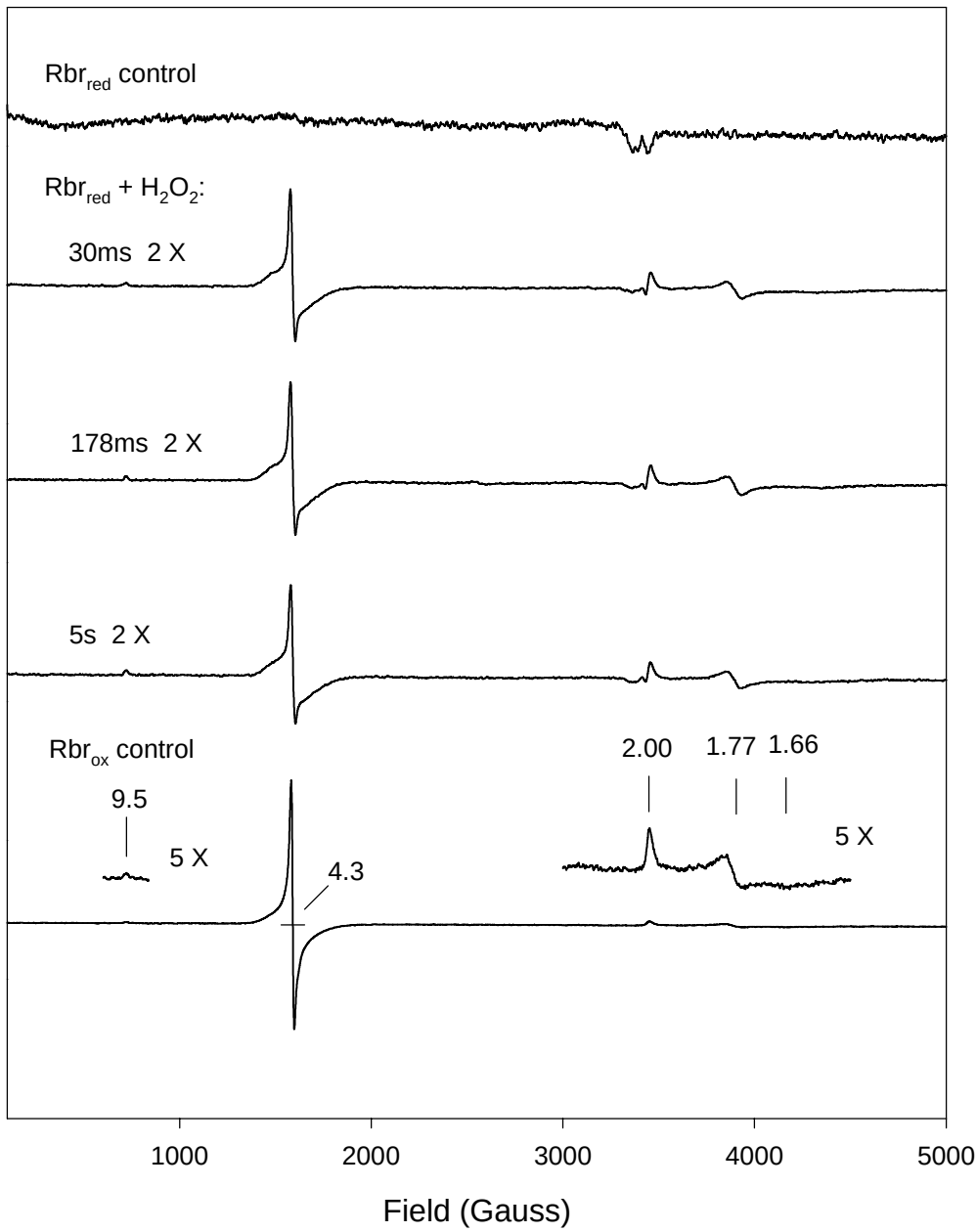

Figure II-18. Rapid freeze quench EPR spectra of the reaction of Rbr_{red} with H_2O_2 (equimolar to the diiron sites of Rbr) at room temperature. After mixing: Rbr_{red}, ~ 0.20 mM, H_2O_2, ~ 0.44 mM, 5-deazaflavin, ~0.02 mM, in 0.1M Tris, pH7.3. EPR conditions: T = 5.0 K; microwave frequency 9.65 GHz; microwave power 2.0mW; modulation amplitude 1 mT; modulation frequency 100 kHz.

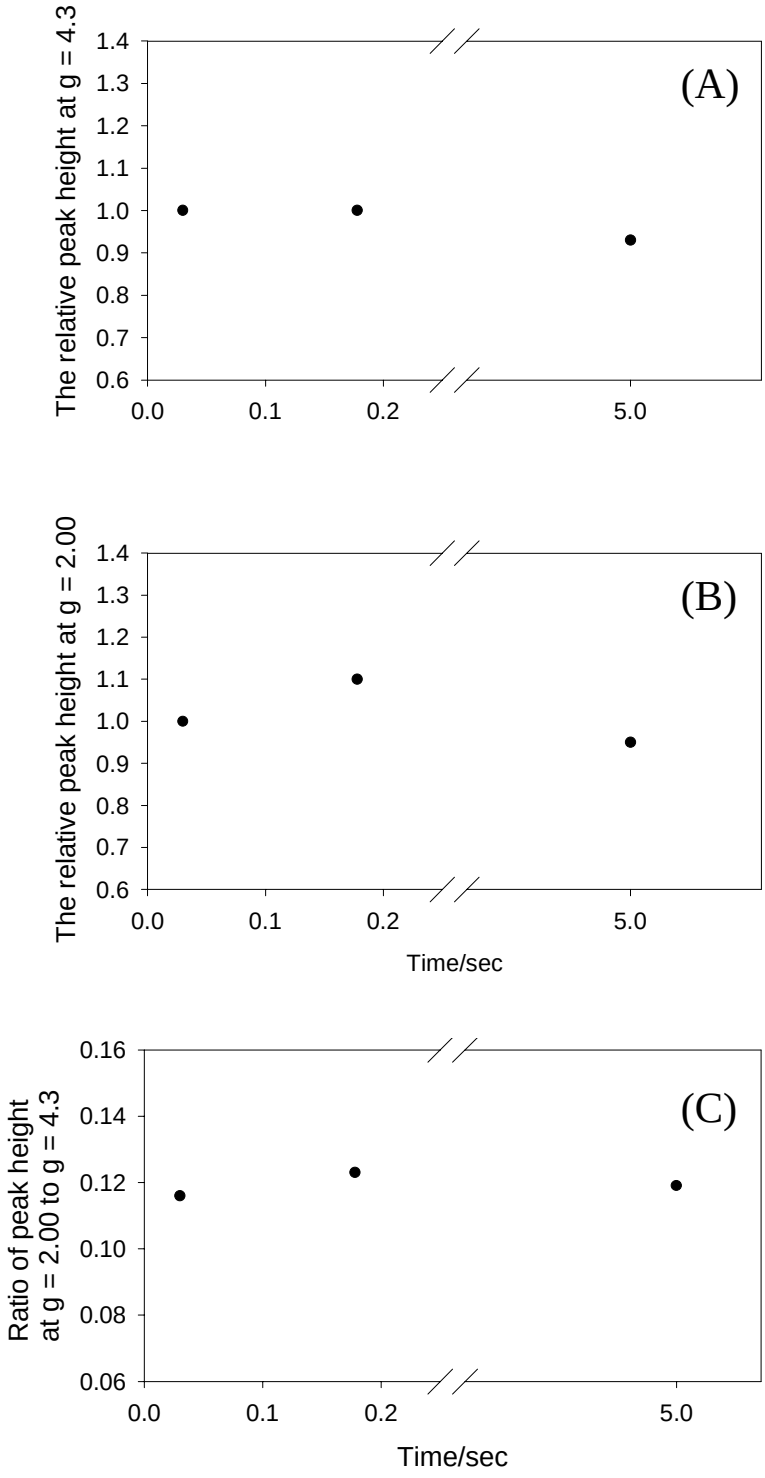

Figure II-19. Time course of (A) relative peak height at g = 2.00, (B) relative peak height at g = 4.3, (C) the ratio of peak height at g = 2.00 to g = 4.3, intensities of EPR signals were measured from the rapid freeze quench EPR spectra (cf. **Figure II-18**) of the reaction of Rbr_{red} with H_2O_2 (equimolar to the diiron sites in Rbr) at room temperature by setting the peak height of t = 30 ms to 1.0. After mixing: Rbr, ~ 0.20 mM, H_2O_2, ~ 0.44 mM, 5-deazaflavin, ~0.02 mM, in 0.1 M Tris, pH 7.3.

expected to increase with the RFQ reaction time until 200 ms, when the electron transfer reaction should be completed. An explanation for this dilemma is that the freeze-quenching did not quench the internal electron transfer reaction, i.e., it continued even at –160 °C when stored in liquid nitrogen. In fact, it has been previously considered that one of the major problems of the RFQ technique is that first-order reactions in proteins such as internal electron and proton transfers may continue in the frozen state (*96*).

RFQ oxidations of Rbr_{red} by a 5-fold molar excess of H_2O_2 over Rbr dimer were also carried out. **Figure II-20** shows the X-band RFQ EPR spectra, including the spectra of Rbr_{red} controls, the spectra of the oxidation reaction at 26 ms, 92 ms, 424 ms and 10 s quenching times. The intensity of the g = 4.3 signal showed no significant change with the reaction time, as seen in **Figure II-21**, which agrees with the RFQ EPR experiments using one molar equivalent of H_2O_2 per Rbr diiron site, and with the internal electron transfer reaction occurring even in the frozen state. The relative peak height of the rhombic signal at g ~1.7 decreases with the reaction time, consistent with the second order reaction of the mixed-valent diiron site with H_2O_2 in the second and third phases. There is also a free radical signal at g = 2.01 found in all four RFQ EPR spectra with excess H_2O_2. The expanded spectrum of the g =2.01 is shown in **Figure II-22**. The intensities of this signal increased first then decreased (cf. **Figure II-21** (B)). However, this signal does not resemble that of the tyrosyl radical, since the tyrosyl radical usually shows hyperfine splitting around g = 2.00. In order to photochemically reduce Rbr, ~20 μM (final concentration after mixing) of 5-deazaflavin was added to the protein solution. Free radical signals likely come from the reaction of 5-deazaflavin with H_2O_2, and probably obscure the tyrosyl radical signals during the reaction.

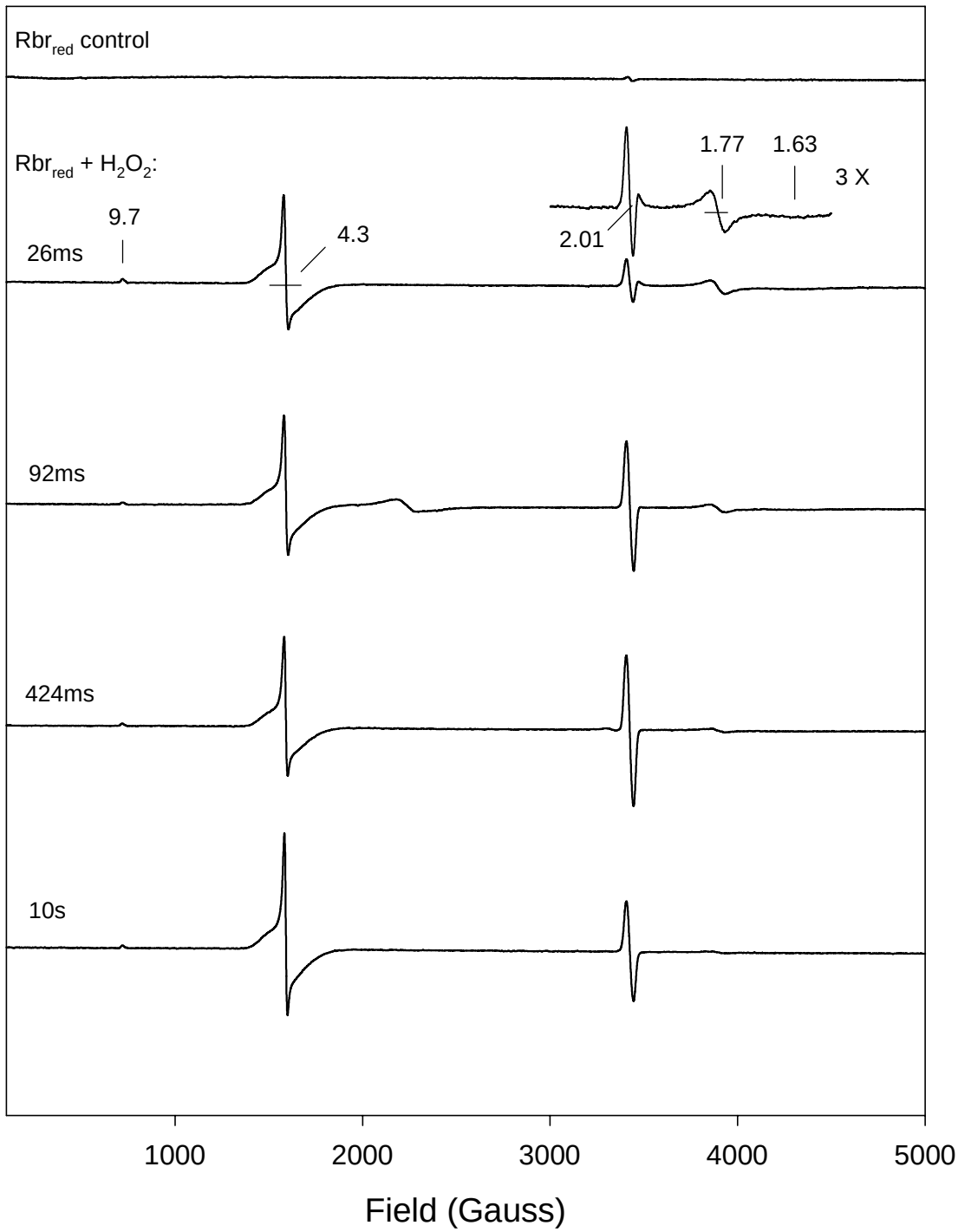

Figure II-20. Rapid freeze-quench EPR spectra of the reaction of Rbr$_{red}$ with 5-fold molar excess H_2O_2 oxidizing equivalents over total iron at room temperature. After mixing: Rbr, ~0.20 mM, H_2O_2, ~3 mM, 5-deazaflavin, ~0.02 mM, in 0.1 M Tris, pH 7.3, 1 mM DTPA. EPR conditions: T = 5.0 K; microwave frequency 9.65 GHz; microwave power 2.0 mW; modulation amplitude 1 mT; modulation frequency 100 kHz.

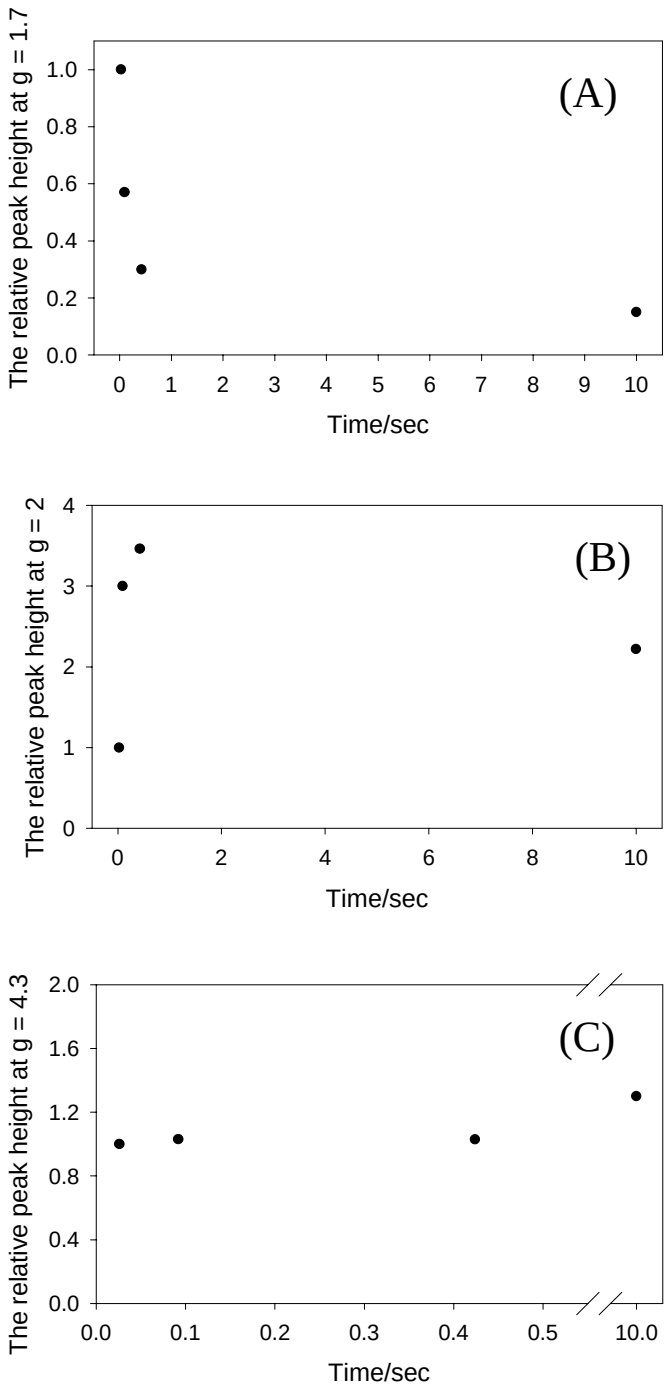

Figure II-21. Time course of (A) relative peak height at g = 1.7, (B) relative peak height at g = 2.0, and (C) relative peak height at g = 4.3, intensities of EPR signals were measured from the rapid freeze quench EPR spectra (cf. **Figure II-20**) of the reaction of Rbr_{red} with 5-fold molar excess H_2O_2 oxidizing equivalents over total iron at room temperature by setting the corresponding peak heights at t = 26 ms to 1.0 . After mixing: Rbr, ~0.20 mM, H_2O_2, ~3 mM, 5-deazaflavin ~0.02mM, in 0.1 M Tris, pH 7.3, 1mM DTPA.

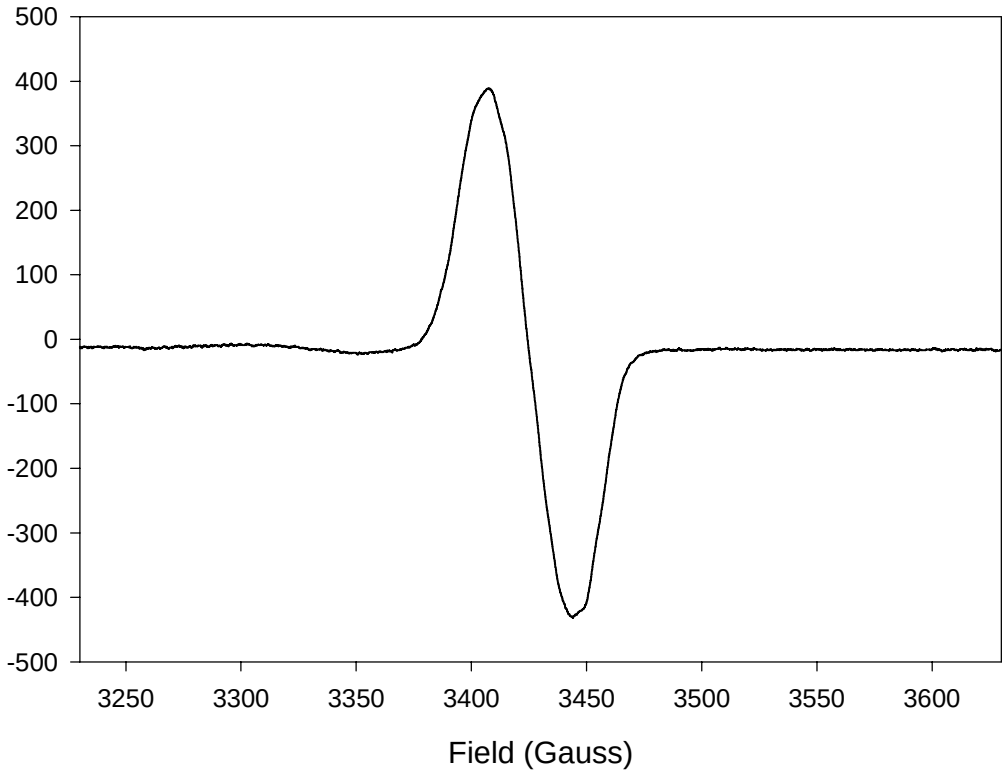

Figure II-22. Rapid freeze-quench EPR spectrum of the g = 2.01 region of the reaction of Rbr_{red} with 5-fold molar excess oxidizing equivalents of H_2O_2 over total iron of Rbr (room temperature) at time point of 424 ms. After mixing: Rbr, ~0.20 mM, H_2O_2, ~3 mM, 5-deazaflavin, ~0.02 mM, in 0.1 M Tris, pH 7.3, 1 mM DTPA. EPR conditions: T = 5.0 K; microwave frequency 9.65 GHz; microwave power 2.0 mW; modulation amplitude 1 mT; modulation frequency 100 kHz.

II.C.2.4. EPR monitoring disproportionation of Rbr mixed-valent diiron site

Figure II-23 and **Figure II-24** show the EPR spectra of the Rbr generated from manually mixing the Rbr_{red} with one-molar equivalent of H_2O_2 per Rbr_{red} diiron site anaerobically and the percentage of Rbr_{mv} with time, respectively. The percentage of mixed-valent diiron site in Rbr showed no significant change over the time course of 3 min to 3 hours reaction time at room temperature. The average percentage is about 60% (cf. **Figure II-24**), which agrees with the maximal fraction observed during the redox titration of the diiron site of Rbr (*59*). The disproportionation of mixed-valent diiron site in Rbr, therefore, seems to be finished before 3 min.

II.C.2.5. The mechanism of the oxidation reaction of Rbr by H_2O_2

Figure II-25 shows the proposed mechanism of oxidation of Rbr_{red} by H_2O_2. The first phase of the reaction can be assigned to a rapid oxidation of the diferrous diiron site to the diferric form by H_2O_2. The rate constant for this phase exceeds 700 s^{-1}, and, therefore, this phase is already complete on the time scale of the stopped-flow instrument (1-2 msec dead time). This two-electron oxidation of Rbr_{red} reduces H_2O_2 to two water molecules. In the second phase, the reduced rubredoxin-like site transfers electrons to the diferric site across the head-to-tail dimer interface of Rbr, and the diferric site is one-electron reduced to the mixed-valent diiron site. This phase is $[H_2O_2]$-independent. Excess H_2O_2 then oxidizes the mixed-valent diiron site to the fully oxidized species. This one-electron oxidation reaction creates hydroxyl radicals from H_2O_2. Tyrosyl phenol side chains from the conserved residues Tyr27 and Tyr127, which are hydrogen bonded to carboxylate ligands of the diiron sites (cf. **Figure III-5**, Chapter III), may rapidly react with some of

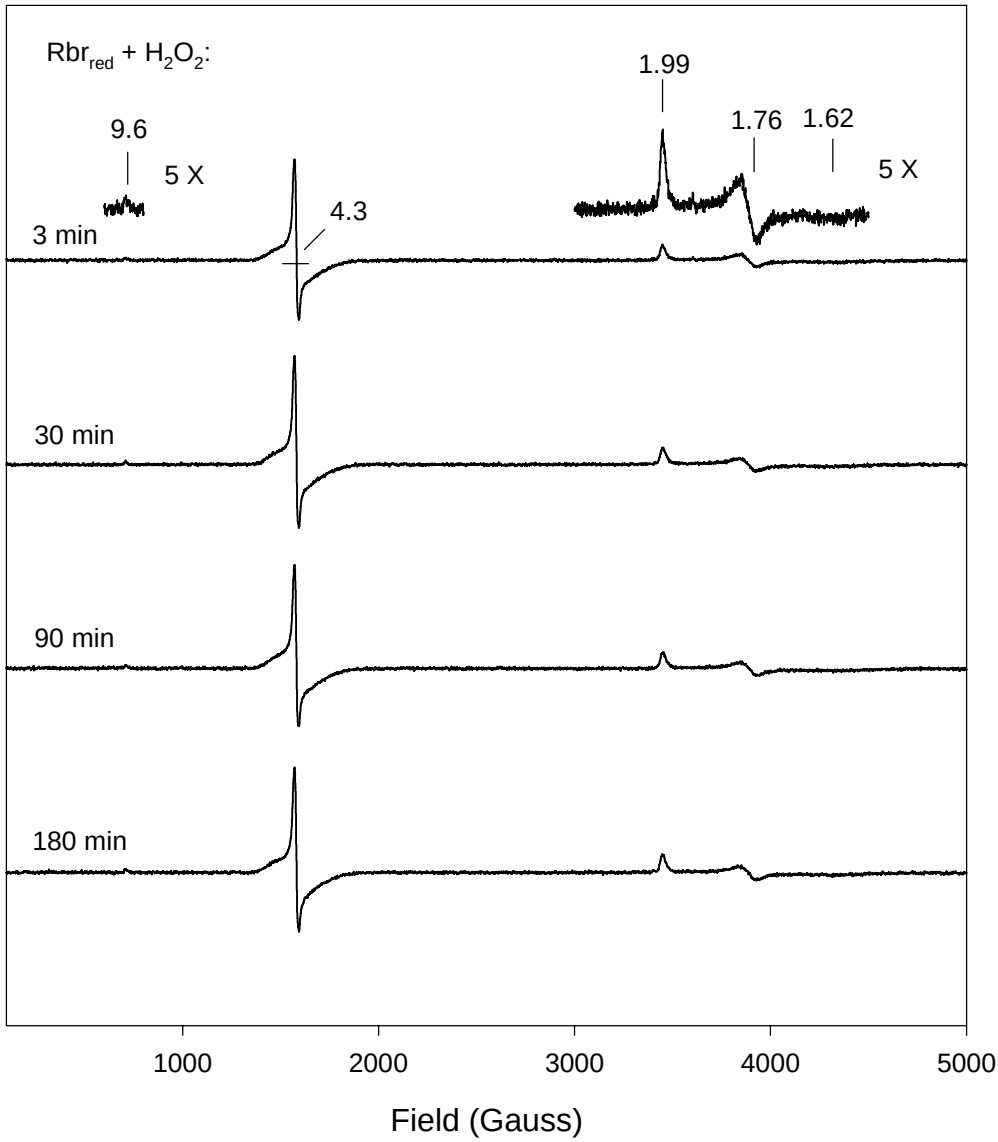

Figure II-23. The EPR spectra of the disproportionation reaction of Rbr_{mv} at room temperature. Rbr_{mv} was prepared by manually mixing Rbr_{red} ~ 86.7 µM (final concentration), 5-deazaflavin, ~8.7 µM (final concentration), in anaerobic buffer 0.1 M Tris at pH 7.3 with 177 µM H_2O_2 in anaerobic buffer 0.1 M Tris at pH 7.3. EPR conditions: T = 5.9 K; microwave frequency 9.65 GHz; microwave power 2.0 mW; modulation amplitude 6.366 G; modulation frequency 100 kHz.

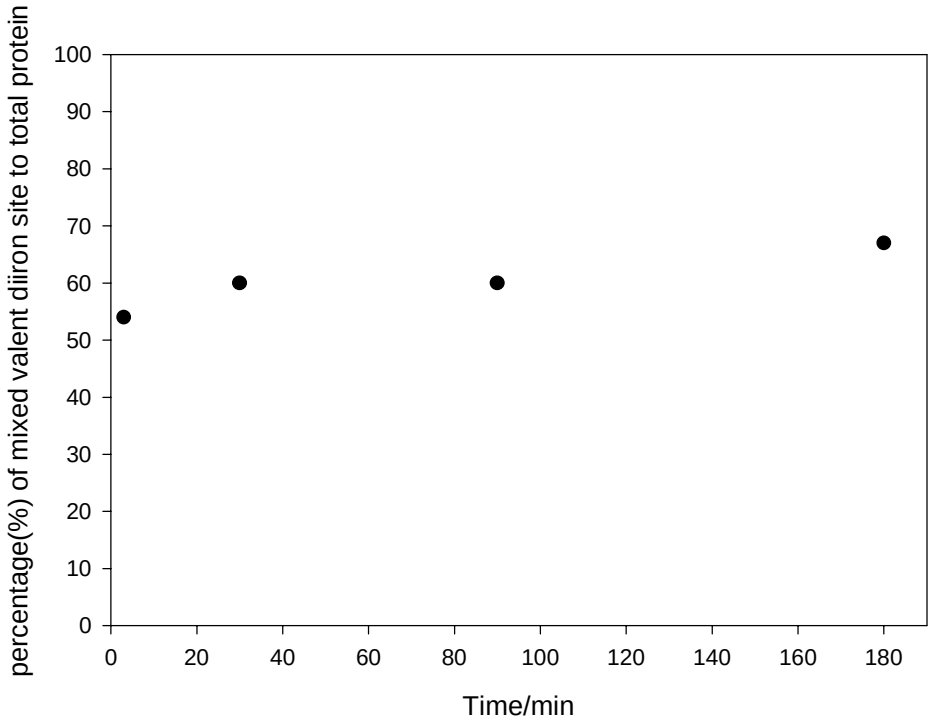

Figure II-24. Percentage of Rbr_{mv} using Cu-EDTA as the standard with time. Rbr_{mv} was prepared by manually mixing Rbr_{red} ~ 86.7 µM (final concentration), 5-deazaflavin, ~8.7 µM (final concentration), in anaerobic buffer 0.1 M Tris at pH 7.3 with 177 µM H_2O_2 in anaerobic buffer 0.1 M Tris at pH 7.3. EPR conditions: T = 5.9 K; microwave frequency 9.65 GHz; microwave power 2.0 mW; modulation amplitude 6.366 G; modulation frequency 100 kHz.

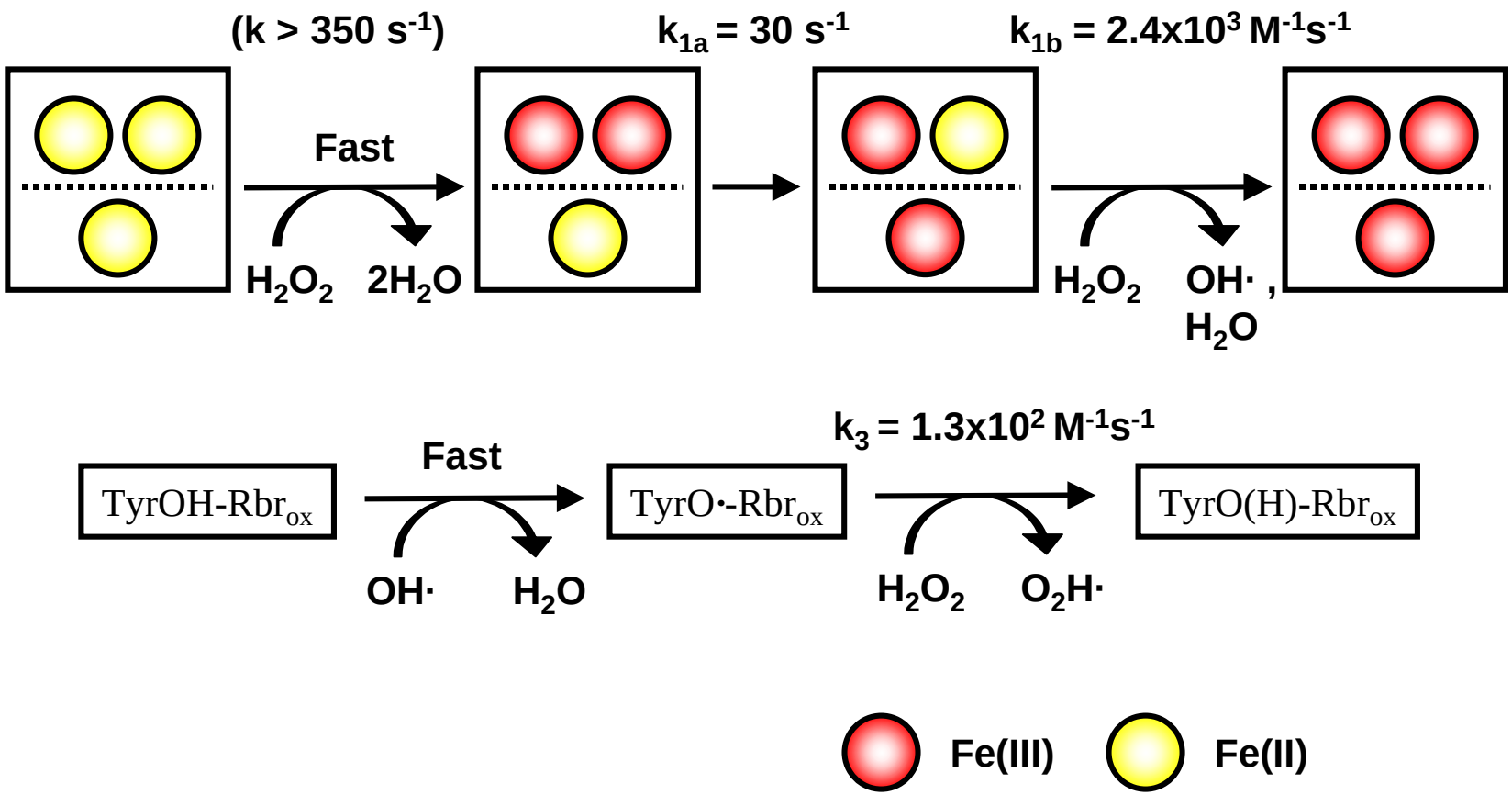

Figure II-25. Schematic drawing of the mechanism of oxidation of Rbr_{red} by H_2O_2. Dashed lines represent the "head-to-tail" dimer interface. Spheres above and below the dashed lines represent the diiron and rubredoxin-like sites, respectively.

these hydroxyl radicals. The decomposition of the tyrosyl radicals in Rbr in the final phase is H_2O_2-dependent.

The first phase of the oxidation reaction of reduced Rbr by H_2O_2 from the diferrous form to diferric form indicates that it is the diiron site, not the rubredoxin site that reacts with H_2O_2. The fast reaction rate of first phase was not observed in other diiron proteins. The diferrous site in RNR R2 can be oxidized by excess H_2O_2 to the diferric with no tyrosyl radicals generated, unlike the oxidation of R2 proteins by dioxygen (*102, 103*), and the mechanism of the reaction of R2 and H_2O_2 is unknown. Some synthetic diferric complexes were found to irreversibly bind with H_2O_2 to form μ-1,2-peroxo complexes, which are more stable than those obtained from the reaction of the synthetic diferrous complexes with dioxygen (*70*). For Rbr, no peroxo intermediates were observed for mixed-valent diiron species or diferric species of Rbr during its further oxidation reaction with H_2O_2. Whether it is possible that the H_2O_2 forms a transient peroxo bridge with the diferrous site before the formation of the μ-oxo bridge of the diferric form upon oxidation is discussed in Chapter III, where the crystal structures of the Rbr_{red} and $Rbr_{red}N_3$, a reduced Rbr azide adduct, are described and a structural basis for the proposed mechanism is provided. The one electron oxidation of the mixed-valent diiron site to the diferric form by H_2O_2 is much slower than the oxidation of the diferrous form by H_2O_2, and the rate of oxidation of the mixed-valent diiron site of Rbr by H_2O_2 only becomes comparable to the [H_2O_2]-independent internal electron transfer reaction between rubredoxin site and diferric site in Rbr when using high concentration of H_2O_2. The physiological concentration of H_2O_2 that may occur within *D. vulgaris* cells is still unknown. However, heme-containing catalase from *D. vulgaris* has been isolated (*104*),

which may consume the majority of the H_2O_2 and maintain the concentration of H_2O_2 at a low level in the cell (*38*). In *E. coli* the steady state of H_2O_2 concentrations is estimated to be only 10^{-7} to 10^{-6} M (*2*). If the concentration of H_2O_2 in *D. vulgaris* were at same level, the reaction rate for one-electron oxidation of the Rbr mixed valent diiron site by H_2O_2 would be less than 10^{-3} s^{-1}, which, based on the kinetic results, is much slower than the internal electron transfer. Therefore, the oxidation of mixed-valent diiron site of Rbr by H_2O_2 should be less relevant to the Rbr NADH peroxidase activity. In the NADH peroxidase reaction, the mixed-valent diiron site may be re-reduced to the diferrous form by NADH/BenC much faster than it is oxidized by H_2O_2. The mechanism for Rbr catalyzed NADH/peroxidase reaction (1) is proposed below:

$$[Fe(II)Fe(II)]/[Fe(II)(SCys)_4]Rbr + H_2O_2 + 2H^+ \longrightarrow$$
$$[Fe(III)Fe(III)]/[Fe(II)(SCys)_4]Rbr + 2H_2O \quad \text{(fast)} \quad (3a)$$

$$[Fe(III)Fe(III)]/[Fe(II)(SCys)_4]Rbr \longrightarrow [Fe(III)Fe(II)]/[Fe(III)(SCys)_4]Rbr \quad (3b)$$

$$[Fe(III)Fe(II)]/[Fe(III)(SCys)_4]Rbr + NADH \longrightarrow$$
$$[Fe(II)Fe(II)]/[Fe(II)(SCys)_4]Rbr + NAD^+ + H^+ \quad \text{(slow)} \quad (3c)$$

CHAPTER III

X-RAY CRYSTAL STRUCTURES OF REDUCED RUBRERYTHRIN AND ITS AZIDE ADDUCT: A STRUCTURE-BASED MECHANISM FOR A NON-HEME DI-IRON PEROXIDASE

III.A. Background and significance

A protein containing a unique combination of an [$Fe(SCys)_4$] site and a non-sulfur, oxo-bridged diiron site was first isolated from the anaerobic sulfate-reducing bacterium, *Desulfovibrio vulgaris* (*52*). At the time of its initial isolation, this protein had no known function and was, therefore, given the trivial name, rubrerythrin (Rbr), a contraction of rubredoxin and hemerythrin, which were the prototypical proteins containing the respective iron sites listed above. A subsequent X-ray crystal structure of recombinant oxidized (all-ferric) *D. vulgaris* Rbr (Rbr_{ox}) confirmed the initial spectroscopic identifications of these iron sites (*58*). More than a dozen Rbr homologues or their genes have since been identified from a variety of air-sensitive bacteria and archaea (*49*). Within the past few years, Rbr has been implicated as one component of a novel oxidative stress protection system in these microorganisms (*105*). Both in vivo (*38, 50, 51*) and in vitro (*48, 49, 91*) evidence indicates that Rbr can function as a peroxide reductase (peroxidase) (reaction 1):

$$2e^- + 2H^+ + H_2O_2 \longrightarrow 2H_2O \qquad (1)$$

Candidates for physiological electron donors in Rbr-catalyzed reaction 1 include Fe^{2+}, rubredoxin, and flavoprotein NADH:acceptor oxidoreductases (*48, 49, 88, 91*). Kinetics results on wild type and site-directed variant Rbrs are consistent with a mechanism for reaction 1 in which the diferrous site of Rbr rapidly reduces H_2O_2 and the [$Fe(SCys)_4$] site funnels electrons from the exogenous donors to the diiron site (*49, 105*). The reduced (all-ferrous) Rbr (Rbr_{red}) reacts with H_2O_2 on the millisecond time scale or faster, whereas, its reaction with O_2 is orders of magnitude slower (several minutes) (*48, 49*). Rbr_{ox}, on the other hand, shows little or no reactivity with hydrogen peroxide and no detectable catalase activity (i.e., catalysis of hydrogen peroxide disproportionation) (*54*).

The relatively sluggish reaction of Rbr_{red} with O_2 is somewhat puzzling, because the diiron-ligating amino acid sequence of Rbr (*58*) is homologous to those in a class of enzymes in which the diiron sites are known to rapidly (millisecond time scale) activate O_2 for oxidation of another substrate or co-factor. These enzymes include ribonucleotide reductase R2 subunit (RNR-R2) and methane monooxygenase hydroxylase (MMOH) (*63*). One possible source of the difference in dioxygen reactivity may lie in an unanticipated ligation feature of the diiron site in Rbr_{ox}, which is shown in **Figure III-1** (*58*).

The diiron structural motif in the O_2-activating enzymes typically consists of a four-helix bundle that supplies six protein ligands, four carboxylates (from Asp or Glu) and two histidyl imidazoles, within a pair of $D/EX_{29\text{-}37}EX_2H$ sequences (*63*). Based on this characteristic diiron-ligating sequence motif, both His131 and His56 in *D. vulgaris* Rbr had been predicted to furnish ligands to the diiron site (*106*). However, the crystal structure of the diferric site showed that while His131Nδ is indeed a ligand, the Nδ of

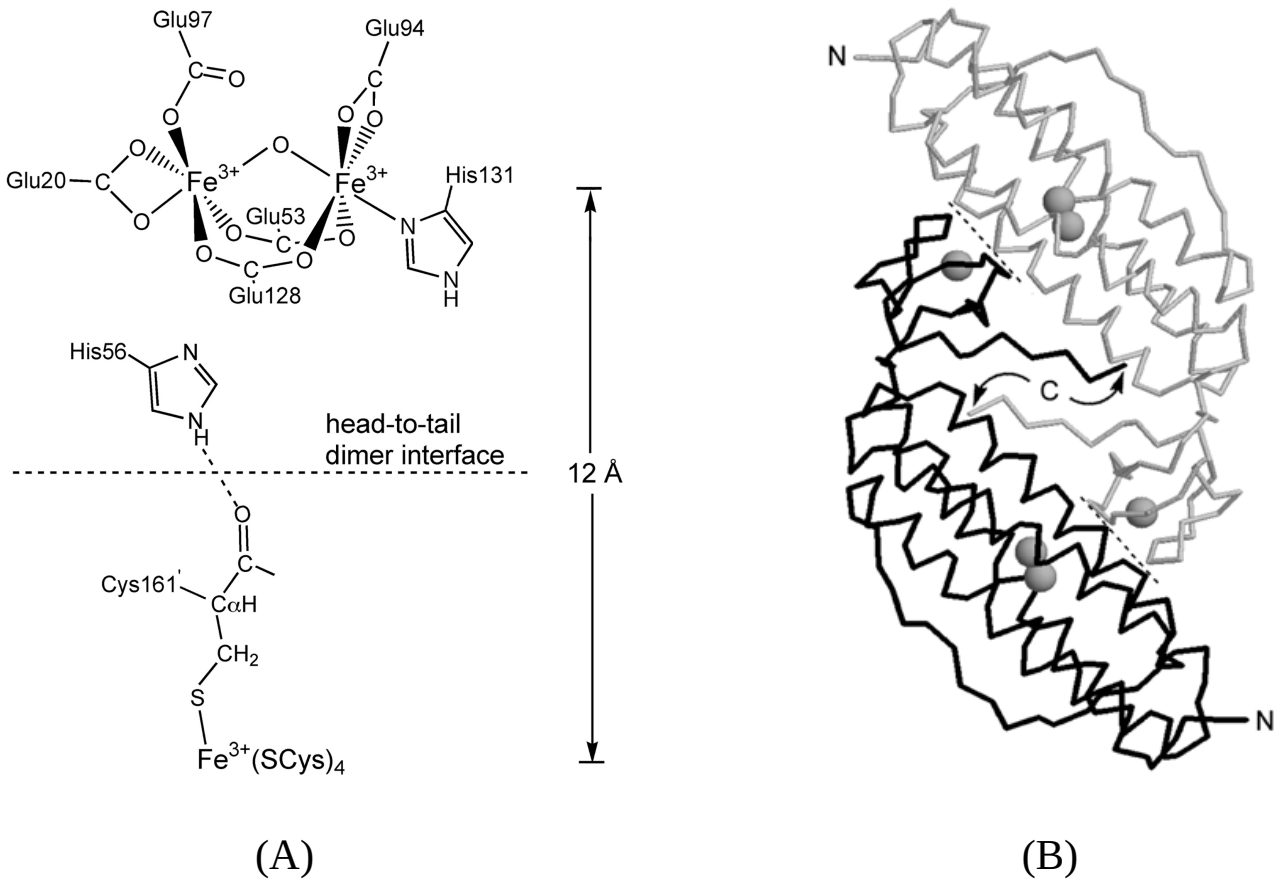

Figure III-1. (A) Schematic structure of the oxo-bridged diferric site in *D. vulgaris* Rbr showing its proximity to the [Fe(SCys)$_4$] site across the subunit interface of the "head-to-tail" dimer. (B) Protein backbone tracing of the *D. vulgaris* Rbr head-to-tail dimer viewed along its two-fold rotational axis drawn from the published X-ray crystal structure coordinates (PDB ID 1RYT). Iron atoms are represented as spheres, amino (N) and carboxyl (C) termini are labeled, and dashed lines indicate subunit interface contact regions between the [Fe(SCys)$_4$] and diiron domains.

His56 is 4.2 Å away from the nearest iron, i.e., too far away to be a ligand. Instead, Glu97, which has no structural homolog in the O_2-activating diiron enzymes, but which is conserved in all known Rbrs (*49*) provides a fifth carboxylate ligand (Fe-Oε1Glu 2.1 Å) that is approximately trans to the His56 "non-ligand". The His56NδH is hydrogen-bonded to the carbonyl of a cysteine residue, whose Sγ provides a ligand to the $[Fe(SCys)_4]$ site across the subunit interface of the "head-to-tail" dimer. This subunit interface between the $[Fe(SCys)_4]$ and diiron domains, shown schematically in **Figure III-1**, provides the closest approach between the two metal sites (~12 Å) in the crystal structure, and is, therefore, presumed to be the principal route of electron transfer between these sites.

Redox-induced His56 ↔ Glu97 ligand switching at the Rbr diiron site had been suggested (*58*), and supported by a crystal structure of a Glu97Ala variant (*62*). However, no crystal structure of Rbr_{red} has been reported. We now report the X-ray crystal structure of recombinant *D. vulgaris* Rbr_{red} and its azide adduct ($Rbr_{red}N_3$). We have also re-determined the structure of recombinant *D. vulgaris* Rbr_{ox} to a higher resolution than the previously published structure (*58*). The redox-induced structural changes and the azide-binding mode provide a basis for delineating the nature and selectivity of the dioxygen vs hydrogen peroxide reactivities of this non-heme diiron protein.

III.B. Experimental Section

III.B.1. Protein expression, purification, and crystallization

Recombinant *D. vulgaris* Rbr was overexpressed in *E. coli*, iron-constituted and purified as previously described (*49, 59*) but with one additional purification step. After the gel filtration, Rbr was loaded onto a Hitrap-Q (Amersham Pharmacia Biotech)

column pre-equilibrated with 25 mM 3-[*N*-morpholino]propanesulfonic acid (MOPS) pH7.3. The fraction containing Rbr (monitored as A_{280}) was eluted with the same buffer, concentrated to ~1 mM in Rbr homodimer in a Centricon cell and stored at -80 ºC until further use. Oxidized Rbr (Rbr_{ox}) solutions prepared in this fashion were used for all crystallizations. Crystals of Rbr_{ox} were grown by the hanging drop method as previously described (*58*) except that 12% glycerol was added to the reservoir. Deep red crystals were observed within hours of setting up the crystallization and these were allowed to continue growing for 2-3 days, as shown in **Figure III-2** (A). Rbr_{ox} crystals ~ 0.3 x 0.2 x 0.2 mm in size were mounted in 20-micron CryoLoops and flash-frozen to 95 K in a nitrogen cryostream. In order to obtain reduced (all ferrous) Rbr (Rbr_{red}) crystals, a reducing reservoir solution containing 15% PEG 1450, 10 mM NADH, 5 mM sodium dithionite, in 0.1 M Tris-(hydroxymethyl)-aminomethane (Tris), pH 8.5 was degassed and flushed with argon using a vacuum manifold. Crystallization was carried out in an anaerobic chamber using the hanging drop method. Five microliters of Rbr_{ox} solution was mixed with an equal volume of the reducing reservoir buffer. Neither the sodium dithionite nor the NADH in the reservoir buffer noticeably reduced the iron sites in Rbr_{ox}, as judged by retention of the red color in the mixed solution. To this mixture was added 1 µl of 0.4 mM BenC, a Fe-S, FAD-containing NADH oxidoreductase (*107*) that has been demonstrated to catalyze reduction of Rbr_{ox} by NADH (*49*). Upon mixing, the deep red color of the solution quickly bleached to colorless, indicating full reduction of Rbr. Colorless, diffraction-quality Rbr_{red} crystals (**Figure III-2** (B))were observed within two days using a Stender Dish (Hampton Research Company) for a better seal. For mounting, Rbr_{red} crystals and a dewar of liquid nitrogen were brought into an argon-purged glove

(A)

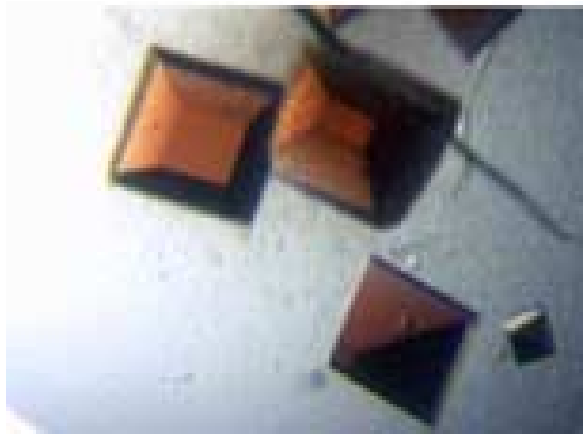

(B)

Figure III-2. Photographs of *D. vulgaris* Rbr crystals. (A) Rbr_{ox}, obtained from 1.0 mM Rbr_{ox} dimer in 25 mM MOPS, pH 7.3 mixed with 15% (w/v) PEG1450, 0.1M Tris, pH 8.0 in 1:1 (v/v) ratio. (B) Rbr_{red}, obtained from 1.0 mM Rbr_{ox} dimer, in 25 mM MOPS, pH 7.3 mixed 15% PEG 1450, 10 mM NADH, 5 mM sodium dithionite, in 0.1 M Tris, pH 8.5 and 0.04 mM BenC in 1:1 (v/v) ratio anaerobically.

bag using the protruding eyepiece of a microscope for visualization. The crystals (~ 0.3 x 0.2 x 0.2 mm) were mounted on cryoloops, rinsed with mineral oil (which had been degassed by argon flow), flash-frozen and stored in liquid nitrogen. Colorless crystals of the Rbr_{red} azide adduct ($Rbr_{red}N_3$) (~ 0.3 x 0.2 x 0.2 mm) were obtained and mounted using the same methods described for Rbr_{red}, except that the reservoir buffer contained 25 mM MOPS pH 7.3 and 150 mM sodium azide in place of the Tris.

III.B.2. Data collection

All data were collected on a Rigaku Raxis IV detector using CuKα X-rays generated on a Rigaku RU200 rotating anode in the Georgia X-ray Crystallography Center at the University of Georgia. The temperature of the crystals was maintained at 95 K throughout data collection in a cryostream of nitrogen gas. For Rbr_{ox} and Rbr_{red} crystals, data were collected using a total of 360 one-degree oscillations for 5-minute exposures. For $Rbr_{red}N_3$ crystals, a total of 180 one-degree oscillations were used. The data were indexed and integrated using DENZO, and scaled using SCALEPACK (*108*). The molecular replacement calculations and refinement steps were carried out using CNS 1.0 (*109*), and model rebuilding was performed in O (*110*).

III.B.3. Refinement

Rbr_{ox}

The Rbr_{ox} structure was determined by molecular replacement, using the published Rbr_{ox} coordinates in PDB code 1RYT as the search model. The coordinate file of the search model with all solvent (including the oxo bridge at the diiron site) removed was converted to a format suitable for CNS. The correlation coefficient of best solution after cross-rotation and translation searches was 0.758 and θ_1= 157.09, θ_2= 0.23, θ_3= 203.25, x

= 24.43, y = -0.02, z = 49.87. At this point, 8% of the reflections were excluded to monitor the refinement. The full resolution range of the data was used in rigid-body refinement. The starting *R* factor was lowered from 0.351 to 0.347, and R_{free} was 0.339 with no significant change. After refinement by conjugate gradient energy minimization, $R(R_{free})$ dropped to 0.301(0.317). Because simulated annealing refinement did not lower either *R* factor, the model generated in minimization refinement was used to calculate a composite omit map ($2F_o$-F_c). After this first round of refinement both the model and the electron density map were displayed in O. The N-terminal methionine was not observed in the map and was assumed to be disordered. Several disoriented side chains of residues were manually rebuilt to better fit into the electron density map. The new model was refined by minimization and simulated annealing, which lowered the $R(R_{free})$ to 0.295(0.307). Grouped *B*-factor refinement followed by individual *B*-factor refinement further reduced $R(R_{free})$ to 0.268(0.278). At this point, 129 water molecules with peak heights above 3σ were picked by difference Fourier analysis and refined as oxygen atoms, which decreased $R(R_{free})$ to 0.227(0.241). The occupancies for all atoms were constrained to 1.0 (excluding atoms in multi-conformers of Arg54, discussed below) throughout refinement, which means that *B*-factor values reflect both thermal motion and disorder. Another minimization refinement reduced $R(R_{free})$ to 0.218(0.234). After this second round of refinement, the new model was checked and adjusted against a composite omit map in O. A third round of refinement using an iterative process, during which 102 new water molecules were picked, resulted in $R(R_{free})$ decreasing to 0.193(0.214). The composite omit map at this point did not match the side chain and backbone atoms of residues Gly78 and Ile79 from the model, so these residues were

manually rebuilt with a *cis*-peptide bond connecting them. An obvious electron density connecting Fe1 and Fe2 at the diiron site and corresponding to the oxygen bridge in 1RYT, was manually fitted as a water molecule. The electron density map at the position of the Arg54 side chain was initially interpreted as one conformation with two water molecules located nearby. However, a better visual fit was obtained as two alternative side chain conformations, so these two water molecules were deleted, and the alternate conformation of Arg54 was fitted to the map. The final round of refinement was carried out including minimization, grouped and individual *B*-factors, and simulated annealing. The parameter file of the *cis*-peptide bond between Gly78 and Ile79, and the topology file including added information of multiple conformers of Arg54 were used during the final refinement. The final $R(R_{free})$ was 0.190(0.210). The coordinates of the final model, including 230 water molecules per protein subunit, were confirmed using a new composite omit map in O.

Rbr_{red}

Difference Fourier analysis was used to refine the structure of Rbr_{red}. The initial Rbr_{red} model used the coordinates for Rbr_{ox} obtained just after the third round of refinement described above and before the third round of rebuilding in O with solvent coordinates removed. After rigid body refinement, $R(R_{free})$ decreased from 0.353(0.336) to 0.342(0.324). The subsequent refinement route followed that described above for Rbr_{ox} except that simulated annealing refinement was omitted if it did not improve the model. After the first round of refinement, $R(R_{free})$ decreased to 0.303(0.322). The first composite omit map showed a large unassigned electron density at the diiron site, which was connected to the electron densities of residues Glu20, Glu53, Glu128, and His 56.

However, Fe1 was in a relatively much weaker electron density nearby with no connection to other residues. Fe1 was, therefore, manually moved into the center of the large density, and the smaller density was assigned to a water molecule. After the second round of refinement with the first shell of 150 water molecules picked, $R(R_{free})$ decreased to 0.212(0.226). A simulated annealing composite omit map ($2F_o$-F_c) was calculated, omitting residue Gly78 and Ile79. (It was at this point that the decision was made to build a *cis* rather than *trans* peptide bond for Gly78-Ile79 into the models for all three Rbr structures. The third round of map fitting for Rbr_{ox} was, therefore, delayed until the refinement of Rbr_{red} was completed). The parameter file for the *cis*-peptide bond between Gly78 and Ile79 was used in the refinement following the second model rebuilding in O. Another 124 water molecules were assigned. After this third round of refinement, $R(R_{free})$ decreased to 0.185(0.205). In O, two water molecules appeared to be ligands to each of the iron atoms at the diiron site. Three other water molecules were removed from the coordinate list written out from O after the third model rebuilding, thereby reducing the total number of water molecules to 271. Two of these removed water molecules were due to the alternate conformation of Arg54. The other removed water molecule was located at a position with no detectable electron density. A final round of refinement using the topology file for two alternative Arg54 conformers gave no significant improvement of the model; the final $R(R_{free})$ factors were 0.184(0.205).

$Rbr_{red}N_3$

Refinement of the $Rbr_{red}N_3$ structure was performed similarly to that described for Rbr_{red}. The initial model used the third coordinate file of Rbr_{red} that had been written out from O with solvent coordinates removed. The parameter file for the *cis*-peptide bond

between Gly78 and Ile79 was used from the first step. This initial model gave $R(R_{free})$ of 0.307(0.299). After the first round of refinement, R decreased to 0.286, but R_{free} increased slightly to 0.303. The first composite omit map showed a rod-shaped electron density connecting the two irons at the diiron site. Since published EPR/ESEEM evidence indicates that that azide perturbs the ferrous ions at the diiron site (*59*, *111*), the rod-shaped electron density was modeled as a μ-1,3 bridging azide ion. The topology and parameter files for the azide ion were obtained from Gerard Kleywegt's HIC-UP server (*112*). The bond angle of the three nitrogens of the coordinated azide was 173°, and this angle was restrained during subsequent refinement. During the second round of refinement, 144 water molecules were picked and R dropped to 0.213 and R_{free} to 0.224. One water molecule was removed from the model after the second map fitting, because it was in the position of the alternative conformation of Arg54. The topology file for the two Arg54 conformers was then used during the next round of refinement. Another 121 waters were picked, and $R(R_{free})$ decreased to 0.198(0.208). During the third model rebuilding, a disordered water molecule was deleted, and another water molecule at the protein surface was remodeled to an azide ion, based on the rod shape of the corresponding electron density. A final round of refinement was carried out, after which $R(R_{free})$ decreased to 0.178(0.203). The final model had 262 water molecules and 2 azide ions per protein subunit.

Data collection and refinement statistics for all three structures are summarized in **Table III-1**. Some atoms on side chains of several residues in each model were disordered, as evidenced by incomplete electron densities in the composite omit maps. These residues are Lys2, Lys5, Lys11, Lys35, Leu69, Glu151 and Gln152 in Rbr_{ox}, Lys2,

Table III-1. Data collection and refinement statistics

Parameter	Rbr_{ox}	Rbr_{red}	$Rbr_{red}N_3$
A. Data collection and processing statistics			
Temperature (K)	95	95	95
Unit cell dimensions (Å)			
a	48.9	48.5	48.3
b	80.6	80.0	80.1
c	100.1	100.1	100.2
Maximum Resolution (Å)	1.69	1.63	1.64
Total reflections	257523	273708	133046
Unique reflections	21164	22434	21509
Completeness[a] (%)	93.7	90.6	88.6
R_{merge}[b] (%)	6.5 (20.9)	7.7 (18.3)	5.8 (18.6)
R_{ano}[c] (%)	6.5 (20.9)	7.7 (18.4)	5.8 (18.6)
$\langle I \rangle / \langle \sigma(I) \rangle$	44.8	48.8	46.5
B. Refinement statistics			
Resolution range for refinement	25.95 – 1.69	25.75 – 1.63	23.37 – 1.64
R_{work} (%)	18.96	18.35	17.80
R_{free}[d] (%)	21.02	20.48	20.23
Number of water molecules	230	271	262
Number of azide ions	-	-	2
RMSDs from ideality[e]			
Bond lengths (Å)	0.005	0.004	0.005
Bond angles (°)	1.1	1.1	1.1
Dihedral angles (°)	19.1	19.3	19.4
Improper angles (°)	0.73	0.75	0.73
Wilson *B*-value ($Å^2$)	24.0	21.5	18.9
Mean *B*-value ($Å^2$)	22.3	18.9	17.5
Coordinate error[f] (Å)	0.19	0.18	0.17
Ramachandran plot[g]			
Residues in most favored regions (%)	93.5	92.9	92.9
Residues in additional allowed regions (%)	6.5	7.1	7.1
Residues in generously allowed regions (%)	0	0	0
Residues in disallowed regions (%)	0	0	0

[a]Values in parentheses correspond to the resolution shell.
[b]$R_{merge} = \Sigma(|I - \langle I \rangle|)/\Sigma\langle I \rangle$.
[c]Anomalous difference, $R_{ano} = \Sigma(|\langle I_+ \rangle - \langle I_- \rangle|)/\Sigma\langle I \rangle$.
[d]Calculated with 8% of the complete data set excluded from refinement.
[e]Stereochemical check was made using CNS.
[f]Estimated coordinate error from the Luzatti plot.
[g]Ramachandran plot was calculated using PROCHECK.

Lys5, Lys11, Lys35, Leu69, Glu111, Arg119, Glu151 and Gln152 in Rbr_{red}, and Lys5, Lys11, Leu69, Glu111, Arg119, Glu151 and Gln152 in $Rbr_{red}N_3$. All of these residues are located at the protein surface. The positions of the three irons in each structure were confirmed by anomalous difference Fourier maps. For each structure, a Hendrickson-Lattman coefficient was generated using an anomalous reflection file and the coordinate file from the final refinement, but with irons excluded from phase calculations. An anomalous difference Fourier map was then computed in O using data to 3.0-Å resolution. In order to examine differences between structures, $F_{obs}(Rbr_{red}N_3) - F_{obs}(Rbr_{red})$ electron density maps were calculated after removing solvent molecules from the models, including the two iron-ligating solvent molecules in Rbr_{red}. $Rbr_{red}N_3$ and Rbr_{red} reflection files were merged to one file containing two data sets, which was required for map calculations. The atomic coordinates for Rbr_{ox}, $Rbr_{red}N_3$ and Rbr_{red} have been deposited in the Protein Data Bank with accession numbers 1LKM, 1LKO and 1LKP, respectively.

III.C. Results and discussion

III.C.1. Overall Structures

Crystals obtained for all three *D. vulgaris* Rbr forms examined in this work, Rbr_{ox}, Rbr_{red} and $Rbr_{red}N_3$ belonged to space group *I*222, which is isomorphous with that published for the original *D. vulgaris* Rbr_{ox} crystal structure (*58*). Even though only homodimers have been detected for this Rbr in solution, all three forms of Rbr examined here crystallized as tetramers. The asymmetric unit contains one Rbr subunit, which is related to the remaining subunits of the tetramer by crystallographic two-fold axes. All three models have good stereochemistry with low r.m.s.d.s from ideality in bond length

and angles (cf. **Table III-1**). Ramachandran plots from PROCHECK (*113*) showed no residues in disallowed regions, or even generously allowed regions. The overall structures of Rbr_{ox}, Rbr_{red} and $Rbr_{red}N_3$ are all very similar to that of the published Rbr_{ox} (1RYT) (*58*). Apart from some disordered side chains at the solvent-accessible protein surface (listed in the Experimental Section) and residues at the diiron site discussed below, the corresponding residues in Rbr_{ox}, Rbr_{red} and $Rbr_{red}N_3$ all have very similar conformations. Two conformers of Arg54 are clearly visible in $2F_o$-F_c electron density maps of all three Rbr structures, and their occupancies were refined as 0.6 and 0.4. The peptide bond connecting residues Gly78 and Ile79 in all three Rbr structures is in a *cis* conformation. The *cis* conformation of this peptide bond was reported previously in a different metal derivative of *D. vulgaris* Rbr (1DVB) (*61*). No atom of the aforementioned residues is closer than ~8 Å to any iron atom, and these residues have no obvious effect on the iron sites in any of the various Rbr structures.

The overall r.m.s.d. of Rbr_{ox} vs 1RYT, Rbr_{red} vs. Rbr_{ox}, $Rbr_{red}N_3$ vs. Rbr_{ox}, and $Rbr_{red}N_3$ vs. Rbr_{red} are 0.86 Å, 0.50 Å, 0.50 Å and 0.31 Å, respectively. The better r.m.s.d. agreement of the Rbr_{red} and $Rbr_{red}N_3$ structures with that of Rbr_{ox} than with 1RYT may be due to the X-ray diffraction data being collected at room temperature for 1RYT vs 95K for the three structures reported here. Since the Rbr_{ox} structure reported here has a higher resolution than that of 1RYT (1.7 vs 2.1 Å), but similar to that of Rbr_{red}, and the R and R_{free} factors of Rbr_{ox} are reasonably low (cf. **Table III-1**), the subsequent comparisons will be confined to the three structures reported here. Important interatomic distances for the diiron sites in all three structures are listed in **Table III-2**.

Table III-2. Interatomic distances for iron sites of *D. vulgaris* Rbr_{ox}, Rbr_{red} and $Rbr_{red}N_3$

	Distance (Å)		
Atoms	Rbr_{ox}	Rbr_{red}	$Rbr_{red}N_3$
Fe1 – oxo	1.8	-	-
Fe1 – Glu 20OE1	2.1	2.2	2.2
Fe1 –Glu 20OE2	2.3	2.3	2.3
Fe1 – Glu 53OE1	2.2	2.1	2.1
Fe1 – Glu 128OE2	2.0	2.1	2.1
Fe1 – Glu 97OE1	2.1	-	-
Fe1 – His 56 ND1	-	2.3	2.3
Fe1 – HOH 1	-	2.2	-
Fe1 – N_3^- N1	-	-	2.2
Fe2 – oxo	2.1	-	-
Fe2 – Glu 94OE1	2.2	2.2	2.2
Fe2 –Glu 94OE2	2.2	2.3	2.3
Fe2 – Glu 53OE2	2.0	2.1	2.0
Fe2 – Glu 128OE1	2.1	2.1	2.1
Fe2 – His 131 ND1	2.2	2.2	2.2
Fe2 – HOH 2	-	2.2	-
Fe2 – N_3^- N3	-	-	2.2
Fe3 – Cys 158SG	2.4	2.3	2.3
Fe3 – Cys 161SG	2.3	2.3	2.3
Fe3 – Cys 174SG	2.3	2.3	2.3
Fe3 – Cys 177SG	2.3	2.3	2.3
average Fe3-CysSG	2.3	2.3	2.3
Fe1 --- Fe2	3.3	4.0	3.9
Fe1 --- Fe3	12.4	11.0	11.0
Fe2 --- Fe3	12.0	12.2	12.2

Both the diiron and [Fe(SCys)$_4$] site structures are nearly identical in 1RYT vs Rbr$_{ox}$, with r.m.s.d.'s of 0.24 Å for the diiron site (including residues 20, 53, 56, 94, 97, 128 and 131), and 0.14 Å for the [Fe(SCys)$_4$] site (including residues 158,161, 174, and 177). Ordered water molecules near the diiron site and in the crevice leading to it are in different positions in 1RYT and Rbr$_{ox}$. In 1RYT an ordered water (water 1) is within hydrogen bonding distance (2.8 Å) of the oxo bridge, and a second water further away from the diiron site is within hydrogen bonding distance (2.9 Å) of water 1. These two waters are not found in Rbr$_{ox}$, where several ordered waters that are >4 Å away from the oxo bridge are instead observed. The average Fe-O oxo bridge bond distances in both Rbr$_{ox}$ and 1RYT (2.0 Å) are longer than, but only slightly outside of experimental error from, the 1.8 Å typical for diferric oxo/carboxylato-bridged complexes (*114*). Resonance Raman spectroscopy, however, has unambiguously established the presence of an oxo bridge at the diiron site of *D. vulgaris* Rbr$_{ox}$ (*56*).

III.C.2. Comparison of Rbr$_{ox}$ and Rbr$_{red}$ Diiron Sites

The major structural differences between Rbr$_{red}$ and Rbr$_{ox}$ were found at and near the diiron sites. **Figure III-3** and **Figure III-4**, show the $2F_o$-F_c electron density maps and final models at the diiron sites of Rbr$_{ox}$ and Rbr$_{red}$. The two irons of the diiron site are labeled Fe1 (terminally ligated by Glu20) and Fe2 (terminally ligated by Glu94). The $2F_o$-F_c electron density map of Rbr$_{red}$ shows two peaks at the diiron site (Fe1: 19.7σ, Fe2: 21.1σ), which are of higher intensity than those in the Rbr$_{ox}$ map (Fe1: 14.4σ, Fe2: 14.6σ), whereas the peak intensities of Fe3 at the [Fe(SCys)$_4$] sites were similar to each other (18.4σ in Rbr$_{red}$ and 17.9σ in Rbr$_{ox}$). These relative intensities are reflected in the respective *B*-factors (Å^2) of the three irons in Rbr$_{red}$ vs Rbr$_{ox}$, namely, Fe1: 12.4 vs 19.9,

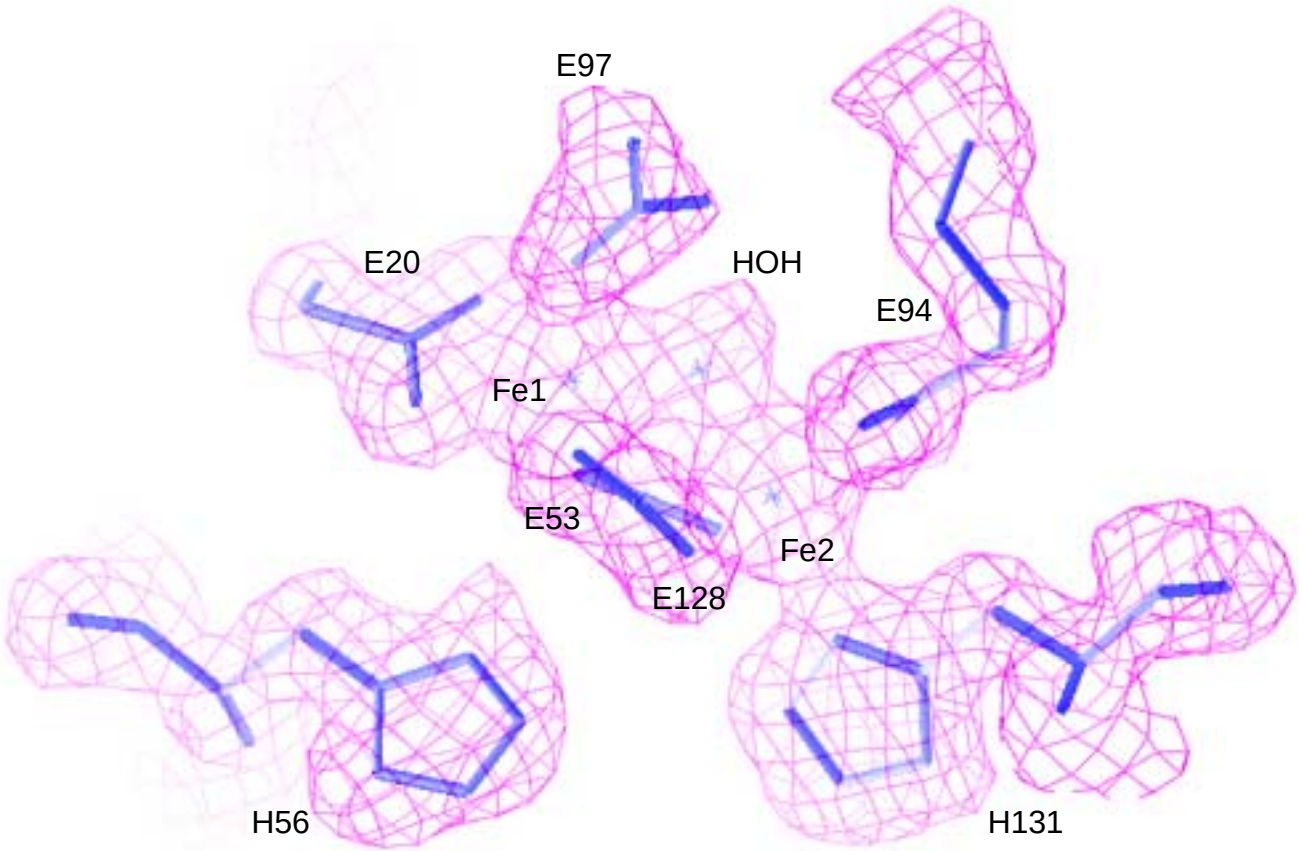

Figure III-3. The final model and the composite omit map ($2F_o$-F_c) contoured at 1.0σ at the diiron site of Rbr_{ox}.

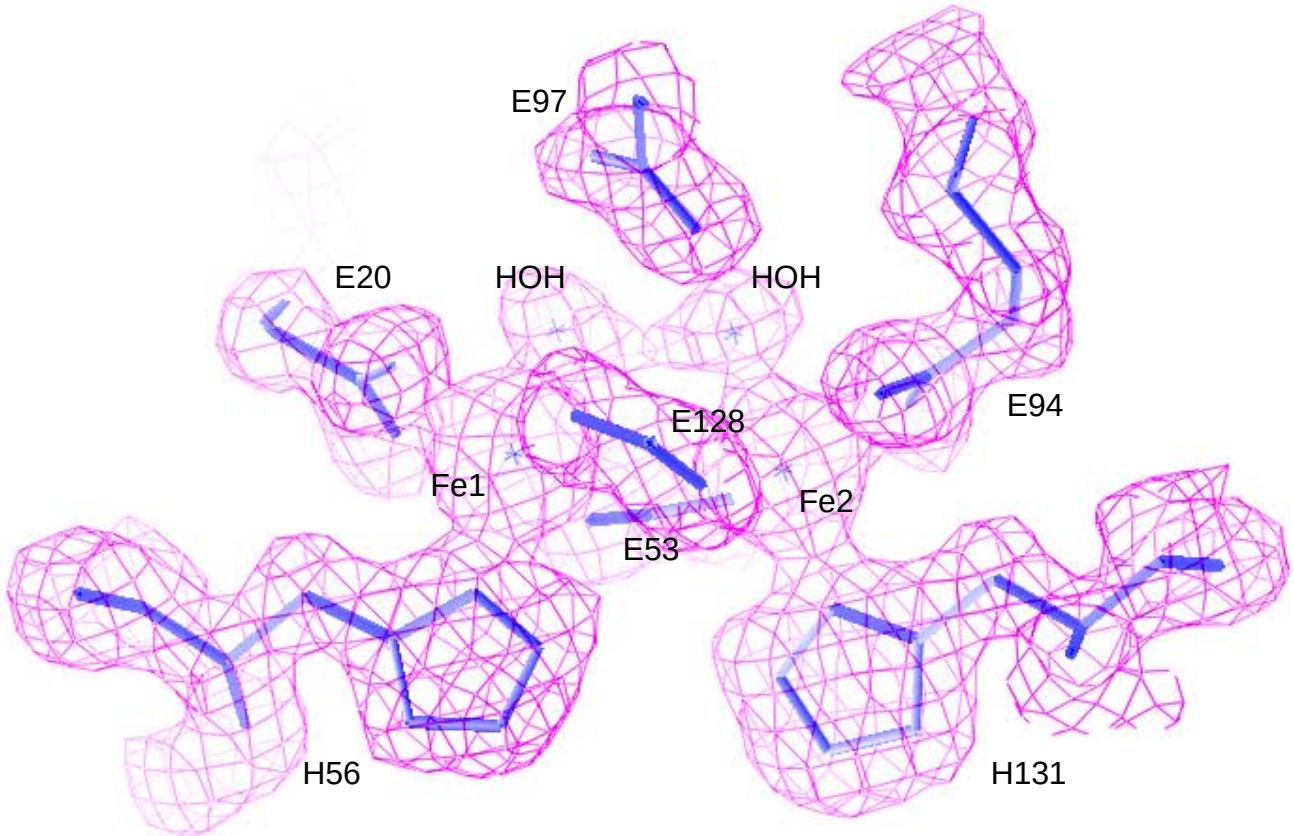

Figure III-4. The final model and the composite omit map ($2F_o$-F_c) contoured at 1.0σ at the diiron site of Rbr_{red}.

Fe2: 11.9 vs 18.4, Fe3: 11.9 vs 14.3. The higher intensities in the composite omit maps and the significantly lower *B*-factors together indicate that the diiron site irons are more ordered in Rbr_{red} than in Rbr_{ox}, perhaps reflecting a more rigid diferrous than diferric site.

Figure III-5 shows the final models of the Rbr_{ox} and Rbr_{red} diiron sites and the best fit superposition of the final Rbr_{ox} and Rbr_{red} subunit models in the region of the diiron sites. The two irons of the diiron site are labeled Fe1 (terminally ligated to by Glu20) and Fe2 (terminally ligated by Glu94). Both Fe1 and Fe2 in Rbr_{red} are pseudo-octahedrally coordinated; each iron is ligated terminally by one bidentate glutamate, one histidine, and one solvent, and the irons are bridged by two bidentate glutamate ligands. The single largest structural change at the diiron site of Rbr_{red} relative to Rbr_{ox} is a 1.8-Å movement of Fe1 towards Nδ1 of His56. The imidazole ring of His56 has also moved 0.4 Å towards Fe1 upon conversion to Rbr_{red}. These movements have resulted in His56 replacing Glu97 as a ligand to Fe1 upon conversion of Rbr_{ox} to Rbr_{red}. The other side chains furnishing ligands to Fe1 have also moved significantly in Rbr_{red} relative to their Rbr_{ox} positions. The carboxyl plane of Glu97 has rotated by ~80 degrees away from Fe1, resulting in ~1.4 Å movements of the Glu97 carboxylate oxygens from their Rbr_{ox} positions. The carboxyl plane of Glu20 has rotated ~70 degrees and moved 1.2 Å away from the original position of Fe1 in Rbr_{ox}, the carboxyl planes of the bridging Glu53 and Glu128 ligands have both rotated 20-30 degree towards Fe1. Fe2, on the other hand has moved only ~0.2 Å relative to its Rbr_{ox} position, and no significant conformational changes or movements in Glu94 or His131, which furnish terminal ligands to Fe2, occur upon conversion to Rbr_{red}. The Fe1---Fe2 distance has elongated from 3.3 Å in Rbr_{ox} to 4.0 Å in Rbr_{red}, and this elongation is accompanied by loss of the oxo bridge between Fe1 and Fe2, which has

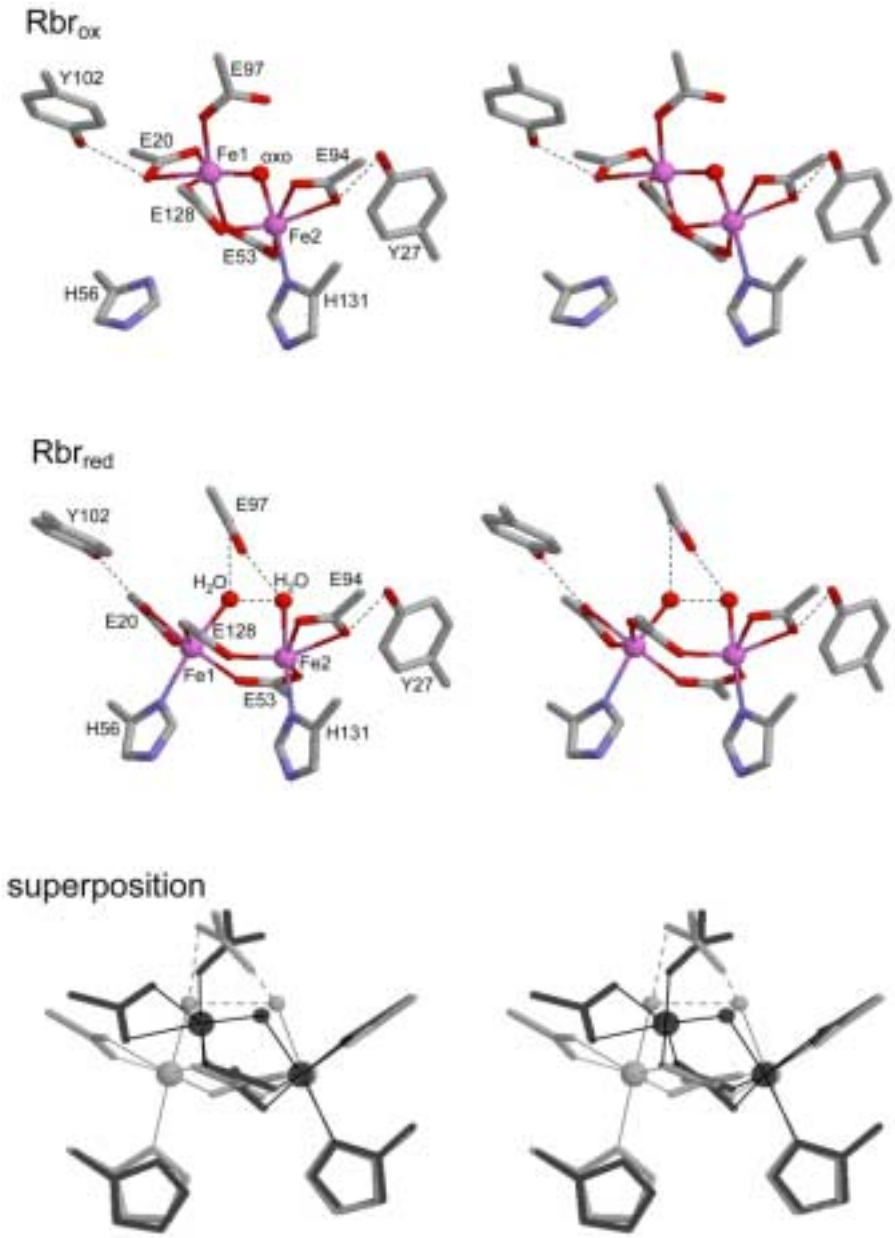

Figure III-5. Stereo views of diiron site structures in Rbr_{ox} (top), Rbr_{red} (middle), and superposition of the subunits (bottom, with Rbr_{ox} darker shaded and Rbr_{red} lighter shaded) in the region of the diiron sites. Tyrosine side chains in the second coordination spheres are shown in the top two views. Dashed lines indicate hydrogen bonds. For clarity, the glutamate beta carbons are not shown. Views are oriented so that the head-to-tail dimer interface is at the bottom and the protein crevice exposing the site to solvent is at the top.

been replaced in Rbr_{red} by the two terminally ligated solvent molecules. The solvent oxygen ligands, O1 and O2, are 2.6 Å apart from and presumably hydrogen bonded to each other. This distance is significantly longer than has been reported for the short hydrogen bond of the bridging $H_3O_2^-$ ion in dimetal complexes (O1---O2 < 2.5 Å) (*115, 116*). For this reason and because of the essentially identical Fe1-O1 and Fe2-O2 bond lengths (2.2 Å), we favor formulation of both solvent ligands as aqua rather than hydroxo. Two aqua ligands would also result in an overall zero net charge on the diferrous site. If the non-ligating Glu97 carboxylate is included, the overall charge becomes -1, which is identical to that on the Glu97-ligated, oxo-bridged diferric site of Rbr_{ox}. The Fe1, Fe2 and their solvent ligand oxygens form a slightly twisted trapezoid in Rbr_{red} with a Fe1-O1---O2-Fe2 torsion angle of 21º. The imidazole rings of the His56 and His131 ligands lie approximately parallel to this trapezoidal plane and *trans* to the solvent ligands, whereas the two bridging carboxylate ligands lie on opposite sides of the trapezoidal plane.

An unusual structural feature of the Rbr diferric site, not noted previously, is that both iron atoms lie well out of the two bridging carboxylate planes, whereas, these irons lie approximately in the planes of their respective bidentate terminal carboxylate ligands, as can be seen qualitatively in **Figure III-5**. A measure of this out-of-plane geometry is the Fe1(2)-Oε1(2)-Cδ-Cγ torsion angle around the Cδ-Oε1(2) glutamate bonds. Placement of the irons in the carboxylate ligand planes, i.e., torsion angles of 180º, presumably optimizes sigma bonding interactions. For the bridging Glu128, and Glu53, these angles range from 126º to 149º, compared to 176-180º for the terminal Glu20 and Glu94. Irons located significantly out of the bridging carboxylate planes have not been observed in

other non-heme diiron proteins or synthetic oxo-bridged diferric complexes, except in those of a conformationally constrained dicarboxylate ligand (*117, 118*). The diiron location out of the bridging carboxylate planes in Rbr_{ox} is notable now because of its contrast to the diiron site in Rbr_{red}. A consequence of the movements of Fe1 and its ligands in Rbr_{red} is a shift of the Fe1-Fe2 axis nearly into the average plane of the two *anti*-disposed bridging carboxylates, as can be seen in **Figure III-5** and **Figure III-6**.

The diiron site in Rbr_{red} is, thus, more symmetric than in Rbr_{ox}. In fact, as shown in **Figure III-6**, the corresponding side chains and solvent providing the coordination spheres of Fe1 and Fe2 in Rbr_{red} can be nearly superimposed onto each other by a 180-degree rotation around an axis bisecting the Fe1---Fe2 and solvent ligand (O1---O2) axes. This pseudo two-fold rotational symmetry extends out even to the main chain atoms of the ligand residues, but is broken by the second coordination sphere. The carboxylate of the displaced Glu97, lies on the Glu128 side of the Fe1-Fe2-solvent-ligand trapezoid and appears to form a strong hydrogen bond with the solvent oxygen ligand of Fe2 (Glu97Oε2---O2(solvent ligand) distance = 2.6 Å), and perhaps a weaker hydrogen bond to the solvent oxygen ligand of Fe1 ((Glu97Oε1---O1(solvent-ligand) distance = 2.9 Å) (cf. **Figure III-5**).

The Glu97Oε1 is also hydrogen-bonded to at least one of several ordered solvent molecules that occupy a crevice exposing the diiron site to bulk solvent (cf. **Figure III-7**). The two His ligands also participate in distinctly different hydrogen bonding interactions. As is the case for Rbr_{ox} (cf. **Figure III-1**), His56N□2 is hydrogen-bonded to the carbonyl of Cys161′ across the subunit interfaces of the head-to-tail dimer in Rbr_{red}, whereas, His131N□2 is hydrogen-bonded to the side chain carbonyl of Gln52. A

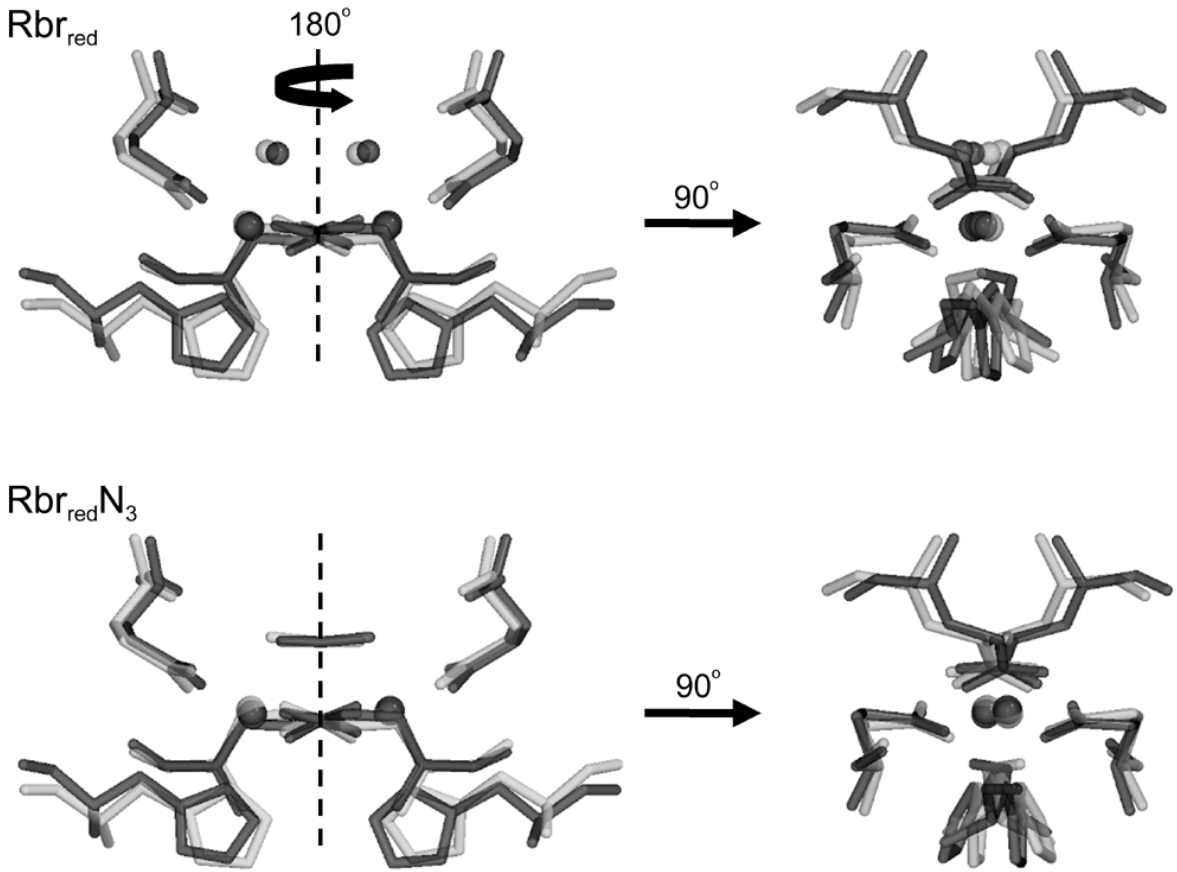

Figure III-6. Views depicting the pseudo two-fold rotational axes superimposing the Fe1 and Fe2 coordination spheres onto each other in Rbr_{red} (top) and $Rbr_{red}N_3$ (bottom). Lighter and darker shadings indicate structures before and after 180º-rotations around the axis represented by the dashed line. The structures to the right of the"90º"-labeled arrows are the same as those to the left but rotated 90º around the dashed-line axis. Iron atoms and solvent are represented as larger and smaller spheres, respectively. Azide in $Rbr_{red}N_3$ is represented in wireframe above the Fe1---Fe2 axis.

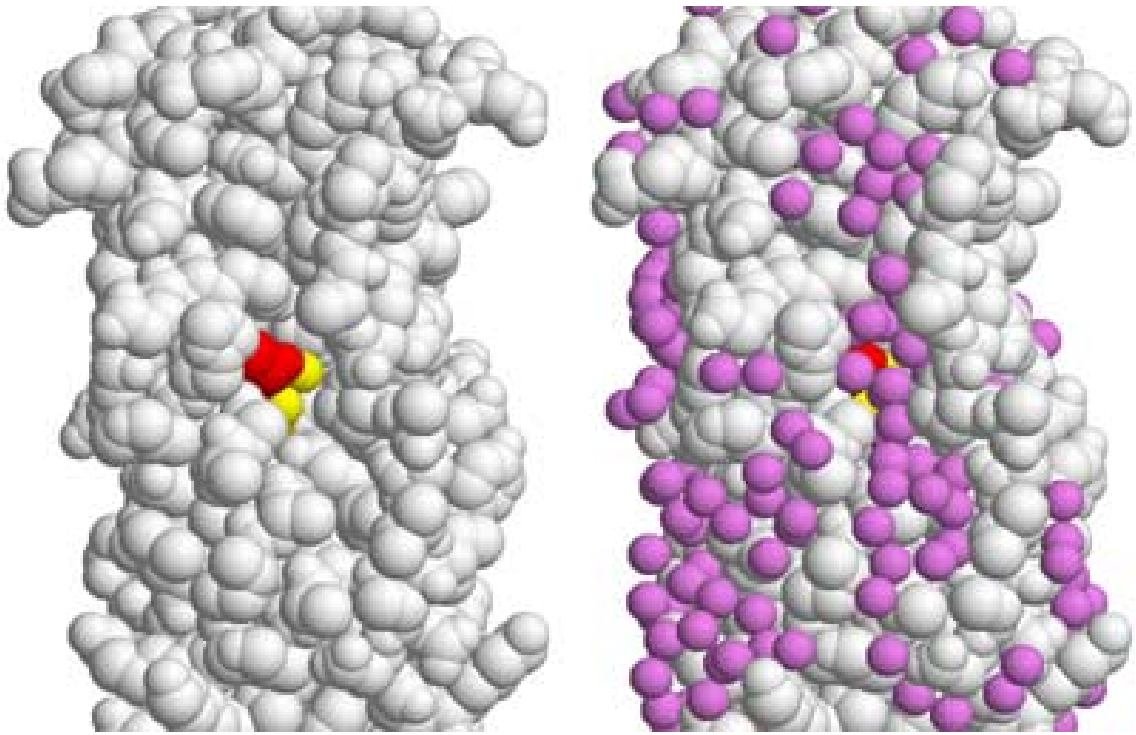

Figure III-7. Stereo space-filling views of Rbr_{red} four-helix bundle domain (long axis oriented vertically) vertically) showing crevice exposing the diiron site. Iron atoms (orange), barely visible under solvent ligands (yellow), and Glu97(red) are highlighted. Right image shows ordered solvent molecules (purple).

conserved Arg residue (Arg26) lines the crevice leading to solvent, but its guanidinium group is too far away for direct interaction with any atoms of the diiron coordination sphere. In Rbr_{red} an Arg26 guanidinium NH_2 is 5.8 Å from a Glu97 carboxylate oxygen, and these two atoms appear to be bridged by an intervening water molecule. A possible role for Arg26 is charge compensation for Glu97.

In contrast to the diiron site, the $[Fe(SCys)_4]$ sites of Rbr_{ox} and Rbr_{red} show no significant structural differences. The r.m.s.d. between Rbr_{red} and Rbr_{ox} of the diiron ligating residues (Glu20, Glu53, Glu94, Glu97 Glu128, His56 and His 131) is 0.50 Å, whereas the analogous r.m.s.d. for the four residues (Cys158, Cys161, Cys174 and Cys177) furnishing ligands to the $[Fe(SCys)_4]$ site is only 0.04 Å. Six N-H---S hydrogen bonds from backbone amides to these ligating Cys residues are also nearly superimposable in Rbr_{ox} and Rbr_{red}. This hydrogen bonding pattern was described previously to be very similar to that in rubredoxins (*58*). Therefore, the unusually high reduction potential of the $[Fe(SCys)_4]$ site in Rbr (*59*) relative to those of rubredoxins (*119*) cannot be attributed to significant alterations in either its first or second coordination spheres upon redox interconversion.

Because of the movement of Fe1 towards His56 described above, the distance between Fe1 in one subunit and Fe3 (the $[Fe(SCys)_4]$ site iron) in the other subunit of a head-to-tail dimer has decreased significantly from 12.4 Å in Rbr_{ox} to 10.9 Å in Rbr_{red}. In contrast, the Fe2---Fe3 head-to-tail intersubunit distance has increased only slightly from 11.9 Å in Rbr_{ox} to 12.2 Å in Rbr_{red}. These intersubunit distance changes are demarcated in **Figure III-8**.

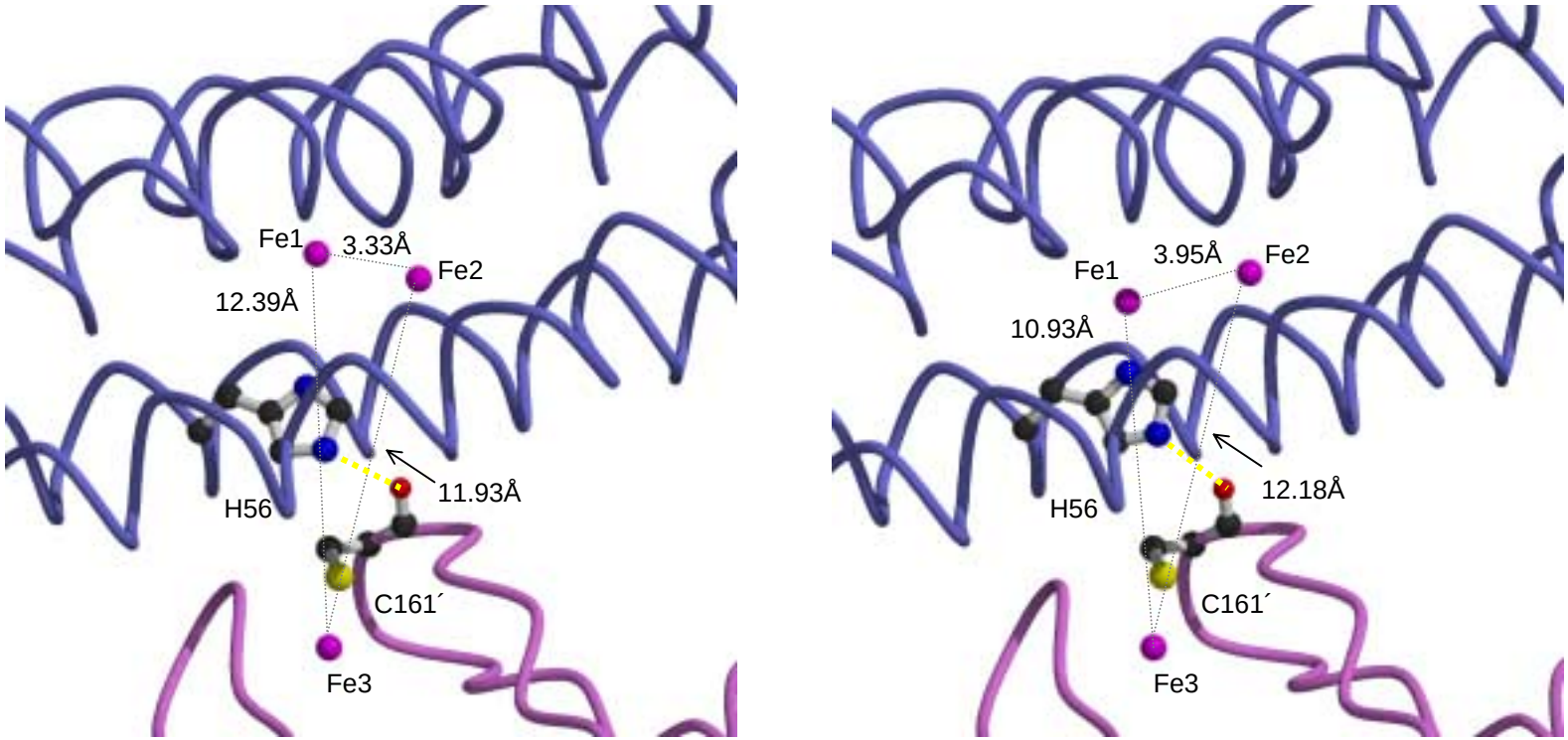

(A) (B)

Figure III-8. Inter-iron distances for (A) Rbr_{ox} and (B) Rbr_{red} at the head-to-tail dimer interface. Peptide backbones are represented as smooth loops, iron atoms as spheres, and His56 and Cys161´ as ball-and-stick. Grey dotted lines connecting iron atoms are labeled with inter-iron distances in angstroms. Hydrogen bonds between His56 and Cys161´ are represented in yellow dotted lines.

III.C.3. $Rbr_{red}N_3$

Figure III-9 (top) shows the $2F_o$-F_c electron density map and final model for the diiron site of $Rbr_{red}N_3$. The r.m.s.d.s between $Rbr_{red}N_3$ and Rbr_{red} structures for the diiron ligating residues and Glu97 and for the four cysteine residues of the [Fe(SCys)$_4$] site are very low: 0.04 and 0.02, respectively. The only significant structural difference between $Rbr_{red}N_3$ and Rbr_{red}, is that the two solvent ligands at the diiron site of Rbr_{red} are substituted by a μ-1,3-bridging azide ion in $Rbr_{red}N_3$. The positions of N1 and N3 of this bridging azide are very similar to those of the two water molecules in Rbr_{red}, but the intra-azide N1-N3 distance of 2.4 Å is significantly shorter than that between the two ligating water oxygens in Rbr_{red} (2.6 Å). In the [$F_{obs}(Rbr_{red}N_3) - F_{obs}(Rbr_{red})$] difference electron density map omitting all water molecules and azide ions (cf. **Figure III-9** (bottom)), the highest peak (6.0σ) at the diiron site is a positive difference density, the center of which is located near the position of the central nitrogen of the bridging azide. The average *B*-factor of the three bridging azide nitrogens (15.3 Å^2) is similar to that of the two solvent ligands in Rbr_{red} (14.7 Å^2), although the *B*-factor of the central azide nitrogen, N2, (21.32 Å^2) is slightly higher than those of the two end nitrogens, (12.78 Å^2, 11.88 Å^2, for N1 and N3, respectively). The remaining coordination sphere accommodates the substitution of solvent ligands by azide without significant structural changes compared to Rbr_{red}. The Fe1-Fe2 distance, 4.0 Å, is essentially identical to that in Rbr_{red}. The description of Fe1,Fe2 and their solvent ligands in Rbr_{red} as a slightly twisted trapezoid also applies to Fe1,Fe2 and bridging azide in $Rbr_{red}N_3$, which has an Fe1-N1---N3-Fe2 torsion angle of 18º. The Fe1-N1 and Fe2-N3 distances in $Rbr_{red}N_3$ are virtually identical to each other (cf. **Table III-2**). Similarly to the Rbr_{red} diiron site, the

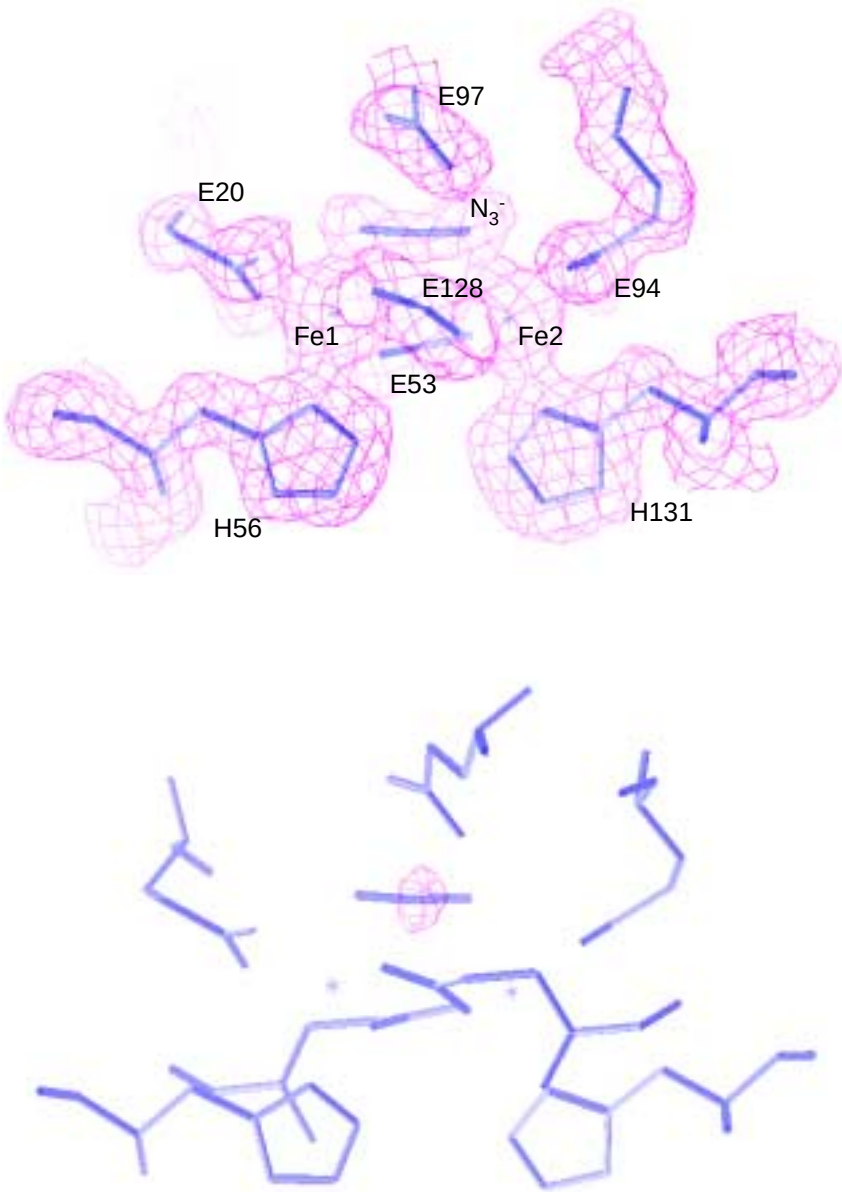

Figure III-9. The final model and the composite omit map ($2F_o$-F_c) (top) contoured at 1.0σ at the diiron site of $Rbr_{red}N_3$, and the (F_o [$Rbr_{red}N_3$] – F_o[Rbr_{red}]) omit map (bottom) contoured at 3.9σ, the azide ion in $Rbr_{red}N_3$ and the two water ligands in Rbr_{red} were omitted from calculation.

side chains and bridging azide nitrogens providing the coordination spheres of Fe1 and Fe2 can be nearly superimposed onto each other by a 180-degree rotation around a two-fold rotation axis passing through the central azide nitrogen (N2) and bisecting the Fe1-Fe2 axis (cf. **Figure III-6**). Similarly to its position in Rbr_{red}, the Glu97 carboxylate sits above and to the Glu128 side of the Fe1-Fe2-μ-azido trapezoidal plane. The two Glu97 carboxylate oxygens show longer and shorter distances to the two coordinated azide nitrogens, N1 and N3, that are similar to those to the respective coordinated solvent ligands in Rbr_{red}. The shorter of the two distances, Glu97Oε2---N3 at 2.5 Å, and the location of N3 close to the Glu97 carboxylate plane implies a hydrogen bond and, therefore, that either the carboxylate or the coordinated azide is protonated. The essentially identical Fe1-N1 and Fe2-N3 distances would suggest the former. The μ-1,3 bridging mode of azide has not been previously reported either in diferrous proteins or diferrous synthetic complexes, where azide invariably exhibits either terminal or bridging η^1 coordination (*120, 121*). Based on resonance Raman spectroscopy, a μ-1,3 bridging geometry was proposed for an azide adduct of the diferric site in stearoyl-acyl carrier protein Δ^9 desaturase (*122*). Examples of μ-1,3 azide-bridged dicopper(II) complexes are available with *cis* Cu1-N1---N3-Cu2 torsion angles, i.e., similar to the geometry in $Rbr_{red}N_3$ (*123-126*). The slight deviation from linearity of the bridging azide in $Rbr_{red}N_3$ (N1-N2-N3 angle = 173°), is also observed in the μ-1,3 azide-bridged dicopper(II) complexes.

The non-Kramers EPR signal from a ferromagnetically coupled diferrous site previously observed for $Rbr_{red}N_3$, but not for Rbr_{red} (*59*), can now be unambigously attributed to alteration of the magnetic coupling and/or the zero-field splitting due to

replacement of the two terminal solvent ligands by the bridging azide. The highly symmetrical $Rbr_{red}N_3$ diiron site also explains why only a single histidine ligand environment was observed when this non-Kramers EPR signal was probed by electron spin echo envelope modulation (ESEEM) spectroscopy (*111*).

III.C.4. Structural Comparisons With Diiron Sites in Non-heme O_2-activating Enzymes

The comparisons made here attempt to highlight those structural differences that help explain the distinctive reactivity of the Rbr diiron site. As noted previously (*58*), the oxo-bridged diferric site of Rbr is quite distinct from that of its namesake, hemerythrin (*127*), most conspicuously in the histidine:carboxylate ligand ratio, which is reversed from 5:2 in hemerythrin to 2:5 in Rbr_{ox}. This structural distinction can now be extended to the reduced diiron sites. In addition to its higher histidine:carboxylate ligand ratio, changes in the diiron coordination sphere of hemerythrin upon reduction are relatively limited, essentially consisting only of protonation of the bridging oxo ligand. One of the iron atoms in diferrous hemerythrin is five-coordinate, whereas, both iron atoms in Rbr_{red} are six-coordinate. These structural distinctions in the hemerythrin vs Rbr diiron sites are reflected in their distinct reactivities. Diferrous hemerythrin has long been known to reversibly bind O_2, whereas, Rbr has never been reported to do so. Conversely, hemerythrin has never been reported to show peroxidase activity, and its diferrous site is relatively slowly (minutes time scale) oxidized by excess hydrogen peroxide (*128*). At least part of this difference in reactivity is also likely due to the hydrophobic O_2 binding pocket in hemerythrin vs the solvent accessible diiron site in Rbr (cf. **Figure III-7**).

The close structural resemblances of both the four helix bundle domains and diiron site environments of Rbr to those of the iron storage proteins, ferritin and (Ftn) and bacterioferritin (Bfr), have been noted previously (*58, 66, 129*). An evolutionary relationship between Rbrs, Ftns and Bfrs has even been suggested (*130*), despite their low overall amino acid sequence homology to the Rbr diiron domain. *D. vulgaris* Rbr does in fact exhibit the ferroxidase activity (i.e., catalysis of Fe^{2+}(aq) oxidation by O_2) characteristic of Ftn in vitro. However, in contrast to all known Ftns and Bfrs, Rbr shows no evidence for formation of 24-mer structures or for binding the colloidal ferric oxyhydroxide product of the ferroxidase reaction. Conversely, Ftn and Bfr have not been reported to show peroxidase activity, and no known Ftn or Bfr contains the $[Fe(SCys)_4]$ domain found in Rbrs. Nevertheless, reinforcing the structural resemblance, **Figure III-10** shows that the best superposition of the four-helix bundle domains of Rbr_{red} and *E. coli* Bfr results in a remarkably close overlap of the Rbr diiron site iron atoms and their ligands with those of the ferroxidase center in Bfr, which was crystallized with Mn^{2+} occupying its dimetal binding site (*131*). A notable distinction is that Bfr has no homolog to Glu97 in Rbr; the corresponding position in Bfr is occupied by a Gly residue. One proposed mechanism of iron incorporation into Bfr invokes migration of iron out of the dimetal site to the ferric/oxyhydroxide core (*132, 133*). Glu97 in Rbr may help localize movement of iron at the diiron site.

As noted in the introduction, the Rbr_{ox} diiron site domain resembles those in the non-heme O_2-activating diiron enzymes, RNR-R2 and MMOH (*73, 134-138*). These latter diferric and diferrous site structures are shown in **Figure III-11**, which may be compared with the corresponding Rbr structures in **Figure III-5**. Common features of the three sites

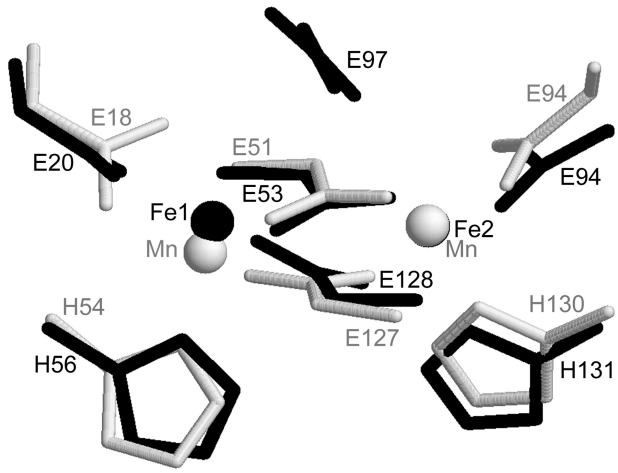

Figure III-10. Superposition of Rbr_{red} (darker shaded) and *E. coli* Bfr (lighter shaded) subunits in the region of the diiron sites. Ligand side chains are shown in wireframe representation, and iron (Rbr) or manganese (Bfr) atoms as spheres. Drawing was generated using coordinates from this work (Rbr_{red}) and 1BCF (Bfr) (*131*).

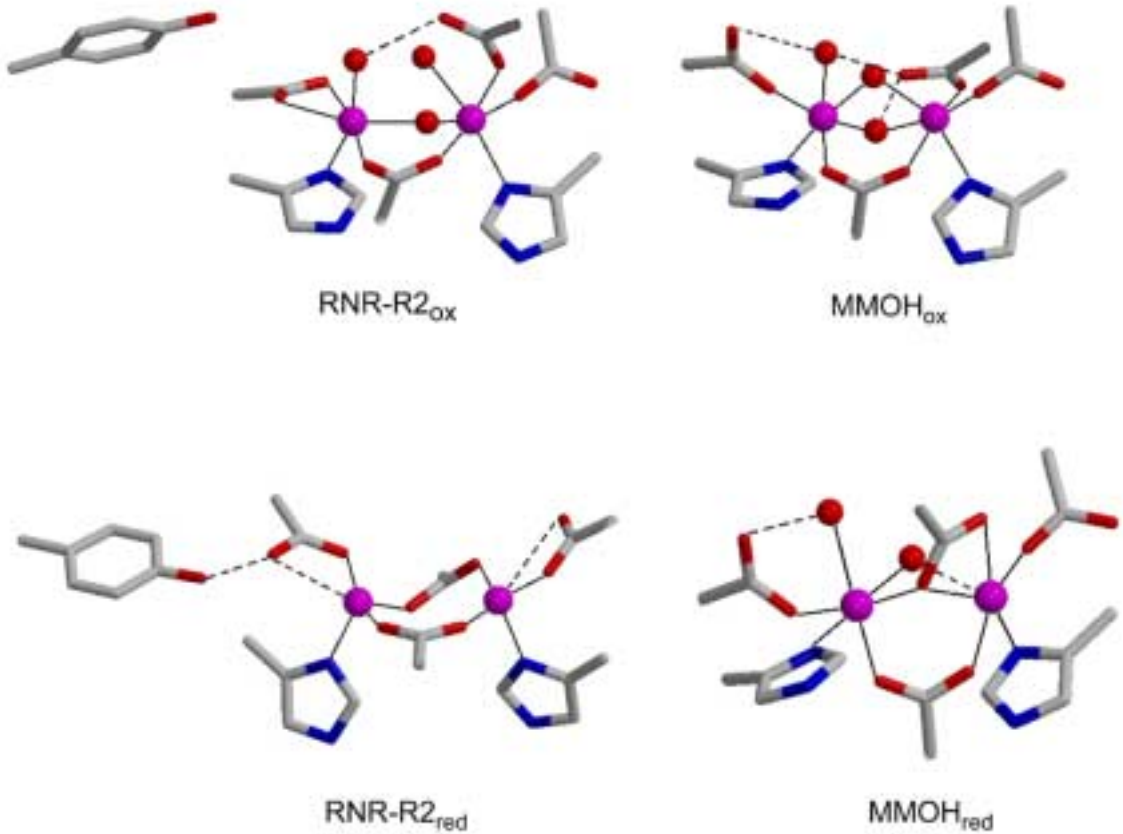

Figure III-11. Diferric and diferrous site structures (labeled with 'ox' and 'red' subscripts, respectively) of *E. coli* RNR-R2 and *Methylococcus capsulatus* (Bath) MMOH Ligand side chains are shown in wireframe and irons and solvent ligands are shown as larger and smaller spheres, respectively. Beta carbons of glutamate residues are omitted for clarity. Dashed lines indicate hydrogen bonds. Structures were drawn using coordinates from PDB IDs 1RIB ($RNR\text{-}R2_{ox}$), 1XIK ($RNR\text{-}R2_{red}$), 1MTY ($MMOH_{ox}$), and 1FYZ ($MMOH_{red}$).

include a 2:4 histidine:carboxylate ligand ratio in the diferrous forms, and solvent-derived oxygen bridges, either oxo (RNR-R2) or hydroxo/aqua (MMOH), in the diferric form, which are broken upon conversion to the diferrous forms. However, several other structural features distinguish the primary coordination spheres of the Rbr diiron site in both its diferric and diferrous forms from those of RNR-R2 and MMOH. The oxo bridge in the diferric RNR-R2 site is coordinated *trans* to the single bridging carboxylate and *cis* to the two His ligands, which is the reverse of the oxo bridge disposition in Rbr_{ox} (*cis* to the two bridging carboxylates and *trans* to the single His131 ligand). The diferric MMOH site contains no oxo bridge, but rather two bridging solvent ligands, modeled as hydroxo and aqua, the latter disposed *trans* to the two His ligands (*136*). The Rbr diiron site retains the same two bidentate bridging carboxylate ligands in both diferric and diferrous forms. The diferric sites of RNR-R2 and MMOH, on the other hand, contain only a single carboxylate bridge (also bidentate), which upon reduction to the diferrous form, is joined by a second bridging carboxylate that enters from a terminal coordination position. The Rbr diiron site shows no evidence for a monodentate bridging carboxylate, unlike diferrous MMOH. The terminal carboxylate ligands, Glu20 and Glu94, to the Rbr diiron site appear to be bidentate in both diferric and diferrous forms, whereas, with one exception, the terminal carboxylate ligands of RNR-R2 and MMOH remain monodentate in both oxidation levels. Both Fe1 and Fe2 of the Rbr diiron site retain their six-coordination upon conversion from the diferric to the diferrous form, whereas the irons in RNR-R2 and MMOH change from six- to either four- or five- coordinate upon reduction. The approximate two-fold rotational symmetry noted above for the diferrous sites of both Rbr_{red} and $Rbr_{red}N_3$ is not duplicated in either RNR-R2 or MMOH. The strikingly unique

redox-induced structural changes of the Rbr diiron site are the Glu97↔His56 ligand switching at Fe1 and the 1.8-Å movement of this iron. The relative structural rigidity of the diferrous Rbr_{red} site upon azide binding is also noteworthy. In an azide adduct of a pocket-mutated diferrous RNR-R2 (*120*), η^1 terminal coordination of azide to one of the irons induced a shift from bidentate to coordination of one of the bridging carboxylate ligands, a 0.4-Å shortening of the Fe1-Fe2 distance and a change from four to six coordination of the azide-bound iron. These structural changes were used as a proposed model for those that occur upon O_2 binding to the wild type diferrous RNR-R2 site.

In both Rbr_{ox} and Rbr_{red}, the Glu20 and Glu94 carboxylate ligands are each hydrogen-bonded to the hydroxyl group of a tyrosine residue, which is depicted in **Figure III-5**. Although not sequentially homologous to those in Rbr, RNR-R2 contains a tyrosine that is hydrogen-bonded to one of its terminal carboxylate ligands in the diferrous form (also shown in **Figure III-11**). Reaction of the diferrous site of RNR-R2 with O_2 produces a stable and functionally essential phenoxyl radical from this tyrosine side chain, whereas no tyrosyl radical has been reported for Rbr (however, see Chapter II). Tyrosine side chains are not evident near the MMOH diiron site; a cysteine residue is instead found in the position analogous to the tyrosine in RNR-R2. A functional role for this conserved cysteine has been proposed (*139*), but not established. ***D. vulgaris*** Rbr contains no cysteine residues other than those of the $[Fe(SCys)_4]$ site. Finally, unlike the buried diiron sites in RNR-R2 and MMOH, the diiron site of Rbr_{red} is readily solvent accessible, as can be seen from **Figure III-7**.

III.C.5. Mechanistic Inferences

A mechanism for hydrogen peroxide reduction by the Rbr_{red} diiron site that is consistent with the new structural data described here is shown in **Scheme III-1**. The first step consists of displacement of the coordinated solvent ligands by the entering hydrogen peroxide, forming a transient diferrous-hydroperoxo adduct. We had previously suggested a μ-η^1 peroxo geometry for this intermediate, based on solvent molecule positions in the 1RYT structure (*49*). However, the relatively symmetrical and rigid Rbr_{red} diferrous site, the *cis* disposition of its only two solvent (i.e, labile) coordination sites, and the 4-Å Fe1---Fe2 distance would more readily accommodate coordination of hydrogen peroxide in a *cis* μ-η^2 fashion, as shown in **Scheme III-1**. This coordination mode, in fact, mimics the *cis* μ-1,3 geometry of the coordinated azide in $Rbr_{red}N_3$.

A concerted mechanism can then be readily envisioned in which transfer of one electron from each iron to its coordinated peroxo oxygen occurs concomitantly with O-O bond cleavage. This process would be rapidly followed by proton transfer and loss of one of the oxygens as water, leaving the remaining oxygen to form the oxo bridge in the resulting diferric site. Proton transfer from one coordinated peroxo oxygen to the other could be facilitated by the Glu97 carboxylate as it rotates into position to displace His56 as a ligand to the ferric Fe1. This rotation coupled with the incipient oxo ligand on ferric Fe2 would tend to draw the ferric Fe1 away from His56. Including the carboxylate of Glu97, there would be no net change in charge (-1) on the diiron site during this transformation. Electron transfer from the $[Fe(SCys)_4]$ site across the subunit interface (cf. **Figure III-1**) could, in principle, re-reduce the diiron site prior to formation of the

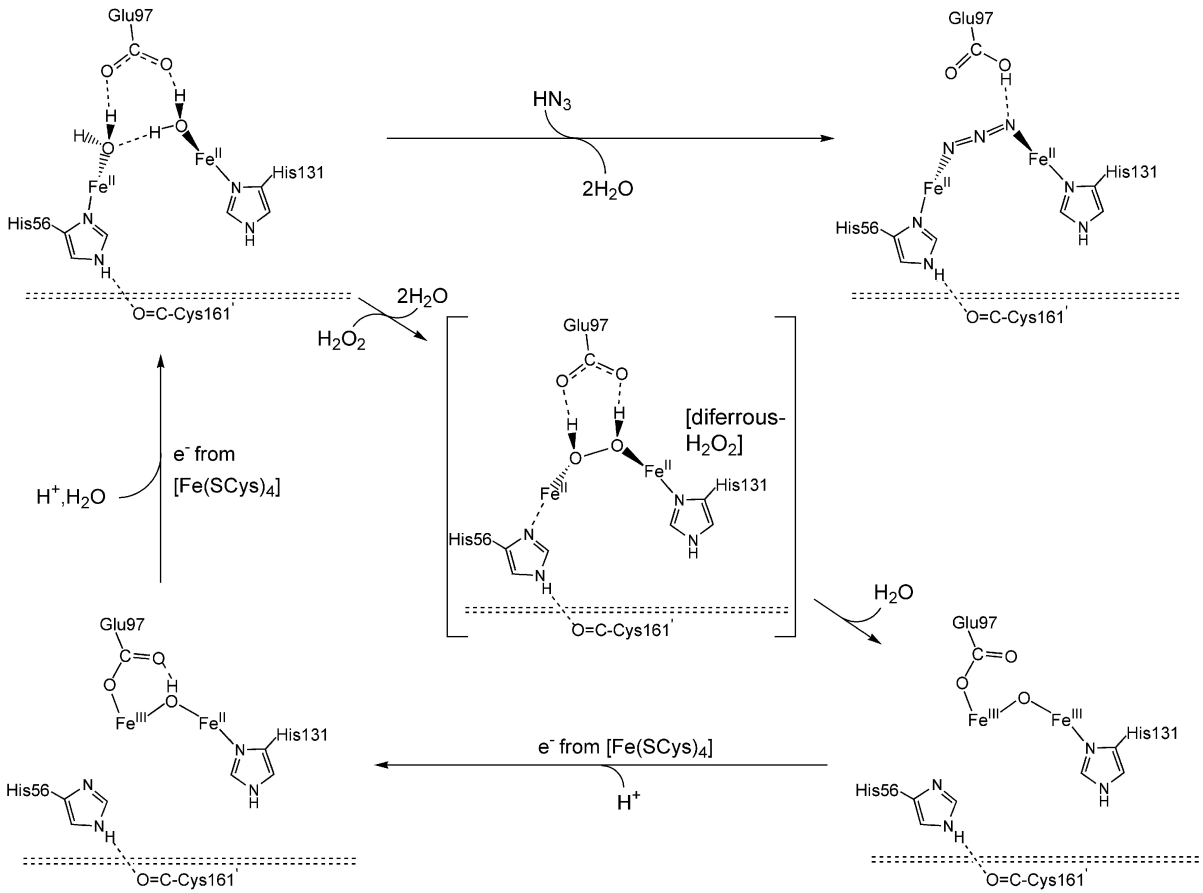

Scheme III-1. The mechanisms of Rbr peroxidase activity and the reaction of Rbr_{red} with azide ion.

oxo-bridged structure in Rbr_{ox}. Our stopped-flow kinetic studies (cf. Chapter II) indicate, however, that, upon mixing hydrogen peroxide with Rbr_{red}, intramolecular $[Fe(SCys)_4]$-to-diiron site electron transfer does indeed occur, but only after formation of the oxo-bridged diferric site, leading to the antiferromagnetically coupled mixed-valent [Fe(II),Fe(III)] diiron site previously identified by EPR spectroscopy (*59, 140*).

The two symmetrically placed tyrosyl side chains that are hydrogen-bonded to terminal carboxylate ligands of the Rbr diiron site (cf. **Figure III-5**) are conserved in all known Rbr amino acid sequences (*49*). One function of these tyrosines may be to reverse Fenton-type chemistry (*141*) at the diferrous site, thereby protecting Rbr from irreversible oxidative damage during turnover. These tyrosyl side chains could, thus, react with hydroxyl radicals adventitiously produced by one-electron reduction of coordinated peroxide by either ferrous Fe1 or Fe2 in Rbr_{red}. The resulting phenoxyl radicals could then be dissipated via oxidation of the remaining diiron site ferrous iron (or possibly the $[Fe(SCys)_4]$ site). Alternatively, the hydrogen-bonded tyrosines could scavenge Fe(IV) produced by two-electron oxidation of either ferrous center by hydrogen peroxide. Protection against similar oxidative species generated by reaction of the mixed-valent or diferric Rbr diiron sites with hydrogen peroxide is also a possibility. Such protection against "hyperoxidation" has been suggested for a similarly hydrogen-bonded tyrosyl residue during reaction of hydrogen peroxide with the dimanganese active site in pseudocatalases (*142*). However, as stated in the introduction, little or no reaction of the diferric Rbr site with hydrogen peroxide has been detected (*49*). On the other hand, evidence for production of tyrosyl radicals from the mixed-valent Rbr diiron site is presented in Chapter II. In any case the concerted two-electron transfer from the diferrous

site of Rbr_{red} to the μ-η^2 bridging peroxide would tend to minimize Fenton-type chemistry, i.e., the one-electron reduction of H_2O_2 to produce OH·.

Although the MMOH diiron site can function as an NADH peroxidase in the absence of hydrocarbon substrates (*143*), and may do so at the expense of NADH oxidase activity (i.e., the competing reduction of O_2), the reported NADH peroxidase turnover for MMOH is at least 100-times slower than for Rbr (*91*). The relatively rapid turnover of hydrogen peroxide by the Rbr diiron site may be due to the much greater solvent exposure and polarity of the site, which would facilitate diffusion of the polar, protic substrate, hydrogen peroxide and product, water into and out of the active site. In addition, the relatively symmetrical Rbr_{red} diiron site as well as the *cis* orientation of its only two solvent (i.e, readily displaceable) coordination sites may facilitate formation and rapid two-electron reduction of a μ-1,2-hydrogen peroxide. On the other hand, the reactions of excess dioxygen with the diferrous sites of RNR-R2 and MMOH are at least 1000-times faster than with Rbr_{red} (*71, 105*), (although the MMOH reaction is "gated", requiring an additional protein component for facile reaction with O_2). The relatively solvent-inaccessible diferrous sites and their coordinative unsaturation in RNR-R2 and MMOH may facilitate their well-established inner sphere reactions with dioxygen (*71*). In the solvent-exposed, Glu97-lined ligand binding pocket at the diferrous site Rbr_{red}, on the other hand, dioxygen may not be able to compete with water for coordination to iron, leading to a slower, outer sphere reaction with dioxygen. This solvent exposure, the relatively inflexible bridging carboxylate ligation, the relatively ordered diferrous irons with nearly superimposable coordination spheres, the redox-induced iron movement, and the Glu↔His ligand switching are all unique features of the Rbr diiron site revealed by

the structures reported here. These structures should, therefore, facilitate delineation of the dioxygen vs hydrogen peroxide reactivity of this unique member of the non-heme, non-sulfur class of diiron enzymes.

CHAPTER IV

STRUCTURES AND SPECTROSCOPY OF RBR ZN ION DERIVATIVES

IV.A. Background and significance

Rubrerythrin (Rbr), found in anaerobic or microaerophilic bacteria and archaea, is a non-heme iron protein containing an oxo-bridged diiron site and a rubredoxin-like [$Fe(SCys)_4$] site (*52, 58*). The diiron site contains one histidine and five carboxylate ligands in the crystal structure of the all-ferric Rbr oxidized form (Rbr_{ox}) (*58*) (cf. **Figure I-9**, Chapter I). The side chain of His56, predicted as a ligand to the diiron site before the crystal structure of Rbr_{ox} was solved, is not, but instead forms a hydrogen bond with the carbonyl of C161′ across a "head-to-tail" dimer interface. C161′ furnishes a thiolate ligand to the [$Fe(SCys)_4$] site.

Rbr has NADH peroxidase activity and it has been proposed as one of a key enzyme pair (superoxide reductase/peroxidase) in the oxidative stress protection system of some anaerobic microorganisms (*38, 48, 49*). Zinc ions (Zn^{2+}) were found to be able to occupy the [$Fe(SCys)_4$] site in place of iron when recombinant *D. vulgaris* Rbr proteins was constituted with first Zn^{2+}, then Fe^{2+}, leading to ZnS_4Rbr with diiron and [$Zn(SCys)_4$] sites (*49*). ZnS_4Rbr showed no peroxidase activity (*49*), which indicates the importance of the [$Fe(SCys)_4$] site in the electron transfer pathway. As described in Chapter II, a transient Rbr species with a diferric diiron site and a ferrous [$Fe(SCys)_4$] site was observed during the oxidation of reduced (all-ferrous) Rbr (Rbr_{red}) by H_2O_2 using stopped-flow spectroscopy. The structure of this intermediate is unknown and cannot be

determined using X-ray crystallography, since the half time of its decomposition is only about 23 ms. Zn^{2+} has the same valence and similar size as Fe^{2+}. Zn^{2+} can be stably substituted into the $[Fe(SCys)_4]$ site of rubredoxin forming a tetrahedrally coordinated $[Zn(SCys)_4]$ site (*144*). Therefore, the structure of ZnS_4Rbr_{ox}, i.e. with a diferric site, should be similar to that of the intermediate Rbr observed during H_2O_2 oxidation of Rbr_{red}.

Zinc ion was reported in place of one iron in the binuclear site of the crystal structure of "as-isolated" *D. vulgaris* Rbr from (*60, 61*) (cf. **Figure I-10** (A), Chapter I). Since spectroscopic results on the same "as-isolated" *D. vulgaris* Rbr (*52, 56*) clearly showed a diiron site and no evidence for a Zn,Fe site, the zinc ions were probably introduced into the Rbr during the aerobic isolation of Rbr from *D. vulgaris* or during the crystallization step (*105*). It was found in the Kurtz lab that zinc could replace some iron ions at the diiron site of the wild type *D. vulgaris* Rbr simply by adding excess $ZnSO_4$ to as-isolated Rbr_{ox}. The structural flexibility of the diiron site is likely to be an important feature for the reactivity of Rbr, and is fundamental to the proposed mechanism of the Rbr peroxidase reaction described in Chapter III. As describer in Chapter III, a large structural change of one iron occurs upon interconversion of the diferric and diferrous forms.

The metal ion occupancies in these various Rbrs can, in principle, be determined using X-ray crystallography. The iron and zinc ions can be differentiated, since they have different anomalous scattering properties. The scattering factor for the anomalous scattering atom can be expressed as $f_{anom}(\lambda) = {}^0f + f'(\lambda) + if''(\lambda)$, where f' and f'' vary with the wavelength, being high near an absorption edge (*145*). The f'' spectrum of certain

atoms can be obtained experimentally by X-ray absorption measurements, and the corresponding f' spectrum may be calculated from f'' via the Kramers-Kronig equation (*146*):

$$f'(\omega) = \frac{2}{\pi} \int_0^\infty \frac{\omega' f''(\omega)\, \partial\omega'}{\omega^2 - \omega'^2}$$

Iron and zinc have opposite anomalous scattering behaviors at the X-ray wavelengths of 1.0 Å and 1.7 Å. As shown in **Figure IV-1**, theoretically, the iron anomalous scattering coefficient f'' without the effects of neighboring atoms is 3.75 at 1.7-Å, which is about 4.6 times that of zinc. On the other hand, at 1.0-Å, the iron anomalous scattering coefficient f'' decreases to 1.55, which is 42% that of zinc at 1.0 Å. Therefore, in each Bijvoet difference Fourier map calculated for X-ray diffraction data collected at wavelengths of 1.0 Å, or 1.7 Å, zinc and iron in the protein should be distinguishable from their electron densities corresponding to their anomalous scattering coefficients.

IV.B. Experimental Section

IV.B.1. Protein expression, purification, crystallization

IV.B.1.1. ZnS_4Rbr_{ox}

Recombinant *D. vulgaris* ZnS_4Rbr was over-expressed, metal-constituted and purified based on a method developed by Eric Coulter in the Kurtz lab (*49*). All the following steps were carried out at room temperature, unless otherwise noted. Four 1-liter cultures of *E. coli* BL21(DE3)[pDK3-5] (*59*) were grown on M9 media with incubating/shaking at 37 °C and induced with 0.4 mM IPTG when OD_{600} reached ~0.8. The induced cultures were incubated at 37 °C for 5 hr and the cell were harvested by centrifugation at 5,000 g for 5 min. The cells were washed with 250 mL of 50 mM Tris, 2 mM EDTA, pH 8.0, and then resuspended and incubated at 30 °C for 15 min in 120 mL of the same buffer with 4

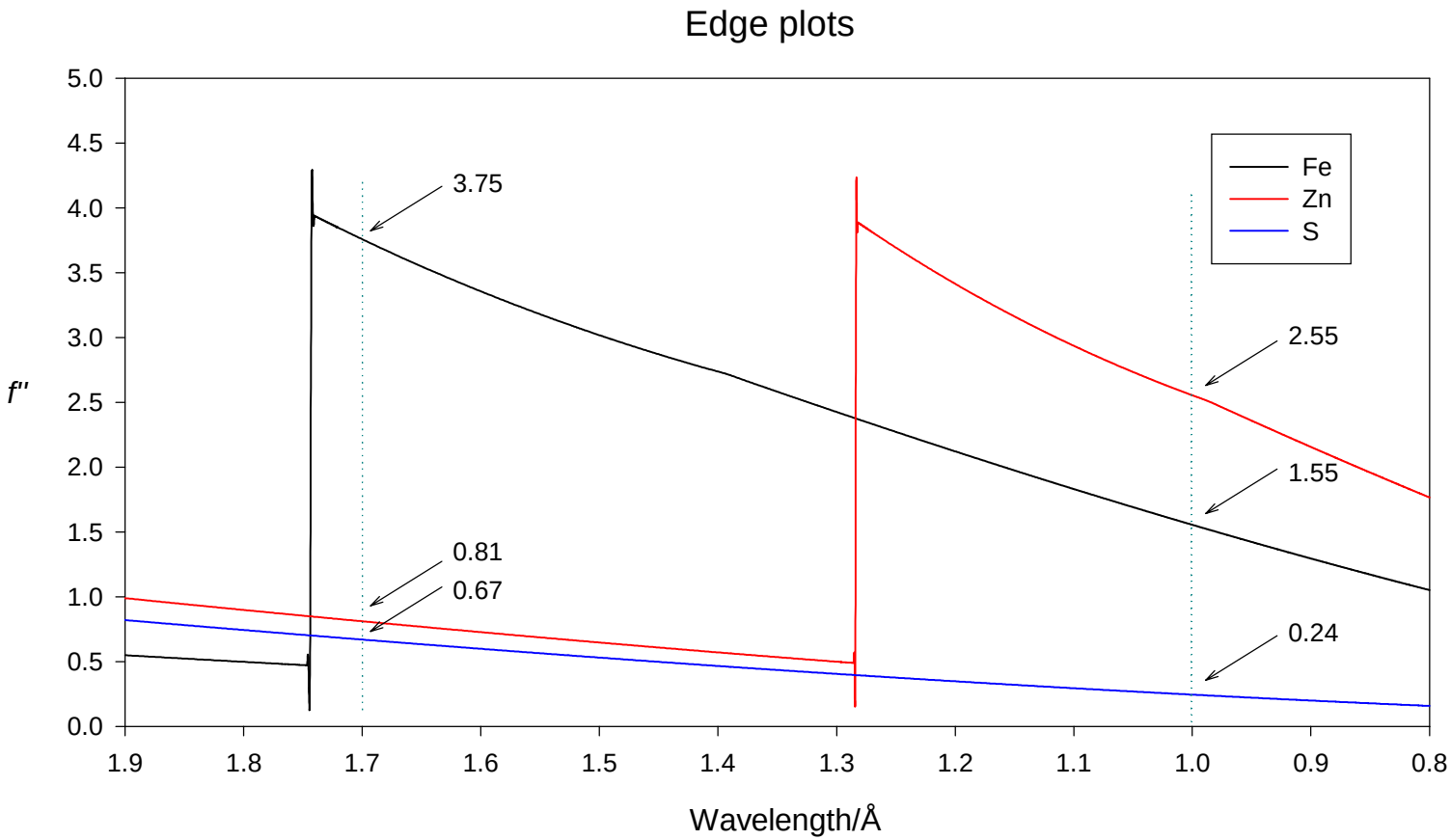

Figure IV-1. Plots of the theoretical anomalous scattering coefficients *f''* *vs* the wavelength of incident X-ray. Data are obtained from (*146*). The vertical dotted lines indicate the wavelength where the X-ray data were collected for ZnS_4Rbr and Zn,FeRbr.

mL 10 mg/mL lysozyme, 40 mL of 1% (v/v) triton X-100 added. About 15 g wet weight of pellet was obtained after sonication by centrifugation of the cell lysate at 12,000g for 30min. Unless otherwise noted, the buffer is 0.1 M Tris, pH 7.5. The pellet was then resuspended in 12 mL 4 M GuHCl in buffer and centrifuged at 30,000 g for 30 min. The supernatant was then transferred into a 250-mL Schlenk-type flask, and was degassed and flushed with nitrogen using a vacuum manifold. After each addition of: (1) 40 μL of 2-mercaptoethanol and 5 mM sodium dithionite, (2) 130 μL of 0.14 M zinc sulfate in anaerobic buffer, and (3) 1.3 mL of 0.14 M ferrous ammonium sulfate in anaerobic buffer, the solution in the flask was equilibrated with stirring for 0.5-1 hr. The mixture then was successively diluted and concentrated similar to that previously described for the iron incorporation procedure (*59*), except that 1 mM EDTA was added to the dilution buffer during the third round of dilution/concentration. The EDTA was diluted out in the following dilution/concentration steps. The purpose of using EDTA was to remove any extra iron ions that could bind at the surface of Rbr. The final yield (10 mg Rbr per liter of culture) of ZnS_4Rbr was lower than for the recombinant all-iron Rbr_{ox} (*59*). The final ZnS_4Rbr was treated with a small amount of H_2O_2 in order to obtain the homogeneous fully oxidized form of [Fe(III)Fe(III)]/[Zn(II)$(SCys)_4$]Rbr. The resulting protein, referred to as ZnS_4Rbr_{ox}, was concentrated to 1.5 mM (dimer), in 50 mM HEPES, 200 mM Na_2SO_4, pH 7.0 using Centricon centrifuge tube (5k membrane) and stored at -80 ºC.

Crystallization of ZnS_4Rbr was carried out at room temperature using the hanging drop vapor diffusion technique. The initially attempted crystallization conditions, namely, 1:1 (v/v) mixing ratio of 1-2 μL of 1.5 mM ZnS_4Rbr_{ox} dimmer in 50 mM HEPES, 200 mM Na_2SO_4, pH 7.0 and any concentration of the precipitant, PEG 1450, in 0.1 M Tris, pH

7.0 from the reservoir that would not denature the protein, however, did not result in protein crystals in hanging drops. Therefore, crystallizations were set up using higher concentration of ZnS_4Rbr_{ox}. Successful crystallization was achieved by mixing 1.5 μL of the same ZnS_4Rbr_{ox} solution with 1 μL of 27% (w/v) PEG1450 in 0.1 M Tris, pH 8.0 from the reservoir solution. Single crystals yellow in color with dimensions of ~ 0.5 x 0.2 x 0.2 mm were obtained in two days at room temperature (**Figure IV-2** (A)). The crystals were rinsed with mineral oil as cryoprotectant and flash-cooled for data collection.

IV.B.1.2. Zn,FeRbr$_{ox}$

It was found in the Kurtz lab that zinc could replace some iron ions at the diiron site of the wild type Rbr simply by adding excess $ZnSO_4$ to as-isolated Rbr_{ox}. In this work, it was found that, highly concentrated Rbr solutions directly mixed with concentrated $ZnSO_4$ solutions resulted in precipitation of Rbr. A procedure was, therefore, developed whereby 100 μM $ZnSO_4$ (5-fold molar excess over diiron sites) was added to 10 μM as-isolated Rbr_{ox}, which had been overexpressed, iron-constituted and purified as previously described (*59*), in 0.1 M Tris, pH 7.3. After incubation for 4 hours at room temperature and then overnight at 4 °C, excess zinc was removed by 3 times concentration/re-dilution with buffer using a Centricon centrifuge tube with 5k membrane and the resulting protein, referred to Zn,$FeRbr_{ox}$, was concentrated to 1.0 mM in homodimer, in 0.1 M Tris, pH7.3 and stored at -80 ºC.

Crystals of Zn,FeRbr were grown in hanging drops under conditions similarly to those previously described for recombinant all-iron Rbr_{ox} (*58*). One microliter of 1.0 mM as-isolated Zn,$FeRbr_{ox}$ dimer in 0.1 M Tris, pH 7.3 was mixed with 1 μL precipitant consisting of 14% (w/v) PEG1450, in 0.1 M Tris, pH 8.0 buffer from reservoir at room

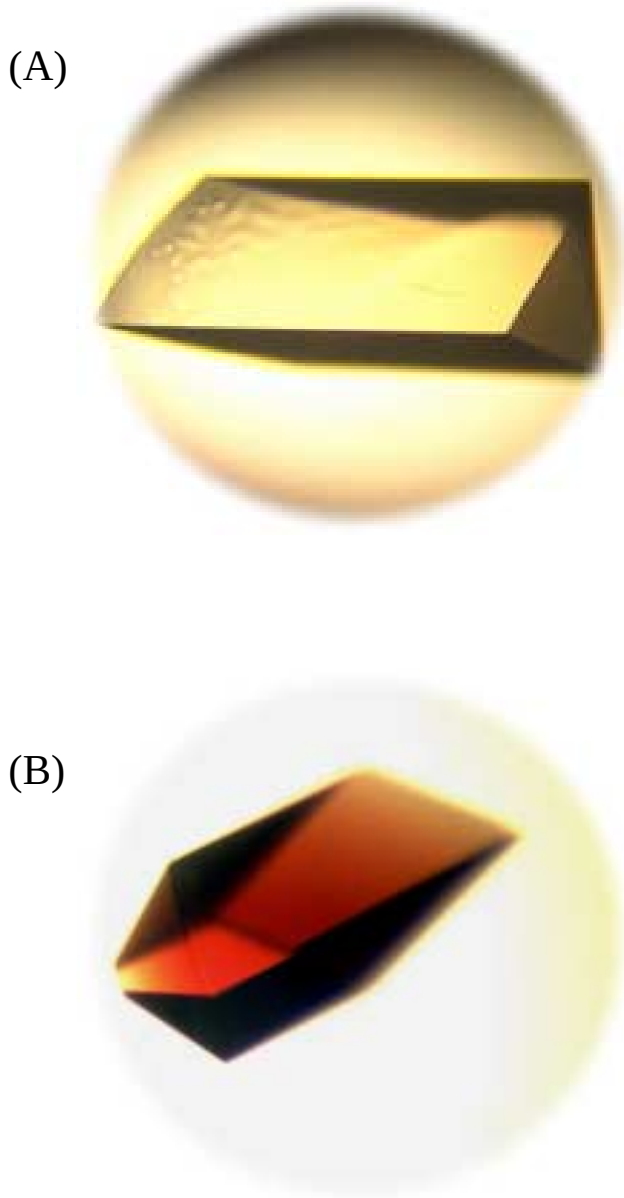

Figure IV-2. Pictures of Zn-substituted Rbr crystals. (A) ZnS_4Rbr_{ox}, obtained from 1.5 mM ZnS_4Rbr_{ox} dimer in 50 mM HEPES, 200 mM Na_2SO_4, pH 7.0 mixed with 27% (w/v) PEG1450, 0.1M Tris, pH 8.0 in 1.5:1 (v/v) ratio. (B) $Zn,FeRbr_{ox}$, obtained from 1.0 mM $Zn,FeRbr_{ox}$ dimer, in 0.1 M Tris, pH 7.3 mixed with 14% (w/v) PEG1450, 0.1 M Tris, pH 8.0 in 1:1 (v/v) ratio.

temperature. The crystals of Zn,FeRbr, which formed in two days at room temperature, were deep red in color, similar to that of as-isolated Rbr_{ox}. (**Figure IV-2** (B)) The best cryoprotectant tested for Zn,FeRbr crystals was found to be a mixture of glycerol with reservoir solution in the ratio of 1:6 (v/v). Crystals were rinsed and flash-cooled in this cryoprotectant, and stored in liquid nitrogen. A crystal ~0.3 x 0.2 x 0.2 mm in size was chosen for data collection.

IV.B.2. Protein characterization

UV-vis absorption spectra of Rbr Zn derivatives were recorded on a Shimadzu UV-210PC spectrophotometer. Electron paramagnetic resonance (EPR) spectrum of $Zn,FeRbr_{ox}$ were measured on a Bruker ESP 300E EPR spectrometer equipped cryostat in the laboratory of Dr. Michael Johnson at the University of Georgia. Metal contents of Rbr Zn derivatives were determined by inductively coupled plasma-atomic emission analysis at the University of Georgia Chemical Analysis Facility. Protein concentrations were determined by the Bio-Rad protein assay using as-isolated Rbr_{ox} as standard, for which the concentration was determined by UV-vis absorption at 494 nm (ε = 10,600 $M^{-1}cm^{-1}$ per Rbr dimer (*59*)). The NADH peroxidase activities of the Rbr various were measured as previously described (*49*) with small modification of protein and substrate concentrations. In this work, the NADH peroxidase assays were carried out in 1-cm pathlength cuvette with 1 mL anaerobic solutions that typically contained 0.5 μM Rbr dimer, 0.5 μM BenC, 300 μM NADH, 350 μM H_2O_2, and 1mM DTPA in 50 mM MOPS (4-morpholinopropanesulfonate), pH 7.0.

IV.B.3. Data collection

X-ray diffraction data for crystals of ZnS_4Rbr_{ox} and $Zn,FeRbr_{ox}$ were collected on the IMCA-CAT insertion device beam line, using the ADSC Quantum 210 CCD detector mounted on a CrystalLogic goniostat (with omega and 2theta rotations) and equipped with the Oxford Cryosystems cryostream sample cooler, at the Advanced Photo Source (Argonne National Laboratory). All data collection was performed on crystals cooled to 95K. For ZnS_4Rbr, two sets of data were collected on one crystal: one at wavelength of 1.0 Å using 720-degree oscillations (resolution 1.75 Å), and the other at 1.7 Å using 180-degree oscillations (resolution 2.05 Å). For Zn,FeRbr, two sets of data were collected on two different crystals: one at wavelength of 1.0 Å using 180-degree oscillations (resolution 1.75 Å), and the other at wavelength of 1.7 Å using 180-degree oscillations (resolution 2.05Å). The programs DENSO and SCALEPACK (*108*) were used for data processing.

Crystals of both ZnS_4Rbr_{ox} and $Zn,FeRbr_{ox}$ are isomorphous with the published oxidized Rbr crystal structure, 1RYT (*58*). They belong to space group I222. Cell dimensions are listed in **Table IV-1** (A) and **Table IV-2** (A), respectively. Each asymmetric unit contained one monomer.

IV.B.4. Refinement

IV.B.4.1. Obtainment of several kinds of electron density maps

Omit map (F_o-F_c) (*145*):

Part of the structure in a defined area of the unit cell is omitted from the phasing, and then F_o and difference maps (F_o-F_c) are checked to determine if the portion that was omitted appears (at least to some extent) in the resulting electron-density map.

Table IV-1. Data collection and refinement statistics

Parameter	ZnS_4Rbr (1.0 Å)	ZnS_4Rbr (1.7 Å)
A. Data collection and processing statistics		
Temperature (K)	95	95
Unit cell dimensions (Å)		
a	48.0	48.0
b	80.2	80.2
c	101.0	101.3
Maximum Resolution (Å)	1.75	2.05
Total reflections		
Unique reflections	36400	
Completeness[a] (%)	95.8	
R_{merge}[b] (%)	4.2 (14.5)[c]	5.8 (13.7)[c]
$\langle I \rangle / \langle \sigma(I) \rangle$		
B. Refinement statistics		
Resolution range for refinement	17.59-1.75	
R_{work} (%)	18.31	-
R_{free}[d] (%)	21.42	-
Number of water molecules	247	-
Number of SO_4^{2-} ions	1	-
RMSDs from ideality[e]		
Bond lengths (Å)	0.005	-
Bond angles (°)	1.0	-
Dihedral angles (°)	19.2	-
Improper angles (°)	0.75	-
Wilson *B*-value ($Å^2$)	16.6	-
Mean *B*-value ($Å^2$)	21.0	-
Coordinate error[f] (Å)	0.18	-
Ramachandran plot[g]		
Residues in most favored regions (%)	94.0	-
Residues in additional allowed regions (%)	6.0	-
Residues in generously allowed regions (%)	0	-
Residues in disallowed regions (%)	0	-

[a]Values in parentheses correspond to the resolution shell.
[b]$R_{merge} = \Sigma(|I - \langle I \rangle|)/\Sigma\langle I \rangle$.
[c]Highest resolution shell.
[d]Calculated with 8% of the complete data set excluded from refinement.
[e]Stereochemical check was made using CNS.
[f]Estimated coordinate error from the Luzatti plot.
[g]Ramachandran plot was calculated using PROCHECK.

Table IV-2. Data collection and refinement statistics

Parameter	Zn,FeRbr (1.0 Å)	Zn,FeRbr (1.7 Å)
A. Data collection and processing statistics		
Temperature (K)	95	95
Unit cell dimensions (Å)		
a	48.7	48.7
b	80.3	80.3
c	100.1	99.9
Maximum Resolution (Å)	1.75	2.05
Total reflections		
Unique reflections	37486	20114
Completeness[a] (%)	98.0	84.6
R_{merge}[b] (%)	4.1 (11.7)[c]	7.0 (11.2)[c]
$\langle I \rangle / \langle \sigma(I) \rangle$		
B. Refinement statistics		
Resolution range for refinement	11.95 – 1.75	22.71 – 2.05
R_{work} (%)	17.78	17.07
R_{free}[d] (%)	19.63	20.87
Number of water molecules	239	185
RMSDs from ideality[e]		
Bond lengths (Å)	0.005	0.005
Bond angles (°)	1.0	1.0
Dihedral angles (°)	19.3	19.3
Improper angles (°)	0.70	0.70
Wilson *B*-value (Å^2)	17.1	16.4
Mean *B*-value (Å^2)	19.2	22.4
Coordinate error[f] (Å)	0.17	0.19
Ramachandran plot[g]		
Residues in most favored regions (%)	93.5	95.2
Residues in additional allowed regions (%)	6.5	4.8
Residues in generously allowed regions (%)	0	0
Residues in disallowed regions (%)	0	0

[a]Values in parentheses correspond to the resolution shell.
[b]$R_{merge} = \Sigma(|I - \langle I \rangle|)/\Sigma\langle I \rangle$.
[c]Highest resolution shell.
[d]Calculated with 8% of the complete data set excluded from refinement.
[e]Stereochemical check was made using CNS.
[f]Estimated coordinate error from the Luzatti plot.
[g]Ramachandran plot was calculated using PROCHECK.

Composite omit map ($2F_o$-F_c) (*147*):

In order to reduce the effects of model bias, a simulated annealing omit map can be calculated. In the case of a molecular replacement solution it cannot be ascertained which parts of the model are in error. Therefore an omit map that covers the entire molecule is most useful. It is not possible to exclude the entire model (at most 10% can be omitted), instead small regions of the model are systematically excluded. A small map is made covering the omitted region. These small maps are accumulated and written out as a continuous map covering the whole molecule (or the defined region). Simulated annealing refinement and minimization are used to remove the bias from the omitted region. A F_o-F_c map is not useful since the whole model is omitted.

Bijvoet difference Fourier map (ΔF; φ+90°) (*146*):

Bijvoet pairs are Bragg reflections which are space group symmetry equivalents to the two members of a Friedel pair ($F(h,k,l)$, $F(-h,-k,-l)$). In the presence of anomalous scattering, the true symmetry equivalents of a Bragg reflection still have equal amplitude. The two members of a Bijvoet pair may have unequal amplitudes, however, for the same reason as the members of a Friedel pair. ($|F^+| \equiv |F(h,k,l)| = |F(-h,k,-l)|$, $|F^-| \equiv |F(-h,-k,-l)| = |F(h,-k,l)|$) The difference in the measured amplitude for a Bijvoet pair is called a Bijvoet difference, or ΔF. ($\Delta F = |F^+| - |F^-|$) If phase estimates for the structure are available, the Bijvoet differences can be used to calculate a Fourier map. The coefficients for this map are (ΔF; φ+90°). Note that the phases used in calculating the map are 90° different from the phase estimates for the structure as a whole, since the Bijvoet difference arises from the imaginary contribution to the total scattering, f''.

IV.B.4.2. ZnS_4Rbr_{ox}

Since the two data sets were collected on the same crystal at different wavelengths, the data collected at 1.0 Å with higher resolution were used for refinement, using the difference Fourier analysis method. The data collected at 1.7 Å were used only for calculating Bijvoet difference Fourier maps in order to compare with the map obtained from the 1.0-Å data. The model refinement and map calculation were performed in CNS 1.0 (*109*), and the model rebuilding against the map was carried out in O (*110*). The initial model was the all-iron Rbr_{ox} described in Chapter III with all the solvent molecules removed, and the label of Fe3 at the rubredoxin-like center changed to Zn3. About 8% of the reflection data were excluded for calculation of the R_{free} factor to monitor the refinement. The first round included rigid body refinement (data with resolution below 3.0 Å), energy minimization, and simulated annealing, which resulted in a decrease of $R(R_{free})$ from 0.388(0.401) to 0.296(0.327). The improved model was then used to calculate the composite omit map ($2F_o$-F_c), and both the model and the map were input into program O. A long bulky electron density overlapping the position of Fe1 in the initial model was found to have connections with the electron densities of both Oε1 of Glu97 and Nδ1 of His56. The Fe1 position was closer to Glu97 than to His56, because the electron density was not distributed evenly. Except for this feature, the overall electron density map at the diiron site fit the model very well. During the second round of refinement, energy minimization, grouped *B*-factor and individual *B*-factor refinement steps were sequentially carried out, and the first 138 waters with peak heights above 3σ were then picked by difference Fourier analysis, followed by another energy minimization refinement before map calculation. This second round of refinement

decreased $R(R_{free})$ to 0.211(0.240). Both the model and composite omit map were displayed in O. Although one end of the bulky electron density occupied by Fe1 was connected with His56, similar to Fe1 in the diferrous site of Rbr_{red} (Chapter III), there was also electron density connecting Fe1 and Fe2 to each other at the position assigned to the oxo bridge in Rbr_{ox}. A water molecule was, therefore, centered into this electron density as an oxo bridge. Another 115 water molecules were selected during the third round of refinement, which decreased $R(R_{free})$ to 0.188(0.221). A large electron density near Gln151 on the protein surface with tetrahedral geometry was fitted to a SO_4^{2-} ion in O, since the protein buffer contained 200 mM $NaSO_4$ and no other added inorganic salts. Six disordered water molecules were found in the map and removed from the coordinate file in the final round of refinement. A total of 247 water molecules were included. Besides energy minimization, grouped *B*-factor, individual *B*-factor and simulated annealing refinement, individual occupancy refinement for all water molecules and metal ions was carried out at the end, assuming the whole protein occupancy as 1. The resulting occupancies, for Fe1, Fe2 and Zn3 were 0.92, 0.93 and 1.03, respectively. $R(R_{free})$ decreased to 0.183(0.214).

Bijvoet difference Fourier maps of ZnS_4Rbr were calculated for both data sets collected at 1.0 Å and 1.7 Å. The Hendrickson-Lattman coefficients generated from each individual anomalous reflection file omitting Fe1, Fe2 and Zn3, and the same coordination file from the refined model of ZnS_4Rbr with data collected at 1.0 Å, were used for each map calculations with resolution range below 3.0 Å.

IV.B.4.3. Zn,FeRbr

The data collected at X-ray wavelengths of 1.0 Å and 1.7 Å were from two different crystals, so the refinement procedures were carried out separately for each data set, using the difference Fourier analysis method. The initial model used for both data sets was the all-iron Rbr_{ox} (Chapter III) with all the solvent molecules removed, and the Fe1 at the diiron site was changed to Zn1, according to the structure of Zn-containing "as-isolated" Rbr (*60, 61*). Eight percent of the reflection data were excluded for calculation of the R_{free} factor to monitor the refinement for each data set.

For the data set collected at 1.0 Å, rigid body refinement was initially carried out using a resolution range of less than 3.0 Å. Subsequent refinement consisting of energy minimization, and simulated annealing with resolution extended to 1.75 Å gave $R(R_{free})$ of 0.301(0.324). Manipulation of the model was performed in O. The position of Zn1 in the model was found at the outside of a large electron density connected with Nδ1 of His56, but not Oε1 of Glu97. Zn1 was, therefore, manually moved into the center of that electron density. The bridging electron density between Fe1 and Fe2 observed in Rbr_{ox} was disconnected from Zn1 but connected to Fe2. During the next two rounds of refinement, including energy minimization, simulated annealing, grouped *B*-factor and individual *B*-factor refinement, a total of 145 water molecules were picked. In O, a water molecule was found as a ligand to Fe2, but no water ligands were found for Zn1. $R(R_{free})$ decreased to 0.202(0.218). Another 94 ordered water molecules were taken into account in the following repetitive refinement cycle and model rebuilding, resulting in a decrease of $R(R_{free})$ to 0.181(0.197). The final cycle, including an individual occupancy refinement for all water molecules and metal ions at the end gave $R(R_{free})$ of 0.178(0.196).

For the data set collected at 1.7 Å, the procedure was the same as that described for the data set collected at 1.0 Å. Not surprisingly, the final composite omit map and structure of the final model with $R(R_{free})$ of 0.171(0.209) were very similar to the one refined from the 1.0 Å wavelength data collection, since the two crystals used for data collection were from the same batch of protein solution.

Unlike ZnS_4Rbr, each individual Bijvoet difference Fourier map of Zn,FeRbr for the two data sets at 1.0 Å and 1.7 Å was calculated using the corresponding coordinate files from the model refinement at the same wavelength. The Hendrickson-Lattman coefficients for each individual data set were generated from each anomalous reflection file omitting Zn1, Fe2 and Fe3. Bijvoet difference Fourier maps for each model were then calculated using a resolution range below 3.0 Å.

IV.C. Results and discussion

IV.C.1. ZnS_4Rbr_{ox}

IV.C.1.1. Protein characterization

As shown in **Figure IV-3**, the UV-vis absorption spectrum of Rbr with Zn substituted into the rubredoxin-like site oxidized form (ZnS_4Rbr_{ox}) features shoulders at 330 nm and 480 nm and a peak at 370 nm that resemble the spectrum of "chopped Rbr" (CRbr), which lacks the rubredoxin-like domain (*59*). These features indicate a Rbr with a diiron site occupied by an Fe^{3+}-O^{2-}-Fe^{3+} unit and a rubredoxin-like site occupied by Zn^{2+}. However, the iron content of as-isolated ZnS_4Rbr_{ox} showed 3.36 Fe/protein dimer (**Table IV-3**), which is lower than the expected number of 4/dimer, but significantly higher than 2/dimer for the ZnS_4Rbr prepared as described by Coulter et al (*49*). The measured absorbance ratio of A_{280}/A_{370}, 8.2, for ZnS_4Rbr_{ox} (see **Table IV-3**) is higher than the

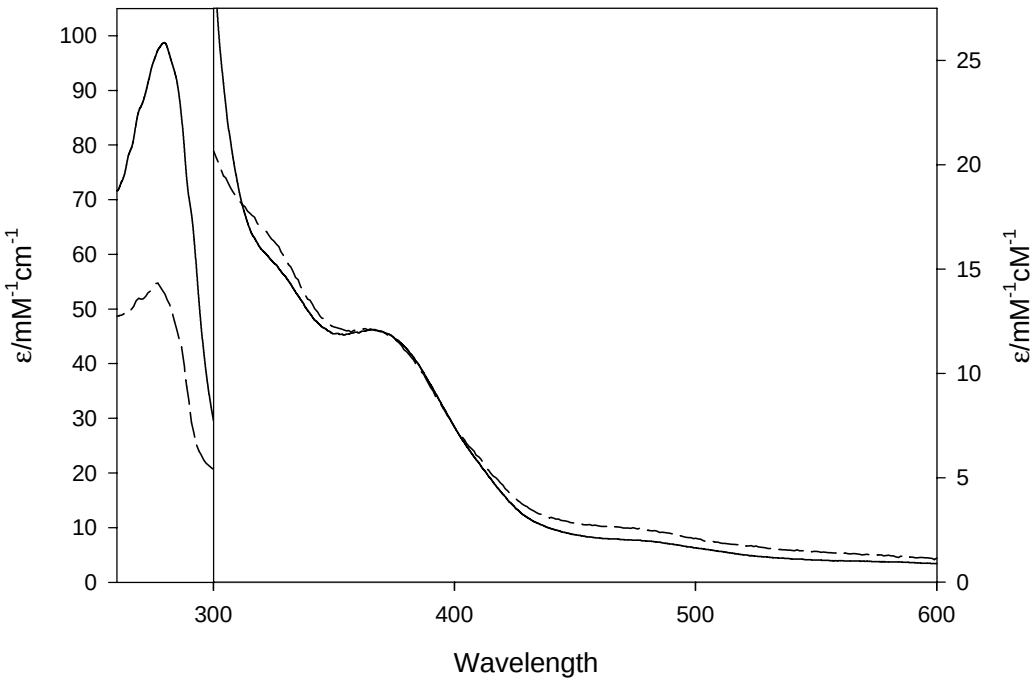

Figure IV-3. UV-vis absorption spectra of ZnS_4Rbr_{ox} (solid line), and CRbr (dash line) in 0.1 M Tris, pH 7.3. The ZnS_4Rbr_{ox} absorbances were multiplied by 1.5 to make them equal to the CRbr absorbance at 370 nm. $CRbr_{ox}$ spectrum was recorded by courtesy of Eric Coulter form Kurtz lab.

Table IV-3. The UV-vis absorbance ratios, extinction coefficients and metal contents of recombinant *D. vulgaris* ZnS_4Rbr_{ox} examined in this work.

Protein		As-isolated ZnS_4Rbr_{ox}
Absorbance ratio	A_{280}/A_{494}	50
	A_{280}/A_{370}	8.2
	A_{370}/A_{494}	6.0
Extinction Coefficient $\varepsilon/mM^{-1}cm^{-1}$ (per dimer)*	280nm	98
	370nm	12
	494nm	2
Metal content	Fe/dimer	3.36
	Zn/dimer	2.66

*The ε values of ZnS_4Rbr were calculated on a protein basis using the Bio-Rad assay with recombinant *D. vulgaris* all-iron Rbr_{ox} as standard.

Table IV-4. The peak heights of the metals in the (F_o-F_c) annealed omit maps (AOM) and Bijvoet difference Fourier maps (BDFM) of ZnS_4Rbr X-ray crystal structures.

	ZnS_4Rbr (1.0 Å)			ZnS_4Rbr (1.7 Å)		
	Fe1	Fe2	Zn3	Fe1	Fe2	Zn3
AOM	11.5σ (AC1)*, 7.6σ (AC2)*	17.1σ	37.6σ	-	-	-
BDFM	14.2σ	13.3σ	42.6σ	23.7σ	20.4σ	8.6σ

*AC1 and AC2 represent the two centers at Fe1 site in ZnS_4Rbr (1.0 Å).

calculated ratio of 5.8 assuming full occupancy of the diiron site by a μ-oxo di-(μ-carboxylato) diferric core, as follows ($\varepsilon/M^{-1}cm^{-1}$ per Rbr monomer):

$\varepsilon_{280}(CRbr) = \varepsilon_{365}(CRbr) \times (A_{280}/A_{370}(CRbr)) = 6{,}000 \times 3.6 = 21{,}600$ (*59*)

ε_{280}(Rbr diferric site) = $\varepsilon_{280}(CRbr) - \varepsilon_{280}$(apo-CRbr) = 21,600 – 6,400 =15,200

$\varepsilon_{280}(ZnS_4Rbr) = \varepsilon_{280}$(Rbr diferric site) + ε_{280}(apo-Rbr) =15,200 + 19,300 = 34,500

$A_{280}/A_{370}(ZnS_4Rbr) = \varepsilon_{280}(ZnS_4Rbr) / \varepsilon_{365}$(CRbr-diferric) = 34,500 / 6,000 = 5.8

(Assuming $\varepsilon_{370}(ZnS_4Rbr) \approx \varepsilon_{365}$(CRbr-diferric))

The apo CRbr and apo Rbr ε_{280}'s were calculated from their aromatic amino acid contents using program RCR/peptidesort, written by John Devereux in the GCG laboratory (*148*). Based on the difference between calculated and measured A_{280}/A_{370}, the diiron sites in as-isolated ZnS_4Rbr were apparently not fully occupied. If it is assumed that the proportion of fully occupied diiron sites in as-isolated ZnS_4Rbr_{ox} is *a* and no singly-iron-occupied diiron sites which might have absorption in the 300 nm-400 nm range exists in ZnS_4Rbr_{ox}, then from the following calculations, the diiron sites in ZnS_4Rbr_{ox} are, thus, approximately 57% double-iron-occupied.

($a \times \varepsilon_{280}$(Rbr diferric site) + ε_{280}(apo-Rbr)) / ($a \times \varepsilon_{370}(ZnS_4Rbr_{ox})$) = A_{280}/A_{370} (as-isolated ZnS_4Rbr_{ox} (**Table II-1**, Chapter II))

$\Rightarrow$ (a x 15,200 + 19,300) / (a x 6,000) = 8.2

$\Rightarrow a = 0.57$

The measured ε_{370} for as-isolated ZnS_4Rbr_{ox} in **Table IV-3** is 0.65 (= 7,800/12,000) of the presumed fully occupied ZnS_4Rbr_{ox}, which is close the value of *a* discussed above.

The zinc content of ZnS_4Rbr (cf. **Table IV-3**) is somewhat higher than the 2 expected for Zn^{2+} occupancy of only the rubredoxin-like sites. The extra ~0.7 zinc is presumably

adventitiously surface bound, since no zinc other than the 2 in the rubredoxin-like site appeared in the X-ray crystal structure. Only a very weak mixed-valent diiron site signal appeared in the EPR spectrum of ZnS_4Rbr_{ox} (**Figure IV-4**), presumably because the protein has been treated with H_2O_2. The EPR signal at 4.3 is due either to adventitious "junk" iron or a small portion of half-occupied diiron sites. This g-4.3 signal could not be due to even a tiny portion of [Fe(III)$(SCys)_4$] sites, because its absorbance feature at 494 nm would have shown in the spectrum of ZnS_4Rbr_{ox}. The ε_{494} of all-iron Rbr_{ox} (10,600 $M^{-1}cm^{-1}$) due to the [Fe(III)$(SCys)_4$] site is much higher than that of the ZnS_4Rbr_{ox} (1,300 $M^{-1}cm^{-1}$). ZnS_4Rbr_{ox} was found to have no NADH peroxidase activity using the modified assay of Coulter et al (*49*) described in the Experiment Section.

IV.C.1.2. Crystal structures of ZnS_4Rbr_{ox}

IV.C.1.2.1. Quality of the model

The data collected for ZnS_4Rbr (1.0 Å) has a resolution of 1.75 Å, and the data for ZnS_4Rbr (1.7 Å) had a resolution of 2.05 Å. The final model of ZnS_4Rbr from refinement of the 1.0-Å data collection has good qualities, as shown in **Table IV-1** (B), with low RMSDs from ideal bond lengths, angles, and torsion angles, as well as reasonable *B*-value and coordinate errors. Ramachandran plots using PROCHECK (*113*) showed that the majority of residues in the model are in the most favored regions, other residues are in additional allowed regions, and no residues are in generously allowed or disallowed regions.

IV.C.1.2.2. Overall structure

The overall ZnS_4Rbr (1.0 Å) structure is similar to the crystal structure of all-iron Rbr_{ox} (cf. Chapter III). The overall r.m.s.d of ZnS_4Rbr (1.0Å) vs Rbr_{ox} is 0.63 Å. As in

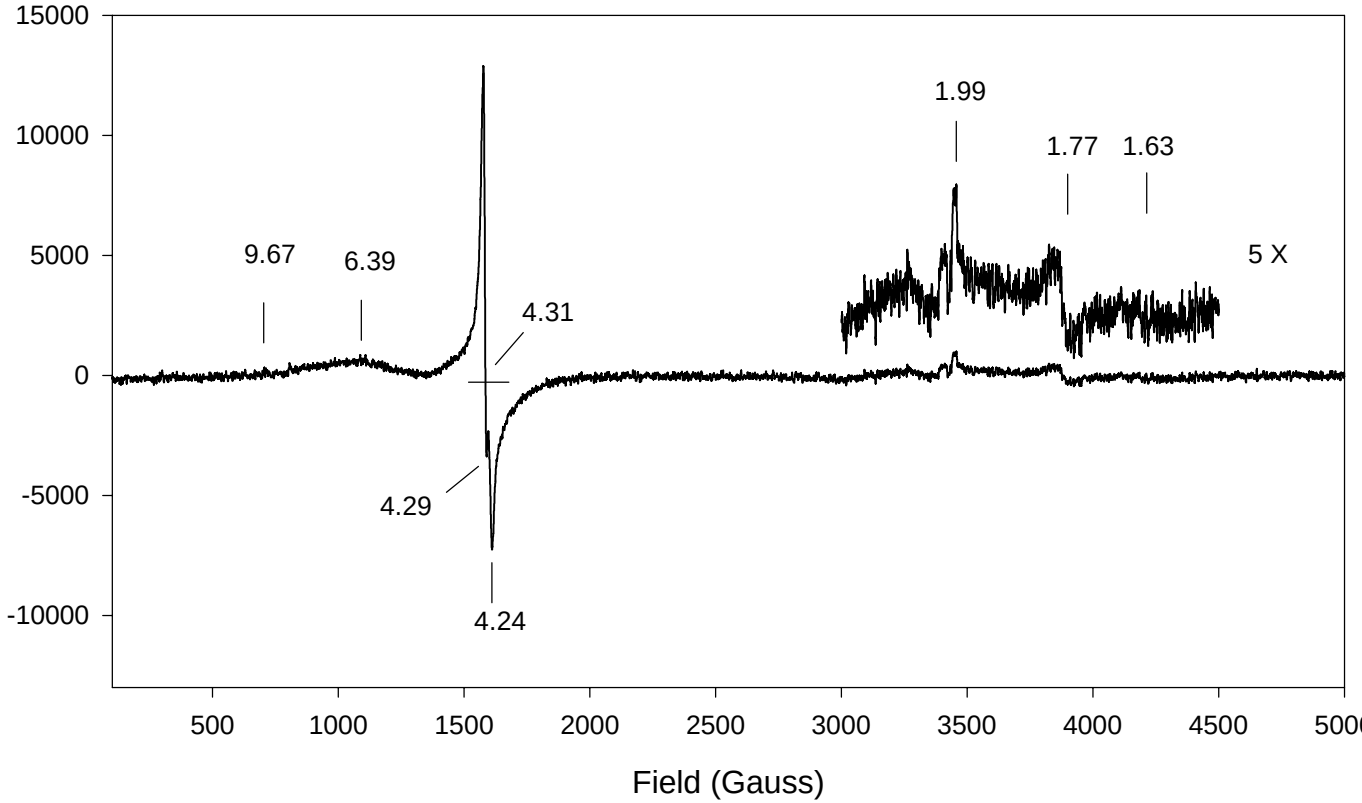

Figure IV-4. X-band EPR spectrum of 0.1 mM ZnS_4Rbr_{ox} in 50 mM Hepes, 200 mM $NaSO_4$, pH 7.0, EPR conditions: T = 7.0 K; microwave frequency 9.604 GHz; microwave power 2.0mW; modulation amplitude 6.37 G; receiver gain 5.00e+04.

Rbr_{ox}, there is a *cis*-peptide bond between Gly78 and Ile79 in ZnS_4Rbr (1.0 Å). The major differences from Rbr_{ox} are the zinc substitution at the $[Fe(SCys)_4]$ site, the position of Fe1 at the diiron site, and the conformations of the surrounding residues at the diiron site in ZnS_4Rbr (1.0 Å).

IV.C.1.2.3. Metal ions in ZnS_4Rbr

The electron density connecting Glu97 and His56 in of ZnS_4Rbr (1.0Å) shown in the composite omit ($2F_o$-F_c) map (cf. **Figure IV-5**) has two centers, Fe1(AC1) and Fe1(AC2). The locations of these two centers were confirmed by the annealed (F_o-F_c) electron density map omitting Fe1, Fe2, Zn3, μ-oxo, and the surrounding residues within 3.5 Å from the omitted atoms, as shown in **Figure IV-6** (A). As listed in **Table IV-4**, in the (F_o-F_c) electron density map, the peak height of Fe1(AC1) (11.5σ) is much higher than that of Fe1(AC2) (7.6σ), but both are lower than that of Fe2 (17.1σ). The sum of the peak heights of Fe1(AC1) and Fe1(AC2) (11.5σ + 7.6σ = 19.1σ) is approximately equal to that of Fe2, which indicates that Fe1 has two alternative locations. Based on the peak height, in the F_o-F_c electron density omit map, Fe1 is located mostly at AC1, and the electron density attributed to an oxo bridge is connected to both Fe1(AC1) and Fe2. If Fe1(AC2) is disregarded, the diiron site structure is very similar to that of Rbr_{ox}: His56 Nδ1 is ~ 4.0 Å away from Fe1(AC1) and is, therefore, not a ligand to Fe1(AC1), and all other bond distances of the diiron site ligands, including the μ-oxo, in ZnS_4Rbr are very similar to the corresponding parameters in Rbr_{ox}, as listed in **Table IV-5**. The Fe1(AC2) is within bonding distance (2.2 Å) of His56 Nδ1, and is in a position similar to that of Fe1 in Rbr_{red}. However, Fe1(AC2) has less influence than Fe1(AC1) on the position of

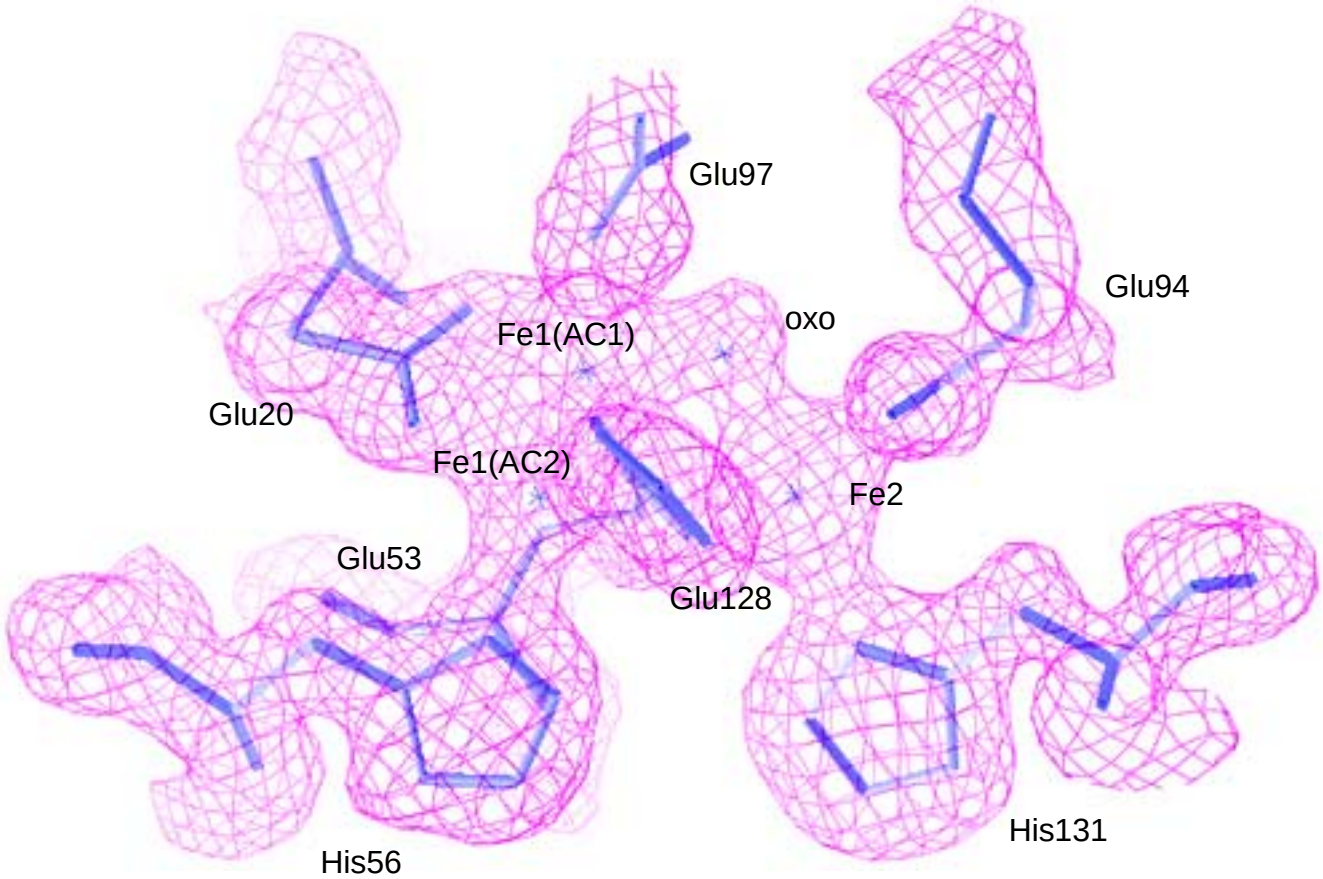

Figure IV-5. The final model and the composite omit map ($2F_o$-F_c) contoured at 1.0σ at the diiron site of ZnS_4Rbr (1.0Å). Glu128 is in the foreground in this view. Stars indicate positions of iron atoms and solvent oxygen ligands.

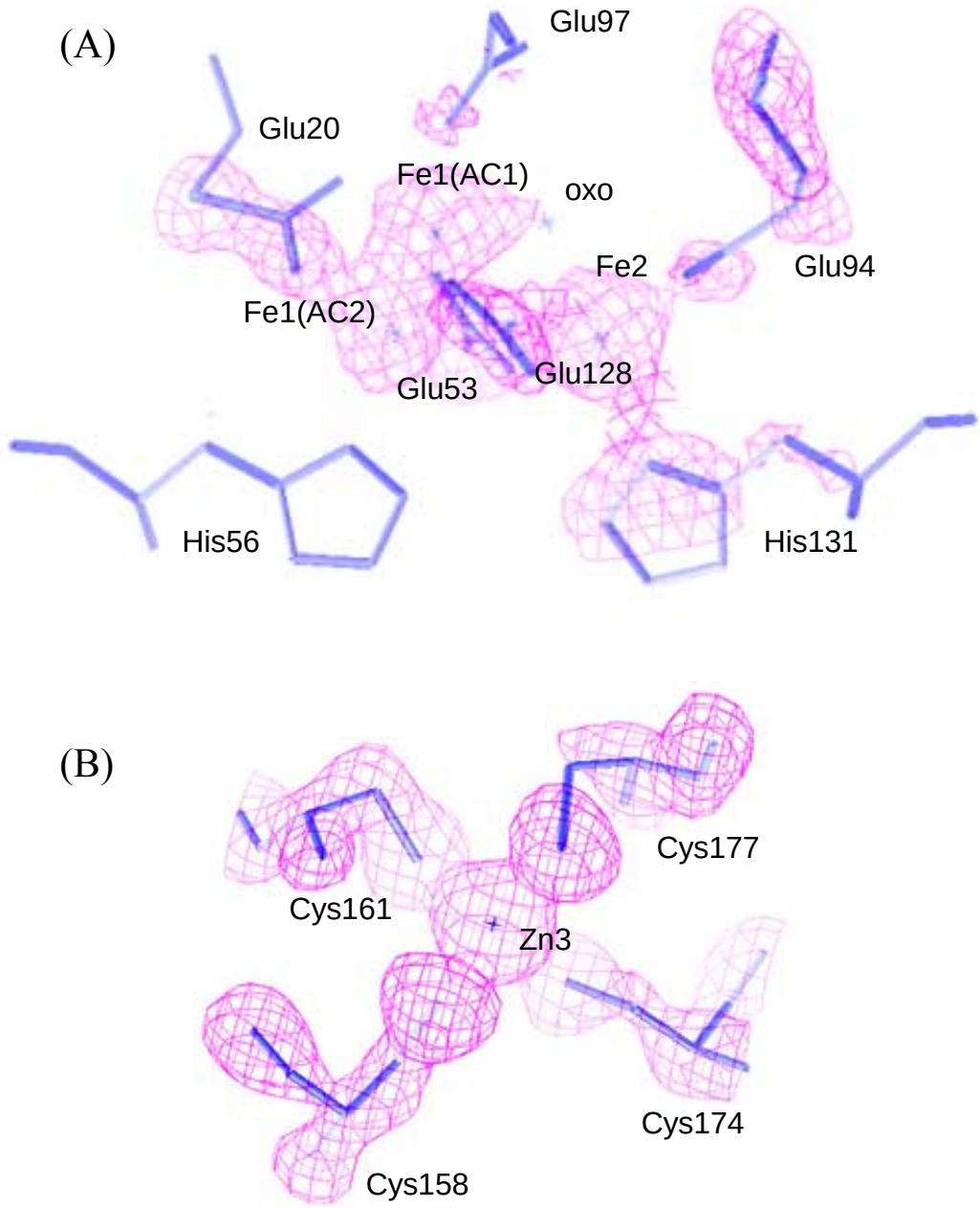

Figure IV-6. The final model and the annealed omit map (F_o-F_c) of ZnS_4Rbr (1.0 Å), contoured at 3σ (A) at the diiron site, and (B) at the rubredoxin-like site, with Fe1, Fe2, Zn3 and μ-oxo, as well as the surrounding residues within 3.5 Å of the above selected atoms omitted. Stars indicate positions of metal atoms and solvent oxygen ligands.

Table IV-5. Interatomic distances for metal sites of *D. vulgaris* ZnS_4Rbr, comparing with all-iron Rbr_{ox}, and Rbr_{red}.[a]

Atoms	ZnS_4Rbr (1.0Å)	Rbr_{ox}[b]	Rbr_{red}[b]
Fe1(AC1) – oxo	2.0	1.8	-
Fe1(AC1) – Glu 20OE1	2.0	2.1	-
Fe1(AC1) –Glu 20OE2	2.6	2.3	-
Fe1(AC1)– Glu 53OE1	2.2	2.2	-
Fe1(AC1) – Glu 128OE2	2.0	2.0	-
Fe1(AC1) – Glu 97OE1	2.3	2.1	-
Fe1(AC1) – His 56 ND1	(4.0)	(4.2)	-
Fe1(AC2) – oxo	(3.3)	-	2.2(Fe1 – HOH 1)
Fe1(AC2) – Glu 20OE1	(2.9)	-	2.2
Fe1(AC2) –Glu 20OE2	2.1	-	2.3
Fe1(AC2)– Glu 53OE1	2.4	-	2.1
Fe1(AC2) – Glu 128OE2	2.2	-	2.1
Fe1(AC2) – Glu 97OE1	(4.0)	-	(4.6)
Fe1(AC2) – His 56 ND1	2.2	-	2.3
Fe2 – oxo	2.2	2.1	2.2(Fe2 – HOH 2)
Fe2 – Glu 94OE1	2.3	2.2	2.2
Fe2 –Glu 94OE2	2.3	2.2	2.3
Fe2 – Glu 53OE2	2.2	2.0	2.1
Fe2 – Glu 128OE1	2.2	2.1	2.1
Fe2 – His 131 ND1	2.2	2.2	2.2
Zn3 – Cys 158SG	2.3	2.4 (Fe3)	2.3 (Fe3)
Zn3 – Cys 161SG	2.3	2.3 (Fe3)	2.3 (Fe3)
Zn3 – Cys 174SG	2.3	2.3 (Fe3)	2.3 (Fe3)
Zn3 – Cys 177SG	2.3	2.3 (Fe3)	2.3 (Fe3)
average Zn3-CysSG	2.3	2.3 (Fe3)	2.3 (Fe3)
Fe1(AC1) --- Fe2	(3.4)	(3.3)	-
Fe1(AC1) --- Zn3	(12.6)	(12.4) (Fe3)	-
Fe1(AC2) --- Fe2	(3.6)	-	(4.0)
Fe1(AC2) --- Zn3	(10.8)	-	(11.0) (Fe3)
Fe2--- Zn3	(12.0)	(12.0) (Fe3)	(12.2) (Fe3)
Fe1(AC1) --- Fe1(AC2)	(1.9)	-	-

[a]Data in parenthesis are non-bonded distances.
[b]Data from Chapter III.

ligands to the diiron site, especially on those of Glu97 and Glu20, the conformations of which are much closer to those in Rbr_{ox} than in Rbr_{red} and which do not appear to occupy alternative positions as in ZnS_4Rbr_{ox}. The changes at the diiron site caused by Fe1(AC2) are discussed further below.

The [$Zn(SCys)_4$] center in ZnS_4Rbr is essentially isostructural with the [$Fe(SCys)_4$] center in Rbr_{ox}, as shown in **Figure IV-6** (B). The r.m.s.d. of the ZnS_4Rbr (1.0 Å) structure vs the all-iron Rbr_{ox} structure for the four cysteine residues (Cys158, 161, 174,177) is only 0.05 Å. As listed in **Table IV-4**, however, the peak height of Zn3 (37.6σ) in the (F_o-F_c) omit map is much higher than those of Fe1 (11.5σ (AC1), 7.6σ (AC2)) and Fe2 (17.1σ) at the diiron site in ZnS_4Rbr (1.0 Å). The Fe1 and Fe2 positions are apparently not fully occupied in ZnS_4Rbr. This conclusion is supported by Bijvoet difference Fourier map calculations. In the Bijvoet difference Fourier map of ZnS_4Rbr (1.0 Å) (cf. **Figure IV-7** (A) and **Figure IV-8** (A)), the peak height at Fe1, Fe2 and Zn3 are 14.2σ, 13.3σ and 42.6σ, respectively, whereas in the Bijvoet difference Fourier map of ZnS_4Rbr (1.7 Å) (cf. **Figure IV-7** (B) and **Figure IV-8** (B)), the peak height at Fe1, Fe2 and Zn3 are 23.7σ, 20.4σ and 8.6σ, respectively. Since the Bijvoet difference Fourier maps were calculated using a resolution range lower than 3 Å, the two centers Fe1(AC1) and Fe1(AC2) in the final model as seen in the annealed (F_o-F_c) electron density map of ZnS_4Rbr (1.0 Å) cannot be distinguished; therefore, only one center at the Fe1 site is shown in the anomalous maps as the arrows pointed in **Figure IV-7**. Comparing the two anomalous maps of ZnS_4Rbr (1.0 Å) and ZnS_4Rbr (1.7 Å) (cf. **Figure IV-8** (A) and (B)), the Zn3 has the most intense anomalous scattering at 1.0 Å among the metal ions: Zn3 (42.6σ) > Fe1 (14.2σ) and Fe2 (13.3σ), and has the weakest anomalous scattering at 1.7

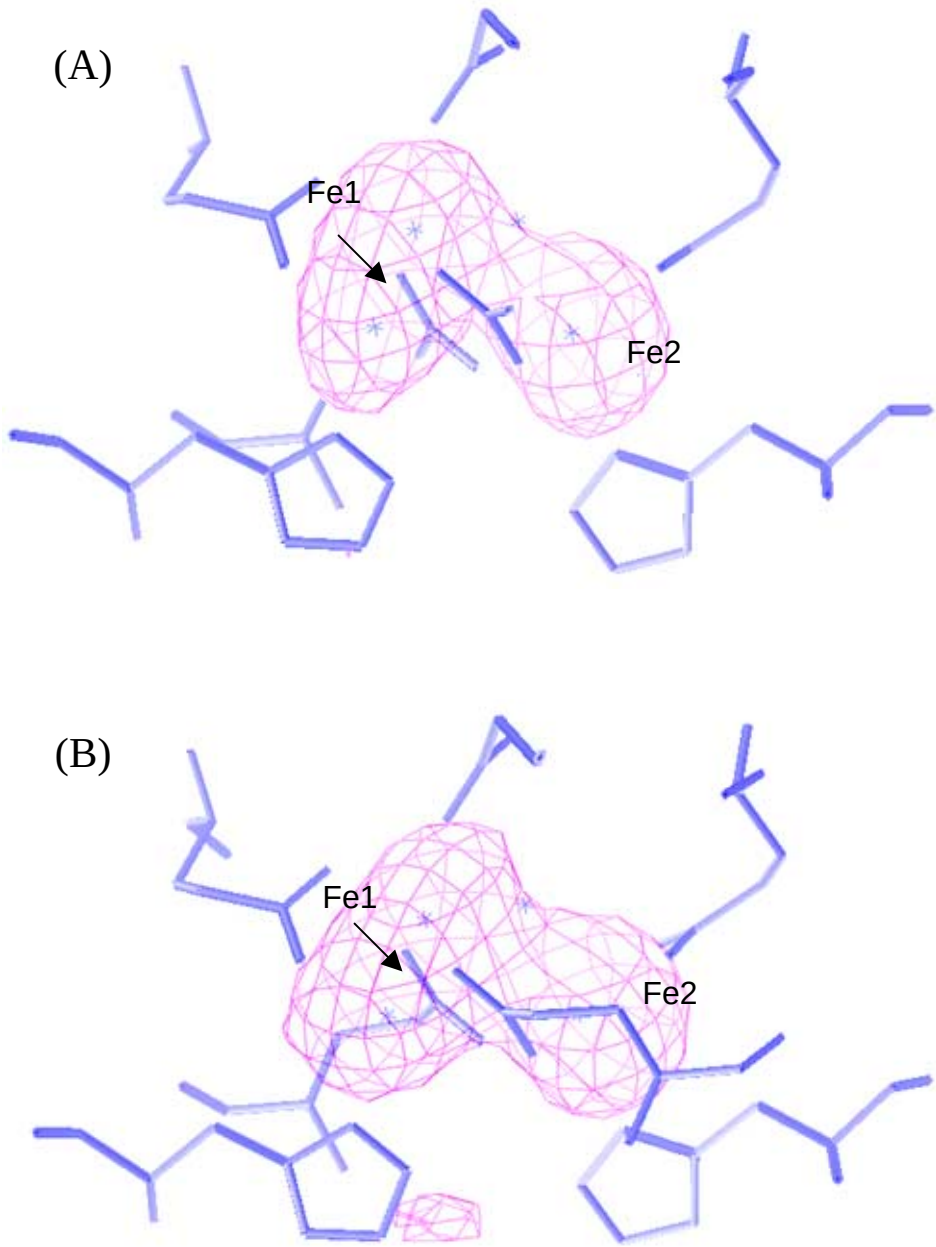

Figure IV-7. The final model and the Bijvoet difference-Fourier map contoured at 3σ at the diiron sites of (A) ZnS_4Rbr (1.0 Å) , (B) ZnS_4Rbr (1.7 Å), with Fe1, Fe2, and Zn3 omitted. Arrows indicate the center of the electron densities of Fe1 sites. Stars indicate positions of iron atoms and solvent oxygen ligands.

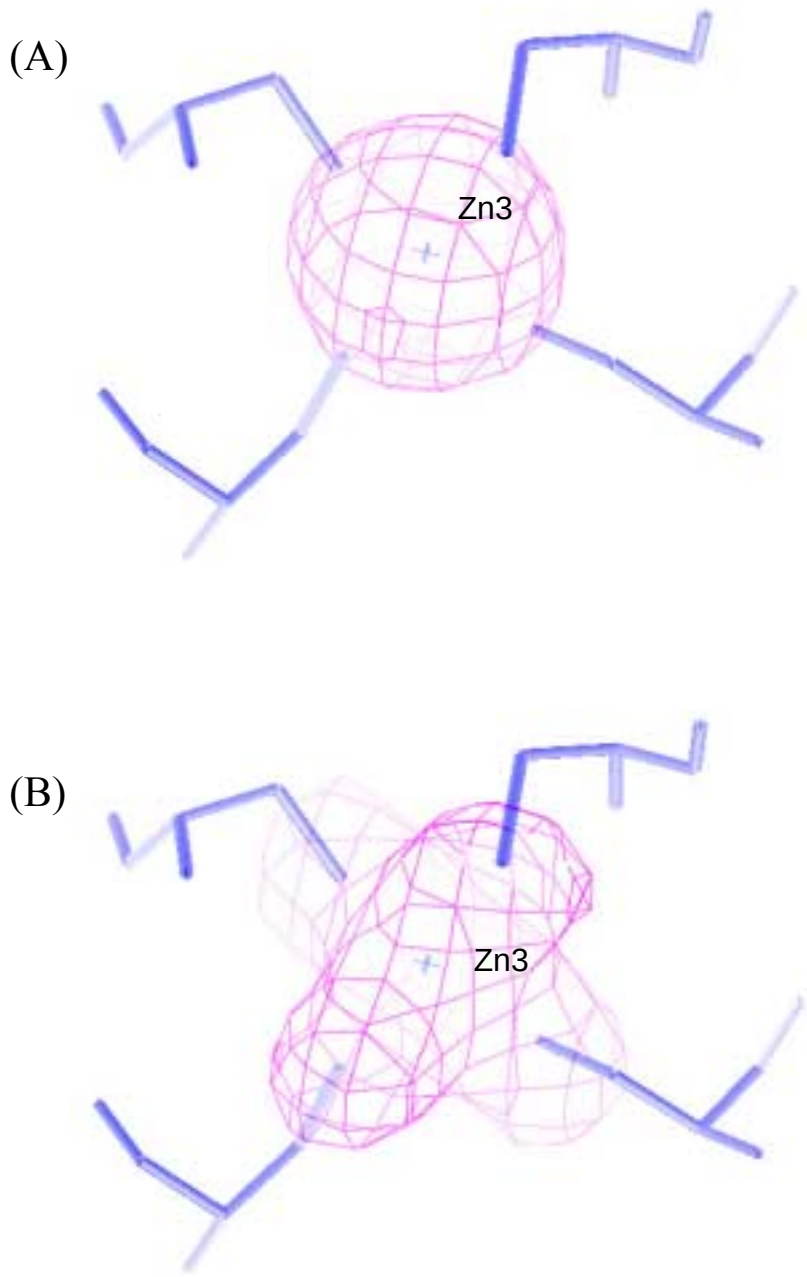

Figure IV-8. The final model and the Bijvoet difference-Fourier maps contoured at 3σ at the [Zn(II)$(SCys)_4$] sites of (A) ZnS_4Rbr (1.0 Å) , (B) ZnS_4Rbr (1.7 Å), with Fe1, Fe2, and Zn3 omitted. Stars indicate positions of zinc atoms.

Å: Zn3 (8.6σ) < Fe1 (23.7σ) and Fe2 (20.4σ), as listed in **Table IV-4**. Four zinc-sulfur bonds appear in the Bijvoet difference Fourier map of ZnS_4Rbr (1.7 Å), but are not detectable in the Bijvoet difference Fourier map of ZnS_4Rbr (1.0 Å), consistent with the anomalous scattering coefficients, *f″*, of sulfur and zinc (cf. **Figure IV-1**). At 1.7Å, *f″*-sulfur is 0.67, which, although relatively weak compared to iron (3.75), is close to that of zinc (0.81). At 1.0 Å, on the other hand, *f″*-sulfur (0.24) is too weak to be observed in the Bijvoet difference Fourier map, whereas zinc (2.55) is readily observed. This analysis of Bijvoet difference Fourier maps demonstrates that it is reliable to assume the occupancy of zinc in ZnS_4Rbr as 1. The intensities of anomalous scattering at 1.0 Å of Fe1 (14.2σ) and Fe2 (13.3σ) as shown in the Bijvoet difference Fourier map (cf. **Figure IV-7** (A)) are lower than expected from the *f″*-Fe (1.55) at 1.0 Å, when compared with Zn3 (42.6σ) and *f″*-Zn (2.55). Theoretically, the anomalous scattering of Fe1 and Fe2 should each be 25.9σ (= 42.6σ x 1.55 / 2.55), if both Fe1 and Fe2 sites were fully occupied by iron. This analysis indicates that the occupancies of both Fe1 and Fe2 are less than 1. Therefore, Fe1 is calculated to be 54.8% (14.2σ /25.9σ = 0.548) occupied and Fe2 is 51.4% (13.3σ /25.9σ = 0.514) occupied at the diiron site of ZnS_4Rbr (1.0 Å). Similar calculations can be carried out for the anomalous scattering data obtained at 1.7 Å. At this wavelength, the *f″*-zinc and *f″*-iron are 0.81 and 3.75, respectively, (cf. **Figure IV-1**) and the intensity of anomalous scattering of Zn3 is 8.6σ. Thus, the anomalous scattering of Fe1 and Fe2 should be 40σ (= 8.6σ x 3.75 / 0.81) if Fe1 and Fe2 sites were both full occupied by iron. In fact, the anomalous scattering intensity of Fe1 is only 23.7σ and Fe2 is only 20.4σ in the 1.7-Å Bijvoet difference Fourier map, which indicates that Fe1 is 60% (23.7σ / 40σ =

0.60) occupied and Fe2 is 51% (20.4σ / 40σ = 0.51) occupied at the diiron site of ZnS_4Rbr. The analysis of the anomalous scattering data at 1.7 Å, thus, agrees with that of the 1.0-Å data. The calculated average occupancies from the 1.0-Å and 1.7-Å data for Fe1 and Fe2 are 57% and 51%, respectively, and the ratio between Fe1 and Fe2 occupancies is 1.1 (= 57% / 51%). The reason for the disagreement of these much lower calculated occupancies of Fe1 and Fe2 from the difference maps with those values obtained from the occupancy refinement in Section IV.B.4.2 is not clear. In the annealed (F_o-F_c) electron density omit map, the ratio of intensities of Fe1 to Fe2 is also 1.1 (19.1σ /17.1σ = 1.12), which is approximately equal to the above results from the anomalous scattering data obtained from the Bijvoet difference Fourier maps. Therefore, the Fe1(AC1) and Fe1(AC2) occupancies relative to the whole protein can be obtained using the data from the annealed (F_o-F_c) electron density omit maps: Fe1(AC1) = 57% x 11.5σ /19.1σ = 34%, and Fe1(AC2) = 57% - 34% = 23%. The metal analysis of ZnS_4Rbr before crystallization shows 3.4 iron/dimer (**Table IV-3**), which is more than the total calculated irons (2.16 = 2 x (57% + 51%)) in the crystal of ZnS_4Rbr. Presumably, some iron was leached out of the diiron site during the crystallization procedure.

Fe1(AC1) of ZnS_4Rbr certainly does not contain zinc or mixtures of zinc and iron, as in Zn(Fe)1 of Zn,FeRbr, discussed in Section IV.C.2. If the percentage of the iron in Fe1 site is *a*, and the percentage of zinc in the Fe1 site is *b*, then, using the data from anomalous scattering of Fe1 and Fe2 (cf. **Table IV-4**) and the appropriate anomalous scattering coefficients (**Figure IV-1**):

Fe1 site, 1.0 Å data: 42.6σ x (1.55/2.55) x *a* + 42.6σ x *b* = 14.2σ

Fe1 site, 1.7 Å data: 8.6σ x (3.75/0.81) x *a* + 8.6σ x *b* = 23.7σ

$\Rightarrow a = 60\%, b = -3.3\%$.

Therefore, ~ 60% iron and ~ -3.3% zinc exist in the entire Fe1 site of ZnS_4Rbr. The small negative zinc percentage is nearly zero, and presumably reflects that zinc does not occupy the Fe1 site.

Similar calculations for Fe2 can be carried out, assuming the percentage of iron in the Fe2 site is *c*, and the percentage of zinc in the Fe2 site is *d*:

Fe2 site, 1.0 Å data: $42.6\sigma \times (1.55/2.55) \times c + 42.6\sigma \times d = 13.3\sigma$

Fe2 site, 1.7 Å data: $8.6\sigma \times (3.75/0.81) \times c + 8.6\sigma \times d = 20.4\sigma$

$\Rightarrow c = 51\%, d = 0.3\%$.

The results again show nearly zero percent of zinc in the Fe2 site.

Fe1(AC2) is more likely to be ferrous than ferric based on the following considerations. The nearby Glu97 Oε1 and the oxo ligand, which are not ligated to Fe1(AC2), are better ligands to ferric than the His56 Nδ1, which <u>is</u> ligated to Fe1(AC2), as can be seen by comparing the structures of all-iron Rbr_{ox} and Rbr_{red} in Chapter III. Fe1(AC1) is six-coordinated, whereas Fe1(AC2) is only four-coordinated, as shown in **Figure IV-9** (bottom). Only two synthetic complexes containing four-coordinated Fe(III) are known (*149, 150*), in which each iron is coordinated only with oxygen ligands. It is possible that the iron at Fe1(AC2) site ZnS_4Rbr (1.0 Å) is due to partial reduction of ferric to ferrous by the synchrotron X-irradiation, a phenomenon which has been observed in other diiron proteins, such as *Methylococcus capsulatus* (Bath) MMOH (*151*), *Salmonella typhimurium nrdF* RNR R2 (*137*), *E. coli* RNR R2 (*135*), and Δ9D(*74*). The yellow color of ZnS_4Rbr crystal after exposure to the synchrotron

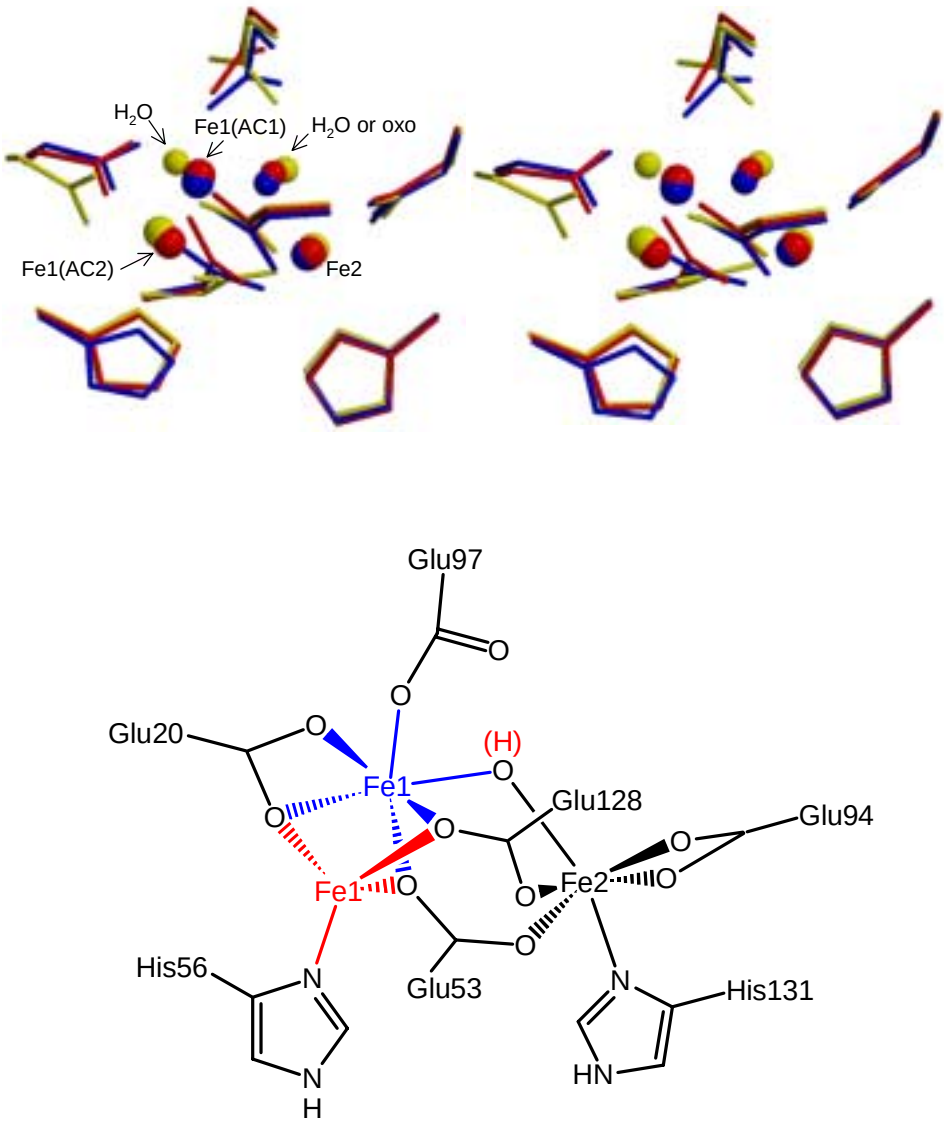

Figure IV-9. (Top) stereoview of the superposition of ZnS_4Rbr_{ox} (1.0 Å) (red), all-iron Rbr_{ox} (blue), and all-iron Rbr_{red} (yellow) at the diiron sites. The smaller spheres represent solvent ligands, and the larger spheres represent metal ions. The solvent ligands were modeled as oxo's in ZnS_4Rbr (1.0 Å) and all-iron Rbr_{ox} and as water in all-iron Rbr_{red}. (Bottom) Schematic drawing of the diiron site structure of ZnS_4Rbr_{ox} (1.0 Å). The iron and its bonds with the surrounding ligands at Fe1(AC1) site are high-lighted in blue, and the iron and its bonds with the surrounding ligands at Fe1(AC2) site are high-lighted in red.

X-irradiation at both wavelengths of 1.0 Å and 1.7 Å became noticeably paler, which is consistent with the reduction of the diiron sites during data collection. (The color fading of the crystals after exposure to synchrotron irradiation was also observed for Zn,FeRbr, which is discussed in Section IV.2.2.3.) When the ZnS_4Rbr crystal that had been exposed to synchrotron radiation was thawed in mineral oil, the pale yellow color became darker and close to the original color before exposure to the synchrotron irradiation within minutes of thawing, which indicate that the protein was reoxidized by dioxygen. The iron at Fe2 sites should be reduced by synchrotron irradiation to some extent too, but it is uncertain about the ratio between ferrous and ferric at Fe2 sites, since the structures of ferrous and ferric complexes at Fe2 sites are indistinguishable, as shown in all-iron Rbr_{ox} and Rbr_{red} structures (cf. ChapterIII).

IV.C.1.2.4. Comparisons of ZnS_4Rbr with all-iron Rbr structures: the influence of [Zn(II)(SCys)$_4$] on the diiron site

The [Zn(II)(SCys)$_4$] site structure in ZnS_4Rbr is very similar to that of the [Fe(III)(SCys)$_4$] site in all-iron Rbr_{ox}. However, the replacement of Fe(III) by Zn(II) in the [Fe(III)(SCys)$_4$] site significantly affects the diiron site structure in that the Fe1 and Fe2 are only about 50-60% occupied in ZnS_4Rbr. The Fe1 site has two alternative conformations: Fe1(AC1) and Fe1(AC2). The position of Fe1(AC1) is close to that of the Fe1 in all-iron Rbr_{ox}, and Fe1(AC1)---Fe2 distance (3.4 Å) in ZnS_4Rbr (1.0 Å) is the same as the Fe1---Fe2 distance (3.3 Å) in all-iron Rbr_{ox} within experimental error. The position of Fe1(AC2) is closer to that of Fe1 in all-iron Rbr_{red} than Rbr_{ox}, as shown in **Figure IV-9** (top), although the distance of Fe1(AC2) and Fe2 (3.6 Å) is significantly shorter than that of Fe1 and Fe2 in all-iron Rbr_{red} (4.0 Å).

The r.m.s.d. of ZnS_4Rbr (1.0 Å) vs all-iron Rbr_{ox} for the residues surrounding the two irons at the diiron site (Glu20, 53, 94, 97, 128, and His56, 131) is 0.29, whereas the r.m.s.d. of ZnS_4Rbr (1.0 Å) vs all-iron Rbr_{red} for the same residues surrounding the two irons at diiron site is 0.53. The side chains of Glu94, and His131, which exclusively ligate Fe2, show no significant changes in ZnS_4Rbr (1.0 Å), compared to all-iron Rbr_{ox} and Rbr_{red} (cf. **Figure IV-9**). The positions of the carboxylate planes of the Fe1 ligands, Glu20 and Glu97, in ZnS_4Rbr (1.0 Å) are closer to those in Rbr_{ox} than Rbr_{red}. The Glu20 appears to be bidentate to Fe1(AC1), as in Rbr_{ox}, but monodentate to Fe1(AC2), unlike Fe1 in Rbr_{red}. The position of the imidazole ring of His56 in ZnS_4Rbr (1.0 Å) is slightly closer to that in Rbr_{red} than Rbr_{ox}, although the difference is not significant. The hydrogen bond between His56 Nε2 and Cys161′ carbonyl is well maintained in ZnS_4Rbr (1.0 Å).

Zn(II) and Fe(II) have identical charges and similar sizes. Zn(II) is readily substituted for Fe(II) in rubredoxin and the sites are isostructural (*144*). The UV-vis absorption spectrum of ZnS_4Rbr_{ox} resembles the spectrum of the CRbr oxidized form (*59*) (**Figure IV-3**) and that of an intermediate [Fe(III)Fe(III)]/[Fe(II)$(SCys)_4$]-Rbr observed during the oxidation of all-ferrous Rbr by H_2O_2 (**Figure II-5** "1ms", Chapter II). Therefore, the [Zn(II)$(SCys)_4$] site in ZnS_4Rbr can mimic the [Fe(II)$(SCys)_4$] site in all-iron Rbr. However, the changes at the diferric site induced by of the [Zn(II)$(SCys)_4$] site in ZnS_4Rbr may have been obscured by reduction of diiron site by synchrotron irradiation, as described above. About 40% (= 23% / 57%) of the total iron at the Fe1 site moves towards His56 Nδ1. It is uncertain if all the iron at Fe1(AC2) site is due to the reduction or the influence of [Zn(II)$(SCys)_4$] site. The remaining 60% of the iron at the Fe1(AC1) site is still bridged with Fe2 through a μ-oxo, as in the all-iron Rbr_{ox}, which indicate that

the majority of the iron at Fe1 site was not affected by the [Zn(II)$(SCys)_4$] site in the other subunit across the "head-to-tail" dimer interface. Therefore, the product after the first phase of the oxidation of Rbr_{red} by H_2O_2 described in Chapter II, [Fe(III)Fe(III)]/[Fe(II)$(SCys)_4$], would be closer to the structure of ZnS_4Rbr, with Fe at AC1 than AC2 with the majority of iron at the diferric site in the first-phase product oxo-bridged as in the all-iron Rbr_{ox}. The structure of the Fe1(AC2)---Fe2 site is different from that proposed for the mixed-valent diiron site in Chapter III (cf. **Scheme III-1**) which retains the hydroxo bridge and ligation to Glu97, may mean that those sites containing ferrous Fe1(AC2) also contain ferrous Fe2.

IV.C.2. Zn,FeRbr$_{ox}$

IV.C.2.1. Protein characterization

Rbr with Zn^{2+} substituted for iron at the diiron site (Zn,FeRbr) could be prepared by adding a 5-fold molar excess over diiron sites of $ZnSO_4$ to as-isolated Rbr_{ox}. Following this addition, the absorbance at 494 nm showed no significant change, but the absorbance at 370 nm decreased with time such that the ratio of A_{370}/A_{494} decreased from ~2.1 to ~1.6 (**Figure IV-10** (A)). After this treatment there was hardly any detectable mixed-valent diiron site EPR signal (**Figure IV-11**) compared to the weak signal for as-isolated Rbr_{ox} (**Figure II-16**, Chapter II). The rubredoxin-like site EPR signals at 4.3 and 9.6 stayed intact consistent with the retention of the 494-nm absorbance in **Figure IV-10**. These observations indicate that the iron at the rubredoxin-like center stayed intact, but that some of the iron at the diiron site was replaced by Zn^{2+}. The increased zinc content of Zn,FeRbr$_{ox}$ compared to that of the as-isolated Rbr_{ox} supports this conclusion (cf. **Table II-1** in Chapter II, and **Table IV-6**). The final absorption spectrum of Zn,FeRbr$_{ox}$

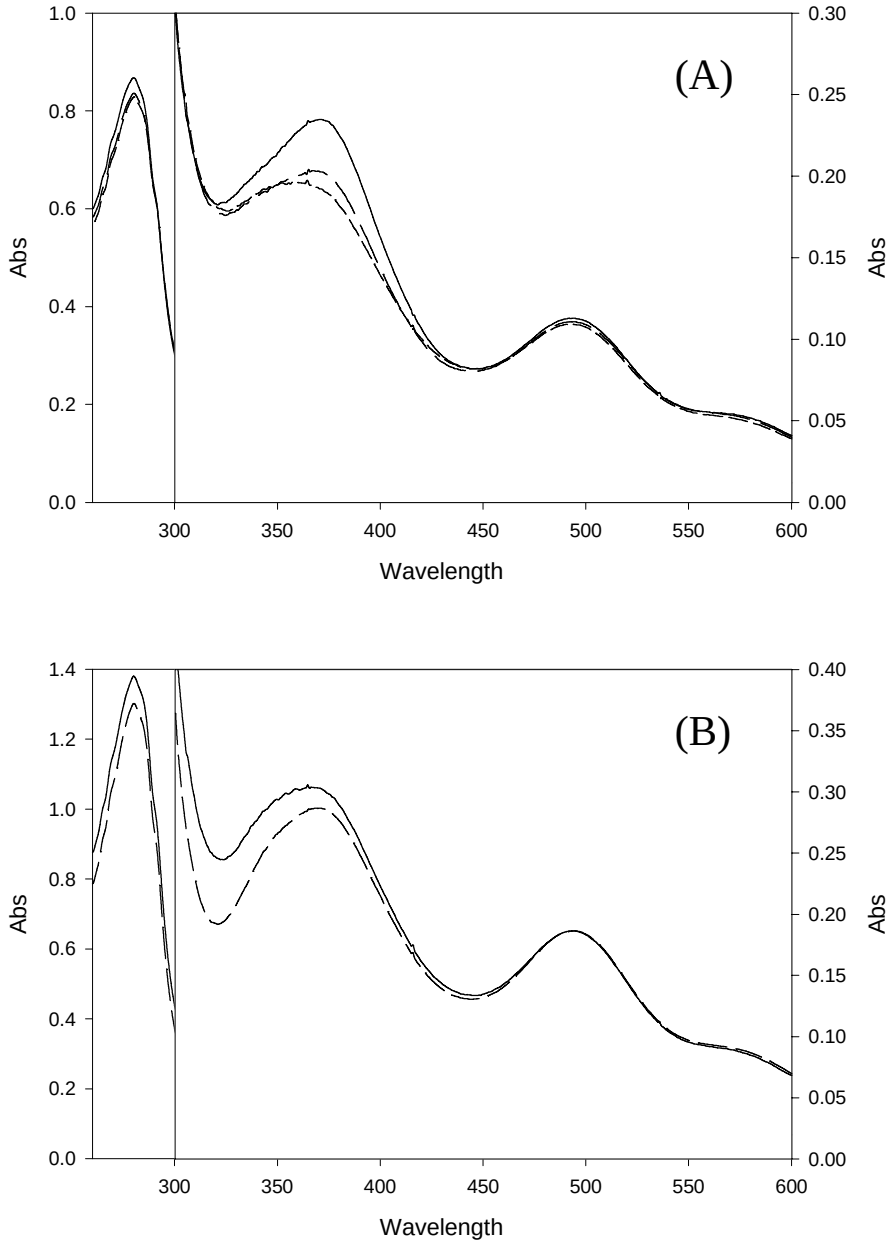

Figure IV-10. The UV-vis absorption spectra of (A) Rbr_{ox} (solid line), Rbr_{ox} + $ZnSO_4$ (5-fold molar excess over Rbr diiron sites), after 10 min (long-dashed line), after 1.5 hr (short-dashed line). Rbr_{ox} ~10 µM, $ZnSO_4$ ~100 µM, in 0.1 M Tris, pH 7.3. (B) Zn,$FeRbr_{ox}$ before crystallization (solid line), and after crystallization (crystal dissolved in buffer without $ZnSO_4$) (dashed line). Zn,$FeRbr_{ox}$ ~ 17.5 µM, in 0.1 M Tris, pH 7.3.

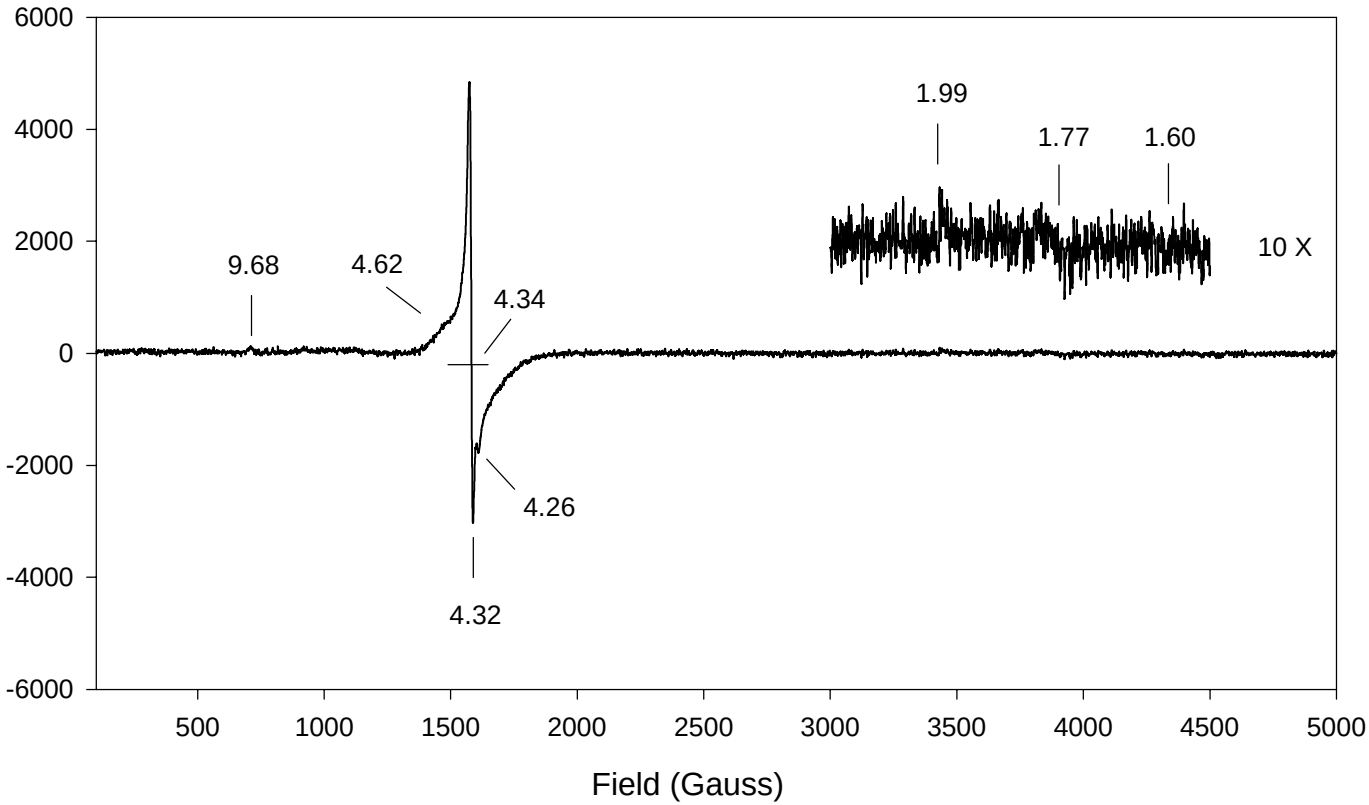

Figure IV-11. X-band EPR spectra of 0.076 mM Zn,FeRbr$_{ox}$ in 0.1 M Tris, pH 7.3, EPR conditions: T = 5.9 K; microwave frequency 9.601 GHz; microwave power 2.0 mW; modulation amplitude 6.37 G; receiver gain 2.00e+03.

Table IV-6. The UV-vis absorbance ratios, extinction coefficients and metal contents of recombinant *D. vulgaris* Zn,FeRbr$_{ox}$ examined in this work.

Protein		Zn,FeRbr$_{ox}$ before crystallization	Zn,FeRbr$_{ox}$ after crystallization
Absorbance ratio	A_{280}/A_{494}	7.4	7.0
	A_{280}/A_{370}	4.6	4.5
	A_{370}/A_{494}	1.6	1.5
Extinction Coefficient $\varepsilon/mM^{-1}cm^{-1}$ (per dimer)*	280nm	78	74
	370nm	17	16
	494nm	10.6	10.6
Metal content	Fe/dimer	3.23	2.22
	Zn/dimer	3.46	4.02

*The ε values of Zn,FeRbr was calculated based on the ε_{494} of *D. vulgaris* all iron Rbr$_{ox}$ (*59*).

Table IV-7. The peak heights of the metals in the (F_o-F_c) annealed omit maps (AOM) and Bijvoet difference Fourier maps (BDFM) of Zn,FeRbr X-ray crystal structures.

	Zn,FeRbr (1.0 Å)			Zn,FeRbr (1.7 Å)		
	Zn1	Fe2	Fe3	Zn1	Fe2	Fe3
AOM	22.0σ	29.7σ	31.3σ	16.4σ	19.3σ	19.9σ
BDFM	24.3σ	24.2σ	22.0σ	10.5σ	14.2σ	25.2σ

(**Figure IV-10** (B)) is similar to that of oxidized rubredoxin (cf. **Figure I-8** in Chapter I), but the ratio of A_{370}/A_{494} (1.6) is still higher than for oxidized rubredoxin (1.1). The ratio of A_{370}/A_{494} Zn,FeRbr$_{ox}$ after crystallization (crystals grown for at least 2 days) is slightly lower (1.5) than before crystallization, and the iron/zinc contents and ratio are also significantly lower than before crystallization (cf. **Table IV-6**). It is likely that more zinc ions entered the diiron site of Rbr during the crystallization, and that some of the iron ions that were at the diiron site have been replaced by zinc. The Zn,FeRbr$_{ox}$ after crystallization when re-dissolved still had ~37% of the NADH peroxidase activity compared to as-isolated Rbr$_{ox}$. This residual activity is probably due to a small portion of intact diiron sites in the Zn,FeRbr$_{ox}$.

IV.C.2.2. Crystal structures of Zn,FeRbr$_{ox}$

IV.C.2.2.1. Quality of models

The data collected for Zn,FeRbr (1.0 Å) and ZnFeRbr (1.7 Å) have a resolution of 1.75 Å and 2.05 Å, respectively. Both of the final models from refinements of data collection, Zn,FeRbr (1.0 Å) and Zn,FeRbr (1.7 Å), have good qualities with low RMSDs from ideal bond lengths, angles, and torsion angles, as well as reasonable *B*-value and coordinate errors, as shown in **Table IV-2** (B). Ramachandran plots using PROCHECK (*113*) show that the majority of residues in each model are in the most favored regions, other residues are in additional allowed regions, and no residues are in generously allowed or disallowed regions.

IV.C.2.2.2. Overall structures

The overall protein structures of Zn,FeRbr (1.0 Å) and Zn,FeRbr (1.7 Å) are very similar to each other and also similar to the structure of all-iron Rbr$_{ox}$: the r.m.s.d. of

Zn,FeRbr (1.0 Å) vs Zn,FeRbr (1.7 Å) is 0.28 Å, and the r.m.s.d. of Zn,FeRbr (1.0 Å) vs all-iron Rbr_{ox} is 0.25 Å. The *cis*- peptide bond formed between Gly78 and Ile79 is also conserved in Zn,FeRbr. The [$Fe(SCys)_4$] site of Zn,FeRbr is almost identical to that of the all-iron Rbr_{ox}, whereas the structure of the diiron site of Zn,FeRbr shows significant differences from the all-iron Rbr_{ox}: the r.m.s.d. of Zn,FeRbr (1.0 Å) vs all-iron Rbr_{ox} at the rubredoxin-like center is 0.03 Å, and the r.m.s.d. of Zn,FeRbr (1.0 Å) vs all-iron Rbr_{ox} at the diiron site is 0.23 Å.

IV.C.2.2.3. Metal ions in Zn,FeRbr

Both the composite omit ($2F_o$-F_c) maps (cf. **Figure IV-12**) of Zn,FeRbr (1.0 Å) and Zn,FeRbr (1.7 Å), and both their annealed omit (F_o-F_c) maps (cf. **Figure IV-13**) omitting all metal ions, solvent ligands and the surrounding residues of the metal binding sites within 3.5 Å of the omitted atoms, clearly show two distinct metal ion centers, labeled Zn1 and Fe2, at the binuclear site. The electron density centered at Zn1 is connected with the electron density of His56 Nδ1, and an electron density due to a solvent molecule is connected with Fe2, but not with Zn1. The metal ion at the rubredoxin-like center is labeled Fe3. In the annealed omit (F_o-F_c) maps (**Figure IV-13** and **Figure IV-14**), the peak heights of Zn1, Fe2, and Fe3 are 22.0σ, 29.7σ and 31.3σ, respectively, in Zn,FeRbr (1.0 Å), and 16.4σ, 19.3σ and 19.9σ, respectively, in Zn,FeRbr (1.7 Å), as listed in **Table IV-7**. The ratios of the peak heights of Zn1, Fe2, and Fe3 between Zn,FeRbr (1.0 Å) and Zn,FeRbr (1.7 Å), are 1.34 (22.0σ /16.4σ), 1.54 (29.7σ /19.3σ), and 1.57(31.3σ /19.9σ), respectively, which are approximately equal to each other. This indicates that the two different crystals chosen for data collection at different wavelength have similar metal contents. The binuclear site of Zn,FeRbr was assigned as Zn1 and Fe2 during the

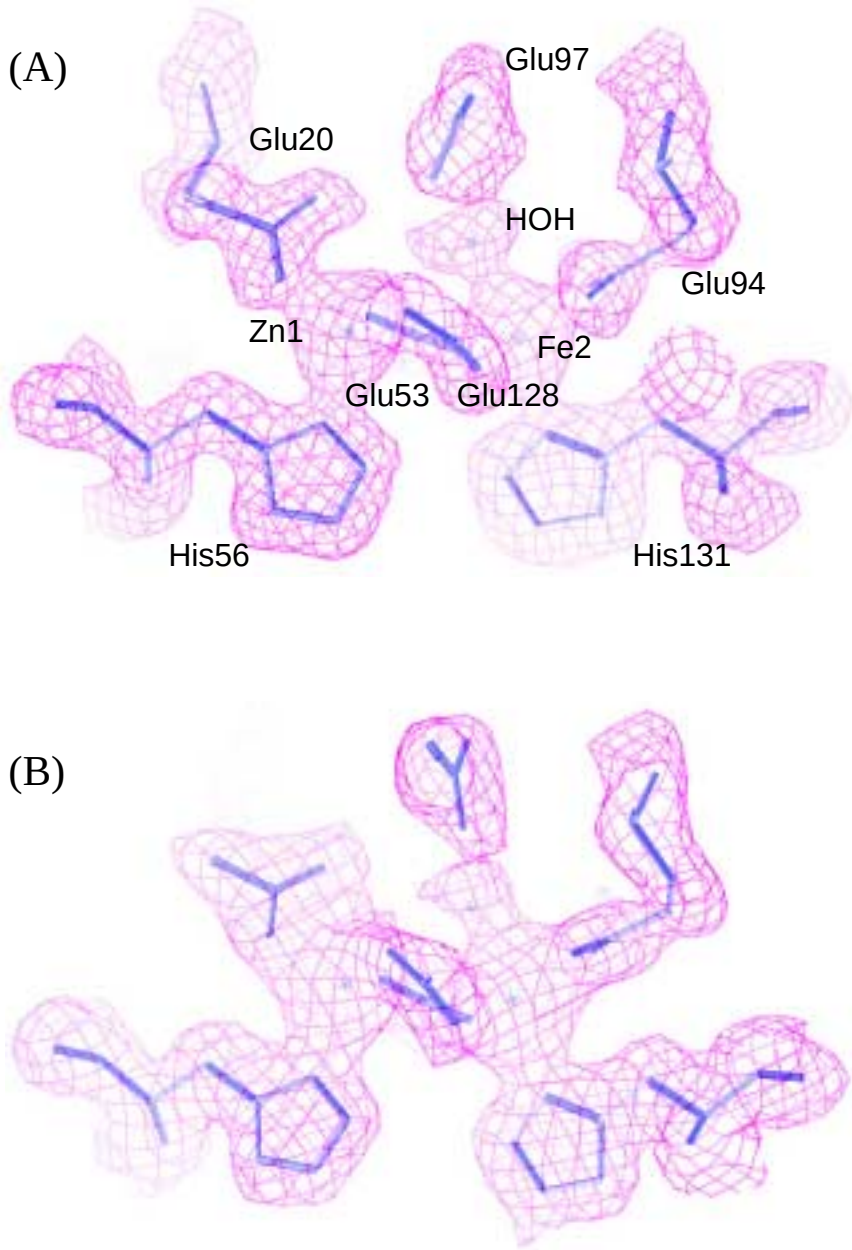

Figure IV-12. The final models and the composite omit maps ($2F_o$-F_c) contoured at 1.0σ at the binuclear site of (A) Zn,FeRbr (1.0 Å), (b) Zn,FeRbr (1.7 Å). Stars indicate positions of metal atoms and solvent oxygen ligands.

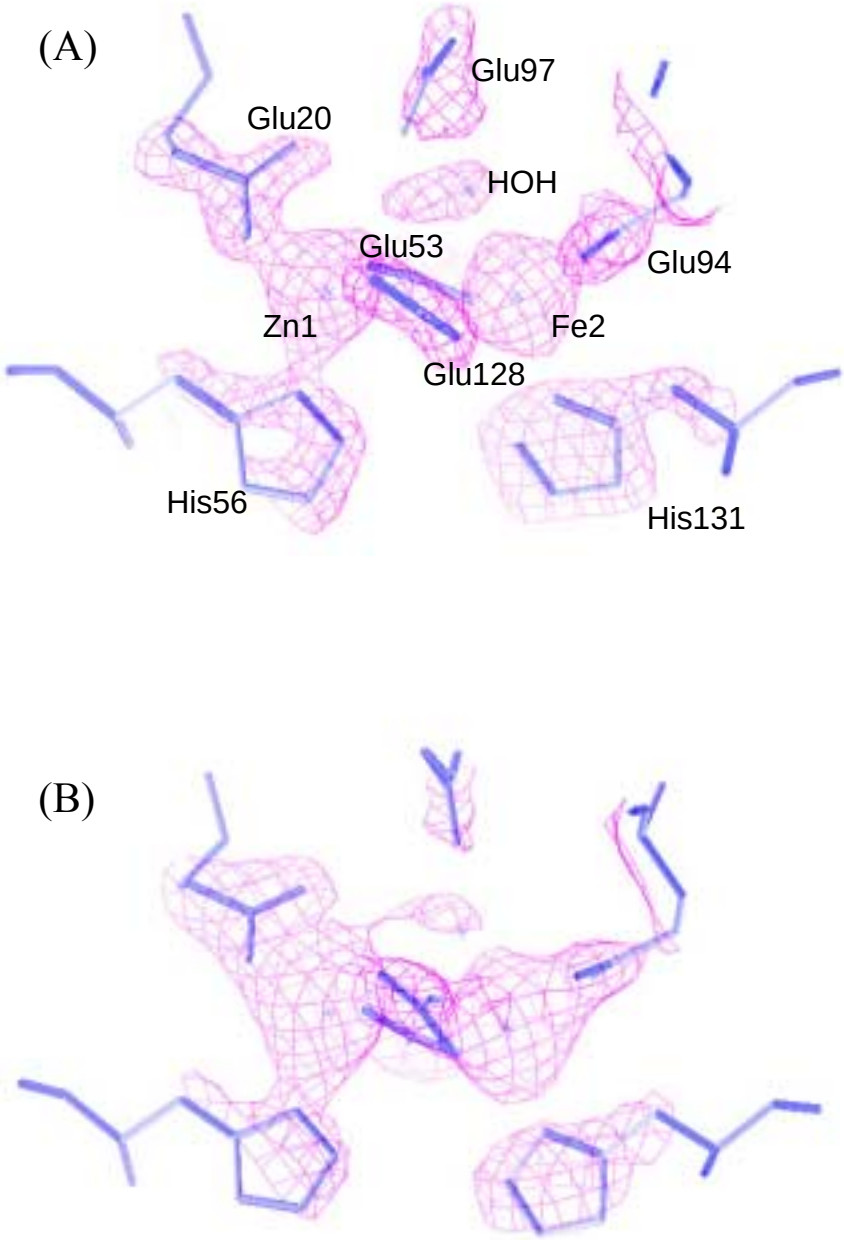

Figure IV-13. The final models and the annealed omit maps (F_o-F_c) contoured at 3σ, at the binuclear site of (A) Zn,FeRbr (1.0 Å), (B) Zn,FeRbr (1.7 Å), with Zn1, Fe2, Fe3 and HOH, as well as the surrounding residues within 3.5 Å of the above selected atoms omitted. Stars indicate positions of metal atoms and solvent oxygen ligands.

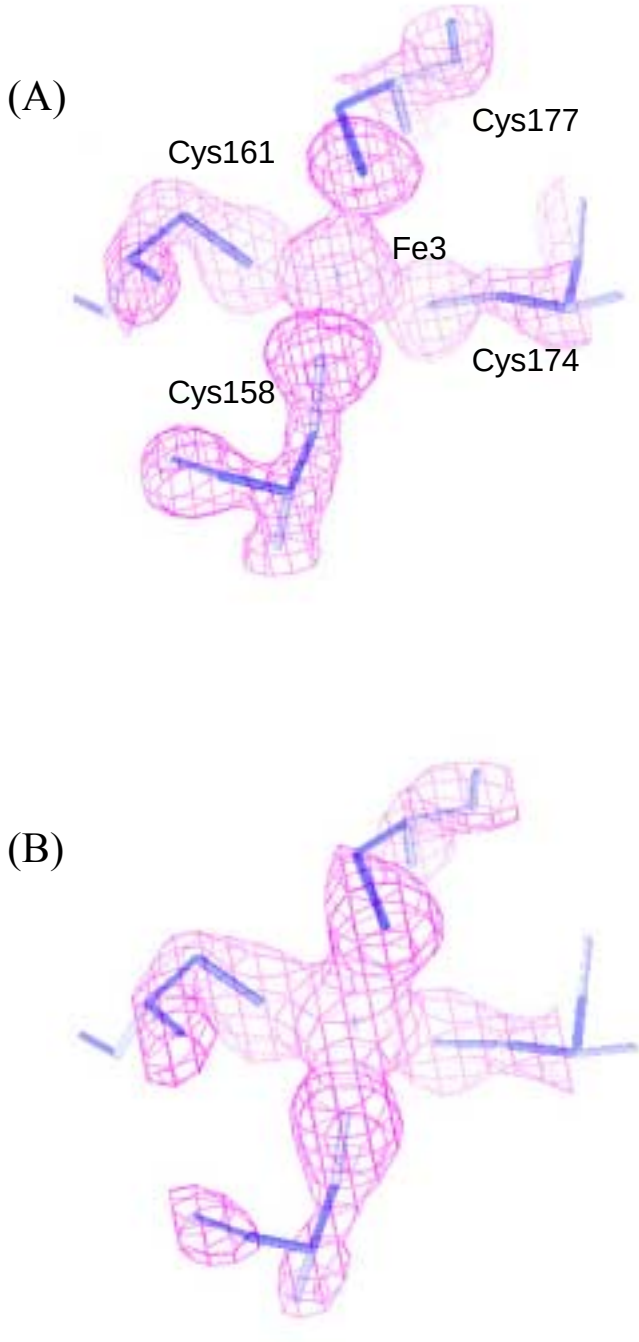

Figure IV-14. The final models and the annealed omit maps (F_o-F_c) contoured at 3σ, at the rubredoxin-like sites of (A) Zn,FeRbr (1.0 Å), (B) Zn,FeRbr (1.7 Å), with Zn1, Fe2, Fe3 and HOH, as well as the surrounding residues within 3.5 Å of the above selected atoms omitted. Stars indicate positions of iron atoms.

refinement, according to the structure of 1dvb (*60, 61*). However, the results of the anomalous scattering analysis of Zn1, Fe2, and Fe3 imply mixtures of zinc and iron at both Zn1 and Fe2 sites. Based on the peak heights in the Bijvoet difference Fourier maps (cf. **Table IV-7**), Zn1 and Fe2 seem to have more similar anomalous scattering behaviors to each other than either does to Fe3. The intensities of anomalous scattering for Zn1 and Fe2 are slightly higher than Fe3 for the 1.0 Å data, and both are much lower than Fe3 for the 1.7 Å data (cf. **Figure IV-15** and **Figure IV-16** and **Table IV-7**). The data, thus, also indicate that the metal contents at Fe2 and Fe3 differ from each other. In the following discussion, the labels of Zn1 will be changed to Zn(Fe)1, and Fe2 will be changed to Fe(Zn)2, to better represent the metal contents of the binuclear site of Zn,FeRbr obtaining from analysis of the anomalous scattering data. In **Figure IV-15** (B), the Bijvoet difference Fourier map of Zn,FeRbr (1.7 Å) shows an asymmetric electron density at the Zn(Fe)1 site. The center of this electron density is above the position of Zn(Fe)1 in the final model. This difference in position is probably due to partial iron occupancy at Zn(Fe)1 site, which has significantly higher anomalous scattering behavior than zinc at 1.7 Å (cf. **Figure IV-1**), whereas, at 1.0 Å, where the f'' for iron and zinc are more similar to each other, the shifted iron is indistinguishable from the Zn(Fe)1 center in the Bijvoet difference Fourier map as shown for Zn,FeRbr (1.0 Å) in **Figure IV-15** (A). Based on analysis of the absorption and EPR spectra discussed above, crystallization did not affect occupancies of the [$Fe(SCys)_4$] site which was fully occupied by iron. Therefore, the occupancy by iron at Fe3 can be assumed to be 1 in the Zn,FeRbr crystal structures. The percentages of iron and zinc in Zn(Fe)1 and Fe(Zn)2 sites can be calculated from their

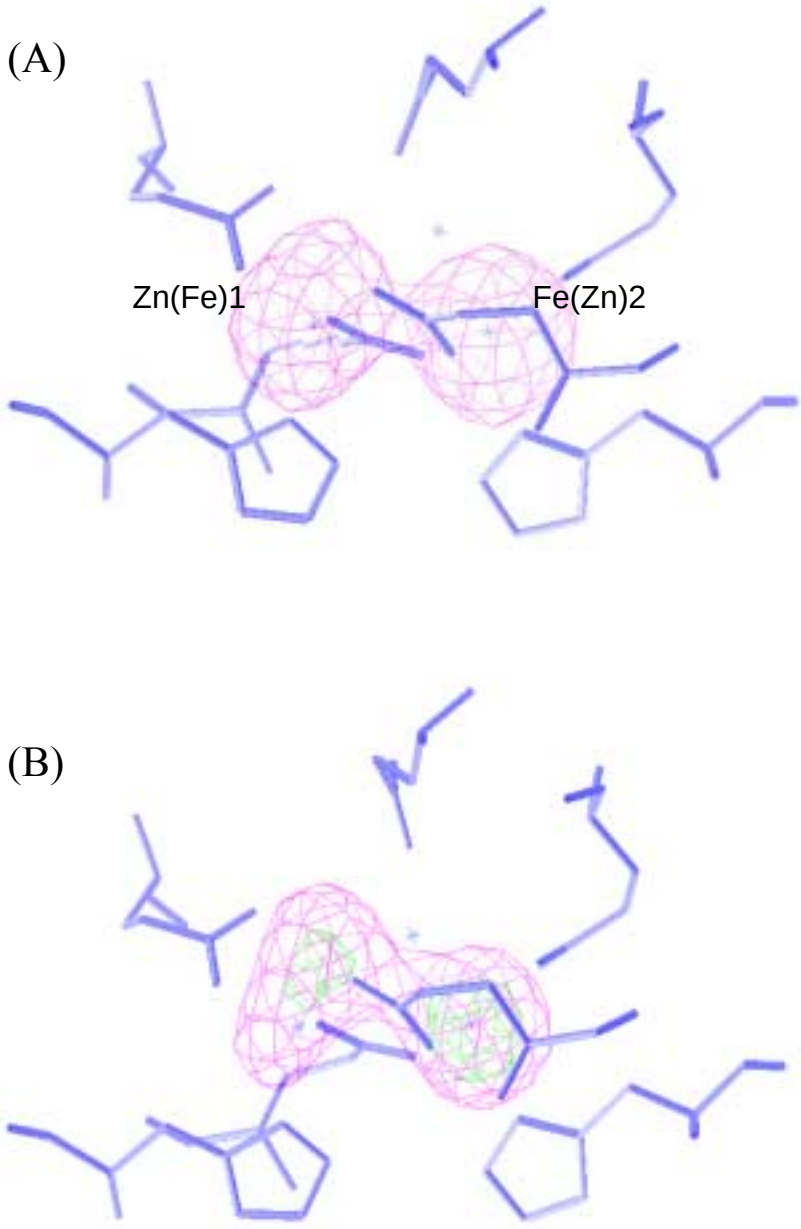

Figure IV-15. (A) The final model and the Bijvoet difference-Fourier map contoured at 3σ at the diiron sites of Zn,FeRbr (1.0 Å), and (B) the final model and the Bijvoet difference-Fourier map contoured at 3σ (magenta) and at 8σ (green) at the diiron sites of Zn,FeRbr (1.7 Å). Zn(Fe)1, Fe(Zn)2, and Fe3 were omitted from map calculations. Stars indicate positions of metal atoms and solvent oxygen ligands.

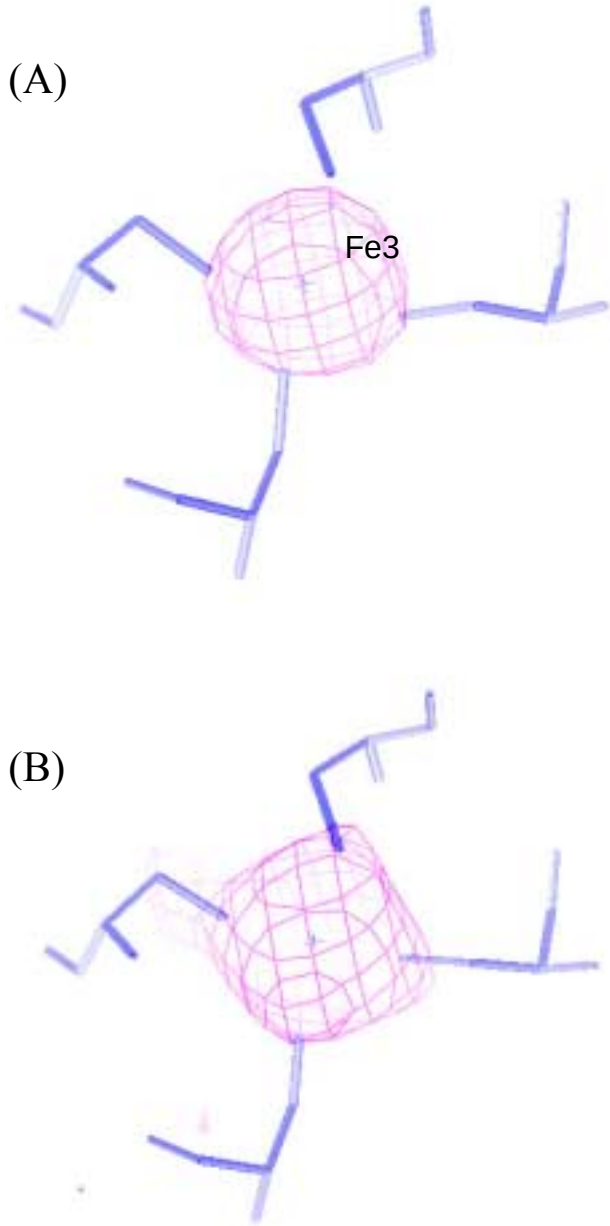

Figure IV-16. The final model and the Bijvoet difference-Fourier maps contoured at 3σ at the [Fe(III)$(SCys)_4$] sites of (A) Zn,FeRbr (1.0 Å) , (B) Zn,FeRbr (1.7 Å), with Zn(Fe)1, Fe(Zn)2, and Fe3 omitted. Stars indicate Fe3 center of the model.

anomalous scattering data (cf. **Table IV-7**) and the anomalous scattering coefficients of *f″* of zinc and iron (cf. **Figure IV-1**). Assuming the percentage of iron in Zn(Fe)1 is *a*, zinc in Zn(Fe)1 is *b*, Fe in Fe(Zn)2 is *c*, and Zn in Fe(Zn)2 is *d*, the values of *a*, *b*, *c*, and *d*, can be obtained by solving the following four simultaneous equations:

Zn(Fe)1 site, 1.0Å data: $22.0\sigma \times a + 22.0\sigma \times (2.55/1.55) \times b = 24.3$

Zn(Fe)1 site, 1.7Å data: $25.2\sigma \times a + 25.2\sigma \times (0.81/3.75) \times b = 10.5$

Fe(Zn)2 site, 1.0Å data: $22.0\sigma \times c + 22.0\sigma \times (2.55/1.55) \times d = 24.2$

Fe(Zn)2 site, 1.7Å data: $25.2\sigma \times c + 25.2\sigma \times (0.81/3.75) \times d = 14.2$

The solution gives $a = 31\%$, $b = 48\%$, $c = 48\%$, and $d = 37\%$. Thus, there are approximately 31% iron, 48% zinc, and 21% apo in Zn(Fe)1 site, and 48% iron, 37% zinc, and 15% apo in Fe(Zn)2 site. The total calculated metal content is, therefore, 3.58 iron (= 2 x (0.31 + 0.48 +1)) and 1.70 zinc (= 2 x (0.48 + 0.37)) per dimer in the crystal form of Zn,FeRbr.

The distances of metal ions with their ligands in Zn,FeRbrs are listed in **Table IV-8**. As shown in **Figure IV-17** (bottom), Zn(Fe)1 in Zn,FeRbr is tetrahedrally coordinated with one terminal monodentate carboxylate ligand from Glu20 Oε2, one histidine ligand from His56 Nδ1 and two μ-1,3 bridging bidentate carboxylate ligands shared with Fe(Zn)2 from Glu53 and 128. The Oε2 of Glu 20 is about 3.0 Å from Zn(Fe)1, too far to form a bond with Zn(Fe)1. Fe(Zn)2 is octahedrally coordinated by one His131 Nδ1, a bidentate carboxylate ligand of Glu94, one solvent ligand, and the bridging Glu53 and Glu128. Oε1 of Glu97 is 4.0 Å away from Zn(Fe)1, but within hydrogen bonding distance (~ 2.6 Å) of the solvent ligand to Fe(Zn)2; His56 is a ligand to Zn(Fe)1 with bond distance of 2.1 Å. Although the anomalous scattering calculation reveals that both

Table IV-8. Interatomic distances (Å) for iron/zinc sites of *D. vulgaris* Zn,FeRbrs

Atoms	Zn,FeRbr (1.0 Å)	Zn,FeRbr (1.7 Å)
Zn(Fe)1 – Glu 20OE1	2.0	2.0
Zn(Fe)1 –Glu 20OE2	(3.0)	(2.9)
Zn(Fe)1 – Glu 53OE1	2.0	2.1
Zn(Fe)1 – Glu 128OE2	2.0	2.0
Zn(Fe)1 – Glu 97OE1	(4.0)	(4.5)
Zn(Fe)1 – His 56 ND1	2.1	2.2
Zn(Fe)1 – HOH1	(3.4)	(3.3)
Fe(Zn)2 – Glu 94OE1	2.2	2.3
Fe(Zn)2 –Glu 94OE2	2.2	2.2
Fe(Zn)2 – Glu 53OE2	2.0	2.1
Fe(Zn)2 – Glu 128OE1	2.1	2.1
Fe(Zn)2 – His 131 ND1	2.2	2.3
Fe(Zn)2 – HOH1	2.3	2.3
Fe3 – Cys 158SG	2.4	2.4
Fe3 – Cys 161SG	2.3	2.3
Fe3 – Cys 174SG	2.3	2.3
Fe3 – Cys 177SG	2.4	2.3
average Fe3-CysSG	2.3	2.3
Zn(Fe)1 --- Fe(Zn)2	(3.8)	(3.7)
Zn(Fe)1 --- Fe3	(10.7)	(10.7)
Fe(Zn)2 --- Fe3	(12.0)	(12.0)

*Data in parenthesis are non-bonded distances.

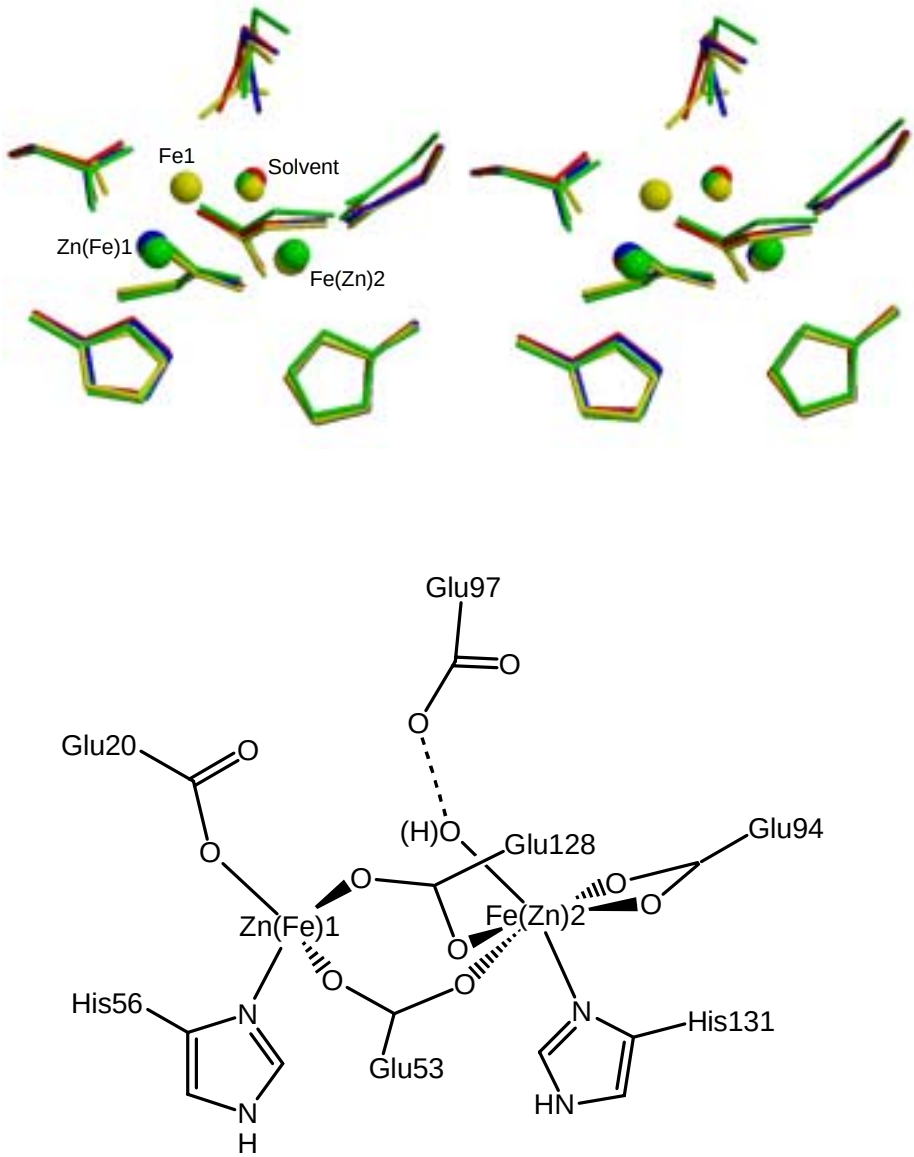

Figure IV-17. (Top) stereoview of the superposition of Zn,FeRbr (1.0 Å) (red), Zn,FeRbr (1.7 Å) (blue), all-iron Rbr_{ox} (yellow), and 1dvb (green) at the diiron sites. The smaller spheres represent solvent ligands, and the larger spheres represent metal ions. (Bottom) Schematic drawing of the diiron site structure of Zn,FeRbr (1.0 Å).

Zn(Fe)1 and Fe(Zn)2 site contain >30% iron, no solvent bridge is present in the Zn,FeRbr.

The oxidation states of the iron at Zn(Fe)1 and Fe(Zn)2 sites are unclear. The difference spectra of Zn,FeRbr minus oxidized rubredoxin seems to indicate residual oxo-bridged diferric sites, as shown in **Figure IV-18**. However, the iron at the Zn(Fe)1 sites is less likely to be ferric than ferrous, since the nearby Glu97 Oε1 and the solvent ligand of Fe(Zn)2 are available and better ligands to ferric than His56 Nδ1, as seen in the structure of all-iron Rbr_{ox} in Chapter III, and tetrahedrally coordinated Fe(III) with O or N ligands would be very unusual, as discussed in Section IV.C.1.2.3. From Lewis acidity considerations, the Fe(II) is more likely to bind Nδ1 in His56 than the Oε1 in Glu97, as seen in the crystal structure of all-iron Rbr_{red}. For Zn,FeRbr, the crystal used to collected data at 1.7 Å was also shown a very pale pink color compared to the deep red color of the original crystal before data collection, which implies the reduction of the rubredoxin-like center during data collection, whereas the reduction of the iron in the dimetal sites of Zn,FeRbr cannot be determined from the color change of the crystal. However, since partial reduction of the diiron site apparently occurred in ZnS_4Rbr exposed to synchrotron radiation, the iron in the dimetal sites in Zn,FeRbr was presumably reduced, too. When Zn,FeRbr was thawed in mineral oil, the color gradually changed to a deeper red close to the original color before exposure to the synchrotron radiation within minutes after thaswing, which indicates that the protein in the crystal was reoxidized by dioxygen. It seems that, unlike ZnS_4Rbr, all the iron at Zn(Fe)1 site in Zn,FeRbr became reduced, but the oxidation state of the iron at Fe(Zn)2 site is still uncertain. If assuming the iron and zinc are randomly distributed at both of the Zn(Fe)1 and Fe(Zn)2 sites, there will be 15%

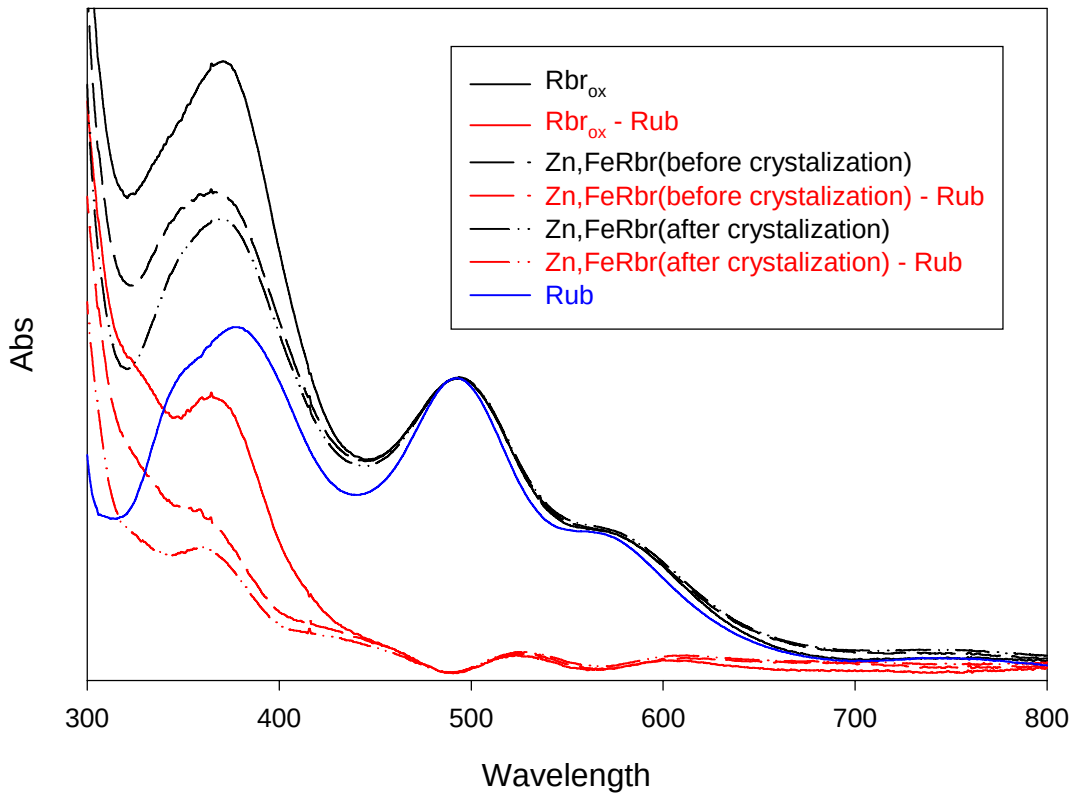

Figure IV-18. UV-vis spectra of *D. vulgaris* Rbr$_{ox}$, Zn,FeRbr$_{ox}$ before and after crystallization, and their difference spectra from *D. vulgaris* Rubredoxin (Rub), respectively. The protein absorbances are equalized at A_{494}.

Fe1(II),Fe2(?) (= 31% x 48%), 12% Fe1(II),Zn2(II) (= 31% x 37%), 23% Zn1(II),Fe2(?) (= 48% x 48%), 18% Zn1(II),Zn2(II) (= 48% x 37%), 5% Fe1(II),apo2 (= 31% x 15%), 7% Zn1,apo2 (= 48% x 15%), 10% apo1,Fe2(?) (= 21% x 48%), 8% apo1,Zn2 (= 21% x 37%), 3% apo1,apo2 (= 21% x 15%). To maintain the neutral charge of those binuclear sites, the solvent ligand to Fe(Zn)2 could be either a OH^- for 5 total charges (II, III) metal ions or a H_2O for 4 total charges (II,II) on the metal ions. The NADH peroxidase activities of dissolved Zn,FeRbr crystals (not exposed to synchrotron radiation) were ~37% that of all-iron Rbr. Considering that redox reactions are not possible for Zn^{2+}, and the one-electron oxidation of Rbr is quite slow and would generate hydroxyl radicals as discussed in Chapter II, the 37% activities of Zn,FeRbr were most likely due to the 15% diiron sites.

IV.C.2.2.4. Comparisons of Zn,FeRbr with other Zn/Fe-dimetal proteins

The diiron site structure of Zn,FeRbr is significantly different from the all-iron Rbr_{ox} or Rbr_{red}, but very similar to the binuclear center of 1dvb, an *D. vulgaris* Rbr structure, which was reported to contain an Zn1,Fe2 binuclear site (*60, 61*). The comparison of the binuclear site structures of Zn,FeRbr (1.0 Å), Zn,FeRbr (1.7 Å), all-iron Rbr_{ox} and 1dvb is shown in **Figure IV-17** (top). It is noteworthy that Zn^{2+} can displace a significant amount of $Fe^{2+,3+}$ at the Fe(Zn)2 sites, which indicates that although the structure of the corresponding Fe2 sites in all-iron Rbr_{ox} and Rbr_{red} is less flexible than the Fe1 site, it still shows significant liability. Based on the metal analysis before and after crystallized at least some of this substitution may have occurred during or after crystallzation.

The distance between Zn(Fe)1 and Fe(Zn)2 is 3.8 Å, which is close to the Zn(II) and Fe(III) distance in the binuclear site of 1dvb (3.7Å) (*60, 61*). In the binuclear site of 1dvb,

the assumption of a zinc ion occupancy at Zn(Fe)1 was made from a comparison of the relative anomalous scattering between the metal 1 and metal 2 sites, with data collected only at 1.54 Å. It is still possible that each putative zinc site and iron site in 1dvb actually contain mixtures of both zinc and iron.

Di-zinc or zinc and iron bimetal sites (**Figure IV-19**) are also found in Ferritin (EcFtnA) of *E. coli* (Zn(II) + Zn(II)) (*129*), purple acid phosphatases (PAPs), such as kidney bean purple acid phosphatase (KBPAP) (*64, 152*) and Uteroferrin (FeZnUf) (Fe(III) + Zn(II)) (*153*). The distances of the two metals in each binuclear site of EcFtnA (Zn(II) + Zn(II), ~ 3.4 Å) (*129*), and KBPAP (*64*) and FeZnUf (*153*) (Fe(III) + Zn(II), ~ 3.3 Å) are much shorter than the distance of Zn(Fe)1 and Fe(Zn)2 in Zn,FeRbr. A solvent-bridge between the two metals is maintained in dizinc EcFtnA and a hydoxo-bridge in Zn,Fe-binuclear KBPAP and FeZnUf. The conformations of the ligands to the dizinc site in EcFtnA undergo fewer changes from their original diferric site positions than the corresponding sites in Zn,FeRbr and all-iron Rbr_{ox}, and both Zn ions in EcFtnA are almost five-coordinated, whereas in Zn,FeRbr, the Zn(Fe)1 is only four-coordinated, whereas the Fe(Zn)2 site stays six-coordinated. The Zn(Fe)1---Fe(Zn)2 distance in Zn,FeRbr is also close to the Zn(II)---Zn(II) distance in a de novo designed protein crystal structure (3.9Å) (*154*), a mimic of diiron proteins with EXXH motifs, as shown in **Figure IV-19** (C). This de novo designed dizinc site structure is very close to that of the diferrous site in reduced Δ9D (**Figure I-14** (bottom), Chapter I), but significant different from EcFtnA and Zn,FeRbr.

The capabilities of exchanging iron with zinc at the diiron site of Rbr is most probably due to the solvent accessibility of the diiron site such that zinc ions could approach the

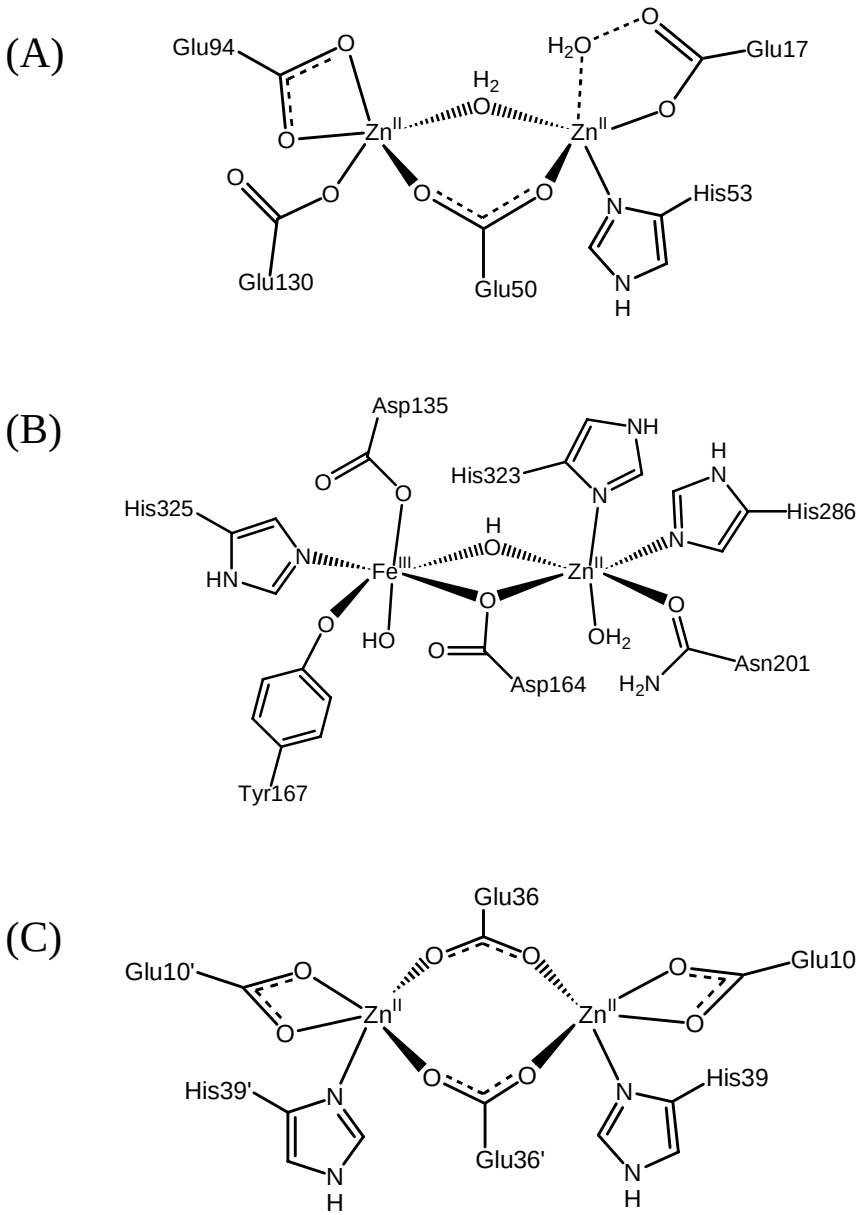

Figure IV-19. Schematic drawing of the binuclear sites of (A) *E. coli* ferritin (EcFtnA) (*129*), (B) kidney bean purple acid phosphatase (KBPAP) (*64*), and (C) de novo designed protein (*154*).

diiron site, even reaching the Fe2 site, which is relatively more buried in the protein matrix. It is clear that the all-iron Rbr has significantly higher peroxidase activity than do the zinc derivatives. According to comparison of the activities and the structures of Zn,FeRbr and all-iron Rbr, we can conclude that the iron and its ligands at the Fe2 site could stabilize the diiron site, while the iron at Fe1 site could move back and forth to mediate the electrons transferred from the rubredoxin site during the catalytic reaction of all-iron Rbr_{ox}.

REFERENCES

1. Mukhopadhyay, S. N., and Das, K. D. (1994) *Oxygen responses, reactivities, and measurements in biosystem.*, CRC Press, Inc., Boca Raton.
2. Storz, G., and Imlay, J. A. (1999) *Curr. Opin. Microbiol. 2*, 188-94.
3. Valentine, J. S., Wertz, D. L., Lyons, T. J., Liou, L. L., Goto, J. J., and Gralla, E. B. (1998) *Curr. Opin. Chem. Biol. 2*, 253-62.
4. Packer, L., Rosen, P., Tritschler, H. J., King, G. L., and AzzI, A. (2000) *Antioxidants in diabetes management*, Marcel Dekker, Inc., Boca Raton.
5. Sies, H. (1991) *Oxidation stress: oxidants and antioxidants*, Academic press, Inc.
6. Sawyer, D. T. (1991) *Oxygen chemistry*, Oxford University Press, Inc., New York.
7. Ingraham, L. L., and Meyer, D. L. (1985) *Biochemistry of dioxygen*, Plenum Press, New York.
8. Yan, X. S., and Wang, C. F. (1999) *General inorganic chemistry*, 2 ed., Beijing Daxue Chubanshe, Beijing.
9. Halliwell, B., and Gutteridge, J. M. C. (1989) *Free radicals in biology and medicine*, 2 ed., Oxford University Press, Oxford.
10. McCord, J. M., and Fridovich, I. (1969) *J. Biol. Chem. 244*, 6049-55.
11. Chance, B., Sies, H., and Boveris, A. (1979) *Physiol. Rev. 59*, 527-605.
12. Fridovich, I. (1986) *Adv. Enzymol. Relat. Areas. Mol. Biol. 41*.
13. Steinman, H. (1982) *Superoxide dismutase: protein chemistry and structure-function relationship*, Vol. 1, CRC Press, Boca Raton.

14. Bannister, J. V., Bannister, W. H., and Rotilio, G. (1987) *CRC Crit. Rev. Biochem. 22*, 111–80.

15. Holm, R. H., Kennepohl, P., and Solomon, E. I. (1996) *Chem. Rev. 96*, 2239-14.

16. Youn, H. D., Kim, E. J., Roe, J. H., Hah, Y. C., and Kang, S. O. (1996) *Biochem. J. 318*, 889–96.

17. Kim, E. J., Kim, H. P., Hah, Y. C., and Roe, J. H. (1996) *Eur. J. Biochem. 241*, 178–85.

18. Youn, H. D., Youg, H., Lee, J. W., Yim, Y. I., Lee, J. K., Hah, Y. C., and Kang, S. O. (1996) *Arch. Biochem. Biophys. 334*, 341–8.

19. Sugio, S., Hiraoka, B. Y., and Yamakura, F. (2000) *Eur. J. Biochem. 267*, 3487-95.

20. Gonzalez-Flecha, B., and Demple, B. (1995) *J. Biol. Chem. 270*, 13681-7.

21. Zamocky, M., and Koller, F. (1999) *Prog. Biophys. Mol. Biol. 72*, 19-66.

22. Kono, Y., and Fridovich, I. (1983) *J. Biol. Chem. 258*, 6015-9.

23. Allgood, G. S., and Perry, J. J. (1986) *J. Bacteriol. 168*, 563-7.

24. Kalko, S. G., Gelpi, J. L., Fita, I., and Orozco, M. (2001) *J. Am. Chem. Soc. 123*, 9665-72.

25. Flohe, L. (1985) *Curr. Top. Cell. Regul. 27*, 473-8.

26. Flohe, L. (1989) *The selenoprotein glutathione peroxidase. In Glutathione: chemical, biochemical, medical aspects*, John Wiley, Sons, New York.

27. Ross, R. P., and Claiborne, A. (1991) *J. Mol. Biol. 221*, 857-71.

28. Claiborne, A., Yeh, J. I., Mallett, T. C., Luba, J., Crane, E. J. 3rd., Charrier, V., and Parsonage, D. (1999) *Biochemistry 38*, 15407-16.

29. Crane, E. J. 3rd., Vervoort, J., and Claiborne, A. (1997) *Biochemistry 36*, 8611-8.

30. Isaac, I. S., and Dawson, J. H. (1999) *Essays Biochem. 34*, 51-69.

31. Yonetani, T., and Ohnishi, T. (1966) *J. Biol. Chem. 241*, 2983-4.

32. Villalain, J., Moura, I., Liu, M. C., Payne, W. J., LeGall, J., Xavier, A. V., and Moura, J. J. G. (1984) *Eur. J. Biochem. 141*, 305-12.

33. Raven, E. L. (2000) *Subcell. Biochem. 35*, 317-49.

34. Coves, J., Eschenbrenner, M., and Fontecave, M. (1991) *Biochem. Biophys. Res. Commun. 178*, 54-9.

35. Gregory, E. M., Moore, W. E. C., and Holdeman, L. V. (1978) *Applied and environmental microbiology 35*, 988-91.

36. Loewen, P. C., Klotz, M. G., and Hassett, D. J. (2000) *ASM News 66*, 76-82.

37. Lehmann, Y., Meile, L., and Teuber, M. (1996) *J. Bacteriol. 178*, 7152-8.

38. Lumppio, H. L., Shenvi, N. V., Summers, A. O., Voordouw, G., and Kurtz, D. M., Jr. (2001) *J. Bacteriol. 183*, 101-8.

39. Jenney, F. E., Jr., Verhagen, M. F., Cui, X., and Adams, M. W. (1999) *Science 286*, 306-9.

40. Brumlik, M. J., and Voordouw, G. (1989) *J. Bacteriol. 171*, 4996-5004.

41. Chen, L., Sharma, P., Le Gall, J., Mariano, A. M., Teixeira, M., and Xavier, A. (1994) *Eur. J. Biochem. 226*, 613-8.

42. Coehlo, A. V., Matias, P., Fülop, V., Thomson, A., Gonzalez, A., and Carrondo, M. A. (1997) *J. Inorg. Biochem. 2*, 680-9.

43. Lombard, M., Fontecave, M., Touati, D., and Niviere, V. (2000) *J. Biol. Chem. 275*.

44. Coulter, E. D., Emerson, J. P., and Kurtz, D. M., Jr. (2000) *J. Am. Chem. Soc. 122*, 11555-6.

45. Voordouw, J. K., and Voordouw, G. (1998) *Appl. Environ. Microbiol. 64*, 2882-7.

46. Liochev, S. I., and Fridovich, I. (1997) *J. Biol. Chem. 272*, 25573-5.

47. Pianzzola, M. J., Soubes, M., and Touati, D. (1996) *J. Bacteriol. 178*, 6736-42.

48. Coulter, E. D., Shenvi, N. V., and Kurtz, D. M., Jr. (1999) *Biochem. Biophys. Res. Commun. 255*, 317-23.

49. Coulter, E. D., Shenvi, N. V., Beharry, Z. M., Smith, J. J., Prickril, B. C., and Kurtz, D. M., Jr. (2000) *Inorg. Chim. Acta. 297*, 231-41.

50. Alban, P. S., Popham, D. L., Rippere, K. E., and Krieg, N. R. (1998) *J. Appl. Microbiol. 85*, 875-82.

51. Alban, P. S., and Krieg, N. R. (1998) *Can. J. Microbiol. 44*, 87-91.

52. LeGall, J., Prickril, B. C., Moura, I., Xavier, A. V., Moura, J. J., and Huynh, B. H. (1988) *Biochemistry 27*, 1636-42.

53. Moura, I., Tavares, P., and Ravi, N. (1994) *Methods Enzymol. 243*, 216-40.

54. Pierik, A. J., Wolbert, R. B., Portier, G. L., Verhagen, M. F., and Hagen, W. R. (1993) *Eur. J. Biochem. 212*, 237-45.

55. GenBank. *C. acetobutylicum,* Acc. No. AJ012353.1; *C. perfringens,* Acc. No. X92844.1; *C. dificile,* www.tigr.org; *T. maritima,*Acc. No. AE001739.1; *P. gingivalis,* www.tigr.org; *M. jannaschii,* Acc. No. U67520.1; *M. thermoautotrophicum,* Acc. No. AE000854.1; *A. fulgidus,* Acc. Nos.

AE001047.1, AE000944.1, AE000989.1, AE001081.1; *P. abysii,* Acc. No. AJ248285.1; *P. furiosus,*Acc. No. AF156097.1.

56. Dave, B. C., Czernuszewicz, R. S., Prickril, B. C., and Kurtz, D. M. J. (1994) *Biochemistry 33*, 3572-6.

57. Lei, Q. P., Cui, X., Kurtz, D. M., Jr., Amster, I. J., Chernushevich, I. V., and Standing, K. G. (1998) *Anal. Chem. 70*, 1838-46.

58. deMare, F., Kurtz, D. M., Jr., and Nordlund, P. (1996) *Nat. Struct. Biol. 3*, 539-46.

59. Gupta, N., Bonomi, F., Kurtz, D. M., Jr., Ravi, N., Wang, D. L., and Huynh, B. H. (1995) *Biochemistry 34*, 3310-8.

60. Sieker, L. C., Holmes, M., Le Trong, I., Turley, S., Santarsiero, B. D., Liu, M. Y., LeGall, J., and Stenkamp, R. E. (1999) *Nat. Struct. Biol. 6*, 308-9.

61. Sieker, L. C., Holmes, M., Le Trong, I., Turley, S., Liu, M. Y., LeGall, J., and Stenkamp, R. E. (2000) *J. Biol. Inorg. Chem. 5*, 505-13.

62. deMare, F., Nordlund, P., Gupta, N., Shenvi, N., Cui, X., and Kurtz, D. M., Jr. (1997) *Inorg. Chim. Acta. 263*, 255-62.

63. Kurtz, D. M. J. (1997) *J. Biol. Inorg. Chem. 2*, 159-167.

64. Klabunde, T., Strater, N., Frohlich, R., Witzel, H., and Krebs, B. (1996) *J. Mol. Biol. 259*, 737-48.

65. Wilkins, R. G., and Harrington, P. C. (1983) *Adv. Inorg. Biochem. 5*, 51-85.

66. Nordlund, P., and Eklund, H. (1995) *Curr. Opin. Struct. Biol. 5*, 758-66.

67. Stenkamp, R. E., Sieker, L. C., and Jensen, L. H. (1984) *J. Am. Chem. Soc. 106*, 618-22.

68. Holmes, M. A., Letrong, I., Turley, S., Sieker, L. C., and Stenkamp, R. E. (1991) *J. Mol. Biol. 218*, 583-93.

69. Merkx, M., Kopp, D. A., Sazinsky, M. H., Blazyk, J. L., Muller, J., and Lippard, S. J. (2001) *Angew. Chem. Int. Ed. Engl. 40*, 2782-807.

70. Westerheide, L., Muller, F. K., Than, R., Krebs, B., Dietrich, J., and Schindler, S. (2001) *Inorg. Chem. 40*, 1951-61.

71. Wallar, B. J., and Lipscomb, J. D. (1996) *Chem. Rev. 96*, 2625-58.

72. Reichard, P. (1993) *Science 260*, 1773-7.

73. Hogbom, M., Huque, Y., Sjoberg, B. M., and Nordlund, P. (2002) *Biochemistry 41*, 1381-9.

74. Lindqvist, Y., Huang, W., Schneider, G., and Shanklin, J. (1996) *EMBO J. 15*, 4081-92.

75. Fox, B. G., Shanklin, J., Somerville, C., and Munck, E. (1993) *Proc. Natl. Acad. Sci. U. S. A. 90*, 2486-90.

76. Fox, B. G., Shanklin, J., Ai, J., Loehr, T. M., and Sanders-Loehr, J. (1994) *Biochemistry 33*, 12776-86.

77. Shu, L., Broadwater, J. A., Achim, C., Fox, B. G., Munck, E., and Que, L., Jr. (1998) *J. Biol. Inorg. Chem. 3*, 392-400.

78. Broadwater, J. A., Ai, J., Loehr, T. M., Sanders-Loehr, J., and Fox, B. G. (1998) *Biochemistry 37*, 14664-71.

79. Broadwater, J. A., Achim, C., Munck, E., and Fox, B. G. (1999) *Biochemistry 38*, 12197-204.

80. Moenne-Loccoz, P., Krebs, C., Herlihy, K., Edmondson, D. E., Theil, E. C., Huynh, B. H., and Loehr, T. M. (1996) *Biochim. Biophys. Acta. 1275*, 161-203.

81. Harrison, P. M., and Arosio, P. (1996) *Biochim. Biophys. Acta. 1275*, 161-203.

82. Moenne-Loccoz, P., Krebs, C., Herlihy, K., Edmondson, D. E., Theil, E. C., Huynh, B. H., and Loehr, T. M. (1999) *Biochemistry 38*, 5290-5.

83. Pereira, A. S., Small, W., Krebs, C., Tavares, P., Edmondson, D. E., Theil, E. C., and Huynh, B. H. (1998) *Biochemistry 37*, 9871-6.

84. Hwang, J., Krebs, C., Huynh, B. H., Edmondson, D. E., Theil, E. C., and Penner-Hahn, J. E. (2000) *Science 287*, 122-5.

85. Sliva, K. E., Stankovich, M. T., and Que, L., Jr. (1993) *J. Inorg. Biochem. 51*, 306.

86. Paulsen, K. E., Liu, Y., Fox, B. G., Lipscomb, J. D., Munck, E., and Stankovich, M. T. (1994) *Biochemistry 33*, 713-722.

87. Liu, M. Y., and LeGall, J. (1990) *Biochem. Biophys. Res. Commun. 171*, 313-8.

88. Bonomi, F., Kurtz, D. M., Jr., and Cui, X. (1996) *J. Biol. Inorg. Chem. 1*, 67-72.

89. Lumppio, H. L., Shenvi, N. V., Garg, R. P., Summers, A. O., and Kurtz, D. M., Jr. (1997) *J. Bacteriol. 179*, 4607-15.

90. Neidle, E. L., Shapiro, M. K., and Ornston, L. N. (1987) *J. Bacteriol. 169*, 5496-503.

91. Coulter, E. D., and Kurtz, D. M., Jr. (2001) *Arch. Biochem. Biophys. 394*, 76-86.

92. Bsat, N., Herbig, A., Casillas-Martinez, L., Setlow, P., and Helmann, J. D. (1998) *Mol. Microbiol. 29*, 189-98.

93. Lumppio, H. L. (2000) *Characterization of oxidative stress proteins from the anaerobic Desulfovibrio vulgaris*, University of Georgia, Athens.

94. Massey, V., and Hemmerich, P. (1978) *Biochemistry 17*, 9-16.

95. http://www.olisweb.com/.

96. Ballou, D. P. (1978) *Methods Enzymol. 54*, 85-93.

97. Bollinger, J. M. J., Tong, W. H., Ravi, N., Huynh, B. H., Edmondson, D. E., and Stubbe, J. A. (1995) *Methods Enzymol. 258*, 278-303.

98. Bossek, U., Hummel, H., Weyhermuller, T., Bill, E., and Wieghardt, K. (1995) *Angew. Chem. Int. Ed. Engl. 34*, 2642-5.

99. Payne, S. C., and Hagen, K. S. (2000) *J. Am. Chem. Soc. 122*, 6399-410.

100. Feitelson, J., and Hayon, E. (1973) *J. Phys. Chem. 77*, 10-5.

101. Bonomi, F., Iametti, S., Kurtz, D. M., Jr., Ragg, E. M., and Richie, K. A. (1998) *J. Biol. Inorg. Chem. 3*, 595-605.

102. Gerez, C., and Fontecave, M. (1992) *Biochemistry 31*, 780-6.

103. Davydov, A., Schmidt, P. P., and Graslund, A. (1996) *Biochem. Biophys. Res. Commun. 219*, 213-8.

104. Hatchikian, E. C., J., L., and Bell, G. R. (1977) in *Superoxide and superoxide dismutase.* (Michelson, A. M., McCord, J. M., and I., F., Eds.), Academic Press, London, United Kingdom.

105. Kurtz, D. M., Jr., and Coulter, E. D. (2001) *Chemtracts 14*, 407-35.

106. Kurtz, D. M., Jr., and Prickril, B. C. (1991) *Biochem. Biophys. Res. Commun. 181*, 337-41.

107. Karlsson, A., Beharry, Z. M., Eby, D. M., Coulter, E. D., Neidle, E. L., Kurtz, D. M., Jr., Eklund, H., and Ramaswamy, S. (2002) *J. Mol. Biol. in press*.

108. Otwinowski, Z. (1993) *Proceedings of the CCP4 weekend.*, Daresbury Laboratories, Warrington, UK.

109. Brünger, A. T., Adams, P. D., Clore, G. M., DeLano, W. L., Gros, P., Grosse-Kunstleve, R. W., Jiang, J. S., Kuszewski, J., Nilges, M., Pannu, N. S., Read, R. J., Rice, L. M., Simonson, T., and Warren, G. L. (1998) *Acta Crystallogr. D Biol. Crystallog. 54*, 905-21.

110. Jones, T., Zou, J., Cowan, S., and Kjeldgaard, M. (1991) *Acta. Cryst. A 47*, 110-9.

111. Sturgeon, B. E., Doan, P. E., Liu, K. E., Burdi, D., Tong, W. H., Nocek, J. M., Gupta, N., Stubbe, J., Kurtz, D. M., Jr., Lippard, S. J., and Hoffman, B. M. (1997) *J. Am. Chem. Soc. 119*, 375-86.

112. Kleywegt, G. J., and Jones, T. A. (1998) *Acta. Cryst. D54*, 1119-31.

113. Laskowski, R. A., Macarthur, M. W., Moss, D. S., and Thornton, J. M. (1993) *J. Appl. Cryst. 26*, 283-91.

114. Kurtz, D. M., Jr. (1990) *Chem. Rev. 90*, 585-606.

115. Dong, Y. H., Fujii, F., Hendrich, M. P., Keising, R. A., Pan, G. F., Randall, C. R., Wilkinson, E. C., Zang, Y., Que, L., Jr., Fox, B. G., Kauffmann, K., and Münck, E. (1995) *J. Am. Chem. Soc. 117*, 2778-92.

116. Ardon, M., and Bino, A. (1987) *Struct. Bonding (Berlin) 65*, 1-28.

117. Mizoguchi, T. J., and Lippard, S. (1997) *J. Inorg. Chem. 36*, 4526-33.

118. Mizoguchi, T. J., Davydov, R. M., and Lippard, S. J. (1999) *Inorg. Chem. 38*, 4098-103.

119. Eidsness, M. K., Burden, A. E., Richie, K. A., Kurtz, D. M., Jr., Scott, R. A., Smith, E. T., Ichiye, T., Beard, B., Min, T., and Kang, C. (1999) *Biochemistry 38*, 14803-9.

120. Andersson, M. E., Hogbom, M., Rinaldo-Matthis, A., Andersson, K. K., Sjoberg, B. M., and Nordlund, P. (1999) *J. Am. Chem. Soc. 121*, 2346-52.

121. DeMunno, G., Poerio, T., Viau, G., Julve, M., Lloret, F., Journaux, Y., and Riviere, E. (1996) *Chem. Commun.*, 2587-88.

122. Ai, J. Y., Broadwater, J. A., Loehr, T. M., Sanders-Loehr, J., and Fox, B. G. (1997) *J. Biol. Inorg. Chem. 2*, 37-45.

123. Mckee, V., Zvagulis, M., Dagdigian, J. V., Patch, M. G., and Reed, C. A. (1984) *J. Am. Chem. Soc. 106*, 4765-72.

124. Sorrell, T. N., O'Connor, C. J., Anderson, O. P., and Reibenspies, J. H. (1985) *J. Am. Chem. Soc. 107*, 4199-206.

125. Kitajima, N., Fujisawa, K., Hikichi, S., and Morooka, Y. (1993) *J. Am. Chem. Soc. 115*, 7874-5.

126. Tuczek, F., and Bensch, W. (1995) *Inorg. Chem. 34*, 1482-6.

127. Stenkamp, R. E. (1994) *Chem. Rev. 94*, 715-26.

128. Armstrong, G. D., and Sykes, A. G. (1986) *Inorg. Chem. 25*, 3514-6.

129. Stillman, T. J., Hempstead, P. D., Artymiuk, P. J., Andrews, S. C., Hudson, A. J., Treffry, A., Guest, J. R., and Harrison, P. M. (2001) *J. Mol. Biol. 307*, 587-603.

130. Harrison, P. M., Hempstead, P. D., Artymiuk, P. J., and Andrews, S. C. (1998) in *Metal ions in biological systems* (Sigel, A., and Sigel, H., Eds.), Marcel-Dekker, Inc., New York.

131. Frolow, F., Kalb Gilboa, J., and Yariv, J. (1994) *Nature Struct. Biol. 1*, 453-60.

132. LeBrun, N. E., Thomson, A. J., and Moore, G. R. (1997) *Struct. Bond. 88*, 103-38.

133. Yang, X., Le Brun, N. E., Thomson, A. J., Moore, G. R., and Chasteen, N. D. (2000) *Biochemistry 39*, 4915-23.

134. Nordlund, P., and Eklund, H. (1993) *J. Mol. Biol. 232*, 123-64.

135. Logan, D. T., Su, X. D., Aberg, A., Regnstrom, K., Hajdu, J., Eklund, H., and Nordlund, P. (1996) *Structure 4*, 1053-64.

136. Whittington, D. A., and Lippard, S. J. (2001) *J. Am. Chem. Soc. 123*, 827-38.

137. Eriksson, M., Jordan, A., and Eklund, H. (1998) *Biochemistry 37*, 13359-69.

138. Elango, N., Radhakrishnan, R., Froland, W. A., Wallar, B. J., Earhart, C. A., Lipscomb, J. D., and Ohlendorf, D. H. (1997) *Protein Sci.*, 556-68.

139. Feig, A. L., and Lippard, S. J. (1994) *Chem. Rev. 94*, 759-805.

140. Smoukov, S. K., Davydov, R. M., Doan., P. E., Sturgeon, B., Hoffman, B. M., and Kurtz, D. M., Jr. (2002) *Biochemistry submitted*.

141. Branchaud, B. P. (1999) in *Metal ions in biological systems* (Sigel, A., and Sigel, H., Eds.), Marcel-Dekker, Inc., New York.

142. Barynin, V. V., Whittaker, M. M., Antonyuk, S. V., Lamzin, V. S., Harrison, P. M., Artymiuk, P. J., and Whittaker, J. W. (2001) *Structure 9*, 725-38.

143. Gassner, G. T., and Lippard, S. J. (1999) *Biochemistry 38*, 12768-85.

144. Dauter, Z., Wilson, K. S., Sieker, L. C., Moulis, J. M., and Meyer, J. (1996) *Proc. Natl. Acad. Sci. U. S. A. 93*, 8836-40.

145. Glusker, J. P., Lewis, M., and Rossi, M. (1994) *Crystal structure analysis for chemists and biologists*, VCH Publishers, Inc., New York.

146. http://www.bmsc.washington.edu/scatter/.

147. http://cns.csb.yale.edu/v1.1/.

148. Copyright (c) 1982, 1985, 1986, 1987, 1989, 1991, 1994, 1995, 1996, 1997, 1998 Genetics Computer Group Inc., a wholly owned subsidiary of Oxford Molecular Group, Inc. All rights reserved.

149. Schreiber, P., Wieghardt, K., Nuber, B., and Weiss, J. (1990) *Z. Naturforsch. B 45*, 619-28.

150. Marlin, D. S., Olmstead, M. M., and Mascharak, P. K. (2000) *Inorg. Chim. Acta. 297*, 106-14.

151. DeWitt, J. G., Bentsen, J. G., Rosenzweig, A. C., Hedman, B., Green, J., Pilkington, S., Papaefthymiou, G. C., Dalton, H., Hodgson, K. O., and Lippard, S. J. (1991) *J. Am. Chem. Soc. 113*, 9219-35.

152. Strater, N., Klabunde, T., Tucker, P., Witzel, H., and Krebs, B. (1995) *Science 268*, 1489-92.

153. Wang, X., Randall, C. R., True, A. E., and Que, L., Jr. (1996) *Biochemistry 35*, 13946-54.

154. Lombardi, A., Summa, C. M., Geremia, S., Randaccio, L., Pavone, V., and DeGrado, W. F. (2000) *Proc. Natl. Acad. Sci. U. S. A. 97*, 6298-305.